Search for New Physics in Electron-Positron Interactions with Photons in the Final State

DISSERTATION

zur Erlangung des akademischen Grades
doctor rerum naturalium
(Dr. rer. nat.)
im Fach Physik

eingereicht an der
Mathematisch-Naturwissenschaftlichen Fakultät I
Humboldt-Universität zu Berlin

von
Herr Dipl.-Phys. Daniel Ruschmeier
geboren am 16.12.1968 in Minden

Präsident der Humboldt-Universität zu Berlin:
Prof. Dr. Dr. h.c. Hans Meyer

Dekan der Mathematisch-Naturwissenschaftlichen Fakultät I:
Prof. Dr. Jürgen Rabe

Gutachter:

1. Prof. Dr. Thomas Hebbeker
2. Prof. Dr. Guy Coignet
3. Prof. Dr. Hermann Kolanoski

eingereicht am: 14. September 1999
Tag der mündlichen Prüfung: 30. November 1999

Zusammenfassung

Diese Arbeit beschreibt die Messung von Ereignissen mit einem oder mehreren Photonen und fehlender Energie im Endzustand wie sie in Elektron-Positron-Wechselwirkungen entstehen. Mit den Ergebnissen wurde der Wirkungsquerschnitt der Neutrinopaarproduktion gemessen und die Anzahl leichter Neutrinosorten bestimmt. Es wurde nach verschiedenen Prozessen „Neuer Physik“ gesucht, bei denen Photonen und fehlende Energie im Endzustand auftreten. Diese Prozesse beinhalten die Erzeugung supersymmetrischer Teilchen, fermiophobischer Higgsbosonen und massiver Gravitonen.

Die Analyse wurde mit einem Datensatz durchgeführt, der mit dem L3-Detektor am LEP-Beschleuniger bei Schwerpunktsenergien zwischen 130 GeV und 190 GeV aufgezeichnet wurde und der einer Luminosität von 265 pb^{-1} entspricht. Der Wirkungsquerschnitt der Reaktion $\text{e}^+\text{e}^- \rightarrow \nu\bar{\nu}\gamma(\gamma)$ mit $E_\gamma > 5$ GeV und $|\cos\theta_\gamma| < 0.97$ bei $\sqrt{s} = 189$ GeV wurde zu

$$\sigma_{\nu\bar{\nu}\gamma(\gamma)} \ = \ (5.25 \pm 0.22 \pm 0.07) \text{ pb}$$

bestimmt. Hieraus wurde der totale Wirkungsquerschnitt für Neutrinopaarproduktion extrapoliert mit einem Ergebnis von

$$\sigma_{\nu\bar{\nu}(\gamma)} \ = \ (58.3 \pm 2.7) \text{ pb}\,.$$

Die Energiespektren der Photonen wurden benutzt um die Anzahl leichter Neutrinogenerationen zu berechnen. Das Ergebnis lautet

$$N_\nu \ = \ 3.05 \pm 0.11 \pm 0.04\,,$$

welches sich in guter Übereinstimmung mit der Hypothese von drei leichten Neutrinoarten befindet und das Standardmodell mit seinen drei Teilchenfamilien untermauert.

Da kein Anzeichen neuer Physik festgestellt wurde, konnten obere Grenzen auf Produktionswirkungsquerschnitte neuer Teilchen abgeleitet und die erlaubten Massenbereiche solcher Teilchen unter der Annahme von $N_\nu = 3$ eingeschränkt werden. Falls das Gravitino das leichteste supersymmetrische Teilchen ist und sich die Massen aller anderen SUSY-Teilchen über der Produktionsschwelle befinden, könnte Gravitinopaarproduktion der einzige SUSY-Teilchen beinhaltende Prozeß bei LEP sein. Aus einer Analyse der Reaktion $\mathrm{e^+e^-} \rightarrow \tilde{\mathrm{G}}\tilde{\mathrm{G}}\gamma$ konnte ein unteres Limit von

$$m_{\tilde{\mathrm{G}}} \; > \; 8.9 \cdot 10^{-6} \text{ eV}$$

mit 95% Konfidenzniveau auf die Gravitinomasse bestimmt werden. Es wurden sowohl für die Produktion von $\tilde{\chi}_1^0\tilde{\mathrm{G}}$ und $\tilde{\chi}_1^0\tilde{\chi}_1^0$ und nachfolgenden Zerfall $\tilde{\chi}_1^0 \rightarrow \tilde{\mathrm{G}}\gamma$, als auch für die Produktion von $\tilde{\chi}_1^0\tilde{\chi}_2^0$ bzw. $\tilde{\chi}_2^0\tilde{\chi}_2^0$ und Zerfall $\tilde{\chi}_2^0 \rightarrow \tilde{\chi}_1^0\gamma$ obere Grenzen auf den Wirkungsquerschnitt in Abhängigkeit der Masse der beteiligten Teilchen gesetzt. Innerhalb von Modellen der durch Eichbosonen vermittelten Supersymmetriebrechung wurde unter der Annahme, daß das leichteste Neutralino das zweitleichteste supersymmetrische Teilchen ist, eine untere Grenze auf die Neutralinomasse von

$$m_{\tilde{\chi}_1^0} \; > \; 88.2 \text{ GeV}$$

mit 95% Konfidenzniveau abgeleitet.

Zur Suche nach fermiophobischen Higgsbosonen wurde der Prozeß $\mathrm{e^+e^-} \rightarrow \mathrm{hZ} \rightarrow \gamma\gamma\nu\bar{\nu}$ analysiert. Es wurden Grenzen auf den Wirkungsquerschnitt und auf das Verzweigungsverhältnis des Higgs nach Photonpaaren bestimmt. Eine untere Grenze auf die Higgsmasse von

$$m_{\mathrm{h}} \; > \; 89.9 \text{ GeV}$$

mit 95% Konfidenzniveau wurde für ein solches Higgsboson ermittelt.

Die Suche nach der Erzeugung massiver Gravitonen in Quantengravitationsmodellen mit zusätzlichen räumlichen Dimensionen wurde anhand der Reaktion $\mathrm{e^+e^-} \rightarrow \gamma\mathrm{G}$ durchgeführt. Untere Grenzen auf die Energieskala zwischen 1018 GeV und 349 GeV für zwei bis zehn zusätzliche Dimensionen wurden bestimmt. Deren Größe wurde auf höchstens 0.46 mm für zwei und auf maximal $8.3 \cdot 10^{-13}$ mm für zehn zusätzliche Dimensionen begrenzt.

Abstract

This thesis describes a measurement of single and multi-photon events with missing energy in electron-positron interactions. The results have been used to measure the neutrino pair-production cross section and to determine the number of light neutrino species. A search for various kinds of new physics processes involving photons and missing energy in the final state like the production of supersymmetric particles, a fermiophobic Higgs boson and massive gravitons has been carried out.

The analysis has been performed using data collected with the L3 detector at LEP at centre-of-mass energies between 130 GeV and 190 GeV corresponding to a total luminosity of 265 pb^{-1}. The cross section of the process $\mathrm{e}^+\mathrm{e}^- \rightarrow \nu\bar{\nu}\gamma(\gamma)$ for $E_\gamma > 5$ GeV and $|\cos\theta_\gamma| < 0.97$ at $\sqrt{s} = 189$ GeV has been measured to be

$$\sigma_{\nu\bar{\nu}\gamma(\gamma)} \; = \; (5.25 \pm 0.22 \pm 0.07) \ \mathrm{pb}$$

and has been extrapolated to a total cross section for neutrino pair-production yielding

$$\sigma_{\nu\bar{\nu}(\gamma)} \; = \; (58.3 \pm 2.7) \ \mathrm{pb}\,.$$

The measured photon energy spectra have been used to derive the number of light neutrino species. The combined value determined from all data analysed in this thesis is

$$N_\nu \; = \; 3.05 \pm 0.11 \pm 0.04\,,$$

which is in good agreement with the hypothesis of three light neutrino types and supports the Standard Model with its three generations of particles.

Since no indication for the appearance of new physics processes has been found, upper limits on cross sections of new particle production have been set

and lower limits on particle masses have been derived assuming $N_\nu = 3$. If the gravitino is the lightest supersymmetric particle and all other SUSY particles are too heavy to be created at LEP energies, gravitino pair-production could be the only process involving SUSY particles accessible at LEP. From an analysis of the process $\mathrm{e^+e^-} \rightarrow \tilde{\mathrm{G}}\tilde{\mathrm{G}}\gamma$ a lower limit of

$$m_{\tilde{\mathrm{G}}} \ > \ 8.9 \cdot 10^{-6} \text{ eV}$$

has been determined at the 95% confidence level. Cross section limits have been set depending on the masses of the particles involved in $\tilde{\chi}_1^0\tilde{\mathrm{G}}$ and $\tilde{\chi}_1^0\tilde{\chi}_1^0$ production and $\tilde{\chi}_1^0 \rightarrow \tilde{\mathrm{G}}\gamma$ decay, and for $\tilde{\chi}_1^0\tilde{\chi}_2^0$ and $\tilde{\chi}_2^0\tilde{\chi}_2^0$ production and $\tilde{\chi}_2^0 \rightarrow \tilde{\chi}_1^0\gamma$ decay. Within the framework of gauge-mediated supersymmetry breaking a lower limit on the neutralino mass of

$$m_{\tilde{\chi}_1^0} \ > \ 88.2 \text{ GeV}$$

at the 95% confidence level has been derived under the assumption that the lightest neutralino is the second lightest supersymmetric particle.

Fermiophobic Higgs bosons have been searched for investigating the process $\mathrm{e^+e^-} \rightarrow \mathrm{hZ} \rightarrow \gamma\gamma\nu\bar{\nu}$. Cross section bounds on this process have been determined depending on the Higgs mass and limits on the branching ratio of the Higgs decaying into photons have been derived. A lower mass limit for such a fermiophobic Higgs boson is set to

$$m_{\mathrm{h}} \ > \ 89.9 \text{ GeV}$$

at the 95% confidence level.

A search for the production of massive gravitons in quantum gravity models with extra spatial dimensions has been performed investigating the process $\mathrm{e^+e^-} \rightarrow \gamma\mathrm{G}$. Lower limits on the energy scale ranging from 1018 GeV to 349 GeV have been derived at the 95% confidence level for two to ten extra dimensions. Their size has been limited to at most 0.46 mm and to at most $8.3 \cdot 10^{-13}$ mm for two and ten extra dimensions, respectively.

Contents

Chapter 1

Introduction

The aim of physics is to describe the interactions of matter in the language of mathematics. In elementary particle physics, the static and dynamic properties of the most fundamental constituents of nature are subject to investigation. Two main questions arise from this goal: What is matter made of and how do its constituents interact with one another?

Our current understanding of the world and especially its smallest pieces is formulated in the Standard Model [1]. The theoretical framework of the Standard Model describes all phenomena observed in experiments so far, and all parameters of the Standard Model have been measured by experiments, partly to high accuracy [2]. There are two major exceptions: firstly, the so-called Higgs mechanism [3], introduced to give masses to the gauge bosons of the weak force, predicts the existence of an additional scalar boson, the Higgs particle, which has not been seen in experiments yet. The second problem is that there exists no consistent quantum theory of gravity.

Supplemental weak points of the Standard Model connected to the Higgs mechanism like the hierarchy problem [4] show up when asking the theory to be natural in a sense that radiative corrections to the Higgs mass should not be quadratically divergent. This implies the necessity of fine-tuning them with the Higgs bare mass to end up with a value for the physical mass orders of magnitude lower. The most elegant solution to this defect is the existence of a symmetry between bosons and fermions called supersymmetry [5, 6].

Here, an extra spectrum of particles constituting the supersymmetric partners of the known particles is predicted [7]. These new particles are supposed to have the same characteristics as their Standard Model associates, except that they differ by half a unit in their spin. Since, by now, no supersymmetric particle has been discovered in any experiment, supersymmetry must obviously be broken. Thus, the supersymmetric companions have to be much heavier than Standard Model particles, otherwise they would have been found already – if they exist at all.

There are several notions about the mechanism which breaks supersymmetry. They all lead to different predictions on the phenomenology of the theory. An important issue here is the energy scale at which this supersymmetry breaking happens.

In gauge-mediated supersymmetry breaking [8], the Standard Model gauge interactions act as messengers of supersymmetry breaking and thus the messenger scale is situated well below the Planck scale. Here, the gravitino, supersymmetric associate of the graviton, is the lightest supersymmetric particle. In a large region of the parameter space within these models, the lightest neutralino – partner of the neutral electroweak gauge bosons – turns out to be the second lightest supersymmetric particle and decays into gravitino and photon. Neutralinos can be pair-produced in electron-positron interactions leading to an experimental signature of two photons and missing energy due to the gravitinos which are invisible in particle detectors.

If the supersymmetry breaking takes place just above the electroweak scale, which can be the case in no-scale supergravity models [9–12], again the gravitino would be the lightest supersymmetric particle. In this scenario, it could even be created directly in an electron-positron collision, either in pairs or in association with the lightest neutralino. In the first instance, an initial state photon would be necessary to detect the process, since the gravitinos escape detection due to their weakly interacting nature. In the latter instance, again, the radiative decay of the neutralino manifests as finger print of the reaction. Hence, both possibilities have a common signature which is a single photon and nothing else visible in the detector.

Lastly, the messenger sector interactions can be of gravitational strength and the intrinsic scale of supersymmetry breaking is then of the order of the Planck scale [13, 14]. The neutralino takes over the role of the lightest supersymmetric particle within this class of models called supergravity. Even here, photons could enter the scene under special circumstances, although this is not compulsory. For certain values of parameters that define the phenomenology, radiative decays of the second lightest neutralino can be enhanced and once again single and two-photon signatures with missing energy uncover new physics [15].

An alternative solution of the hierarchy problem different from supersymmetry has recently been proposed. Here, the characteristic gravitational scale can be as low as the electroweak scale leaving only one fundamental energy scale in nature [16]. In this theory, massive gravitons propagate not only in space and time but also in extra dimensions and interact with other particles with sizable strength. In association with a photon, gravitons can be produced in electron-positron collisions and lead to a single photon and missing energy signature, since the graviton is not observed in the detector.

Some models [17–23] predict that the couplings of the Higgs boson to fermions are suppressed thus changing the branching fractions of the Higgs decay with respect to what is predicted by the Standard Model [24]. Here, for Higgs masses accessible at present centre-of-mass energies, the decay to two photons is dominant. In e^+e^- interactions, the Higgs particle is produced together with a Z boson, and a two-photon and missing energy signature arises when the Z decays invisibly into neutrinos, which takes place in about 20% of the Z decays.

A fundamental question in particle physics is the determination of the number of generations of particles. As proposed a long time ago [25–27], this can be achieved in a direct and simple way by the study of the final state $\nu\bar{\nu}\gamma$ in e^+e^- collisions under the assumption that neutrinos are light. Due to the invisibility of neutrinos, again, a single photon and missing energy is what is observed in the detector. Actually, when searching for new physics in theories as described above, the $\nu\bar{\nu}\gamma$ process is the main source of background one has to deal with.

The outline of this thesis reads as follows: In chapter 2 the Standard Model of particle physics is briefly sketched with special emphasis on neutrino pair-production followed by an introduction to supersymmetry and its various manifestations involving photons in the final state, and a brief presentation of the phenomenology of quantum gravity models with extra dimensions. Chapter 3 is devoted to the explanation of the Large Electron Positron Ring and the L3 experiment, with which this analysis has been performed, including a presentation of reconstruction and simulation of the data. The selection of single and multi-photon events from a large data sample is described in detail in chapter 4, taking systematic studies of detector parts into account. Chapter 5 deals with the extraction of physics information from the photon events selected. First, the cross section of neutrino pair-production is measured and the number of neutrino families is derived, assuming that new physics processes do not contribute to the photon spectra. Then, various interpretations within the respective supersymmetric models are shown including mass limits on the gravitino and the lightest neutralino. Moreover, from the investigation of graviton-photon and Higgs-Z production, limits are derived on the energy scale in quantum gravity models and on the mass of the Higgs boson, respectively. The main part of the thesis ends with a summary and concluding remarks in chapter 6, comparing the results obtained here with measurements performed by other experiments. Furthermore, an outlook to future experiments and preliminary recent results are presented. A number of appendices is added to the body of the thesis. Appendix A contains a feasibility study on the measurement of massive neutrinos, appendix B is on the comparison of Monte Carlo generators used to model the most relevant physics process for this analysis, namely $\nu\bar{\nu}\gamma(\gamma)$ production, and appendix C includes the selection results from centre-of-mass energies below 183 GeV.

Chapter 2

Theoretical Basis

In this chapter the essential features of the supersymmetric theory will be introduced from a phenomenological view point. First, a brief overview on the Standard Model of strong and electroweak interactions is provided (see, *e.g.*, [28] for a more detailed description) including electroweak symmetry breaking because of its analogy to supersymmetry breaking. Special emphasis is put on neutrino pair-production accompanied by an initial state radiation photon because of the dominance of this process when final states with photons and missing energy are investigated.

2.1 Standard Model of Particle Physics

The Standard Model of particle physics is the theory which quantitatively explains strong and electroweak forces, but not gravity. Interactions and properties of elementary particles are defined. Fundamental particles of the model are quarks and leptons of three families of particles and gauge bosons which transmit forces as listed in table 2.1. Each family of fundamental fermions contains an up-type quark, a down-type quark, a charged lepton, and a neutrino. All of the fundamental interactions derive from a single general principle, the requirement of local gauge invariance. The group representation of the Standard Model is given by (see, *e.g.*, [29])

$$G_{\mathrm{SM}} \;=\; \mathrm{U}(1)_{\mathrm{Y}} \times \mathrm{SU}(2)_{\mathrm{L}} \times \mathrm{SU}(3)_{\mathrm{C}}. \tag{2.1}$$

The strong interaction as formulated in quantum chromodynamics (QCD) is based on the symmetry group $\mathrm{SU}(3)_{\mathrm{C}}$, where the subscript C stands for colour –

Fermions						
Family	Lepton	Electric charge	Mass (MeV)	Quark	Electric charge	Mass (MeV)
1.	ν_e	0	$< 15 \cdot 10^{-6}$	u	2/3	1.5 – 5
	e	–1	0.51099907	d	–1/3	3 – 9
2.	ν_μ	0	< 0.17	c	2/3	1100 – 1400
	μ	–1	105.658389	s	–1/3	60 – 170
3.	ν_τ	0	< 18.2	t	2/3	168600 – 179000
	τ	–1	1777.05	b	–1/3	4100 – 4400

Gauge bosons				
Interaction	Symbol	Electric charge	Spin	Mass (GeV)
Electromagnetic	γ	0	1	0
Weak	W	± 1	1	80.41
	Z	0	1	91.187
Strong	g	0	1	0
Gravity	G	0	2	0

Table 2.1: *Fundamental constituents of the Standard Model. Masses or mass limits are taken from [2]. The Graviton, believed to be the transmitter of gravity, is also listed.*

name for the interaction charge. All coloured particles feel the strong force which is transmitted by eight gluons (g), the generators of $SU(3)_C$ [30]. Besides quarks, gluons themselves carry colour with gluon self-interactions being a consequence of this fact.

The electroweak interaction is based on the $U(1)_Y \times SU(2)_L$ symmetry group with generators B and $W^i, i = 1 \ldots 3$ [1]. The coupling constants belonging to the two subgroups are denoted by g_1 and g_2. Left-handed fermion fields are grouped in doublets, whereas right-handed fermions are singlets under $SU(2)_L$ (table 2.2).

In the electroweak part of the minimal Standard Model the underlying symmetry is spontaneously broken by the introduction of a complex Higgs doublet [3].

Generation		
1.	2.	3.
$\begin{pmatrix}\nu_\mathrm{e} \\ \mathrm{e}^-\end{pmatrix}_\mathrm{L}$ e^-_R	$\begin{pmatrix}\nu_\mu \\ \mu^-\end{pmatrix}_\mathrm{L}$ μ^-_R	$\begin{pmatrix}\nu_\tau \\ \tau^-\end{pmatrix}_\mathrm{L}$ τ^-_R
$\begin{pmatrix}\mathrm{u} \\ \mathrm{d}'\end{pmatrix}_\mathrm{L}$ u_R d_R	$\begin{pmatrix}\mathrm{c} \\ \mathrm{s}'\end{pmatrix}_\mathrm{L}$ c_R s_R	$\begin{pmatrix}\mathrm{t} \\ \mathrm{b}'\end{pmatrix}_\mathrm{L}$ t_R b_R

Table 2.2: *Multiplet assignments of electroweak symmetry eigenstates of leptons and quarks. Mass eigenstates of left-handed down-type quarks are mixings of symmetry eigenstates where the mixing is given by the Cabbibo-Kobayashi-Maskawa matrix [31].*

The two electrically neutral states, B and W^3, mix producing one massless linear combination – the photon field A – and an orthogonal massive combination – the Z:

$$\begin{aligned} A &= W^3 \sin\theta_\mathrm{W} + B \cos\theta_\mathrm{W} \\ Z &= W^3 \cos\theta_\mathrm{W} - B \sin\theta_\mathrm{W}. \end{aligned} \tag{2.2}$$

The parameter θ_W is called weak mixing angle. The fields representing the $\mathrm{W}^\pm$ particles are given by:

$$W^\pm = \frac{1}{\sqrt{2}}\left(W^1 \mp iW^2\right). \tag{2.3}$$

Carriers of the weak force after electroweak symmetry breaking are W and Z bosons. Electromagnetic interactions between charged particles are mediated by the photon. The electromagnetic fine-structure constant α is related to the coupling constants g_1 and g_2 by

$$\alpha = \frac{1}{4\pi}\frac{(g_1 g_2)^2}{g_1^2+g_2^2} = \frac{1}{4\pi}\, g_1^2 \cos^2\theta_\mathrm{W} = \frac{1}{4\pi}\, g_2^2 \sin^2\theta_\mathrm{W}\,. \tag{2.4}$$

W and Z bosons acquire mass through the Higgs mechanism [3],

$$\begin{aligned} m_{\mathrm{Z}} &= \frac{v}{2}\sqrt{g_1^2+g_2^2} \\ m_{\mathrm{W}} &= \frac{v}{2}\,g_2\,, \end{aligned} \tag{2.5}$$

where v is the vacuum expectation value of the Higgs field. A new massive particle, the spin-zero Higgs boson, is predicted by the Higgs mechanism in the minimal Standard Model. This Higgs boson has not yet been observed by experiments. Direct searches yield a lower bound of 102.6 GeV on its mass [32]. An upper mass limit of 245 GeV at the 95% confidence level is derived from Standard Model fits to electroweak precision data [33], where the logarithmic dependence of radiative corrections on the Higgs mass is exploited. The Higgs field is also responsible for the generation of fermion masses. They are produced via Yukawa couplings [34] of left and right-handed fermion fields to the Higgs field [3].

In the minimal Standard Model, the Higgs boson decays into two photons via a quark or W boson loop [24]. However, the rate is too small for the observation at existing accelerators even for a kinematically accessible Higgs boson. Nevertheless, other theoretical models can accommodate large $\mathrm{h} \to \gamma\gamma$ branching fractions [17–23].

2.1.1 Neutrino Production in Electron-Positron Interactions

As pointed out in the introduction, neutrino pair-production accompanied by one or more photons is an irreducible background for new physics processes involving photons and missing energy in the final state. On the other hand, the study of this process is interesting for its own sake since it allows to determine the number of light[1] neutrino species and thus an indication for the number of particle families in general can be derived. Furthermore, massive stable neutrinos could be searched for in the same way, too. A feasibility study addressing this

---

[1] Recently, experimental evidence for the occurrence of neutrino oscillations has been reported [35] with non-zero neutrino masses as a consequence. However, detailed analyses of the measured data yield masses in the sub-eV range, and even neutrino masses within the – less stringent – mass limits from other experiments [2] would not have any impact on the physics results of this thesis.

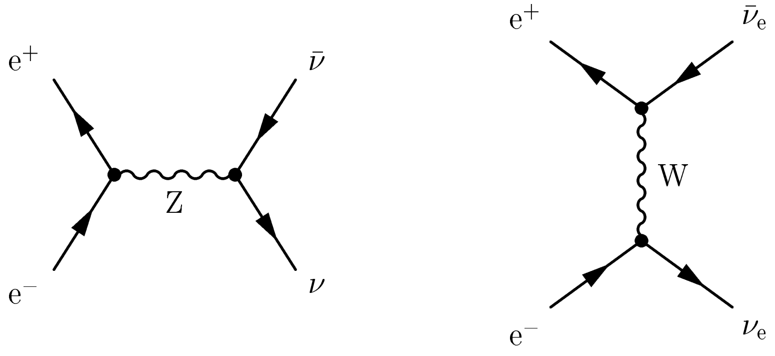

Figure 2.1: *Feynman diagrams of the tree level contribution to* $e^+e^- \to \nu\bar{\nu}$*. In the* s*–channel diagram on the left hand side, all three neutrino species are pair-produced via* Z *exchange, whereas only electron neutrinos are created when a* W *is exchanged in the* t*–channel (right hand side).*

topic has been performed and is presented in appendix A assuming one heavy neutrino in addition to three light ones.

Tree Level Process

The initial state particles in electron-positron collisions – electrons and positrons – interact electroweakly, as seen in the previous chapter, whereas the final state particles – neutrinos – only couple to W and Z bosons. The lowest order contributions for this process as derived from the theoretical framework of the Standard Model are visualised by Feynman diagrams [36] in figure 2.1. Feynman diagrams not only give an idea for the course processes of elementary particles take, but also provide a mathematical instruction for the calculation of related physical quantities like the cross section. Considering only the tree level diagrams shown in figure 2.1, the total cross section is calculated to be [37]

$$\begin{aligned}\sigma(e^+e^- \to \nu\bar{\nu}) \;=\; \frac{G_F^2\, s}{6\pi}\Bigg(& N_\nu \frac{1}{4}\left[(g_V+g_A)^2+(g_V-g_A)^2\right]\frac{1}{|Z|^2} \\ & - 2\sin^2\theta_W \frac{\mathrm{Re}Z}{|Z|^2} + 1\Bigg)\,,\end{aligned} \tag{2.6}$$

where $\sqrt{s}$ is the centre-of-mass energy. Here, the following notation is used for Z, the Fermi constant G_F and vector and axial vector couplings g_V and g_A,

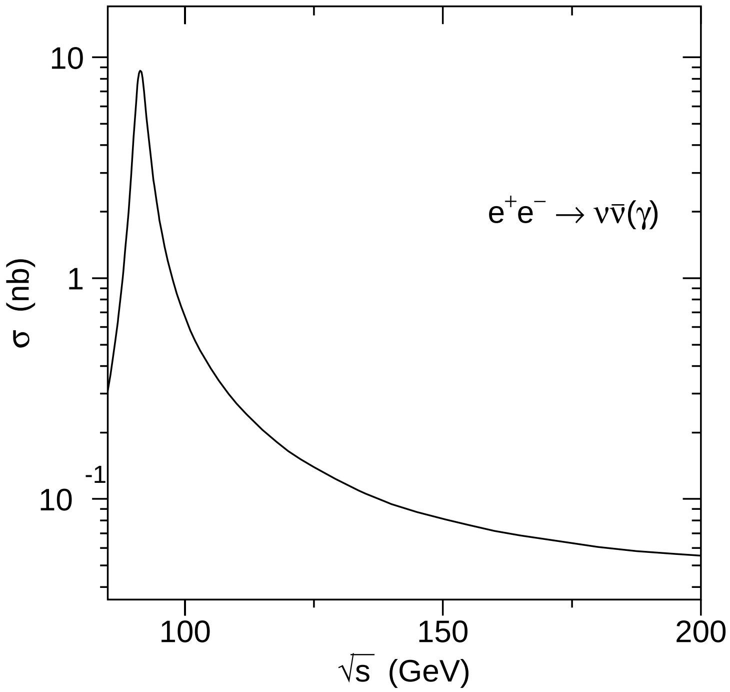

Figure 2.2: *Production cross section of* $e^+e^- \to \nu\bar{\nu}(\gamma)$ *versus centre-of-mass energy. In the region of the Z resonance, the cross section is more than 100 times bigger than in the regime of LEP 2 energies near* 200 GeV.

respectively,

$$\begin{aligned} Z &= s - m_Z^2 + i m_Z \Gamma_Z \,, \\ \frac{G_F}{\sqrt{2}} &= \frac{g_2^2}{8 m_W^2} \,, \\ g_V &= -\frac{1}{2} + 2\sin^2\theta_W \,, \qquad g_A = -\frac{1}{2} \,. \end{aligned} \tag{2.7}$$

Γ_Z is the width of the Z boson. The three terms in equation 2.6 are s–channel contribution, interference and W exchange. The first term is the only one sensitive to the number of light neutrino types N_ν, since only in the s–channel all neutrino species are produced. The behaviour of the cross section of

$$e^+e^- \to \nu_l \bar{\nu}_l(\gamma), \quad l = e, \mu, \tau \tag{2.8}$$

in the energy region of interest for this thesis is shown in figure 2.2. The “γ”

in the formula accounts for the possible emission of one or more photons off the beam particles (initial state radiation). Photons are also radiated off the W in the t–channel. In the following, the index l for the different neutrino species is omitted and all generations are included by the notation "$\nu\bar{\nu}$".

Initial State Radiation

Not only the amount of initial state radiation (ISR) but also energy and angular distributions of the photons can be calculated. Technically, this is achieved in an approximate manner by convoluting the neutrino-pair cross section with a radiation function to attach external photons to the charged fermions as it is done in the `KORALZ` Monte Carlo event generator [38] using the Yennie-Frautschi-Suura method [39]. Another way is to exactly calculate the Born-level matrix elements associated to the process $\mathrm{e^+e^-} \to \nu\bar{\nu}\, n\gamma$, with $n = 1, 2, 3$, in the Standard Model framework and then treat higher order QED corrections using a structure function approach as in `NUNUGPV` [40,41]. The two Monte Carlo generators `KORALZ` and `NUNUGPV` have been compared in order to estimate the systematic uncertainty on this process introduced by the theory as described in appendix B.

The differential cross section in photon energy E_γ and $\cos\theta_\gamma$, where θ_γ is the photon angle with respect to the beam electron, in the range of LEP energies has been calculated analytically [42] in lowest order (figure 2.3), *i.e.* for the reaction

$$\mathrm{e}^+\,(p_+) + \mathrm{e}^-\,(p_-) \;\longrightarrow\; \bar{\nu}\,(q_+) + \nu\,(q_-) + \gamma\,(k). \qquad (2.9)$$

Neglecting the width of the W, electron mass and photon radiation from the W in the t–channel[2], the following expression is derived

$$\frac{d\sigma}{d\cos\theta_\gamma\, dE_\gamma} = \frac{G_\mathrm{F}^2\,\alpha}{12\pi^2}\frac{s' E_\gamma}{s\kappa_+\kappa_-}\left[(s-\kappa_+)^2 F(\eta_+) + (s-\kappa_-)^2 F(\eta_-)\right] \qquad (2.10)$$

---

[2] Photon radiation from the W in the t–channel adds a fairly small contribution (less than 1%) to the cross section due to two W propagators in the matrix element, *i.e.* a factor of $1/m_\mathrm{W}^4$, instead of only one W propagator (factor $1/m_\mathrm{W}^2$).

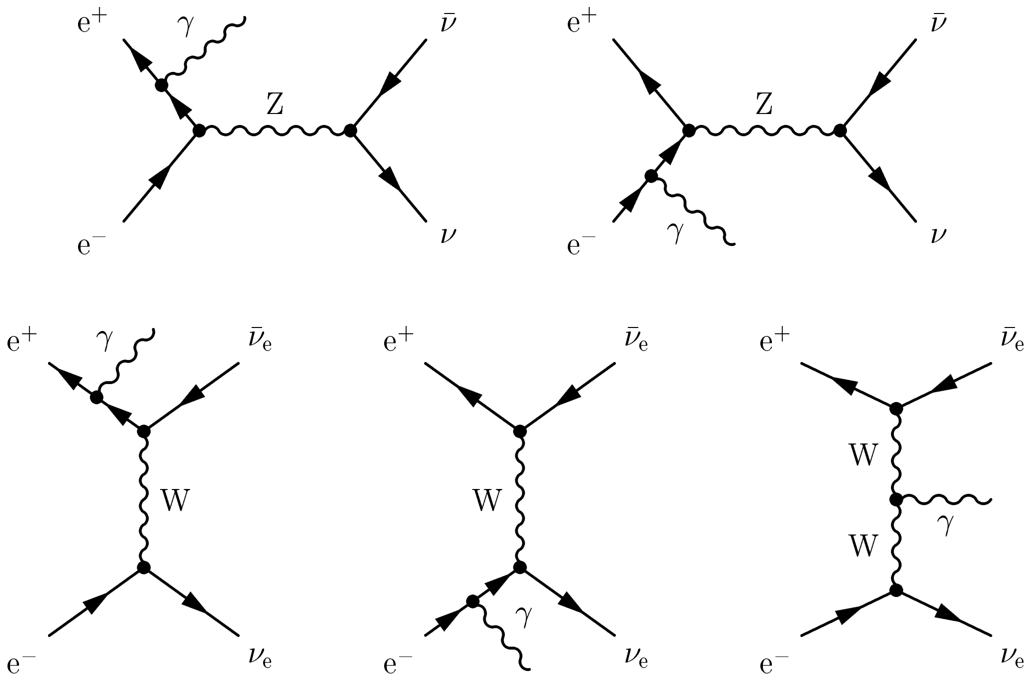

Figure 2.3: *Feynman diagrams of the first order contribution to* $e^+e^- \to \nu\bar{\nu}\gamma$.

with

$$\eta_\pm = \frac{s-\kappa_\pm}{m_W^2}, \tag{2.11}$$

$$\begin{aligned} F(\eta_\pm) = {} & N_\nu \frac{1}{2}\left((g_V+g_A)^2+(g_V-g_A)^2\right)\frac{m_Z^4}{|Z|^2} \\ & + 3\,(g_V+g_A)\,\frac{m_Z^2\,\mathrm{Re}Z}{|Z|^2}\frac{1}{\eta_\pm}\left(3+\frac{2}{\eta_\pm}-2\left(1+\frac{1}{\eta_\pm}\right)^2\ln\left(1+\eta_\pm\right)\right) \\ & + \frac{6}{\eta_\pm^2}\left((1+\eta_\pm)\left(1-\frac{2}{\eta_\pm}\ln\left(1+\eta_\pm\right)\right)+1\right), \end{aligned} \tag{2.12}$$

where N_ν denotes the number of neutrinos. The following notation in addition to equations 2.7 is used

$$\begin{aligned} s &= (p_+ + p_-)^2 \,, \\ s' &= (q_+ + q_-)^2 \,, \\ \kappa_\pm &= 2p_\pm k \ = \ 2E_\mathrm{e}E_\gamma \left(1 \pm \cos\theta_\gamma\right) \,, \\ Z &= s' - m_\mathrm{Z}^2 + i m_\mathrm{Z}\Gamma_\mathrm{Z} \,. \end{aligned} \tag{2.13}$$

The three terms of 2.12 are identified easily within the Feynman calculus: The first one describes the s–channel diagrams (the upper ones of figure 2.3). The last term of 2.12 corresponds to the t–channel diagrams when a photon is radiated off a beam particle (lower left and lower middle graphs of figure 2.3) and the term in the middle accounts for the interference between Z and W exchange diagrams.

The differential cross sections in recoil mass and photon angle are shown in figure 2.4, where the recoil mass of photon(s) is the mass of a – potentially invisible – particle produced in association with the photon(s) and is connected to the photon energy by

$$m_\mathrm{rec} \ = \ \sqrt{\left(\sqrt{s} - E_\gamma\right)^2 - |\vec{p}_\gamma|^2} \,, \tag{2.14}$$

where $E_\gamma = \sum_i E_{\gamma_i}$ and $\vec{p}_\gamma = \sum_i \vec{p}_{\gamma_i}$ are total energy and momentum of the photons. The peaking structure of the recoil mass distribution is caused by $|Z|^2$ in the denominator of the first term of equation 2.12 and is physically explained as the production of an on-shell Z boson in the s–channel (see figure 2.3) – the so-called "radiative return to the Z". The sharp rise at small polar angles in the $\cos\theta_\gamma$ distribution is determined by the $\frac{1}{\kappa_+\kappa_-}$ dependence in equation 2.10.

2.2 Supersymmetry

In 1928, P.A.M. Dirac incorporated the symmetries of the Lorentz group into quantum mechanics [43]. He found as a natural consequence that each known particle had to have a partner particle – namely, antimatter. The matter-antimatter symmetry was not revealed until experimental tools were developed to detect positrons in cosmic rays [44]. In a similar manner, incorporation of supersymmetry into particle physics once again predicts partner particles for all known particles. The beauty of the principle of a symmetry between bosons and fermions is not the only motivation for supersymmetry, though. Especially

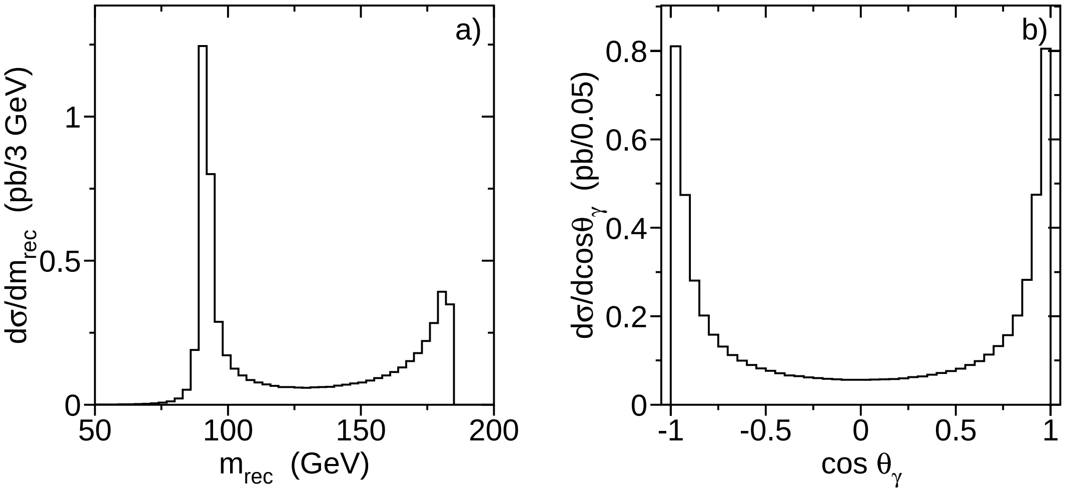

Figure 2.4: *Differential cross section in recoil mass (a) and* $\cos\theta_\gamma$ *(b) of* $\mathrm{e^+e^-} \to \nu\bar{\nu}\gamma(\gamma)$ *calculated with* `KORALZ` *at* $\sqrt{s} = 189$ GeV *for* $E_\gamma > 5$ GeV.

for its realisation on the weak scale, *i.e.* in the range below 1 TeV, several useful prospects come across, when trying to cure some of the weaknesses of the Standard Model.

Naturalness Problem

Thus, we will take a little deeper look into the problem of naturalness already mentioned in the introduction. Radiative corrections to the masses of Higgs and gauge bosons [4] imposed by the one-loop diagrams in figure 2.5 are each quadratically divergent,

$$\delta m^2_{\mathrm{H,W}} = \mathcal{O}\left(\frac{g_2^2}{16\pi^2}\right)\int^{\Lambda} d^4k \frac{1}{k^2} = \mathcal{O}\left(\frac{\alpha}{\pi}\right)\Lambda^2 , \qquad (2.15)$$

where the cutoff Λ in the integral represents the scale up to which the Standard Model remains valid, and beyond which new physics sets in. If one perceives Λ as the Planck mass $M_{\mathrm{P}} \approx 10^{19}$ GeV – where gravity is expected to become as strong as other particle interactions – or the grand unification scale – where electroweak and strong forces unify (see also further below in this section and figure 2.6) – the quantum correction in equation 2.15 is much larger than the physical value of $m_{\mathrm{H,W}} \sim 100$ GeV. This is not a problem in renormalisation theory: There could be a large bare contribution with opposite sign, and one could fine-tune its

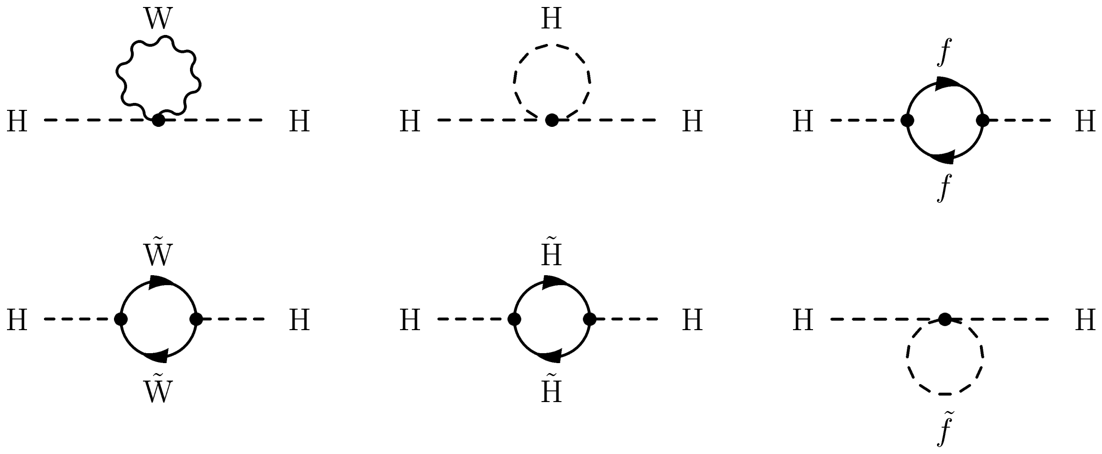

Figure 2.5: *One-loop quantum corrections to m_{H}^2 in the Standard Model (upper row) and in supersymmetry (additionally the lower row).*

value to many significant digits so that the physical value $m_{\mathrm{H,W}}^2$ remains small. However, this seems unnatural, and would have to be repeated order by order in perturbation theory.

The hope to find a symmetry principle to make small boson masses natural is achieved by supersymmetry [45], exploiting the fact that boson and fermion loop diagrams in figure 2.5 have opposite signs. If there are equal numbers of fermions f and bosons b, and if they have equal couplings as in a supersymmetric theory, the quadratic divergences 2.15 cancel

$$\delta m_{\mathrm{H,W}}^2 = -\left(\frac{g_f^2}{16\pi^2}\right)\left(\Lambda^2 + M_f^2\right) + \left(\frac{g_b^2}{16\pi^2}\right)\left(\Lambda^2 + M_b^2\right) = \mathcal{O}\left(\frac{\alpha}{4\pi}\right)\left|m_b^2 - m_f^2\right| . \tag{2.16}$$

This is no larger than the physical value: $\delta m_{\mathrm{H,W}}^2 \lesssim m_{\mathrm{H,W}}^2$, and therefore naturally small, if

$$\left|m_b^2 - m_f^2\right| \lesssim 1\ \mathrm{TeV}^2. \tag{2.17}$$

This means that masses of supersymmetric partner particles should not be larger than about 1 TeV to keep the naturalness argument valid.

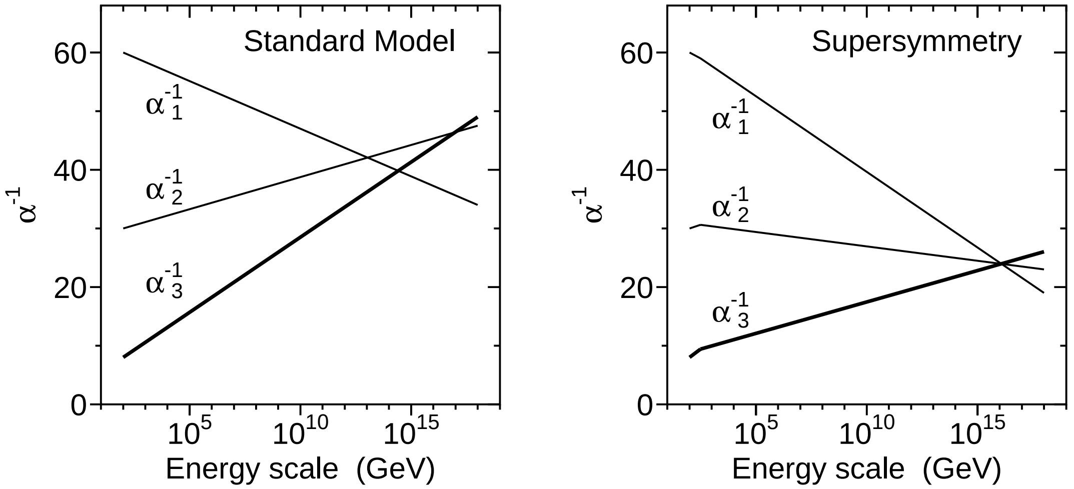

Figure 2.6: *Evolution of the* $\mathrm{SU(3)_C} \times \mathrm{SU(2)_L} \times \mathrm{U(1)_Y}$ *gauge couplings to high energy scales in Standard Model (left) and in supersymmetric generalisation of the Standard Model (right) with* $\alpha_i = \frac{g_i^2}{4\pi}$.

Theoretical Prospects of Supersymmetry

Further theoretical hints and interesting features favouring supersymmetry exist, but shall only be listed up here and not be discussed in detail[3]. If one assumes that there exists an unification of QCD and the electroweak sector of the Standard Model as it is predicted in grand unification theories (GUTs), the three coupling constants[4] should converge and meet in a common point on the energy scale where the grand unification takes place. This does not happen in the Standard Model as shown in figure 2.6, but the three gauge couplings can unify at the grand unification scale if there exist weak-scale supersymmetric particles, leaving a desert (*i.e.* no further new physics) between the weak scale and the GUT scale [47–49]. The new SUSY particles contribute via loop corrections to the coupling of the respective interaction starting from a scale $M_{\mathrm{SUSY}} \lesssim 1$ TeV – if all SUSY particles have a mass of approximately M_{SUSY} – which is visible as kink in the evolution of the coupling constants shown in figure 2.6.

Furthermore, electroweak symmetry breaking is a derived consequence of su-

---

[3] See for example [46] for deeper insights.

[4] Actually, the three couplings are not constant. Their values are changing because of radiative corrections according to the energy scale.

persymmetry breaking in many particle physics models with weak-scale supersymmetry, whereas electroweak symmetry breaking in the Standard Model is put in "by hand". The supersymmetry electroweak symmetry breaking mechanism works best if the top quark has a mass $m_\mathrm{t} \sim 150 - 200$ GeV. The measured value of the top quark mass with $m_\mathrm{t} = 173.8 \pm 5.2$ GeV [2] is consistent with this mechanism.

R–Parity

Last but not least, supersymmetry could provide a candidate for dark matter in the universe. To assure the conservation of baryon (B) and lepton number (L), which is necessary to avoid proton decay, supersymmetry possesses a new multiplicative invariance, the R–parity with

$$\mathrm{R} \; = \; (-1)^{3(B-L)+2S} \tag{2.18}$$

for a particle of spin S [50, 51]. Formula 2.18 implies that all ordinary Standard Model particles have even R–parity, whereas the corresponding supersymmetric partners have odd R–parity. The conservation of R–parity in scattering and decay processes has crucial impact on supersymmetric phenomenology. It follows that supersymmetric particles must be produced in pairs and that there must be one absolutely stable supersymmetric particle remaining at the end of a decay chain initiated by the decay of a heavy unstable supersymmetric particle. Although this is not generally the case, throughout this thesis the R–parity is assumed to be strictly conserved.

Dark Matter

To be consistent with cosmological constraints this stable lightest supersymmetric particle (LSP) should be electrically neutral and colourless [52]. In the very early universe, all sparticles (and particles) were in thermal equilibrium. As the temperature fell, heavier SUSY particles decayed into lighter ones. Eventually, only the lightest supersymmetric particle is left, which can possibly disappear only by pair-annihilation. To reduce the present day number density of the LSP to an acceptable level, this pair-annihilation must be efficient enough. Stable, charged and uncoloured particles would be well mixed with ordinary matter. In particular, they should be found in terrestrial searches for anomalously heavy protons [53], and a lower mass limit of 350 GeV is derived [54]. A strongly interacting LSP would form new hadrons with at least one of them being stable. If there is a stable, charge-one hadron, its existence is ruled out by the anomalous proton search [54] discussed above. However, this argument does not apply if the only stable new hadrons are neutral. Nevertheless, there are experimental bounds on stable, coloured SUSY particles [2,55], and also theoretical arguments suggest that strongly interacting SUSY particles are heavier than colourless particles [56–63]. Only weakly interacting, the LSP behaves like a stable heavy neutrino and potentially builds an important component of the non-baryonic dark matter in the universe.

2.2.1 Concept of Supersymmetry

The simplest supersymmetric model of particle physics which contains the Standard Model is called Minimal Supersymmetric Standard Model (MSSM). The recipe for model building is to start with the Standard Model of particle physics, and to add an extra Higgs doublet of opposite hypercharge. In this way, flavour changing neutral currents[5] are avoided at tree level since the $Y = -1$ doublet couples only to up-type quarks and leptons, and the $Y = 1$ doublet couples only to down-type quarks and leptons [65]. Next, proceed with supersymmetrisation, following specific rules to construct supersymmetric gauge theories. At this stage, one has a globally supersymmetric Standard Model theory. Supersymmetry breaking is incorporated by adding to the Lagrangian explicit soft SUSY-breaking terms consistent with the symmetries of the Standard Model. The resulting theory has more than 100 parameters, mainly coming from various soft SUSY-breaking terms. Such a model is the most conservative approach to realistic SUSY model building but the large parameter space leaves little predictability. The particle content of the MSSM is listed in table 2.3.

Higgs in Supersymmetry

The extended Higgs sector of the MSSM contains two doublets with one coupling exclusively to down-type particles having a vacuum expectation value $v_1 \equiv v_d$,

---

[5] In the minimal Standard Model with only one Higgs doublet, flavour changing neutral currents at tree level are automatically absent, because the same operations that diagonalise the mass matrix automatically diagonalise the Higgs-fermion couplings [64].

Particles	Supersymmetric partners			
	Weak interaction eigenstates		Mass eigenstates	
$l = \mathrm{e}, \mu, \tau$	$\tilde{l}_\mathrm{L}, \tilde{l}_\mathrm{R}$	Slepton	$\tilde{l}_1, \tilde{l}_2$	
ν_l	$\tilde{\nu}_l$	Sneutrino	$\tilde{\nu}_l$	
$\mathrm{q} = \begin{matrix} \mathrm{u, c, t} \\ \mathrm{d, s, b} \end{matrix}$	$\tilde{\mathrm{q}}_\mathrm{L}, \tilde{\mathrm{q}}_\mathrm{R}$	Squark	$\tilde{\mathrm{q}}_1, \tilde{\mathrm{q}}_2$	
g	$\tilde{\mathrm{g}}$	Gluino	$\tilde{\mathrm{g}}$	
$\mathrm{W}^\pm$	$\tilde{\mathrm{W}}^\pm$	Wino	$\tilde{\chi}^\pm_{1,2}$	Charginos
$\mathrm{H}^\pm$	$\tilde{\mathrm{H}}^\pm$	Higgsino		
γ	$\tilde{\gamma}$	Photino	$\tilde{\chi}^0_{1\ldots4}$	Neutralinos
Z	$\tilde{\mathrm{Z}}$	Zino		
h, H, A	$\tilde{\mathrm{H}}_{1,2}$	Higgsino		
G	$\tilde{\mathrm{G}}$	Gravitino	$\tilde{\mathrm{G}}$	

Table 2.3: *Particle content of the MSSM*

and the other coupling to up-type particles with vacuum expectation value $v_2 \equiv v_u$ [64]. The squared sum of the two is fixed by equation 2.5: $v^2 = v_1^2 + v_2^2$, while the ratio

$$\tan\beta = \frac{v_2}{v_1} \tag{2.19}$$

is a free parameter of the model. After electroweak symmetry breaking, five physical Higgs particles remain in this model: A charged Higgs boson pair ($\mathrm{H}^\pm$), two CP–even neutral Higgs bosons (h and H where $m_\mathrm{h} \leq m_\mathrm{H}$), and one CP–odd neutral Higgs boson (A). At tree level, the whole Higgs-sector is determined by two parameters, typically taken to be $\tan\beta$ and m_A [64]. Since up-type particles are mostly heavier than down-type particles, it is expected that $\tan\beta$ is greater than one because the fermion masses generated by the Higgs mechanism are proportional to v_1 and v_2, respectively[6].

---

[6] However, $\tan\beta \geq 1$ is not a general principle since the Yukawa couplings responsible for the mass generation are free parameters and could thus lead to $v_1 > v_2$ although $m_u > m_d$.

Neutralinos and Charginos

As a result of supersymmetry breaking, all SUSY particles with the same quantum numbers can mix, analogous to the mixing of the B and W^3 fields of the Standard Model due to electroweak symmetry breaking. In this way, the charged supersymmetric fermions – winos and higgsinos – mix to physical mass eigenstates called charginos. Clearly, Higgs fermions can no longer be CP eigenstates (see above), and thus they mix with the neutral electroweak gauge fermions – photino and zino – to mass eigenstates called neutralinos. There are two further supersymmetry breaking parameters and one supersymmetry conserving parameter necessary to define the mixing: The gaugino masses M_1 and M_2 – associated with the $\mathrm{U(1)_Y}$ and $\mathrm{SU(2)_L}$ subgroups of the Standard Model – and the Higgs mixing parameter μ. Chargino and neutralino masses are given by diagonalising the mass mixing matrices [46]

$$\mathcal{M}_{\tilde{\chi}^\pm} = \begin{pmatrix} M_2 & \sqrt{2} m_\mathrm{W} \sin\beta \\ \sqrt{2} m_\mathrm{W} \cos\beta & \mu \end{pmatrix} \tag{2.20}$$

for charginos and

$$\mathcal{M}_{\tilde{\chi}^0} = \begin{pmatrix} M_1 & 0 & -m_\mathrm{Z}\, s_\theta \cos\beta & m_\mathrm{Z}\, s_\theta \sin\beta \\ 0 & M_2 & m_\mathrm{Z}\, c_\theta \cos\beta & -m_\mathrm{Z}\, c_\theta \sin\beta \\ -m_\mathrm{Z}\, s_\theta \cos\beta & m_\mathrm{Z}\, c_\theta \cos\beta & 0 & -\mu \\ m_\mathrm{Z}\, s_\theta \sin\beta & -m_\mathrm{Z}\, c_\theta \sin\beta & -\mu & 0 \end{pmatrix} \tag{2.21}$$

with

$$s_\theta = \sin\theta_\mathrm{W} \quad \text{and} \quad c_\theta = \cos\theta_\mathrm{W} \tag{2.22}$$

for neutralinos given in the basis

$$\left(\tilde{B}, \tilde{W}^3, i\tilde{H}_1, i\tilde{H}_2\right), \tag{2.23}$$

where $\tilde{B}$, $\tilde{W}^3$, $\tilde{H}_1$ and $\tilde{H}_2$ denote the two-component spinor fields of the bino, wino[7], and the two neutral higgsinos, respectively.

---

[7] The bino and the wino are the supersymmetric partners of the B, the gauge boson of the $\mathrm{U(1)_Y}$ subgroup, and the W^3, the gauge boson of the $\mathrm{SU(2)_L}$ subgroup.

To reduce parameter freedom, a high energy approach can be made by treating the MSSM parameters as running parameters and imposing a particular structure on the soft supersymmetry-breaking terms at a common high energy scale [56–63]. One of the most common predictions here, is the unification of gaugino mass parameters at some high energy scale. In this way, the effective low energy gaugino mass parameters are related:

$$M_1 \;=\; \frac{5}{3}\tan^2\theta_\mathrm{W}\, M_2\,, \qquad M_3 \;\equiv\; m_{\tilde{\mathrm{g}}} \;=\; \frac{\alpha_\mathrm{s}}{\alpha_\mathrm{em}}\sin^2\theta_\mathrm{W}\, M_2\,, \tag{2.24}$$

where M_3 is the mass parameter associated with $\mathrm{SU(3)_C}$ and $m_{\tilde{\mathrm{g}}}$ is the gluino mass, and M_1 and M_2 enter the neutralino and chargino mass matrices.

Sfermions

The supersymmetric partners of the quarks and leptons are spin-zero bosons: The squarks, charged sleptons and sneutrinos, with the "s" standing for "scalar". For a given fermion f, there are two supersymmetric partners $\tilde{f}_\mathrm{L}$ and $\tilde{f}_\mathrm{R}$, which are scalar partners for the two helicity states (left and right-handed) of the corresponding fermion[8]. In general, $\tilde{f}_\mathrm{L}$ and $\tilde{f}_\mathrm{R}$ are not mass eigenstates since there is $\tilde{f}_\mathrm{L} - \tilde{f}_\mathrm{R}$ mixing. However, the strength of the mixing is proportional to the mass of the corresponding Standard Model partner and, hence, the mixing is expected to be negligibly small for the first two generations of sparticles. Only for the third generation a substantially large mixing is possible. In this case, the squark and slepton mass eigenstates are generically called $\tilde{f}_1$ and $\tilde{f}_2$.

2.2.2 Supersymmetry Breaking

In the MSSM, breaking of global supersymmetry is accomplished by including the most general renormalisable soft supersymmetry-breaking terms consistent with the gauge symmetry of equation 2.1 and R–parity invariance [66,67]. These terms parametrise the ignorance of the origin of supersymmetry breaking.

---

[8] There is no $\tilde{\nu}_\mathrm{R}$ in the MSSM.

Breaking of Global Supersymmetry

According to Goldstone's theorem [68, 69], whenever a continuous symmetry is spontaneously broken[9], a massless particle appears as a result. In the most familiar examples, the continuous symmetry transforms the internal quantum numbers of fields, and the massless particle is a Goldstone boson. If the spontaneously broken symmetry is coupled to a gauge boson, the Goldstone boson combines with the gauge boson to form a massive vector boson; this is called Higgs mechanism. Goldstone's theorem also applies to spontaneous breaking of supersymmetry but in this particular case the massless particle is a Goldstone fermion or goldstino[10]. The goldstino would then be LSP and could play a role in SUSY phenomenology [71, 72].

Breaking of Local Supersymmetry

However, the goldstino is a physical degree of freedom only in models of spontaneously broken global supersymmetry. In local supersymmetry, the gravitino, the spin–$\frac{3}{2}$ supersymmetric partner of the graviton, acts as a gauge field. In analogy to the theory of Goldstone bosons, the gravitino participates in the supersymmetric version of the Higgs mechanism and the goldstino is absorbed by the gravitino [73]. By this super-Higgs mechanism, the goldstino is removed from the physical spectrum and the gravitino acquires a mass:

$$m_{\tilde{\mathrm{G}}} = \frac{F}{\sqrt{3}\, m_{\mathrm{P}}} , \tag{2.25}$$

where $\sqrt{F}$ marks the characteristic scale of local supersymmetry breaking and $m_{\mathrm{P}} = M_{\mathrm{P}}/\sqrt{8\pi} \approx 2.4 \cdot 10^{18}$ GeV is the reduced Planck mass.

SUSY Breaking Schemes

So far though, no-one has managed, to construct a model of spontaneously-broken low-energy supersymmetry where the supersymmetry breaking arises solely as a consequence of interactions of the particles of the MSSM. A more viable scheme posits a theory holding at least two distinct sectors: A "hidden"

---

[9] Explicit symmetry breaking is unlike what occurs in gauge theories and induces inconsistencies when gravity is introduced [70].

[10] This comes from the fact that the supersymmetry charge is fermionic [5].

sector built out of particles that are completely neutral with respect to the Standard Model gauge group and a “visible” sector with the particles of the MSSM. There are no tree level interactions between particles of visible and hidden sectors. Supersymmetry breaking is assumed to occur in the hidden sector, and is then transmitted to the MSSM by some mechanism. Two theoretical scenarios have been examined in detail: Gravity-mediated and gauge-mediated supersymmetry breaking.

Since all particles feel gravitational force, particles in hidden and visible sectors can interact via exchange of gravitons. Thus, supergravity (SUGRA) models provide a natural mechanism for transmitting supersymmetry breaking of the hidden sector to the particle spectrum of the MSSM. In these gravity-mediated supersymmetry breaking models, gravity is the messenger of supersymmetry breaking [13, 14]. Here, the gravitino mass is of the order of the electroweak-breaking scale, while its couplings are gravitational in strength. Hence, it follows that the gravitino would not play any role at high energy colliders.

In gauge-mediated supersymmetry breaking (GMSB), supersymmetry breaking is transmitted to the MSSM via gauge forces. The structure of GMSB models involves a hidden sector where supersymmetry is broken, a “messenger sector” including particles with the quantum numbers of equation 2.1, and a visible sector with the content described above [8,74]. The direct coupling of messengers to the hidden sector generates a supersymmetry breaking spectrum in the messenger sector. Gauge interactions then mediate supersymmetry breaking needed in the observable sector. In this scenario, the gravitino mass is typically in the eV to keV range since the supersymmetry breaking scale $\sqrt{F}$ ranges between 10 TeV and about 1000 TeV, and the coupling of the gravitino to other particles of the MSSM can become strong enough to let the gravitino play an important role in particle physics experiments.

2.2.3 Gauge-Mediated Supersymmetry Breaking

As mentioned in the previous section, the gravitino has taken over the goldstino including its couplings to the rest of the world as a result of the super-Higgs mechanism. Since goldstino couplings are suppressed compared to electroweak and strong interactions, a decay to the gravitino is only relevant for the lightest Standard Model superpartner and next to lightest supersymmetric particle

(NLSP).

GMSB Parameters and Sparticle Masses

The whole mass spectrum of supersymmetric particles in GMSB models is determined by five free parameters of the model plus the gravitino mass [75, 76] in addition to Standard Model parameters. This feature allows for a high degree of predictability. Free parameters are the supersymmetry breaking scale in the messenger sector Λ, the messenger mass M_m, the messenger index N_m (an integer) and $\tan\beta$. The Higgs mixing parameter μ is predicted up to its sign. Examples of mass spectra for certain sets of parameters are shown in figure 2.7 for gauginos and sleptons as calculated with `ISASUSY` [77]. A hierarchy between strongly interacting and weakly interacting particles holds throughout the whole parameter space keeping squarks much heavier than sleptons and the lightest gauginos.

In GMSB theories, the NLSP can either be the lightest neutralino $\tilde{\chi}_1^0$ or the lightest stau $\tilde{\tau}_1$ depending on N_m, M_m and $\tan\beta$ as can been seen in figure 2.8. In a very limited region of GMSB parameter space the sneutrino can become the NLSP, which happens for small values of Λ and M_m and medium values of $\tan\beta \approx 5$. Since final states with photons are subject of the thesis, only $\tilde{\chi}_1^0$ NLSP scenarios will be investigated.

Neutralino Decay

In most cases of GMSB models, the lightest neutralino has a dominant bino component [74] and its decay to a photon and the gravitino [79, 80] – see figure 2.9 – has the largest decay width since the decay to a Z or a Higgs is kinematically suppressed [74, 76, 81]:

$$\begin{aligned}
\Gamma(\tilde{\chi}_1^0 \to \gamma\tilde{\mathrm{G}}) &= \frac{\kappa_\gamma}{48\pi}\frac{m_{\tilde{\chi}_1^0}^5}{m_{\mathrm{P}}^2\, m_{\tilde{\mathrm{G}}}^2}, \\
\frac{\Gamma(\tilde{\chi}_1^0 \to \mathrm{Z}\tilde{\mathrm{G}})}{\Gamma(\tilde{\chi}_1^0 \to \gamma\tilde{\mathrm{G}})} &= \frac{\kappa_{\mathrm{Z}}}{\kappa_\gamma}\left(1-\frac{m_{\mathrm{Z}}^2}{m_{\tilde{\chi}_1^0}^2}\right)^4, \qquad (2.26)\\
\frac{\Gamma(\tilde{\chi}_1^0 \to \mathrm{h}\tilde{\mathrm{G}})}{\Gamma(\tilde{\chi}_1^0 \to \gamma\tilde{\mathrm{G}})} &= \frac{\kappa_{\mathrm{h}}}{\kappa_\gamma}\left(1-\frac{m_{\mathrm{h}}^2}{m_{\tilde{\chi}_1^0}^2}\right)^4,
\end{aligned}$$

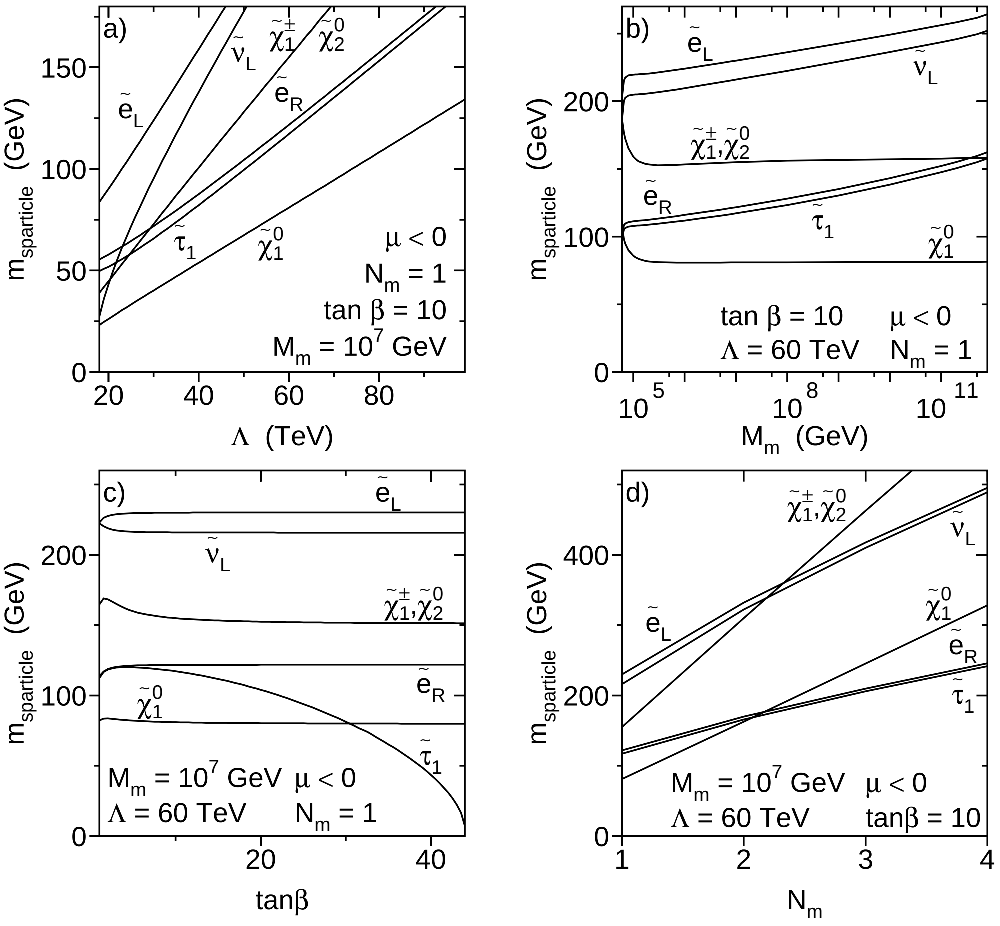

Figure 2.7: *Masses of sleptons and lightest gauginos as function of* Λ *(a),* M_m *(b),* $\tan\beta$ *(c), and* N_m *(d). Values for parameters fixed are indicated in the figures.* $\mu > 0$ *instead of* $\mu < 0$ *alters sparticle masses only slightly.*

with

$$\begin{aligned}
\kappa_\gamma &= \left|N_{11}\cos\theta_{\mathrm{W}} + N_{12}\sin\theta_{\mathrm{W}}\right|^2 , \\
\kappa_{\mathrm{Z}} &= \left|N_{11}\sin\theta_{\mathrm{W}} + N_{12}\cos\theta_{\mathrm{W}}\right|^2 \; + \; \frac{1}{2}\left|N_{13}\cos\beta - N_{14}\sin\beta\right|^2 , \qquad (2.27) \\
\kappa_{\mathrm{h}} &= \left|N_{13}\sin\alpha - N_{14}\cos\alpha\right|^2
\end{aligned}$$

and

$$\tan 2\alpha \;=\; \tan 2\beta \, \frac{m_{\mathrm{A}}^2 + m_{\mathrm{Z}}^2}{m_{\mathrm{A}}^2 - m_{\mathrm{Z}}^2} \, . \qquad (2.28)$$

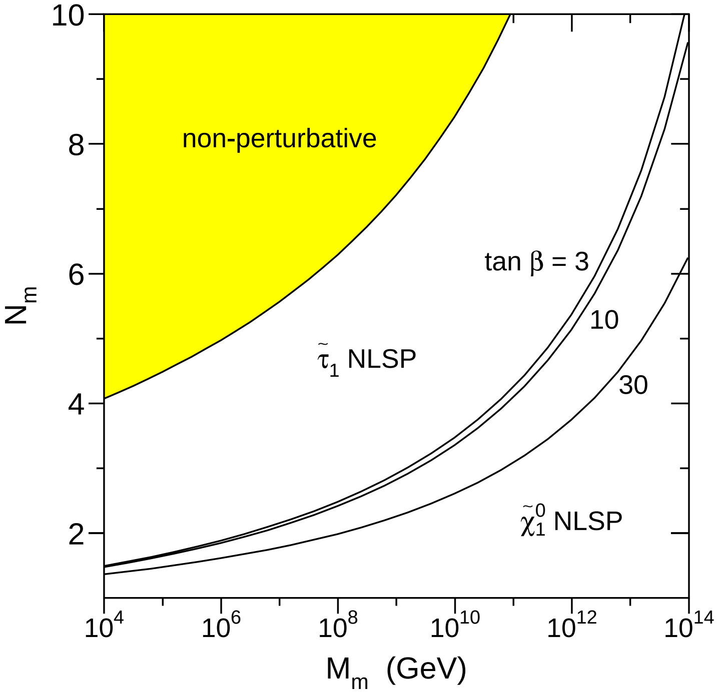

Figure 2.8: *Region of NLSP domains in dependence on N_m and M_m for three different values of* $\tan\beta$ *[78]. For large N_m and small M_m gauge interactions become non-perturbative below the GUT scale [74].*

Here, N_{1i} are the components of $\tilde{\chi}_1^0$ in the neutralino mixing matrix 2.21 in the basis 2.23. Complete expressions for the neutralino decay rates into three-body final states ($\tilde{\chi}_1^0 \to \tilde{\mathrm{G}} f\bar{f}$) can be found in [82]. The decay length of the NLSP can easily be calculated:

$$L_{\tilde{\chi}_1^0} = \frac{c\,\hbar}{\Gamma_{\tilde{\chi}_1^0}} \sqrt{\frac{E^2_{\tilde{\chi}_1^0}}{m^2_{\tilde{\chi}_1^0}} - 1}\,, \tag{2.29}$$

where $E_{\tilde{\chi}_1^0}$ is the energy of the neutralino. The decay length is displayed versus neutralino and gravitino mass in figure 2.10. For a neutralino mean decay length $L_{\tilde{\chi}_1^0}$ larger than about 1 cm the experimental sensitivity drops firstly due to selection cuts on the electromagnetic shower shape (see section 4.1) if the decay takes place before the electromagnetic calorimeter (see section 3.2.1) and secondly because of unidentified photons if the decay takes place outside the detector. For instance for $m_{\tilde{\chi}_1^0} = 10$ GeV and $m_{\tilde{\mathrm{G}}} = 1$ eV, the neutralino decay length is ap-

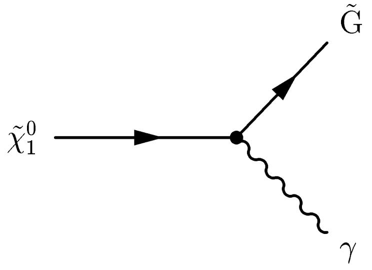

Figure 2.9: *Feynman graph for the decay of the lightest neutralino to gravitino and photon.*

proximately 10 m. Throughout this thesis a prompt decay ($L_{\tilde{\chi}_1^0} \lesssim 1$ cm) of the lightest neutralino into photon and gravitino is assumed when GMSB theories are being investigated.

Neutralino Production

Neutralinos can be pair-produced in e^+e^- collisions via Z exchange in the s–channel and via t–channel selectron exchange (figure 2.11) [83,84]. Only higgsino components of neutralinos, that directly couple to the Z, play a role in the s–channel, whereas only photino and zino components take part in t–channel production, which is because of the very small electron mass suppressing the coupling to the higgsino. Due to the bino nature of the neutralino in GMSB theories, the t–channel contribution dominates and the s–channel is negligible. The cross section of the process

$$e^+e^- \to \tilde{\chi}_1^0\tilde{\chi}_1^0 \tag{2.30}$$

therefore strongly depends on the selectron mass. By varying the model parameters, upper and lower bounds on the production cross section are calculated as shown in figure 2.12. Here, the GMSB parameters have been scanned within boundaries – motivated by [85] – defined as

$$\begin{array}{rcccl} 10\ \text{TeV} & \le & \Lambda & \le & 100\ \text{TeV} \\ \Lambda/0.9 & \le & M_m & \le & \Lambda/0.01 \\ & & N_m & = & 1\ldots 4 \\ 1 & \le & \tan\beta & \le & 60 \\ & & \text{sign}\,\mu & = & \pm\,. \end{array} \tag{2.31}$$

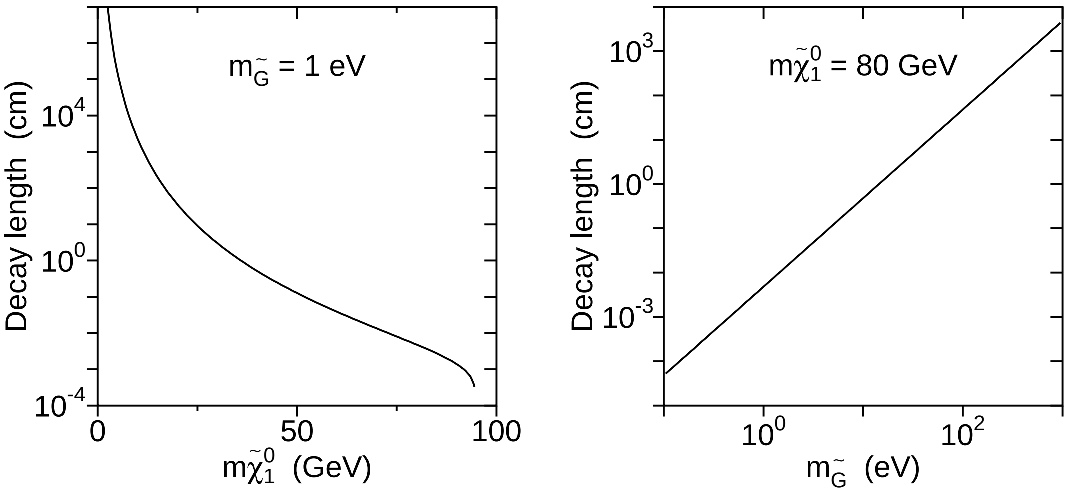

Figure 2.10: *Decay length of a neutralino with energy* $E_{\tilde{\chi}_1^0} = 95$ GeV *versus mass of the neutralino (left hand side) and versus gravitino mass (right hand side).*

Sparticle masses and couplings are calculated from GMSB model parameters using `ISASUSY`, which has been interfaced to `SUSYGEN` [86] to derive the neutralino pair-production cross section including initial state radiation.

Neutralino Signature

Taking into account the previous discussions, the experimental signature of neutralino pair-production in GMSB models is the appearance of two photons and missing energy due to undetectable gravitinos in the final state. The two photons coming from $\tilde{\chi}_1^0$ pair-production and decay have a flat energy distribution in the range $E_{\min} < E_\gamma < E_{\max}$ with

$$E_{\max,\min} = \frac{E_{\tilde{\chi}_1^0}}{2}\left(1 \pm \sqrt{1 - \frac{m_{\tilde{\chi}_1^0}^2}{E_{\tilde{\chi}_1^0}^2}}\right) \tag{2.32}$$

with $E_{\tilde{\chi}_1^0} = \sqrt{s}/2$. Edges in the photon energy distributions get washed out a little bit by the effect of initial state radiation, as can be seen in figure 2.13, where next to the energy distribution of the photons their angular and recoil mass distributions are shown for various neutralino masses. The angular distribution does not depend on the neutralino mass and the shape of all distributions shown

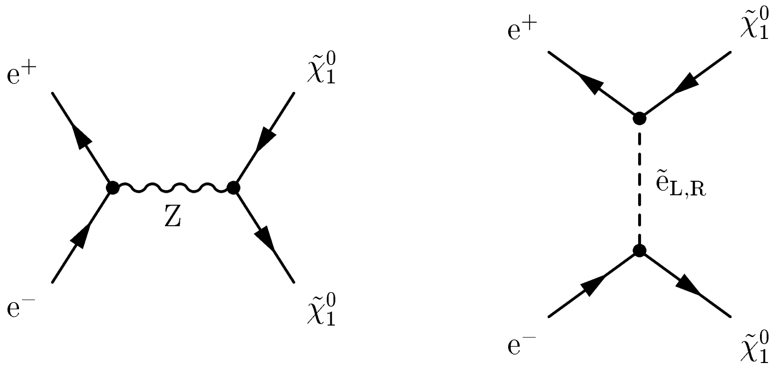

Figure 2.11: *Feynman diagrams of* $e^+e^- \rightarrow \tilde{\chi}_1^0\tilde{\chi}_1^0$.

is very different from the Standard Model process $e^+e^- \rightarrow \nu\bar{\nu}\gamma\gamma(\gamma)$ as displayed in figures B.2 to B.4. The spectra have been calculated using the `SUSYGEN` Monte Carlo program.

Sleptons

Not only neutralinos but also sleptons can possibly be produced at LEP energies (see figure 2.7) [87]. In e^+e^- interactions, sleptons are created via s–channel photon and Z exchange. For selectron production t–channel neutralino exchange contributes, too (figure 2.14). Keeping the neutralino NLSP hypothesis, the slepton decay – figure 2.15 – would proceed via a cascade

$$e^+e^- \rightarrow \tilde{l}^+\tilde{l}^- \rightarrow \tilde{\chi}_1^0\tilde{\chi}_1^0\, l^+l^- \tag{2.33}$$

with the neutralino decaying as discussed above. Hence, the experimental signature of sleptons in GMSB models and neutralino NLSP scenarios equals the two standard model partners of the sleptons and two photons plus missing energy from neutralino decays in the final state.

However, slepton production would not be the discovery process in GMSB neutralino NLSP models, since the neutralino pair-production cross section exceeds the slepton pair-production cross section in a large region of the parameter space. Thus the highest sensitivity is concentrated on the neutralino-pair process – assuming a similar experimental sensitivity for the detection of photon pairs as for lepton plus photon pairs. Only for low neutralino masses and fairly low slepton masses, the slepton pair-production cross section becomes dominant as

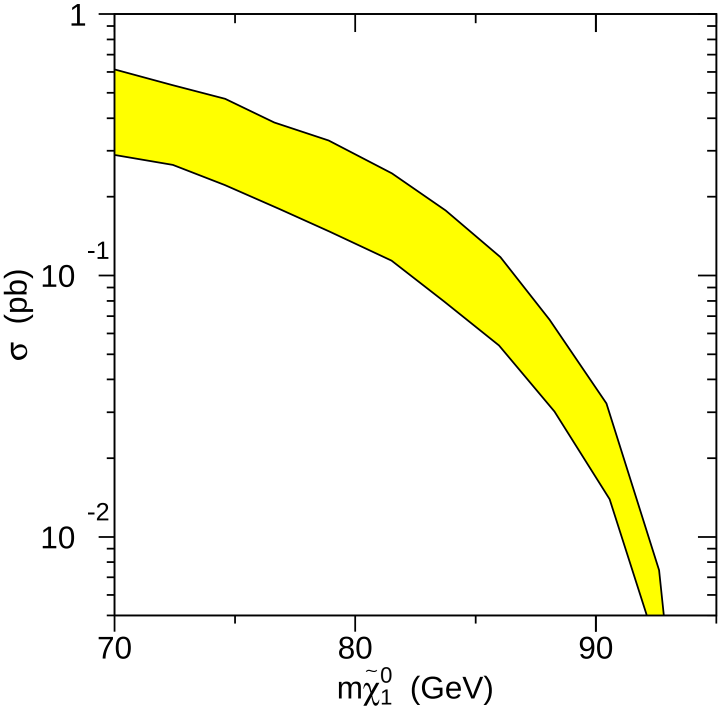

Figure 2.12: *Cross section range (shaded area) for* $e^+e^- \rightarrow \tilde{\chi}_1^0\tilde{\chi}_1^0$ *at* $\sqrt{s} =$ 189 GeV *as a function of the mass of the lightest neutralino in GMSB models. Here, it is assumed that the neutralino is NLSP.*

displayed in figure 2.16 showing the region in the $m_{\tilde{\chi}_1^0}$ versus $m_{\tilde{l}}$ plane, where slepton pair-production has a higher rate than neutralino pair-production. As will be demonstrated in section 5.4, this region of low neutralino masses can be covered by the neutralino search alone without any aid from slepton pairs. Therefore, this thesis will concentrate on the neutralino pair-production process as far as interpretations within GMSB models are concerned.

2.2.4 Supergravity

In supergravity (SUGRA) models the gravitino mass is of the order of the electroweak scale; its couplings are too weak to play any role in collider experiments. In the minimal supergravity framework [88–90], scalar masses and mixings are universal [13]. With these universality conditions, the whole sparticle spectrum is determined by only five free parameters: M_2, μ and $\tan\beta$ described in sec-

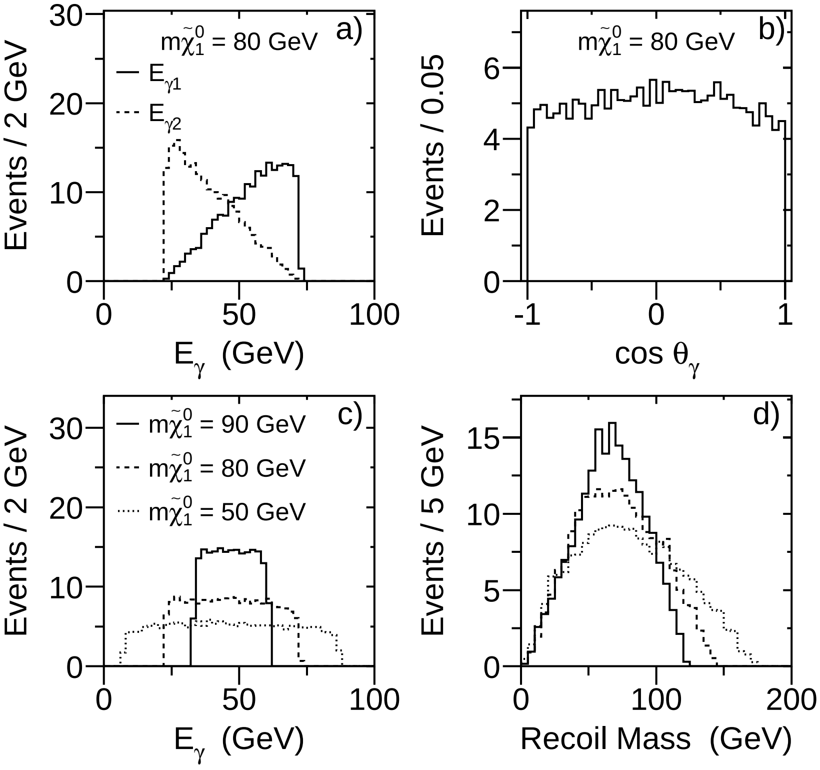

Figure 2.13: *Kinematic distributions for* $e^+e^- \to \tilde{\chi}_1^0\tilde{\chi}_1^0 \to \tilde{G}\tilde{G}\gamma\gamma$ *at* $\sqrt{s} =$ 189 GeV *in arbitrary normalisation. Spectra in (a) and (b) are for* $m_{\tilde{\chi}_1^0} =$ 80 GeV. *In (a) the energy of the more energetic (solid line) and less energetic photon (dashed line) are shown and in (b) their angular distribution. Photon energy (c) and recoil mass spectra (d) for various* $m_{\tilde{\chi}_1^0}$ *are displayed.*

tion 2.2.1, common scalar mass at GUT scale m_0 and common Higgs-sfermion-sfermion trilinear interaction parameter A at GUT scale. In these kinds of models the lightest neutralino is the LSP, being stable if R–parity is conserved [91].

Photons in SUGRA

In SUGRA models appearance of photons in the final state is only possible for a limited region of the parameter space. For certain compositions of neutralino content – as discussed in detail in [15,92] – radiative decay of a heavier neutralino to a lighter neutralino is enhanced with respect to the three body decay $\tilde{\chi}_2^0 \to \tilde{\chi}_1^0 f\bar{f}$. Radiative decay is suppressed for the most common scenarios compared

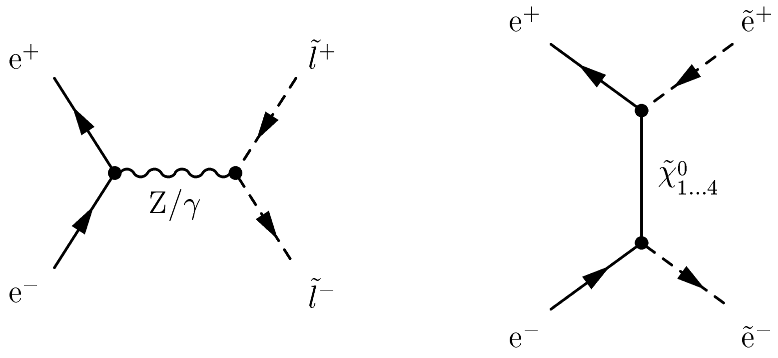

Figure 2.14: *Feynman diagrams of* $e^+e^- \to \tilde{l}^+\tilde{l}^-$.

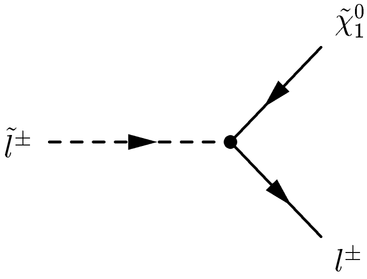

Figure 2.15: *Feynman graph for the decay of a slepton to its Standard Model partner and the lightest neutralino.*

to three body decays, since it is a one-loop process (see figure 2.17). Especially, when the unification of gaugino masses at the GUT scale is not fulfilled (equation 2.24), the decay to a photon can be enhanced [15]. Couplings of sfermions to neutralinos involve only the gaugino component, while the Z only couples to higgsinos [83]. Hence, the direct tree level decays $\tilde{\chi}^0_2 \to \tilde{\chi}^0_1 f\bar{f}$ require either simultaneous gaugino components in both neutralinos for the sfermion exchange process or simultaneous higgsino components for the Z exchange process. The above requirement does not hold for the radiative decay, since in general both, gaugino and higgsino components of neutralinos are involved in each graph of figure 2.17, apart from the two diagrams on the left hand side. Therefore, whenever a lighter neutralino is mainly higgsino and a heavier neutralino is dominated by gaugino components, the tree level $\tilde{\chi}^0_2$ width for direct three body decay falls down and $\tilde{\chi}^0_2 \to \tilde{\chi}^0_1\gamma$ is enhanced.

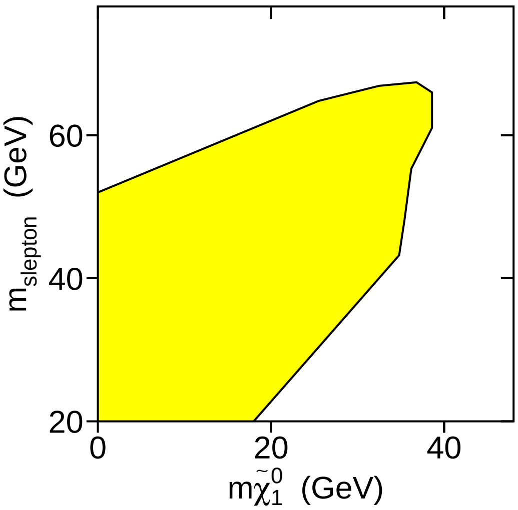

Figure 2.16: *Region in the $m_{\tilde{\chi}^0_1}$ versus $m_{\tilde{l}}$ plane, where slepton pair-production has a higher rate than neutralino pair-production in GMSB neutralino NLSP models. Cross sections are calculated at* $\sqrt{s} = 189$ GeV *with* ***`SUSYGEN`****.*

Energy and angular distributions of the photon(s) coming from neutralino decay have the same flat shape as the spectra shown in figure 2.13 for GMSB models. Due to the fact that the lightest neutralino is not massless like the gravitino was in the previous section[11], the expression for maximum and minimum energy of photons allowed by kinematics needs to be modified with respect to equation 2.32:

$$E_{\text{max,min}} = \frac{E_{\tilde{\chi}^0_2}}{2}\left(1 \pm \sqrt{1 - \frac{m^2_{\tilde{\chi}^0_2}}{E^2_{\tilde{\chi}^0_2}}}\right)\frac{m^2_{\tilde{\chi}^0_2} - m^2_{\tilde{\chi}^0_1}}{m^2_{\tilde{\chi}^0_2}}\,, \tag{2.34}$$

where for the process

$$\mathrm{e}^+\mathrm{e}^- \to \tilde{\chi}^0_2\tilde{\chi}^0_2 \to \tilde{\chi}^0_1\tilde{\chi}^0_1\gamma\gamma\,, \tag{2.35}$$

$E_{\tilde{\chi}^0_2} = \sqrt{s}/2$, and for the process

$$\mathrm{e}^+\mathrm{e}^- \to \tilde{\chi}^0_1\tilde{\chi}^0_2 \to \tilde{\chi}^0_1\tilde{\chi}^0_1\gamma\,, \tag{2.36}$$

---

[11] "Zero" is a good approximation for the gravitino mass from the point of view of kinematics, but certainly not if its couplings are taken into consideration.

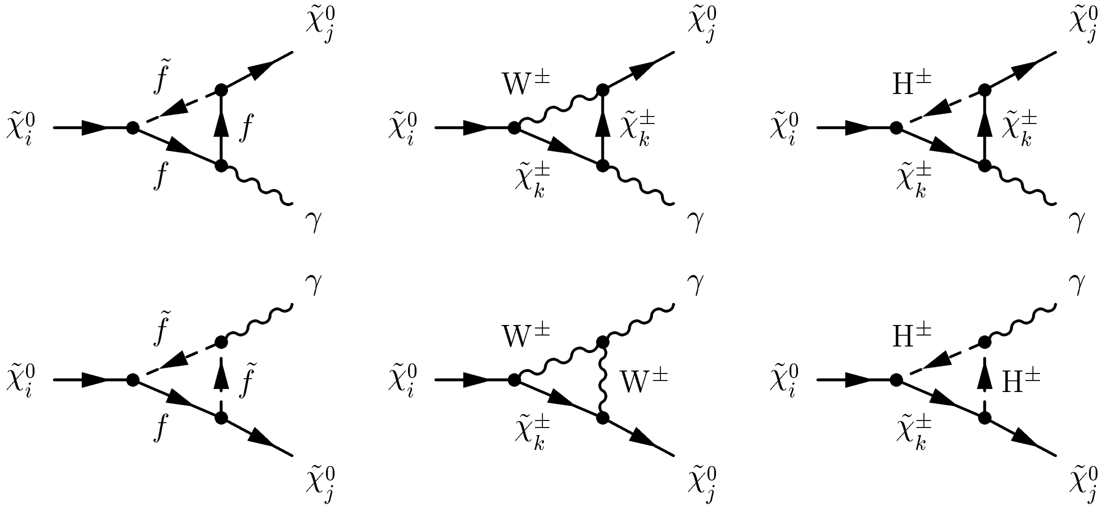

Figure 2.17: *Feynman graphs for the radiative decay of a heavier neutralino $\tilde{\chi}^0_i$ to a lighter neutralino $\tilde{\chi}^0_j$.*

$E_{\tilde{\chi}^0_2} = (s + m^2_{\tilde{\chi}^0_2} - m^2_{\tilde{\chi}^0_1})/(2\sqrt{s})$. Equation 2.34 reduces to equation 2.32 in the limit of $m_{\tilde{\chi}^0_1} \to 0$ and by replacing $\tilde{\chi}^0_2$ by $\tilde{\chi}^0_1$. Process 2.35 leads to a two-photon signature with missing energy due to the undetected neutralinos similar to process 2.30, whereas in process 2.36 only a single photon and missing energy are the characteristics of the reaction. Neutralinos $\tilde{\chi}^0_i, i \geq 2$ can become long-lived only for very small mass differences to the lightest neutralino in the MeV range.

2.2.5 Light Gravitinos and No-Scale Supergravity

In section 2.2.3 the appearance of light gravitinos has been discussed in the context of theories with gauge-mediated supersymmetry breaking. However, also other approaches have been made where a light gravitino can be accommodated.

Without making any assumptions about the mechanism of supersymmetry breaking, the mass of the gravitino is still coupled to the scale of local supersymmetry breaking by equation 2.25. Taking the supersymmetry breaking scale as an arbitrary parameter, the gravitino can be arbitrarily light [71, 72, 93, 94]. A general interpretation of the process $e^+e^- \to \tilde{\chi}^0_1\tilde{\chi}^0_1 \to \tilde{G}\tilde{G}\gamma\gamma$ in terms of the model parameters M_2, μ and $\tan\beta$ as introduced in section 2.2.1, has been proposed recently [95].

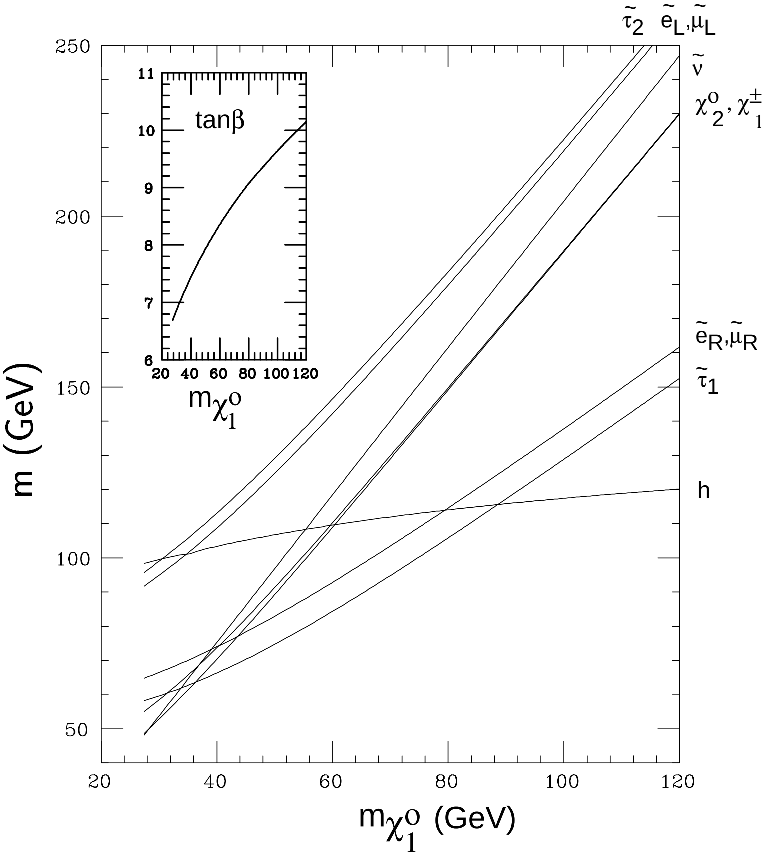

Figure 2.18: *Masses of lighter particles in the LNZ model versus neutralino mass. The inset shows the variation of* $\tan\beta$ *with* $m_{\tilde{\chi}_1^0}$ *[100].*

In no-scale supergravity [9–12], the breaking of local supersymmetry – and therefore the gravitino mass – is decoupled from the breaking of global supersymmetry which determines the spectrum of superpartners of the Standard Model particles. In these models a light gravitino may appear [79]. No-scale supergravity becomes especially predictive in a model with flipped SU(5) gauge symmetry [96, 97] where only one free parameter is needed to determine the whole spectrum of sparticles except the gravitino mass [98–100] as it is shown in figure 2.18.

$\tilde{\chi}_1^0\tilde{G}$ Production

Besides the reaction $e^+e^- \rightarrow \tilde{\chi}_1^0\tilde{\chi}_1^0 \rightarrow \tilde{G}\tilde{G}\gamma\gamma$ discussed in section 2.2.2, two more processes involving very light gravitinos could emerge from e^+e^- interactions:

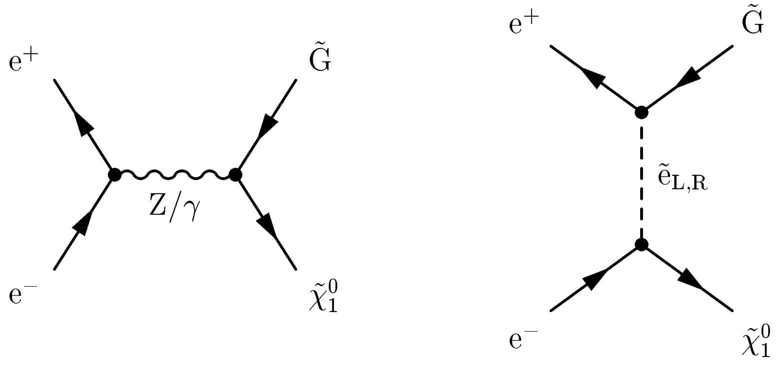

Figure 2.19: *Feynman diagrams of* $e^+e^- \to \tilde{\chi}_1^0\tilde{G}$.

The first one is the production of a neutralino in association with a gravitino (figure 2.19), leading to a single photon signature with missing energy due to the radiative decay of neutralino to gravitino [101, 102]

$$e^+e^- \to \tilde{\chi}_1^0\tilde{G} \to \tilde{G}\tilde{G}\gamma\,. \tag{2.37}$$

The cross section of this process becomes sizeable only for gravitino masses below about 10^{-4} eV and does thus not play a role in GMSB models, where the gravitino is much heavier (see section 2.2.3). In the one-parameter model of no-scale supergravity discussed above – from now on referred to as Lopez-Nanopoulos-Zichichi model (LNZ) – the production cross section of this process depends exclusively on the parameter of the model describing the sparticle sector of the theory like the neutralino mass, and on the gravitino mass. Energy, angular, and recoil mass distributions of the resulting photons of the reaction $e^+e^- \to \tilde{\chi}_1^0\tilde{G} \to \tilde{G}\tilde{G}\gamma$ show, again, a behaviour similar to the spectra shown in figure 2.13 (flat shape). The branching fraction for the radiative decay of the neutralino is due to a large photino content of the neutralino always the dominant one for neutralino masses within the kinematic reach of LEP. However, neutralino masses above m_Z lead to a non-negligible width for the $\tilde{\chi}_1^0 \to \tilde{G}Z$ decay as shown in figure 2.20.

Gravitino Pair-Production

If all supersymmetric partners of the Standard Model particles are too heavy to be produced at centre-of-mass energies available at LEP, still superlight graviti-

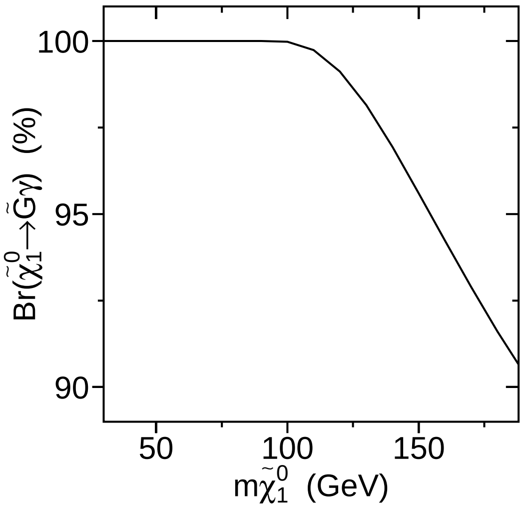

Figure 2.20: *Branching fraction of the lightest neutralino to gravitino and photon within the LNZ model.*

nos could be detected via the process [103–106]

$$e^+e^- \to \tilde{G}\tilde{G}\gamma\,. \tag{2.38}$$

Here, the production cross section only depends on the supersymmetry breaking scale [106] which is in a one-to-one correspondence to the gravitino mass (equation 2.25), and the only assumption made is, that all other sparticles are heavier than $\sqrt{s}$. The photon spectra are very different in this process compared to the previous ones, as can be seen in figure 2.21. In this case, the angular and energy distributions are dominated by initial state radiation showing the usual falling signature in energy – but without "return-to-the-Z" peak – (compare to figure B.1 and the discussion in section 2.1.1) and remaining contributions [106] extending the spectrum to higher energies are very small as visible in figure 2.21.

2.2.6 An Experimental Hint

A physics event reported by the CDF collaboration [107,108] at the TEVATRON proton-antiproton collider, situated at the Fermi National Accelerator Laboratory, Batavia, USA, has brought wide attention to models with light gravitinos [81, 100, 109–118]. This event, as shown in figure 2.22, consists of two high energetic electrons, two high energetic photons and large missing energy. The

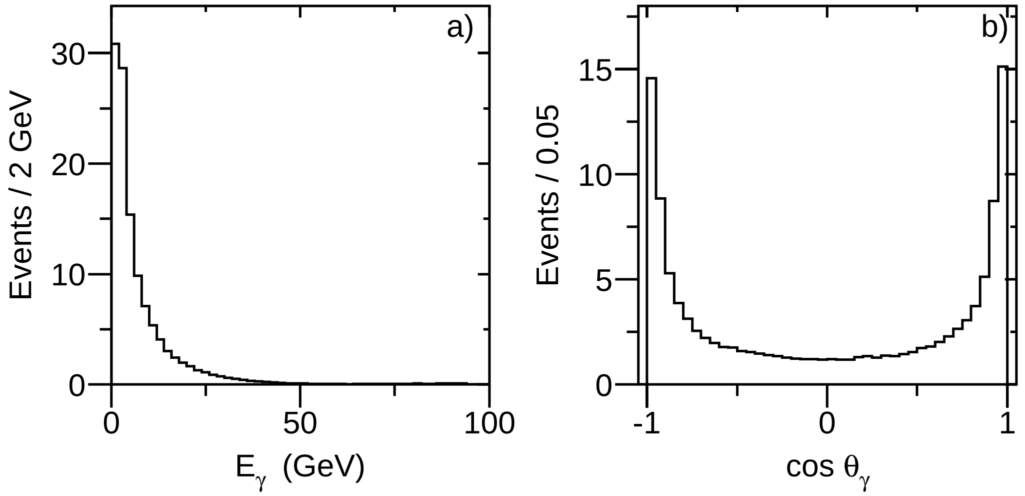

Figure 2.21: *Energy (a) and angular (b) distributions of the photons coming from* $e^+e^- \to \tilde{G}\tilde{G}\gamma$ *at* $\sqrt{s} = 189$ GeV *for* $m_{\tilde{G}} = 10^{-5}$ eV *and* $\mathcal{L} = 176\,\mathrm{pb}^{-1}$.

expected rate for events like this from Standard Model processes is very low and has been estimated by the CDF collaboration to be $(1 \pm 1) \cdot 10^{-6}$ events in the data sample of 85 pb^{-1} [108]. The Standard Model rate is dominated by $\mathrm{WW}\gamma\gamma$ production, where both Ws decay into electron and neutrino.

In models with light gravitinos, this event is a candidate for the process $\mathrm{q\bar{q}} \to \tilde{e}^+_{\mathrm{L,R}}\tilde{e}^-_{\mathrm{L,R}}$ with the subsequent decays $\tilde{e}^\pm_{\mathrm{L,R}} \to e^\pm\,\tilde{\chi}^0_1$ and $\tilde{\chi}^0_1 \to \tilde{G}\,\gamma$, but also chargino production is possible, *i.e.* $\mathrm{q\bar{q}} \to \tilde{\chi}^+_1\tilde{\chi}^-_1$ with the decays $\tilde{\chi}^\pm_1 \to e^\pm\,\nu_e\,\tilde{\chi}^0_1$ and $\tilde{\chi}^0_1 \to \tilde{G}\,\gamma$.

The event has also been interpreted in neutralino LSP models [119]. Again, selectron and chargino production in a $\mathrm{q\bar{q}}$ collision can be the origin of the event with selectron or chargino decaying to electron and $\tilde{\chi}^0_2$, and $\tilde{\chi}^0_2$ then decaying radiatively to $\tilde{\chi}^0_1$. Within this framework, the event can only be accomodated in models with relaxed GUT boundary conditions for the gaugino mass parameters (see equation 2.24).

2.2.7 Signatures and Assumptions

In this section, the signatures searched for and the assumptions made within the various supersymmetric models are summarised.

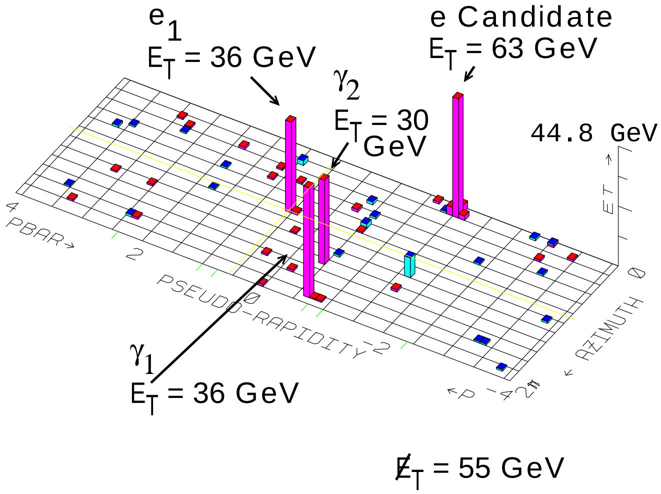

Figure 2.22: eeγγ *event published by the CDF collaboration [107, 108].*

Common to all scenarios are the requirements that R–parity is a conserved quantity and that the lightest supersymmetric particle is colourless and electrically neutral (see section 2.2). Two distinct signatures are investigated: events with a single photon plus missing energy and events with two photons plus missing energy in the final state. Several SUSY models predict processes that lead to these signatures.

Basically, three different SUSY processes yield a single photon signature: $\tilde{\chi}^0_1\tilde{\chi}^0_2$ production in SUGRA models where the neutralino is the LSP (see section 2.2.4), and $\tilde{\chi}^0_1\tilde{\mathrm{G}}$ and $\tilde{\mathrm{G}}\tilde{\mathrm{G}}\gamma$ production in models with superlight gravitinos like no-scale SUGRA (see section 2.2.5). The $\tilde{\chi}^0_1\tilde{\mathrm{G}}$ process is also interpreted within the LNZ model which is a more restricted no-scale SUGRA model. An additional assumption needs to be imposed for the $\tilde{\mathrm{G}}\tilde{\mathrm{G}}\gamma$ process, where all other SUSY particles need to be heavier than the centre-of-mass energy [106].

The two-photon signature can arise from two reactions: $\tilde{\chi}^0_2\tilde{\chi}^0_2$ production in neutralino LSP models and $\tilde{\chi}^0_1\tilde{\chi}^0_1$ production in gravitino LSP models. The first process is discussed in terms of the SUGRA model parameters introduced in section 2.2.4 and also in the CDF motivated case with relaxed GUT boundary conditions for the gaugino mass parameters (see section 2.2.6). The second process is predicted by GMSB (section 2.2.3) and no-scale SUGRA models (section 2.2.5). Here, it is assumed that the lightest neutralino is the next-to lightest supersymmetric particle and that it decays shortly after production, *i.e.* with a

Signature	Process	Model
$\gamma + E_{\text{miss}}$	$\tilde{\chi}_1^0\tilde{\chi}_2^0$	SUGRA [83,84]
	$\tilde{\chi}_1^0\tilde{\mathrm{G}}$	no-scale SUGRA, LNZ [101,102]
	$\tilde{\mathrm{G}}\tilde{\mathrm{G}}\gamma$	no-scale SUGRA [106]
$\gamma\gamma + E_{\text{miss}}$	$\tilde{\chi}_2^0\tilde{\chi}_2^0$	SUGRA [83,84]
	$\tilde{\chi}_1^0\tilde{\chi}_1^0$	GMSB [85]
		no-scale SUGRA [100]

Table 2.4: *Signatures, SUSY processes and models investigated.*

decay length less than about 1 cm. Both assumptions are fulfilled in a significant fraction of GMSB parameter space (see section 2.2.3). In no-scale SUGRA, the gravitino mass – and thus the $\tilde{\chi}_1^0$ decay length – is entirely unrestricted, but the neutralino is the NLSP in (almost) the whole parameter space of the model. All signatures, processes and models are listed in table 2.4.

2.3 Low Scale Quantum Gravity

The large hierarchy between the scales of electroweak and gravitational forces provides one of the major theoretical problems in elementary particle physics. Low energy supersymmetry – as discussed in section 2.2 – provides a natural solution to cure this weakness with effects of quantum gravity occurring only at the Planck scale m_{P}. Experimentally, the gravitational force has only been tested down to distances of no less than a centimetre [120], leaving more than 30 orders of magnitude to the typical distance of gravity m_{P}^{-1}. Recently, it has been proposed that the fundamental gravitational scale is as low as the electroweak scale [16], thus solving the hierarchy problem naturally. In this picture, Standard Model particles live in the usual 3+1 dimensional space while gravity can propagate in a higher dimensional space. Motivated by string theory, Standard Model particles are naturally confined to the lower dimensional space, since they correspond to open strings with the endpoints attached on a D–brane [121], while gravitons (G) correspond to closed strings propagating in the whole higher dimensional space [122–126]. Newton's constant measured in 3+1 dimensional

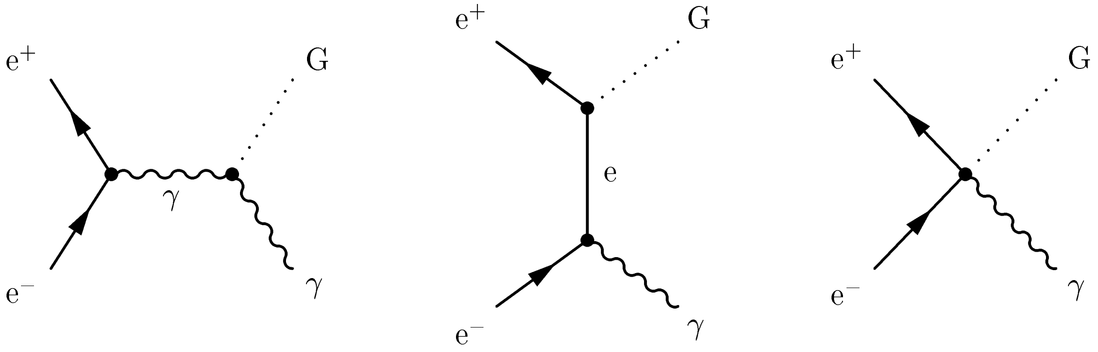

Figure 2.23: *Feynman diagrams contributing to* $\mathrm{e^+e^-} \rightarrow \gamma\mathrm{G}$.

space is related to the fundamental mass scale M_D via [127]

$$G_{\mathrm{N}}^{-1} \;=\; 8\pi R^{\delta} M_D^{\delta+2}\,, \tag{2.39}$$

where δ is the number of extra dimensions and R denotes their size. Models with only one extra dimension are experimentally excluded, since R would be comparable to the size of the solar system when M_D is on the electroweak scale, where gravity has extensively been probed.

Graviton-Photon Production

In this theory massive spin-two gravitons propagating in 4+δ dimensions interact with Standard Model particles with sizable strength. Real gravitons are produced in $\mathrm{e^+e^-}$ collisions through the process

$$\mathrm{e^+e^-} \rightarrow \gamma\mathrm{G}\,, \tag{2.40}$$

where the graviton escapes detection leading to a single photon and missing energy signature. The reaction proceeds through s–channel photon exchange, t–channel electron exchange and four-particle contact interaction as indicated in figure 2.23. The differential cross section of this process in photon energy normalised to beam energy, x_γ, and polar photon angle θ_γ is determined by [127]

$$\frac{d^2\sigma}{dx_\gamma d\cos\theta_\gamma} \;=\; \frac{\alpha}{64}\, S_{\delta-1} \left(\frac{\sqrt{s}}{M_D}\right)^{\delta+2} \frac{1}{s}\, f(x_\gamma, \cos\theta_\gamma) \tag{2.41}$$

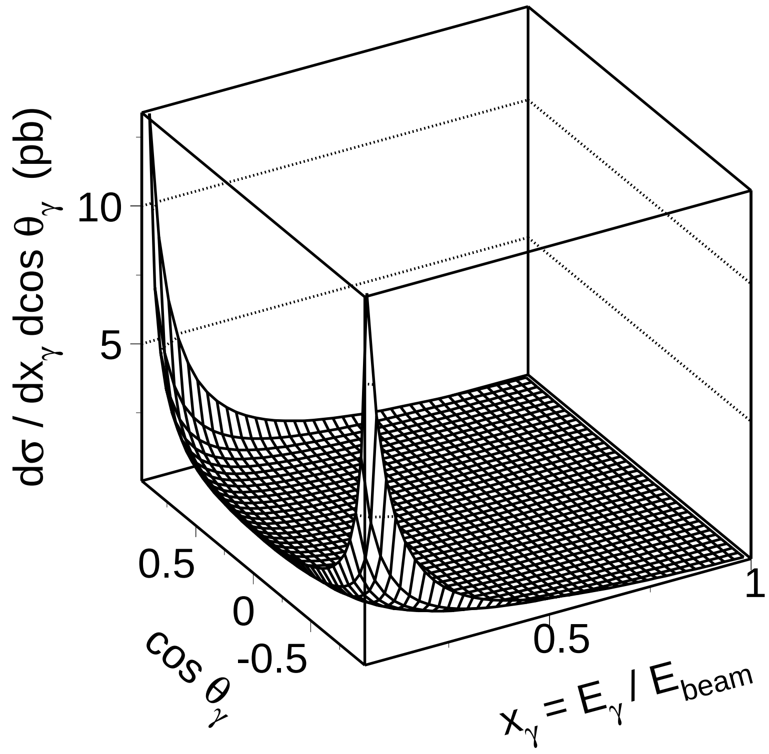

Figure 2.24: *Differential* γG *cross section in* x_γ *and* $\cos\theta_\gamma$ *in low scale gravity with two extra dimensions and* $M_D = 1$ TeV *at* $\sqrt{s} = 189$ GeV.

with

$$f(x,y) \;=\; \frac{2(1-x)^{\frac{\delta}{2}-1}}{x(1-y^2)}\left[(2-x)^2(1-x+x^2) - 3y^2x^2(1-x) - y^4x^4\right] \qquad (2.42)$$

and

$$S_{\delta-1} \;=\; \frac{2\pi^{\frac{\delta}{2}}}{\Gamma(\frac{\delta}{2})}\,. \qquad (2.43)$$

The cross section increases with smaller photon energies and angles as shown in figure 2.24.

Chapter 3

L3 Experiment

The two most obvious experimental questions in elementary particle physics are: How to produce elementary particles and how to detect them? These two topics will be addressed in the order the questions are raised within this chapter by explaining the apparatus worked with in this study.

3.1 Large Electron Positron Collider

The Large Electron Positron (LEP) collider is situated at the European Laboratory for Particle Physics CERN in the vicinity of Geneva, Switzerland. The LEP design follows the principle of a storage ring with electrons and positrons being accelerated and then stored at their final energy for several hours in the same ring. The two beam particle species have identical energy at any time of the acceleration procedure but opposite direction. With a circumference of 26.7 kilometres, LEP is the largest machine of its kind in the world. The beams are brought into collision at four interaction points which are equipped with particle detectors.

LEP Physics

Three main physics goals are addressed by the LEP program: In a first phase – denoted by "LEP 1" – electrons and positrons are being accelerated to an energy of about 45 GeV yielding resonant production of the Z boson and the study of the electroweak theory connected with it. During the second phase – called "LEP 2" – the beam energy is being increased step by step until a maximum of about 100 GeV by the end of the LEP operation time in the years 1999 and 2000 is attained. This exceeds the W boson pair-production threshold and offers the measurement of properties of the charged carrier of the weak force. Finally, with each step towards higher energies and every physics event recorded by an experiment, the possibility of finding particles which have never been detected before opens up. For example, within the Standard Model framework the Higgs particle is the candidate searched for, and any of the particles predicted by supersymmetric theories (see chapter 2.2) is awaiting its discovery.

Acceleration Procedure

Before electrons and positrons get injected into LEP, they have already passed a chain of pre-accelerators as displayed in figure 3.1. The injection system consists of several steps: At first, the LEP Injector Linear accelerator (LIL) ramps electrons to 200 MeV and smashes them onto a tungsten target to produce positrons, or, alternatively, simply passes them to a second LIL which alternately pushes electrons and positrons up to 600 MeV. The following Electron Positron Accumulator (EPA) collects the two particle species into small packages called bunchlets, and groups up to four bunchlets into bunches. When accumulated to a sufficiently large intensity, the particles are passed to the Proton Synchrotron (PS) operating as a 3.5 GeV e^+e^- synchrotron. At last the Super Proton Synchrotron (SPS) is used to bring particle bunches up to an energy of 20–22 GeV. The rest of the job is done by LEP itself: Acceleration to the desired beam energy.

LEP Ring

The LEP machine is formed by eight segments of a circle connected by eight straight sections. The bending sections are equipped with dipole and quadrupole magnets to keep electrons and positrons circulating on their ideal orbit. On both sides of four interaction regions superconducting quadrupole magnets focus the beams to increase the interaction rate. The beam spread at the interaction point is several microns in vertical direction, a few hundred micrometres in horizontal direction, and the bunchlets have a longitudinal extension of about 1 cm. The maximum luminosity[1] delivered to the experiments in 1998 was 10^{32} $\mathrm{cm}^{-2}\mathrm{s}^{-1}$ [128]. Near the interaction points the beam pipe has a radius

---

[1] The luminosity is defined in section 3.4.

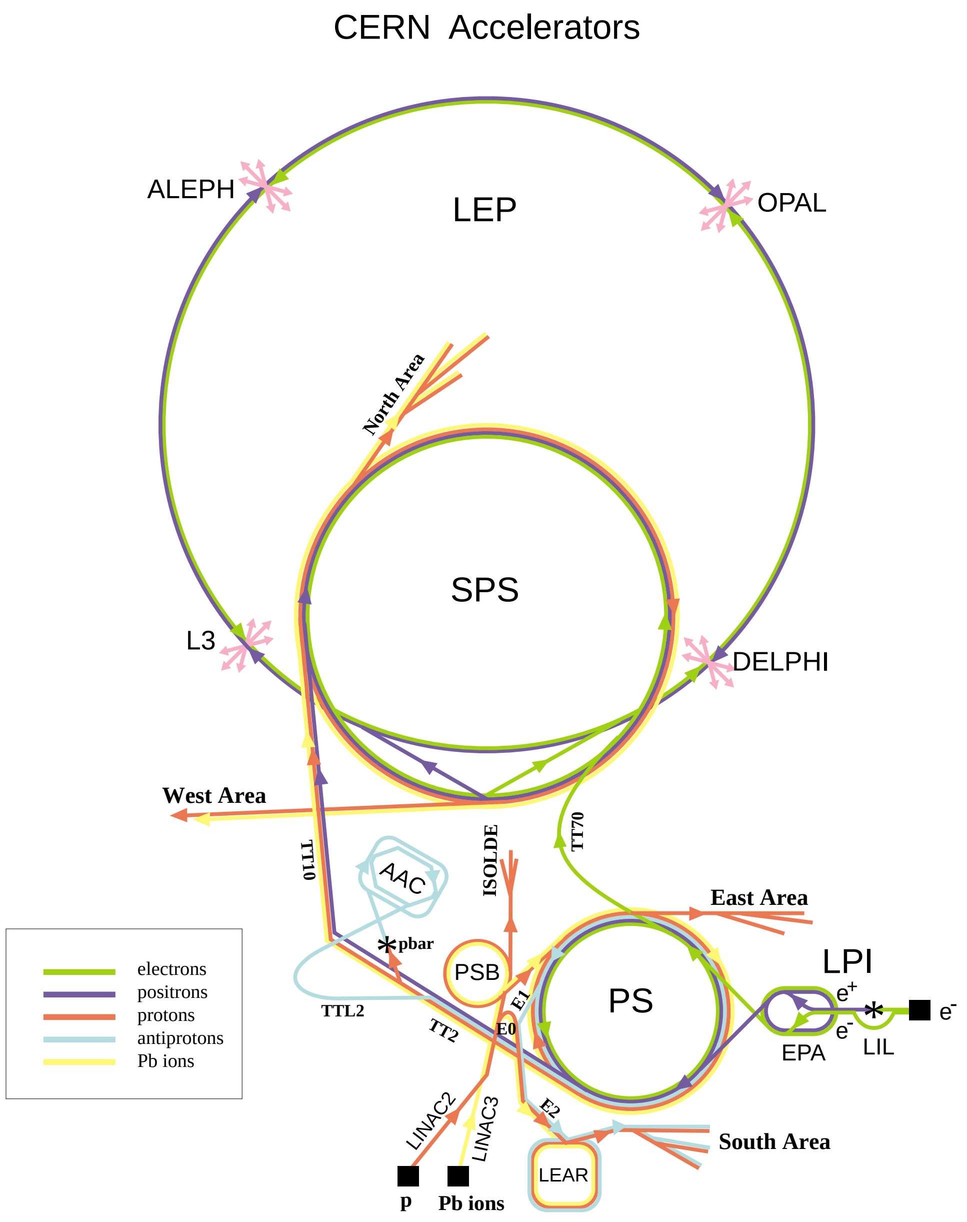

LEP: Large Electron Positron collider
SPS: Super Proton Synchrotron
AAC: Antiproton Accumulator Complex
ISOLDE: Isotope Separator OnLine DEvice
PSB: Proton Synchrotron Booster
PS: Proton Synchrotron

LPI: Lep Pre-Injector
EPA: Electron Positron Accumulator
LIL: Lep Injector Linac
LINAC: LINear ACcelerator
LEAR: Low Energy Antiproton Ring

Figure 3.1: *CERN accelerators including LEP storage ring with interaction points and injection system.*

of 5 cm and is made out of beryllium with 1 mm thickness. To accelerate beams to their design energies 128 radiofrequency (RF) copper cavities are installed at the straight sections, added and partly replaced during the LEP 2 phase by 384 superconducting cavities to be able to reach a higher energy. The beam energy is limited by the RF voltage needed to replenish losses due to synchrotron radiation. Since radiation losses increase as E_{beam}^4 the required RF voltage increases by a factor of 16 as the beam energy goes from 45 GeV at LEP 1 – where the average loss is 120 MeV per particle and turn – to about 90 GeV at LEP 2 – with a loss of 2 GeV per particle and turn.

Energy Measurement

Cross sections are a function of centre-of-mass energy. For a precise measurement of the LEP beam energy the method of resonant depolarisation [129, 130] is exploited, usually performed just before a LEP machine fill is terminated. At LEP 2 energies, however, this method can no longer be used, since disturbances prevent the beam from self-polarisation. Via nuclear magnetic resonance and flux loop measurements to monitor the dipole magnets a relative energy measurement is employed, which is calibrated with resonant depolarisation around $E_{\mathrm{beam}} = 40 - 60$ GeV. This technique measures the average beam energy in LEP under special beam conditions. Therefore the measured value has to be extrapolated to the four interaction regions for each fill. Here, a model is developed to account for time dependent and interaction point specific variations [131–133]. LEP 2 centre-of-mass energies and their errors are listed in section 3.4.

3.2 L3 Detector

L3 [134] is one of the four experiments – besides ALEPH [135], DELPHI [136] and OPAL [137] – installed at the LEP site. It was designed as a multi purpose detector with special emphasis on a precise energy measurement of photons and electrons, and accurate momentum measurement of muons. A perspective view of the detector is shown in figure 3.2 and its inner components are displayed in figure 3.3. The components of the whole apparatus are grouped with respect to their angular coverage into a barrel part, endcap regions, and subdetectors at very low angles relative to the beam axis.

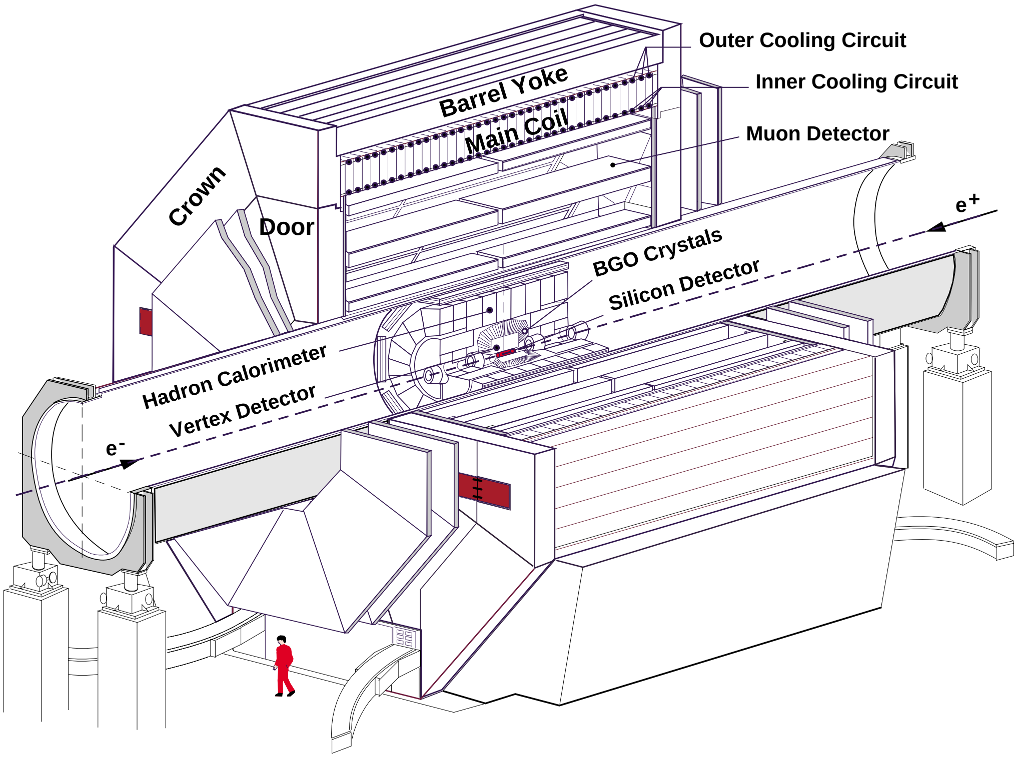

Figure 3.2: *Perspective view of the L3 detector.*

Starting from the interaction point the inner tracking system is surrounded by an electromagnetic calorimeter followed by scintillation counters and a hadron calorimeter. These inner detector parts are mounted within a steel support tube having a diameter of 4.45 metres and a length of 32 metres. Outside the support tube the muon spectrometer is installed. All detector parts[2] are embedded in a solenoidal magnet providing a homogeneous field of 0.5 Tesla parallel to the beam axis. Furthermore, the iron doors (see figure 3.2) are wrapped with coils providing a toroidal field of 1.2 Tesla to allow the measurement of muon momenta in the forward-backward muon chambers. The outer diameter of the L3 experiment is about 16 metres and its length along the beam pipe is about 14 metres.

---

[2] Except for a part of the forward-backward muon spectrometer [138] (see section 3.2.5), which is mounted outside the magnet and the Very Small Angle Tagger (VSAT) [139] (see section 3.2.6).

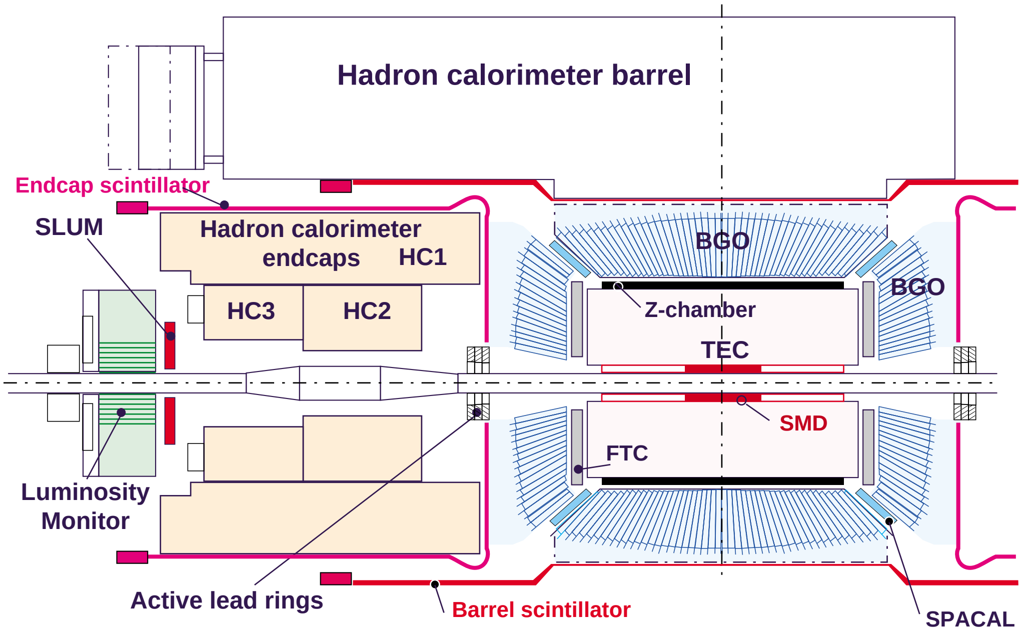

Figure 3.3: *Inner components of the L3 detector. Although not visible in the figure, the L3 detector is symmetric with respect to the plane perpendicular to the beam axis with origin in the centre of the detector.*

Coordinate System

The common coordinate system used within L3 has its origin in the nominal interaction point which is – at the same time – the geometrical centre of the detector. The x axis points to the centre of the LEP ring, the y axis is defined to be vertically upwards and the z axis is given by the flight direction of the beam electrons. Alternatively, a cylindrical coordinate system is used with the same origin and z axis as the Cartesian one. Here, the θ coordinate measures the angle subtended at the origin with respect to the z axis, and ϕ represents the angle in the xy plane (also called rϕ plane), with $\phi = 0$ for the x axis.

3.2.1 Electromagnetic Calorimeter

The electromagnetic calorimeter is by far the most important detector element of the L3 experiment for the detection of events with photons only, since it measures their energy and production angle. The requirement of high energy resolution can only be met by a calorimeter using the same medium for showering and detection, so that the complete shower is measured instead of only a sampled fraction of it. For high electron energies, energy loss comes mainly through the production of bremsstrahlung and the subsequent electron showers which it produces, so that a material with high atomic number is needed in order to facilitate shower production. The same argument holds for high energy photons for which pair-production is the dominant process. Having the highest density and atomic number, inorganic crystal scintillators become the most preferable, *i.e.* the ones with shortest radiation lengths thus allowing for a compact setup. With a radiation length of 1.12 cm [2], Bismuth Germanate ($Bi_4Ge_3O_{12}$, hereafter called BGO) is very suitable for accurate energy measurement. BGO is transparent and its scintillation light emission spectrum ranges from 400 nm to about 600 nm [140]. Another advantage compared to most other inorganic crystals is its non-hygroscopicity.

BGO Setup

The whole electromagnetic calorimeter consists of about 11000 crystals made of BGO. The arrangement of the crystals including the most important geometrical dimensions are shown in figure 3.4. The crystals have the shape of a truncated pyramid with a length of 24 cm (equivalent to more than 21 radiations lengths), a front surface of 2×2 cm^2 and a rear surface of 3×3 cm^2 (figure 3.5). In general, all crystals point to the vertex except for a small angular tilt of 10 mrad in azimuthal direction incorporated to suppress the possibility of particles traversing solely the insensitive carbon fiber support structure, which has a thickness of 200–250 μm. Each crystal is viewed by two photodiodes glued to its rear face to detect the BGO scintillation light. The photodiodes have a sensitive area of 1×1.5 cm^2 each. The noise induced by the photodiodes and their preamplifiers corresponds to an energy of 1 MeV.

Temperature Dependence

The light yield of BGO is correlated to the crystal temperature by -1.5% per °C. Since the temperature coefficient is negative the crystal temperature should be as low as possible to obtain the best light yield. However, as the temperature decreases, the decay time for BGO to emit scintillation light increases. To

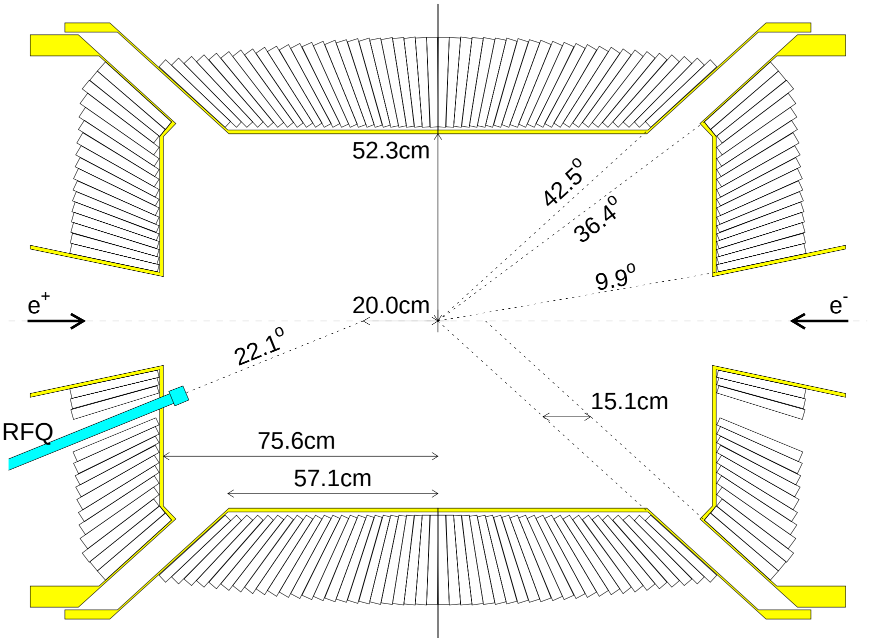

Figure 3.4: *Side view of the BGO electromagnetic calorimeter.*

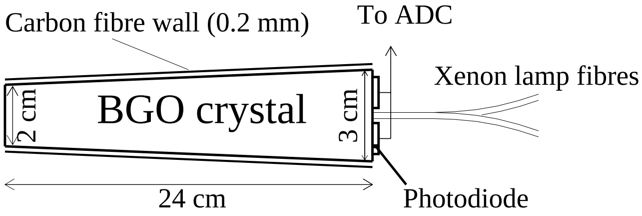

Figure 3.5: *BGO crystal.*

compromise these opposing effects, the BGO is kept at about $T_0 = 18°\text{C}$. The temperature of the calorimeter is monitored for blocks containing 12 crystals each at their front and rear ends. A correction factor C_T for the energy reconstruction is applied given as

$$C_T \;=\; 1 + 0.0155/°\text{C}\;(T_{\max} - T_0)\,, \tag{3.1}$$

where $T_{\max}$ denotes the temperature at the shower maximum in the crystals.

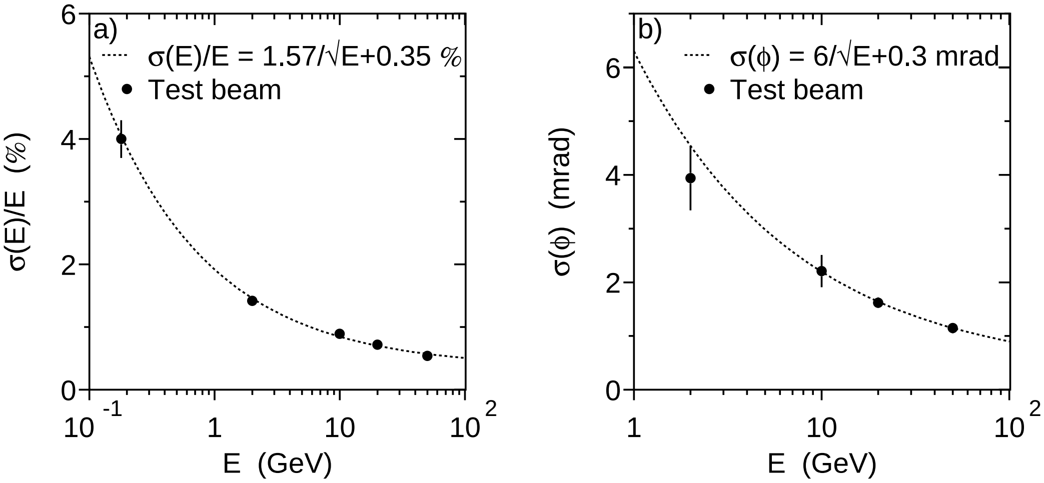

Figure 3.6: *Energy (a) and spatial (b) resolution of the BGO barrel measured in an electron test beam.*

Energy Calibration

To reconstruct the energy of a particle entering the BGO, the detector response as a function of the energy deposition must be known. Two calibration devices are installed to monitor the crystal behaviour. One system is based on light pulses emitted by Xenon lamps to control the transparency of the crystals. The light is transmitted to the rear face of each crystal via optical fibres. With this method an inter-calibration between the crystals is performed and the global absolute energy calibration at the energy of the LEP beams is fixed using electrons and positrons from Bhabha scattering events. The second system is based on a Radiofrequency Quadrupole (RFQ) [141,142] which accelerates hydrogen ions and smashes them onto a Lithium target at the end of the RFQ beam pipe (see figure 3.4). Radiative capture of the protons produces monoenergetic 17.6 MeV photons that are used to calibrate each crystal of the calorimeter. Again, Bhabha events are needed to fix the energy on the high energy side. The RFQ calibration [143] provides an energy reconstruction accuracy of about 0.8% to 1% for non-radiative Bhabha events (see also section 4.2), whereas results of the Xenon calibration method [144,145] are slightly worse (about 1.1% to 1.7%, see appendix C). For lower electron energies the resolution gets worse as measured in a test beam (see figure 3.6(a) and figure 3.7) [146]. The calorimeter shows an excellent linearity over a wide energy range. Calibrated to reproduce the beam energy when measuring non-

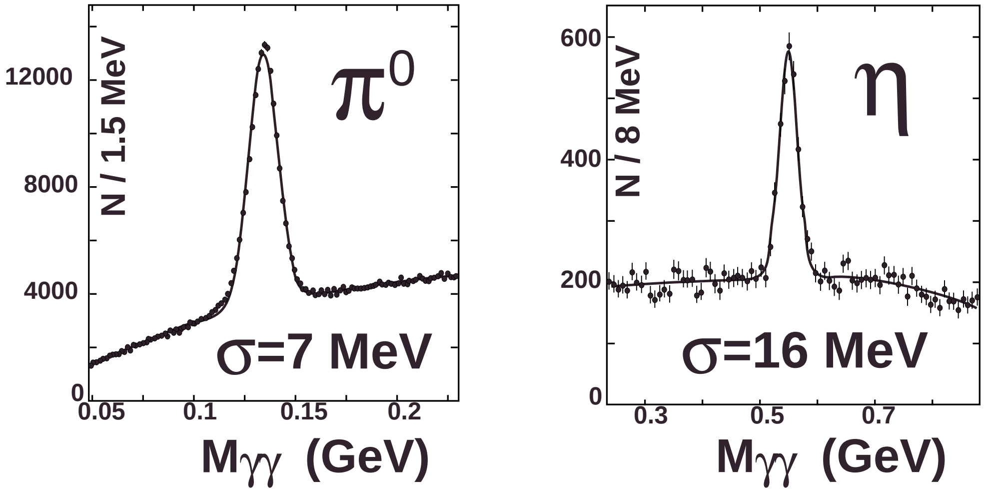

Figure 3.7: *Invariant mass spectra of photon pairs in hadronic events.*

radiative Bhabha events, the energy measurement is still very reliable for much lower energies as the masses of the neutral pion and η meson are reconstructed from their decay to photon pairs (see figure 3.7) measured in $\mathrm{e^+e^-} \rightarrow \mathrm{q\bar{q}}$ events.

Energy Reconstruction

After the reconstruction of the energy deposit of each crystal a pattern recognition algorithm is applied to extract the physics quantities. First, all geometrically connected crystals with at least 10 MeV energy are grouped into clusters with a minimal energy requirement for a cluster set to 40 MeV. The local energy maximum of a cluster is called bump, which is formed if its energy exceeds 40 MeV. A bump is assumed to correspond to a particle penetrating the calorimeter. The particle energy is reconstructed by summing up the energies of the crystals over a 3×3 matrix, E_9, surrounding a bump. An ambiguity arises for the choice of the nine crystals to form a bump in the endcaps as shown in figure 3.8. Here, the crystal with higher energy is chosen from two ambiguous crystals.

Energy leakage of an electromagnetic shower to the rear of the crystals or to the sides of the 3×3 matrix is corrected for. The corrected bump energy is given by

$$E_{\mathrm{bump}} = \frac{E_9}{c_1 \frac{E_1}{E_9} + c_2}, \qquad (3.2)$$

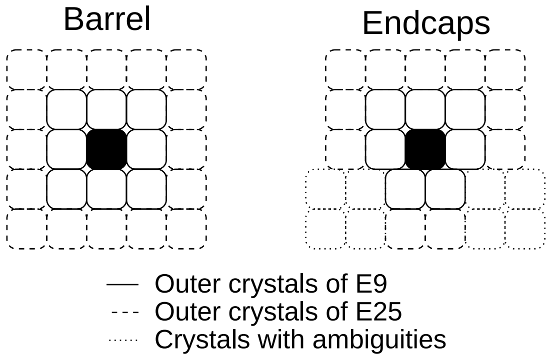

Figure 3.8: *Crystals forming E_9 and E_{25}, respectively.*

where E_1 is the energy of the central crystal and c_1 and c_2 are constants with numerical values depending on the different regions of the BGO. The angle of a bump in the L3 coordinate system is computed with a centre-of-gravity method using the energy depositions of the crystals forming this bump. The position resolution improves with increasing bump energy as displayed in figure 3.6(b) [146].

SPACAL

In 1996 the gaps (see figure 3.4) between barrel and endcap parts of the BGO were equipped with a "spaghetti" calorimeter (SPACAL) [147]. The SPACAL consists of lead bricks with several scintillating fibres inside. It has an energy resolution of $\sigma(E)/E = 11.6\%/\sqrt{E} + 2.3\%$ [147].

3.2.2 Inner Tracking System

The inner tracking system of L3 is situated between beam pipe and BGO. It is composed of a silicon vertex detector and wire chambers.

SMD

The Silicon Microvertex Detector (SMD) [148] is the innermost part of the central tracking system of L3. It is constructed of two cylindrical layers of silicon sensors approximately 6 and 8 cm from the beam axis. Each layer consists of 12 identical ladders, those on the inner layer being tilted slightly to fit into the smaller

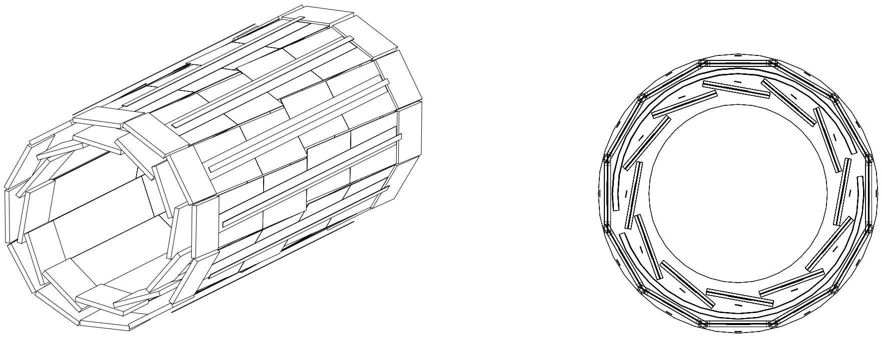

Figure 3.9: *SMD layout.*

circumference (figure 3.9). A ladder consists of four 70 mm long and 40 mm wide wafers. The spatial resolution of the SMD is 7 μm in the rϕ plane and 14 μm in the rz plane. The SMD covers a polar angle of $29^\circ \leq \theta \leq 151^\circ$ with both layers and $21^\circ \leq \theta \leq 159^\circ$ with the inner layer only.

TEC

The central tracking chamber surrounding the SMD was designed to give the best possible resolution in the limited volume available within the electromagnetic calorimeter. To measure the charge of a 50 GeV particle at the 95% confidence level in the 0.5 Tesla magnetic field, a single hit resolution of about 50 μm is required in 50 wires for the available lever arm. Such a demanding target is met by using a drift chamber in which a large drift region with a low, uniform field is separated from the high field amplification region close to the anode by a plane of grid wires (see figure 3.10) – the principle of a Time Expansion Chamber (TEC).

The TEC consists of two concentric cylinders, the inner one is subdivided into 12 sectors and the outer one into 24. Each sector has a central anode plane and is separated from its neighbouring sectors by cathode planes (figure 3.11). Two types of signal wires exist: Standard anode wires measure the x and y coordinates of an ionisation track. Charge division anode wires, where the signal is read out on both sides of the wire, give additionally the z coordinate by comparison of the two pulse integrals. Since the anode wires are radially aligned within a sector a left-right ambiguity arises. To resolve the question on which side of the anode plane the track has passed, pick-up wires – groups of five grid wires – are read out in the outer sectors. Altogether, there are six standard anode wires and

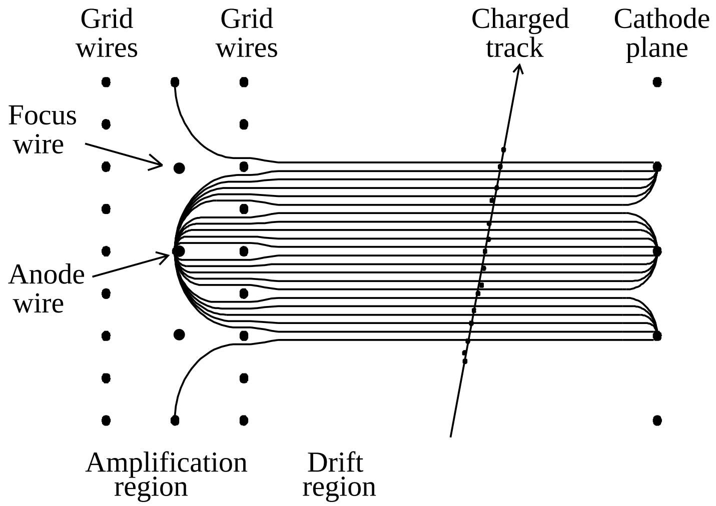

Figure 3.10: *Principle of a time expansion chamber.*

two charge division wires in the inner part of the TEC, whereas 31 standard, nine charge division, and 14 pick-up wires are in the outer part of the TEC. The TEC operates with a gas mixture of 80% CO_2 and 20% ISO-butane, in which the drift electrons have a low longitudinal diffusion, and thus a low drift velocity of less than 6 μm/ns is permitted – about 10 times less than what is used in a conventional drift chamber. The low diffusion results in a good resolution for the drift time measurement.

Z–Chamber

To improve the measurement of the z coordinate, which has a resolution of the order of centimetres using the charge division information alone, the outer surface of the TEC cylinder is equipped with a four-layer cylindrical proportional chamber called Z–chamber [149]. Here, four points of each track using cathode strip readout are measured. The strips have a pitch of 4.45 mm and are inclined with respect to the beam axis by angles of 69°, 90°, –69° and again 90°.

FTC

At lower polar angles not covered by the Z–chamber a Forward Tracking Chamber (FTC) [150, 151] is located between the TEC endflanges and the BGO endcap calorimeter (figure 3.3). During data taking the FTC is used to monitor beam

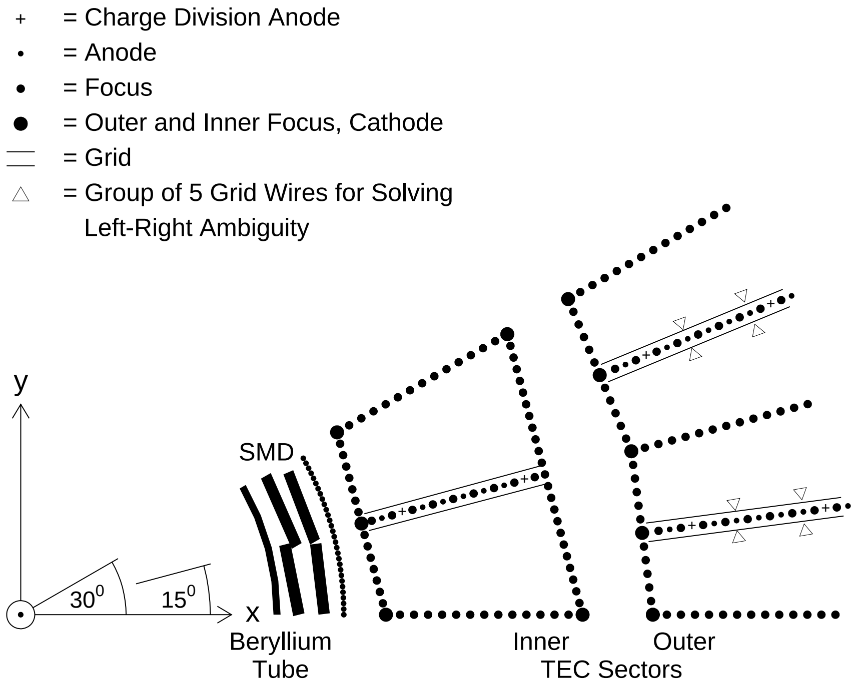

Figure 3.11: *Wire layout of inner and outer sectors.*

related backgrounds.

3.2.3 Scintillation Counters

An array of 30 plastic scintillation counters in the barrel and 16 in the endcap region surrounds the electromagnetic calorimeter (figure 3.3) [152]. The scintillation light is read out by photomultipliers. Providing a precise timing information with a resolution of about 0.8 ns in the barrel region and 1.9 ns for the endcaps, the scintillators are used to identify muons originating from cosmic air showers which are uncorrelated with the beam crossing time. If two scintillators are hit in opposite hemispheres (up and down), cosmic muons could alternatively be tagged by the time difference between the two scintillator hits.

3.2.4 Hadron Calorimeter

The hadron calorimeter (HCAL) [153] is a fine sampling calorimeter made of depleted uranium absorber plates interspersed with proportional wire chambers.

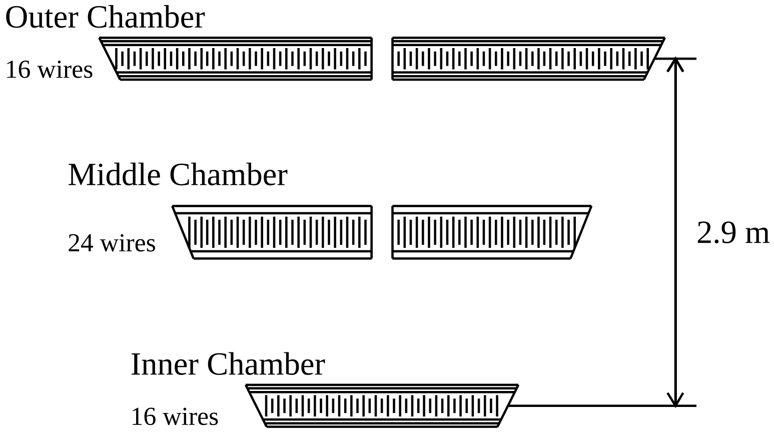

Figure 3.12: *Front view of a barrel muon chamber octant.*

It is divided into a barrel part covering $35^\circ \leq \theta \leq 145^\circ$ in polar angle and two endcaps extending the coverage down to 5.5°. Viewed from the interaction point, the amount of material varies between 6 and 7 nuclear absorption lengths in the region of the endcaps and can be as low as 3.5 nuclear absorption lengths in the barrel. In order to reduce punch-through of hadrons into the muon chambers, an instrumented brass plate muon filter provides an extra absorption length of material around the barrel part of the HCAL.

3.2.5 Muon Spectrometer

Like calorimeters and scintillators, the muon spectrometer is composed of barrel [154,155] and endcaps [138]. The barrel consists of two “ferris wheels”, each made up of eight octants supporting three layers of precision multi-wire drift chambers. There are two chambers in the outer layer with 16 signal wires each, two chambers in the middle layer with 24 signal wires each, and one chamber in the inner layer with 16 signal wires (figure 3.12) all measuring the track coordinates in the rϕ plane (P chambers) which is at the same time the bending plane. The angular coverage for the three layers is $44^\circ \leq \theta \leq 136^\circ$. The transverse momentum – the momentum projected onto the rϕ plane – of muons is extracted from the sagitta of the muon track (see figure 3.13). The single wire resolution of the P chambers of 200 μm yields a momentum resolution of 2.5% at 45 GeV for muons coming from the interaction point. Both sides of the inner and outer P chambers

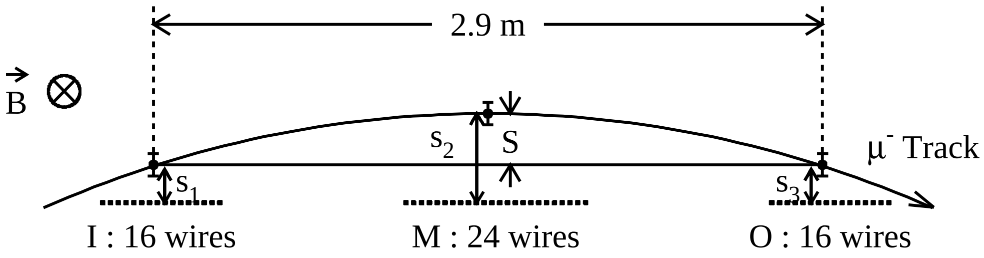

Figure 3.13: *Sagitta measurement in the barrel muon chambers.*

are equipped with additional drift chambers (Z chambers) which measure the coordinate along the beam with a resolution of about 500 μm.

The endcap – or forward-backward – muon chambers extend the angular coverage down to a polar angle of 24°. Both endcaps consist of three layers where one layer is mounted inside and two layers are mounted outside the iron doors, which contain a toroidal magnetic field and return the flux of the L3 solenoid magnetic field. The momentum resolution in the forward-backward chambers varies strongly with the polar angle of the muon from 4% to 35% for 45 GeV muon energy and is limited by multiple scattering in the 90 cm thick doors.

3.2.6 Small Angle Detectors

Three subdetectors are situated close to the beam pipe, 1 m to 8 m away from the interaction region, thus covering small polar angles.

ALR

The first of the small angle subdetectors as seen from the centre of L3 are the so-called Active Lead Rings (ALR) [156]. They cover a polar angle between 3.9° and 8.7° and are situated between BGO and HCAL in z direction about 1 m away from the interaction point (see figure 3.3). The lead rings were installed to protect the inner tracking chamber from stray background particles. Instrumented with plastic scintillators (*i.e.* “activating” them), the ALR improves the hermeticity of the L3 detector. The elements consist of five 10 mm thick scintillator layers placed behind 18.5 mm thick lead converters. Three of the layers have trapezoidal shape and cover 22.5° in ϕ. Successive layers are tilted by 1/3 of the width thus providing an effective segmentation of 7.5°. Furthermore, a segmentation in polar

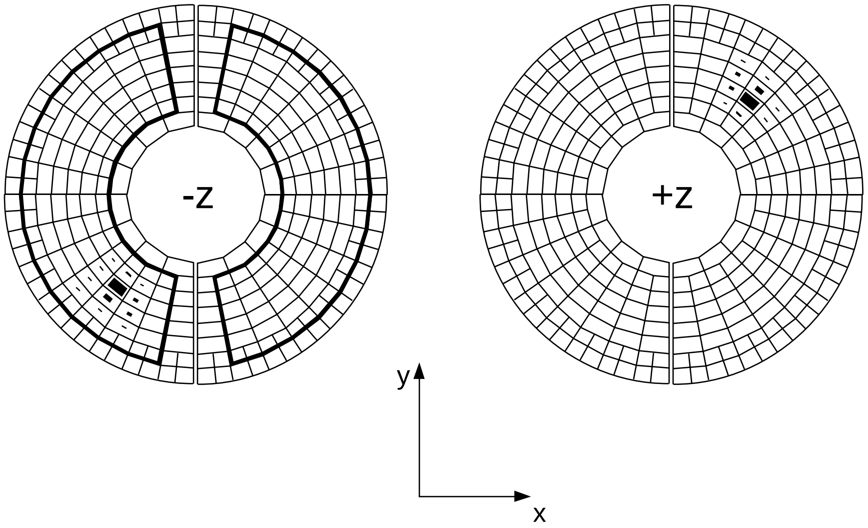

Figure 3.14: *Crystal arrangement in the luminosity monitors. The energy depositions of a small angle Bhabha event are also shown.*

angle has been implemented by two layers of semi-circular shaped scintillators that are read out at both ends. The readout is performed with 10×20 mm^2 photodiodes placed at the outer edges of the scintillators. An energy resolution of 15% has been obtained for electromagnetic showers at 45 GeV.

Luminosity Monitor

Next detector element in line is the luminosity monitor [157] designed to count the rate of small angle Bhabha scattering and, in that way, to provide a measurement of the luminosity (see section 3.4). It consists of a silicon strip tracker called SLUM followed by a highly segmented BGO array. The system covers a polar angle of $1.4^\circ \leq \theta \leq 3.9^\circ$ and is situated 2.73 m away from the interaction point in both directions (see figure 3.3). The two half cylinders of each detector contain 304 BGO crystals which are parallel to the beam axis (see figure 3.14). The energy resolution of the calorimeter is about 2%. The angular resolution of the system is improved by the SLUM providing three layers of a silicon strip detector on each side. Two layers concentric with the beam axis measure the polar angle and one layer perpendicular to the beam axis measures the azimuthal angle of incoming particles.

VSAT

The detector element with greatest distance to the interaction point is the Very Small Angle Tagger (VSAT) [139]. It consists of two boxes with BGO crystals located on each side, 8.17 m away from the centre of L3, behind the first quadrupole magnet and covering a polar angle of 5 to 10 mrad. The magnet defocuses in the horizontal and focuses in the vertical plane, explaining the fact that the boxes are present in the horizontal plane only. The VSAT tags electrons or positrons at very small scattering angles and is used in combination with soft particles detected in the central detectors to study two-photon collision physics.

3.2.7 Trigger

After each beam crossing, the trigger system has to decide whether an event should be recorded or not. This task is performed in a three-level process with increasing complexity at each level, reducing the event rate and thus leaving more time for more elaborate decisions at each stage. In this way, a beam crossing rate of 45 kHz is reduced to a few Hz of events which are finally recorded.

Level-1 Trigger

In the 22 μs before the next beam crossing, the level-1 trigger decides whether to initiate the digitisation of the detector data or whether to drop the event. Therefore, dead time occurs only if an event is accepted by level-1. In case of a positive decision, the detector data is digitised within 500 μs. The level-1 trigger consists of several subtriggers based on different sources. It is gated by the beam crossing signal.

Energy Trigger

The energy trigger [158–161], part of the level-1 subtriggers, processes the information given by electromagnetic and hadron calorimeters and by the luminosity monitor, and it is the most important trigger for the single and multi-photon selection. Here, the full information on crystal energies is not yet available, but instead crystals are grouped into "blocks" which are read out with a somewhat shorter integration time than available for the full digitised data to save time.

Again, the energy trigger is divided into several subtriggers which are connected by a logical OR for the final trigger decision.

The total energy triggers set thresholds on the total energy detected by the two calorimeters, the BGO energy alone, and total energy and BGO energy at large angles. The cluster triggers set thresholds on localised energy deposits observed in different detector layers at the same θ and ϕ coordinates (blocks, see above). As for the total energy trigger, thresholds are different for BGO + HCAL clusters and for BGO clusters alone. The cluster search also takes advantage of the information supplied by the TEC if a track has been detected in the same azimuthal region. In this case the threshold is lowered further. The single photon trigger is given when a BGO cluster, accounting for more than 80% of the total electromagnetic energy of the event, is found in the barrel. The hit-counting-trigger fires if there are at least two cells with more than 5 GeV energy. The luminosity trigger requires two back-to-back luminosity monitor segments, both with an energy above a threshold. An energy deposit greater than 30 GeV is requested in the luminosity monitors by the single tag trigger. Here, a prescaling factor is applied. The BGO cluster trigger with a threshold of 6 GeV and the single photon trigger with a threshold of 0.9 GeV are the ones of biggest importance for triggering single and multi-photon events.

Other Subtriggers

The ALR trigger [162] is made of three subtriggers. The prescaled single tag trigger requires at least one high energy deposit in the ALR. For the Bhabha trigger high energy deposits have to be on both sides of the ALR, whereas for the "gamma-gamma trigger" a high energy deposit in the ALR plus at least one track has to be detected in the TEC. This trigger is used to study physics from so-called two-photon collisions, where the beam electrons are only slightly scattered (tagged in the ALR) and soft particles end up in the central part of the detector (and in this case produce a track in the TEC).

The TEC or charged particle trigger [163] searches for tracks pointing to the interaction vertex in the rϕ projection. Particle tracks are reconstructed from the pick-up wires. The event is accepted if the track topology matches with one of several predefined track patterns.

The scintillator trigger is based on signals in barrel and endcap scintillators.

It is used to select high multiplicity events as well as to reject cosmic muons by requiring the timing to be in a gate around the beam crossing.

The muon trigger [164] matches drift cells with signals with a predefined pattern in order to accept single muon tracks as well as muon pairs. The trigger rate due to cosmic muons is reduced by requiring a hit in the scintillator in a gate around the beam crossing.

The beam gate trigger fires at random time intervals independent of the data taken by the detector. The only condition to be met is that the timing must fall into the gate around beam crossing. Events triggered in this way are mainly used to investigate detector noise (see section 4.3).

Level-2 Trigger

The level-2 trigger [165,166] is designed to reject non-physical background events arising from electronic noise, beam-gas and beam-wall interactions as well as synchrotron radiation. Events triggered by more than one level-1 subtrigger are never rejected. Information not available in time for a level-1 decision is used here. In particular, information on the vertex along the beam axis using the charge division measurement from the TEC, energy depositions in the BGO and hadron calorimeters correlated in a coarse $\theta - \phi$ map and longitudinal and transverse energy imbalance arising from the energy measurement are used. In case of a positive decision the input to level-2 plus all level-2 results are forwarded to the level-3 trigger.

Level-3 Trigger

Level-3 [167] is the first point at which the trigger decision can be made on the basis of the full detector readout. The accurate digital data with its finer granularity and higher resolution allows thresholds to be set tighter than in the lower level triggers. Events with multiple level-1 triggers or with luminosity trigger are passed through untouched. The event selection is based on the correlation of energy deposited in the BGO and HCAL, reconstruction of muon tracks in the Z chambers, and reconstruction of the vertex in the TEC.

3.3 Reconstruction and Simulation of the Data

After the detector response of an event has been recorded in digitised form, the relevant physics quantities, like parameters of tracks of charged particles or energy deposits in the various calorimeters, need to be computed. A common reconstruction program called `REL3` fulfils this task in L3. Applying calibration constants, the energy deposit in each substructure like a BGO crystal is calculated from the measured electronic pulse. In the BGO, bumps are formed by searching for local energy maxima, and several bump specific quantities are derived, such as the total bump energy, its angle in θ and ϕ, the number of crystals in the bump and many more[3]. BGO bumps are matched with geometrically connected hits in the hadron calorimeter to form calorimetric clusters. The drift times in the TEC and the muon chambers are converted into position measurements. Then, a fit is performed in order to extract from the coordinates of hits the parameters of tracks, including curvature, distance of closest approach to the interaction point, and angles θ and ϕ of a track at the vertex.

Monte Carlo Simulation

In order to compare the measured data with theoretical predictions in each step of an analysis and in order to understand the detector acceptance, the relevant physics is simulated. The simulation of data proceeds in two independent steps. The first one is the event generation where the simulation of the physics processes of interest is done. In a second step – the detector simulation – the response of the detector to the generated events is simulated. In both steps the Monte Carlo simulation technique is used.

Event generators of interest for LEP physics form a library common for L3 called `EGL3`. For all programs an interface guarantees the same output structure for the events generated which is read in by the detector simulation program. This structure contains a particle identity code, energy-momentum vector, vertex of creation, decay length, a pointer to a particle's parent as well as pointers to the decay products for each particle of an event. Only particles with a short lifetime, so that their decay length is shorter than the radius of the beam pipe, like the τ lepton, are allowed to decay at this stage. Longer lived particles like muons are left "undecayed" here.

---

[3] The quantities used in this thesis will be defined in chapter 4

The second step in the simulation chain consists of modelling the response of the L3 detector to the final state particles produced by the event generators. The program package `SIL3` written for this purpose is based on the general detector simulation packages `GEANT` [168] and `GHEISHA`[4] [169]. `SIL3` produces output in the same format as the data acquisition plus the information from `EGL3`, so that it can be fed into the same reconstruction program as data. In the reconstruction phase the time dependent detector imperfections like dead or noisy BGO crystals or the TEC high voltage being off for a short period of time are taken care of. For this purpose, a time and date is assigned to each Monte Carlo event, such that all events are distributed over a certain data taking period with the correct luminosity weighting.

3.4 Luminosity Measurement

A measurement of the integrated luminosity $\mathcal{L}$ is crucial for cross section determinations, since for a given process P the cross section is connected to the (background-corrected) number of selected data events N_P by

$$\sigma_P \; = \; \frac{N_P}{\mathcal{L}\,\epsilon_P}, \tag{3.3}$$

where ϵ_P denotes the combined acceptance and selection efficiency for process P.

In principle, the integrated luminosity $\mathcal{L}$ can be calculated from machine parameters. At LEP the instantaneous luminosity L can be derived from

$$L \; = \; \frac{n_b N_{\mathrm{e}^+} N_{\mathrm{e}^-} f}{4\pi\sigma_{\mathrm{x}}\sigma_{\mathrm{y}}}, \tag{3.4}$$

where N_{e^+} and N_{e^-} are the number of positrons and electrons per bunch, n_b is the number of electron (or positron) bunches, and f the revolution frequency. $4\pi\sigma_{\mathrm{x}}\sigma_{\mathrm{y}}$ defines the effective cross section of the interaction zone assuming a Gaussian distribution of the particle density in the colliding bunches in x and y direction. σ_{x} and σ_{y} are the standard deviations of the respective Gaussian distributions.

However, not all parameters in equation 3.4 are known to sufficient precision. Hence, a different approach is chosen by the LEP experiments taking equation 3.3 to estimate the integrated luminosity and using a reference process with a

---

[4] `GHEISHA` is used to simulate hadronic interactions.

Year	$\sqrt{s}$ (GeV)	$\mathcal{L}$ (pb^{-1})
1995 + 1997	130.10 ± 0.05	6.11 ± 0.02
1995 + 1997	136.07 ± 0.05	5.84 ± 0.02
1996	161.34 ± 0.03	10.79 ± 0.07
1996	172.13 ± 0.03	10.19 ± 0.07
1997	182.68 ± 0.03	55.25 ± 0.17
1998	188.64 ± 0.02	176.35 ± 0.37

Table 3.1: *Centre-of-mass energies [133,171–173] and luminosities measured in L3 at LEP 2 until 1998 [174–177].*

large and theoretically well known cross section to keep the statistical error on N_P and the systematic (*i.e.* theoretical) error on σ_P small. The ideal process at LEP is Bhabha scattering at very small scattering angles since this reaction has a very high rate and it is due to dominating γ exchange in the t–channel an almost pure QED process which can be computed with high precision.

The luminosity monitors are used for the electron selection [157]. To determine the selection efficiency, the selection criteria are also applied to a sample of Monte Carlo events, where low angle Bhabha events are generated with the program `BHLUMI` [170] which are processed by the L3 detector simulation program. Measured luminosities at various centre-of-mass energies of the LEP 2 program are listed in table 3.1 until 1998. The theoretical precision is estimated to be 0.12% [178]. The experimental uncertainty decreased from year to year (0.17% in 1998), except for 1996 where it was considerably bigger because in that year the SLUM (see section 3.2.6) was not built in which lead to a worse angular resolution and a larger error in the event selection.

Chapter 4

Selection of Single and Multi-Photon Events

The selection strategy for both, the new physics searches with single and multi-photons in the final state as well as the $\nu\bar{\nu}\gamma(\gamma)$ process, yields in maximising the sensitivity for $\nu\bar{\nu}\gamma(\gamma)$ in a first step to be described in this chapter. However, regarding the multi-photon signature, the prediction for the process $\mathrm{e}^+\mathrm{e}^- \rightarrow \tilde{\chi}^0_1\tilde{\chi}^0_1$ is also taken into account. For new particle processes, the event samples derived in this way are considered as preselected events, which are then in the next step subject to further scrutiny concerning new physics to be explained in sections 5.3 to 5.5.

Basically, the essential concept of selecting single and multi-photon events is threefold and shall be illustrated with the "event picture" shown in figure 4.1. Besides a schematic view of the L3 detector in its projection to the rϕ plane, the energy depositions – called bumps – of two photons are sketched. The size of the representation of a bump corresponds with the energy of the photon. The first part of the selection machinery is the identification of photons. This is achieved via the characteristic bump shape in the BGO, because most energy is concentrated in the central crystals and much less in the surrounding ones as visible in figure 4.1. Details concerning the photon identification are pointed out in section 4.1. The second element in the selection is the requirement to find all other parts of the detector to be "empty" by setting cuts on energies and tracks just above noise level. Section 4.3 is devoted to the explanation of veto cuts on respective subdetectors. The last step makes use of the missing energy signature

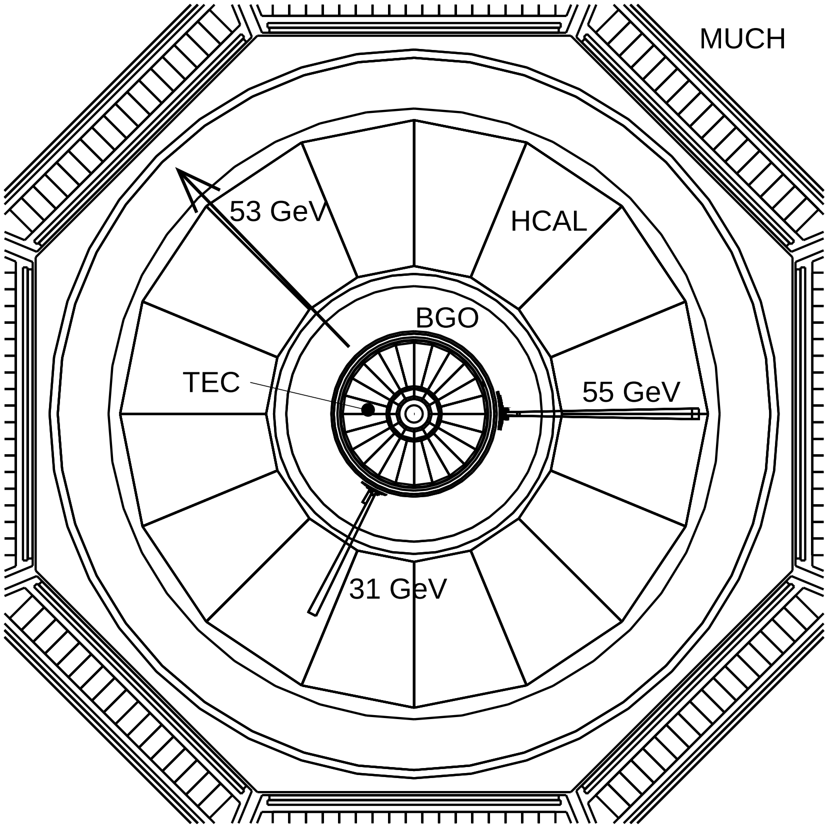

Figure 4.1: *Schematic projection of the L3 detector in the rϕ plane, showing its components only up to the first chamber of the muon spectrometer (see also section 3.2). Energy depositions of two photons in the BGO measured in 1998 are also illustrated. The arrow indicates the direction of missing momentum.*

indicated by the arrow in figure 4.1. Cuts on kinematic variables describing the event shape are applied to suppress physics events also consisting of photons only in the final state but without missing energy. Possible background sources and cut descriptions are enumerated in section 4.6.

There are further issues important for the single and multi-photon selection that need to be addressed. The detector resolution in the measurement of energy and angle has to be understood as far as the agreement between data and the prediction of Monte Carlo simulation is concerned (section 4.2) since cuts depending on energy and angle measurement are applied. The trigger efficiency is a critical point, especially for low energetic photons. The comparison between actual trigger efficiency and its simulation is subject to an investigation described in section 4.5. Muons created by cosmic rays can penetrate the L3 detector and escape undetected, but produce a bremsstrahlung photon faking a single photon event and thus providing a background source which is not simulated. Means to suppress this kind of events are presented in section 4.4 and an estimate of the remaining contribution of cosmics is computed in section 4.7. In matter photons can convert into an electron-positron pair. This process can happen either in the material of the beam pipe or in the SMD. The photon conversion rate measured in the single photon sample is analysed and discussed in section 4.8. Finally, the results obtained by the selection are provided in section 4.9.

Selections and related studies are performed for all centre-of-mass energies listed in table 3.1. Since the selection criteria and the methods to estimate systematic uncertainties and correction factors are exactly the same for all energy points, distributions are only shown and numbers are only quoted for $\sqrt{s} = 188.64$ GeV, from now on referred to as 189 GeV data, unless stated otherwise. The 189 GeV data provides the highest sensitivity to new physics since most luminosity is collected here and because it is the point with highest energy. The most important distributions of the other centre-of-mass energies corresponding to the ones discussed in this chapter are displayed in appendix C as well as correction factors and results for the number of selected events.

4.1 Photon Identification

As mentioned before, photons are identified and measured in the BGO electromagnetic calorimeter. The fiducial angular region to identify a photon is defined as

$$\begin{array}{rcll} & |\cos\theta_\gamma| < & 0.73 & \text{(Barrel)} \\ 0.81 < & |\cos\theta_\gamma| < & 0.97 & \text{(Endcaps)} \end{array} \tag{4.1}$$

and 360° in ϕ_γ leading to 89% angular acceptance of the full solid angle. Within the above defined region the BGO is hermetically sealed with the exception of two small holes from which one is used by the RFQ pipe (see section 3.2.1 and figure 3.4). These holes are located at $257^\circ < \phi < 281^\circ$, $14.1^\circ < \theta < 19.95^\circ$ and

$257° < \phi < 281°$, $160.05° < \theta < 165.9°$, respectively. The SPACAL is not used for photon identification.

Cuts

In the photon identification process the shape of energy distributions of crystals forming a bump in the BGO is tested for being compatible with what is expected for photons and electrons[1], and also the ratio of energy measured in the hadron calorimeter behind a bump and the bump energy ($E_{\mathrm{HCAL}}/E_{\mathrm{bump}}$) is cut upon. To be considered as a photon candidate, a bump must consist of at least three crystals with more than 10 MeV energy each and a total bump energy exceeding 1 GeV.

An important variable discriminating electromagnetic bumps (*i.e.* bumps created by photons or electrons) from others is the ratio of the energy measured in the 3×3 crystal matrix, E_9, to the energy measured in the 5×5 matrix, E_{25}, respectively, around the crystal with the highest energy. These energy sums are corrected for independently, as explained in section 3.2.1 (equation 3.2), to correspond to the real particle energies under the hypothesis that these particles are photons or electrons. Thus, for electrons and photons this ratio should be close to one.

Furthermore, the lateral shower shape is compared to an ideal one coming from electrons. The $\chi^2_{\mathrm{em}}\,(/N_{\mathrm{dof}})$ value calculated in the fit procedure is used to distinguish electrons and photons from other particles as electromagnetic bumps are narrower than hadronic bumps (see figure 4.2). A good agreement in the shower shape yields a small value for χ^2_{em}.

The "skewness" of a bump is a measure for the amount of circularity of energy depositions. Two half axis of an ellipse are computed from energies deposited in crystals forming a bump and the skewness is then defined as the ratio of the smaller half axis to the larger half axis. Hence, for a bump with rotational symmetry like the one of a photon or electron coming from the centre of the detector the skewness is close to one and for very eccentric bumps, like the ones created by particles not originating from the primary interaction vertex, the skewness is small.

---

[1] Since electrons and positrons are identical as far as the BGO response is concerned, also positrons are included when referring to electrons in this context.

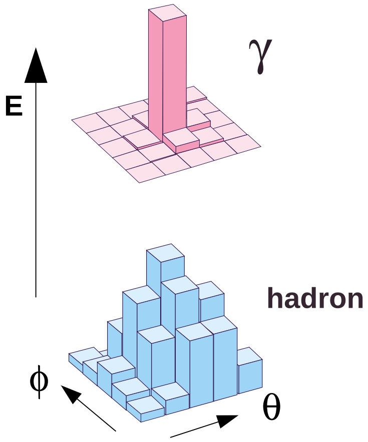

Figure 4.2: *Shower shapes in the BGO.*

E_{bump}	$>$	1 GeV
E_9/E_{25}	$>$	0.94
χ^2_{em} Barrel	$<$	10
χ^2_{em} Endcaps	$<$	25
$E_{\text{HCAL}}/E_{\text{bump}}$	$<$	0.2
Skewness	$>$	0.2

Table 4.1: *Photon identification cuts.*

Cut values applied in this analysis are listed in table 4.1.

Systematics

The systematic uncertainty introduced by photon identification cuts is studied and quantified using a sample of Bhabha scattering events, where only one of the two electrons is tagged, and the other electron is used to estimate the efficiency of photon identification. The difference in the efficiencies extracted from data and Monte Carlo simulation, respectively, determines the systematic error. Although only evaluated for 45 GeV electrons, the error is certainly valid for a wide energy range above and below this value, since the fundamental bump shape hardly changes with energy. Only for very low bump energies, when almost all energy is located in the central crystal, the bump shape changes qualitatively, possibly introducing new systematics.

	Barrel	Endcaps	Total
Data	$(97.92 \pm 0.15)\%$	$(94.33 \pm 0.15)\%$	$(95.33 \pm 0.12)\%$
Simulation	$(97.36 \pm 0.12)\%$	$(94.76 \pm 0.12)\%$	$(95.67 \pm 0.09)\%$
Difference	$(0.56 \pm 0.19)\%$	$(0.43 \pm 0.19)\%$	$(0.34 \pm 0.14)\%$

Table 4.2: *Efficiencies of photon identification cuts.*

The data sample used corresponds to 23.9 pb^{-1} luminosity collected in 1995 at an average centre-of-mass energy of 91.3 GeV. The Bhabha scattering process is simulated using the `BHWIDE` Monte Carlo generator [179]. This selection aims to extract a pure sample of non-radiative Bhabha events, *i.e.* two-electron events with back-to-back topology. It requires at least one electromagnetic object imposing the criteria of table 4.1 within the fiducial region defined by equations 4.1 and a minimum bump energy of 93% of the beam energy. The energy in the small angle detectors – luminosity monitor and ALR – should not exceed 1 GeV, whereas the energy measured in the hadron calorimeter must be less than 20 GeV. There should not be any muons identified in the muon chambers and there are no more than two charged tracks to be reconstructed in the inner tracking system. If there are exactly two well-measured tracks[2], their acoplanarity – *i.e.* the angular deviation from 180° in the projection to the rϕ plane – should be less than 5°. The number of bumps in the BGO has to be exactly two and their acollinearity, *i.e.* the deviation from being back-to-back, has to remain smaller than 5°.

Hereafter, the photon identification cuts from table 4.1 are applied to the second bump. Efficiencies obtained for data and simulation are listed in table 4.2. Distributions of variables cut upon are shown in figure 4.3 in "n–1" form, *i.e.* all cuts are applied except the one on the displayed quantity.

The systematic error introduced by photon identification cuts lies in the permille region (see table 4.2) and is therefore an order of magnitude smaller than the expected statistical error on the cross section measurement of $\nu\bar{\nu}\gamma(\gamma)$. This estimate can be considered as conservative, since the understanding of the BGO, namely its description in the simulation process, has improved a lot since 1995

---

[2] The quality criteria are: Transverse momentum greater than 100 MeV, distance of closest approach to the interaction point (DCA) less than 10 mm, more than 14 wire hits, and the first and last used hit must be at least 15 wires apart (span).

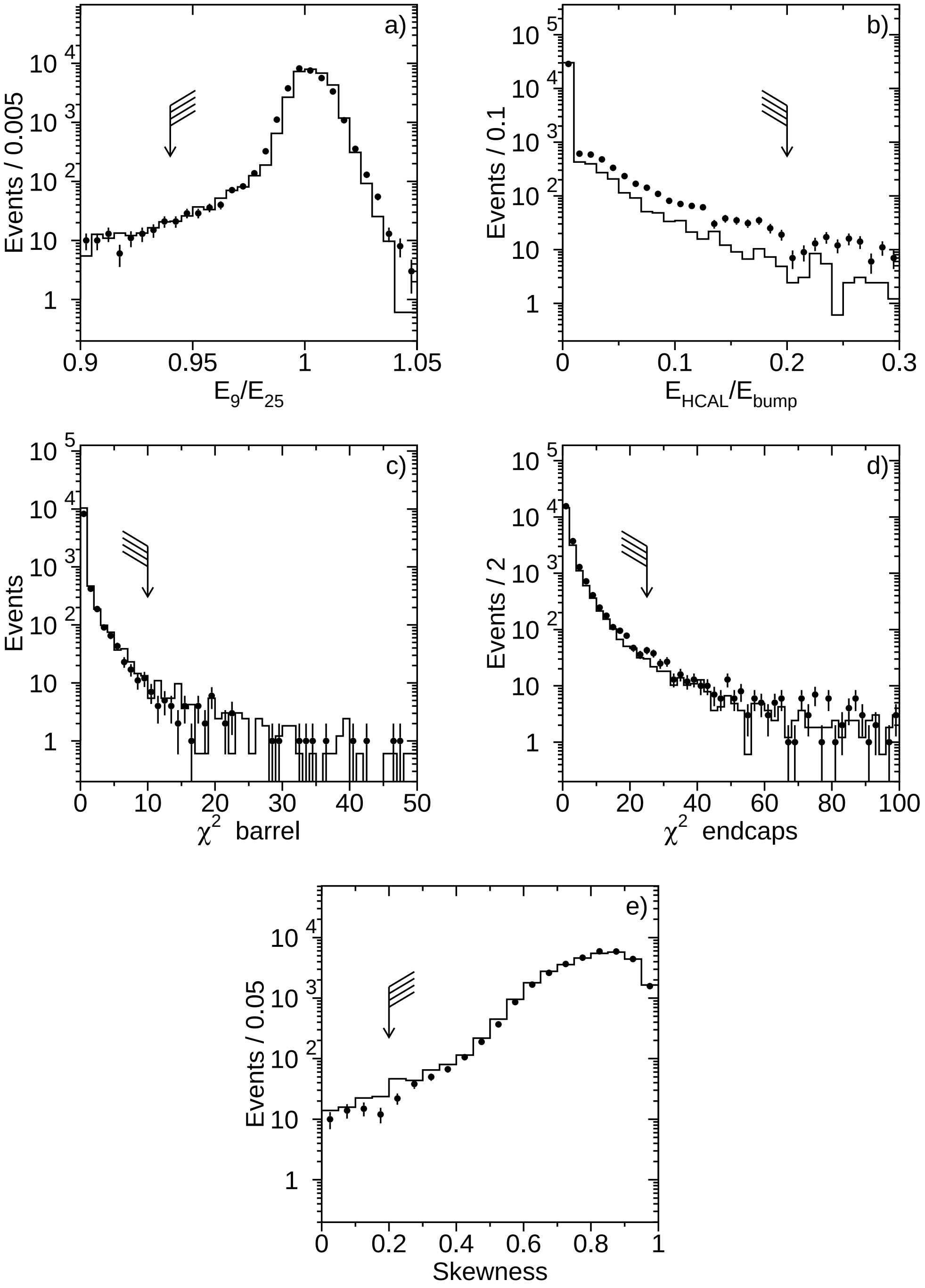

Figure 4.3: *n–1 distributions of photon identification variables showing the 1995 Z data set. Cut positions are indicated by arrows where the flag side is kept. Monte Carlo simulation (line) is normalised to data (full dots).*

as far as the treatment of dead crystals, for example, is concerned (see section 4.2 and appendix C).

Photon-Electron Separation

Essentially, electrons are distinguished from photons by requiring a charged track in the inner tracking system pointing to a bump in the BGO. In the single photon selection only tracks with a minimum transverse momentum of 40 MeV are considered[3], except in the case of the track being measured exclusively in the inner TEC, where momentum measurement is not very reliable. Here, the track is kept if a bump is found in the BGO endcap within the ϕ region, which includes the whole inner TEC sector (see section 3.2.2) where the track is located. Criteria to match a track with a bump depend on the angle θ, since for smaller polar angles the track measurement becomes worse. For large angle tracks, projection of the track to the BGO is not to differ by more than 50 mrad in ϕ from the bump coordinate in order to flag the particle as an electron. If the track only consists of hits measured in the inner TEC, which means it has a small polar angle, the prediction for the projection to the BGO is substantially worse, because of less hits contributing to the track fit[4], a smaller lever arm, and a larger distance from the last wire hit to the BGO crystal surface. Here, only a matching within 10° in ϕ between track and bump is required to identify the particle as an electron. When looking at inner TEC tracks, a left-right ambiguity arises like discussed in section 3.2.2, and thus also the associated "mirror track" is tested for matching the bump. In this case, an additional quality criterion on a track is the requirement that the distance of closest approach – DCA – of the track to the primary interaction vertex is less than 20 mm.

Conversion

In matter a photon can convert into an electron-positron pair. This photon conversion could, for example, take place inside the material of the beam pipe or the SMD. If a second track in a cone of 11.5° opening angle around an electron

---

[3] 40 MeV is the minimum momentum for a particle to be able to leave the TEC: $p_\mathrm{t} = 0.3\ \mathrm{GeV/(Tesla\ m)} \cdot B \cdot R = 0.3\ \mathrm{GeV/(Tesla\ m)} \cdot 0.5\ \mathrm{Tesla} \cdot 0.25\ \mathrm{m} = 0.04\ \mathrm{GeV}$ [2].

[4] At most eight hits are possible and therefore a larger uncertainty for the track parameters comes along.

$E_{\mathrm{e}^\pm}$	$>$	5 GeV	
$N_{\mathrm{tracks,\,11.5^\circ}}$	$=$	1	
$N_{\mathrm{iTEC,\,bump}}$	$=$	2	if $\theta_\gamma < 25^\circ$ or $\theta_\gamma > 155^\circ$

Table 4.3: *Photon conversion identification cuts.*

with DCA less than 20 mm is found ($N_{\mathrm{tracks,\,11.5^\circ}} = 1$), the object is marked as converted photon if the electron energy exceeds 5 GeV. If an electromagnetic bump is identified at a polar angle smaller than 25° and exactly two tracks are found in the sector of the inner TEC which corresponds to the azimuthal angle of the bump and which are measured exclusively in the inner TEC ($N_{\mathrm{iTEC,\,bump}}$), then the bump is also flagged as a converted photon. To summarise, the photon conversion criteria are listed in table 4.3. An event picture of a photon conversion candidate is shown in figure 4.4, while the photon conversion rate will be discussed in section 4.8.

4.2 Measurement of Energy and Angle

The way how energy and angle of photons are measured with the BGO calorimeter is already described in section 3.2.1. In this section the resolution of the device for these two quantities and the amount of agreement between simulation and actual measurement shall be investigated.

High Energy Region

In order to check the energy measurement, the energy of the electron must be known a priori, but, of course, without imposing an explicit cut on it. Since electrons in non-radiative Bhabha events have beam energy, they provide an excellent tool for this purpose and can be selected easily by exploiting the back-to-back nature of the event topology.

Within the barrel region, exactly two identified electrons and no additional leptons are required. Smaller angles in the region of the endcaps are outside the acceptance of the inner tracking system, which is why here either electrons or photons are accepted. Cuts on the back-to-back topology must be rather stringent, since undetected initial state radiation can fake a miss-measurement

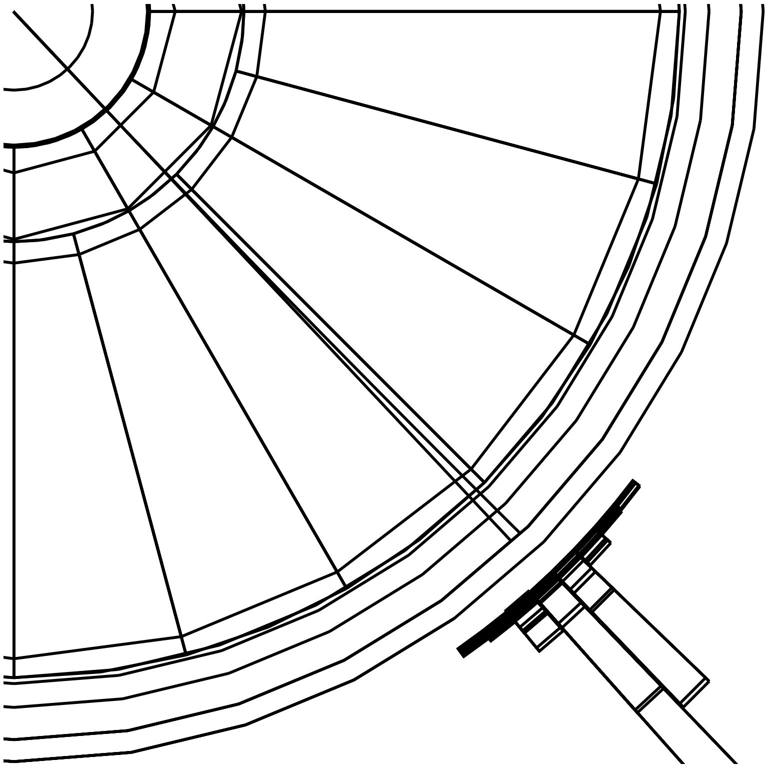

Figure 4.4: *Event picture showing a photon conversion candidate in the 1998 data set. The two tracks are separated by about* 1°.

of the electron energy and thus spoil the resolution. Therefore, acoplanarity and acollinearity of the events are required to be less than 1.2° in the barrel and 0.5° in the endcaps. Furthermore, the total visible energy of an event should not exceed 10 GeV (5 GeV in the endcaps) after having subtracted the energy of the two identified electromagnetic objects. Finally, if electrons/photons are detected in the endcaps, the missing transverse momentum must be smaller than 5 GeV.

Measured energy distributions normalised to the beam energy are displayed in figure 4.5 for data and prediction of Monte Carlo simulation using `BHWIDE` as generator. Apart from the `SIL3` simulation of detector material, an additional energy smearing with a double Gaussian is applied to the simulated bump energies during the reconstruction phase within `REL3`. The peak structure visible in the energy distributions is clearly asymmetric, which can be explained by remaining initial state radiation and by fluctuations in the energy measurement due to leakage to the back of the BGO and in the carbon support structure. A

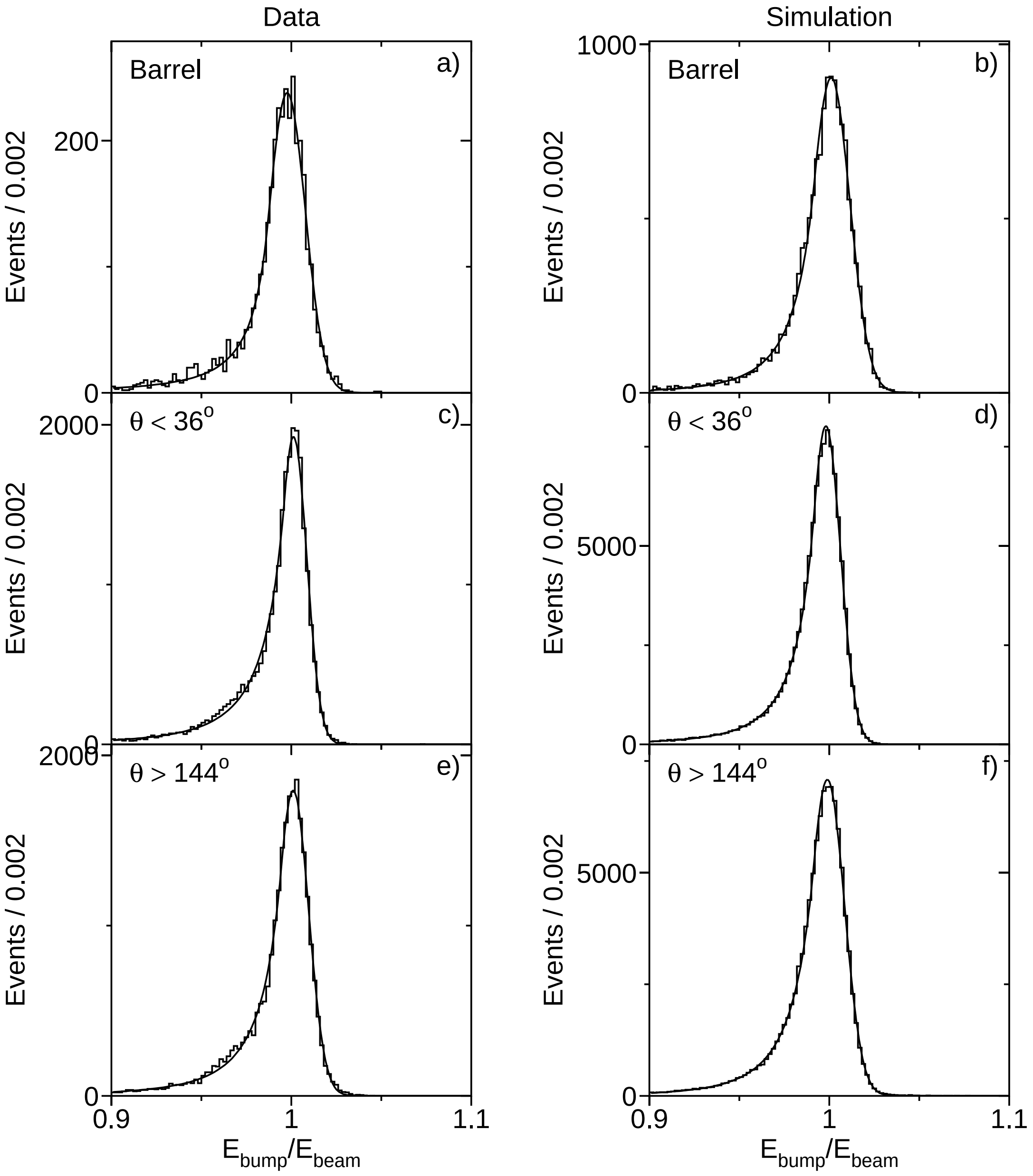

Figure 4.5: *Energy distributions for data (left hand side) and Monte Carlo simulation (right hand side) normalised to the beam energy for* $\sqrt{s}$ = 189 GeV*. The barrel region (a and b) as well as the endcap regions (c to f) are shown.*

		Barrel	Endcap $\theta < 36°$	Endcap $\theta > 144°$
P_1	Data	237.9±5.8	1924±19	1793±17
	MC	904±10	8017±35	7088±31
P_2	Data	$(-2.3\pm0.27)\cdot10^{-3}$	$(1.2\pm0.12)\cdot10^{-3}$	$(1.01\pm0.12)\cdot10^{-3}$
	MC	$(1.04\pm0.18)\cdot10^{-3}$	$(-1.895\pm0.059)\cdot10^{-3}$	$(-1.083\pm0.066)\cdot10^{-3}$
P_3	Data	$(10.12\pm0.23)\cdot10^{-3}$	$(7.411\pm0.087)\cdot10^{-3}$	$(8.664\pm0.094)\cdot10^{-3}$
	MC	$(10.48\pm0.13)\cdot10^{-3}$	$(8.16\pm0.041)\cdot10^{-3}$	$(9.501\pm0.048)\cdot10^{-3}$
P_4	Data	1.085±0.072	0.658±0.019	0.775±0.022
	MC	0.915±0.037	0.781±0.011	0.801±0.012
P_5	Data	2.13±0.28	3.07±0.15	3.07±0.17
	MC	3.93±0.40	3.57±0.10	4.26±0.15

Table 4.4: *Parameters of the fit to energy spectra in figure 4.5 for data and Monte Carlo simulation (MC) in 1998.*

function parametrised as [180]

$$f(x) = \begin{cases} P_1\,\mathrm{e}^{-\frac{(1+P_2-x)^2}{2P_3^2}} & \text{for } x > 1 + P_2 - P_3P_4 \\ P_1\,\mathrm{e}^{-\frac{P_4^2}{2}} \left(\frac{P_3P_5/P_4}{P_3P_5/P_4 + 1 + P_2 - P_3P_4 - x}\right)^{P_5} & \text{for } x \leq 1 + P_2 - P_3P_4 \end{cases} \tag{4.2}$$

with $x = \frac{E_{\text{bump}}}{E_{\text{beam}}}$ is fitted to the spectra. This function is designed to reproduce the measured shape of the distributions as good as possible to be able to make quantitative statements about energy resolutions and shifts. The first term is a Gaussian with mean $(1+P_2)$ and standard deviation P_3, and it basically describes the peak region within about one standard deviation (since $P_4 \approx 1$) and the right hand side of the peak position. The second term parametrises the left hand side of the peak including the tail region with a functional dependence on the energy as $1/(1-x)^{P_5}$. The shift of the peak position with respect to its nominal value of one is parametrised by P_2 and the resolution by P_3. P_4 is a measure for the point in the distribution at which it is no longer described by the Gaussian but by the second term: the bigger P_4, the larger the Gaussian-like region. The steepness of the left hand side of the peak parametrised by the second term can be assigned to P_5: the bigger P_5, the steeper the slope. The values for the fit parameters P_1 to P_5 can be found in table 4.4. Data and Monte Carlo prediction agree very well with each other and shifts of the peak positions are in the permille region.

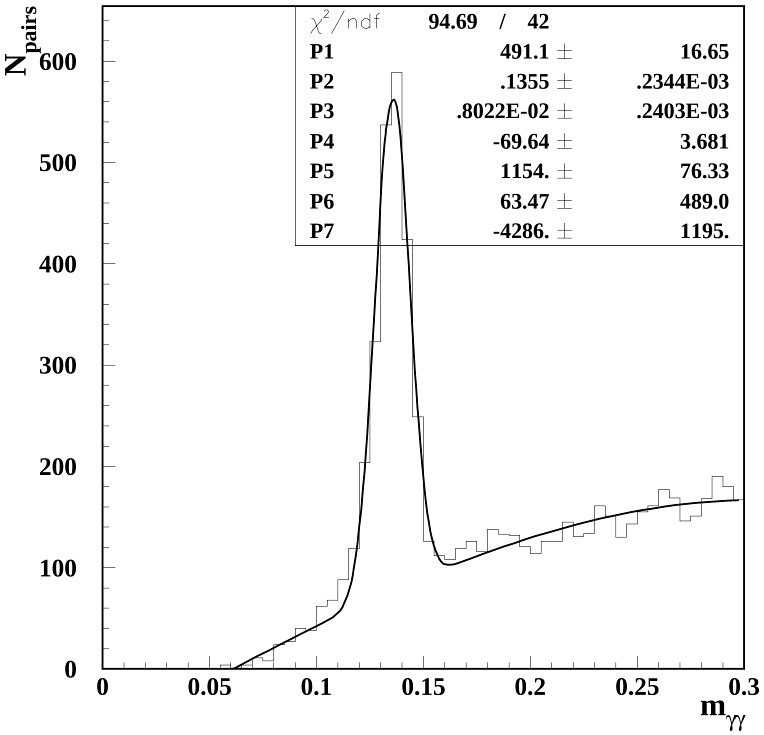

Figure 4.6: *Invariant mass of photon pairs in hadronic events in 1999 calibration data at* $\sqrt{s} = 91.26$ GeV *[182].*

Furthermore, a resolution of 1% in the barrel and 0.8% in the endcaps is achieved due to the refined RFQ calibration method [143,181] (compare to figure C.1 and table C.1 in appendix C).

Low Energy Region

Resolution and linearity of the BGO energy measurement is checked for lower energies by reconstructing two-photon invariant masses in hadronic events. This quantity shows a pronounced peak at the mass of the π^0 meson as displayed in figure 4.6. The π^0 decays dominantly into two photons [2]. The selection requires at least 1 GeV for the highest energetic photon and more than 0.3 GeV for the second photon and is performed on 1999 calibration data with a centre-of-mass energy near the Z mass [182]. A function constructed out of a Gaussian to describe the peak at the π^0 mass and a third-order polynomial to parametrise the background is fitted to the distribution. The values of the fit parameters are enu-

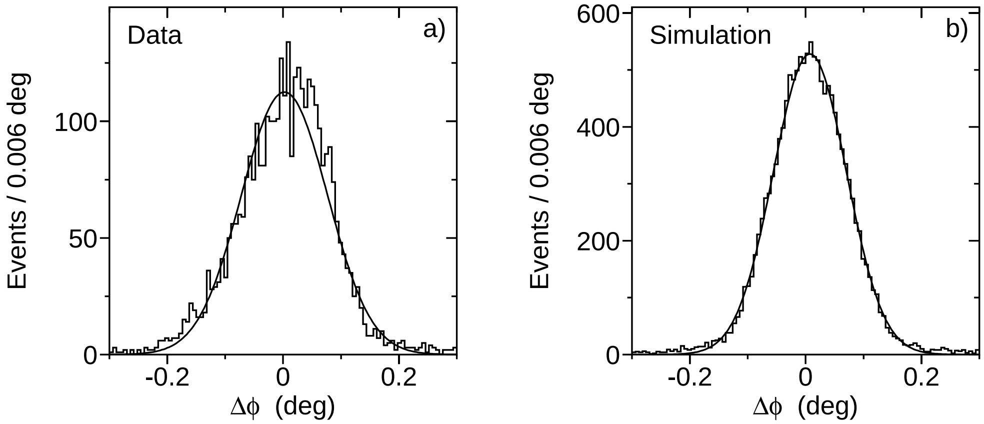

Figure 4.7: *Difference in azimuthal angle between track prediction and bump measurement for data (a) and Monte Carlo simulation (b) at* $\sqrt{s} =$ 189 GeV *for Bhabha events in the barrel. A single Gaussian is fitted to the spectra.*

merated in figure 4.6, where the first three parameters ($P_1 - P_3$) correspond to total normalisation, mean and standard deviation of the Gaussian, and the latter four are the amplitudes of third, second, first and zeroth order terms of the polynomial, respectively. The measured value for the π^0 mass of (135.5 ± 0.2) MeV (see figure 4.6) shows a slight discrepancy with respect to the world average value of $m_{\pi^0} = (134.9764 \pm 0.0006)$ MeV [2], which corresponds to a shift of 0.4%. Having the reference point of 45 GeV in mind at which the energy scale was fixed in the calibration (see section 3.2.1), this observed amount of non-linearity is very small. The peak resolution of $\sim$ 6% (see figure 4.6) roughly corresponds to a photon energy resolution of 4%, neglecting the angular resolution, which is in good agreement with previous results in this energy range between 0.3 GeV and about 2 GeV (see figure 3.6).

Angle

The angular resolution is estimated in ϕ and for the barrel region by calculating the difference between measured bump angle and angle of a track associated to an electron. Since the resolution of the azimuthal angle for track measurement is an order of magnitude higher than the expected BGO resolution, the prediction of the track parameter is thought of as "true" angle of the particle in this respect, and the difference to the bump angle defines the angular resolution of the BGO. As shown in figure 4.7, the angular resolution in data is $0.0746^\circ \pm 0.0011^\circ$ and $0.0633^\circ \pm 0.0004^\circ$ for Monte Carlo prediction which is not in agreement with each other within the statistical error, but, on the other hand, the amount of disagreement is not critical in terms of any of the analyses performed with the photon samples. The angular resolution corresponds to a spatial resolution on the BGO surface of (0.651 ± 0.010) mm for data and (0.552 ± 0.003) mm for the simulation. Since BGO crystals have a quadratic surface, the spatial resolution on the BGO surface in z direction can be assumed to be very similar to the resolution in ϕ, and since the granularity is the same in endcaps as in barrel, the spatial resolution in the endcaps should not differ too much from the one in the barrel.

4.3 Veto Cuts and Detector Noise

As mentioned in the introduction to this chapter, single photon events should consist only of a single bump in the BGO and nothing else in the detector. To guarantee this “emptiness” all detector components are, in principle, required to measure no further energy depositions or charged tracks, apart from what is identified as a photon, to suppress physics events from other sources. Since – possibly beam related – detector noise can fake additional signals in subdetectors while the underlying event is of the desired type, veto cuts must not be set too tight to account for this.

Cuts and Kinematic Regions

Four distinct kinematic regions are distinguished where different background sources become dominant[5] and where different veto cuts are set. The *first and most important region* is the one where at least one photon is detected with an energy larger than 5 GeV. Here, cuts on the number of BGO bumps not identified as photon, energy depositions measured in HCAL[6], luminosity monitor, ALR, SPACAL, and total visible energy not associated with a photon are imposed. Furthermore, the number of tracks in the muon chambers and the number of

---

[5] The background sources are to be discussed in detail in section 4.6.

[6] The HCAL energy found behind an identified photon is subtracted.

clusters of energy depositions in the calorimeters and tracks in the inner tracking chambers (SRCs[7]) are cut upon. There are two different veto cuts on the number of charged tracks measured in the inner tracking chambers depending on quality criteria of the track. The number of tracks, $N_{\mathrm{tracks},\,20}$, is defined as the number of tracks found by the track fit that have a transverse momentum larger than 20 MeV. To be counted as a "good track" ($N_{\mathrm{good\ tracks}}$) a track has to have a transverse momentum of at least 100 MeV, a span[8] greater than 8 and a DCA less than 20 mm.

In the *second kinematic region*, also, at least one photon with more than 5 GeV has to be identified and the total transverse momentum of the detected photon(s) must not exceed 20 GeV. Here, radiative Bhabha events or events of the type $\mathrm{e}^+\mathrm{e}^- \rightarrow \gamma\gamma(\gamma)$, where the initial state photon is lost in the beam pipe, become important. Since there is a small gap between hadron calorimeter and ALR in ϕ ranges of 81.9° – 96.3° and 261.8° – 276.2°, where particles escape undetected, events are discarded with a photon measured in that range in ϕ. In addition to veto cuts for the first region, tighter thresholds are set for the small angle detectors ALR and luminosity monitors to suppress electrons or photons at very low scattering angles which are likely to occur in the above mentioned backgrounds.

Furthermore, within the *third region*, where the total transverse momentum of the identified photon(s) is between 1.3 GeV (see section 4.6) and 10 GeV, only one supplementary constraint is applied. The number of tracks with a transverse momentum larger than 40 MeV, $N_{\mathrm{tracks},\,40}$, must be equal to zero.

Finally, in the *fourth region*, events with a photon energy less than 5 GeV and transverse momentum greater than 1.3 GeV (see section 4.6) are considered. Here, further cuts are set on additional energy depositions in BGO bumps and on the total BGO energy after subtracting the photon energy. The cut values for all four kinematic regions are listed in table 4.5.

Noise Level

The inefficiency due to detector noise introduced by these veto cuts is not simulated very well but is studied using randomly triggered beam gate events[9].

---

[7] Smallest Resolvable Cluster.

[8] The span equals the number of wires between innermost and outermost wire hit.

[9] See section 3.2.7 for a description of the beam gate trigger.

Cut variable Energies in GeV	$E_\gamma > 5$ GeV	$E_\gamma > 5$ GeV $p_t < 20$ GeV	$p_t > 1.3$ GeV $p_t < 10$ GeV	$p_t > 1.3$ GeV $E_\gamma < 5$ GeV
E_{HCAL}	10	10	10	6
E_{Lumi}	20	1	1	1
E_{ALR}	10	0.1	0.1	0.1
E_{SPACAL}	7	7	7	7
$E_{\text{vis}} - E_\gamma$	10	10	10	10
$E_{\text{BGO}} - E_\gamma$	–	–	–	0.5
$E_{\text{bumps}} - E_\gamma$	–	–	–	0.2
$N_{\text{BGO bumps}} - N_\gamma$	2	2	2	2
$N_{\text{muon tracks}}$	1	1	1	1
N_{SRCs}	14	14	14	14
$N_{\text{tracks, 20}}$	7	7	7	7
$N_{\text{tracks, 40}}$	–	–	1	1
$N_{\text{good tracks}}$	1	1	1	1

Table 4.5: *Veto cuts. To pass these cuts the measured values must be less than the listed value.*

In figures 4.8 and 4.9 distributions of variables used in this analysis are displayed except for E_{bumps} which is highly correlated to E_{BGO}. The cut position for the high energy region ($E_\gamma > 5$ GeV) is indicated by an arrow except for E_{BGO} and $N_{\text{tracks, 40}}$ where the arrow indicates the cut position for the low energy ($E_\gamma < 5$ GeV) sample (as indicated). Events where the measurement exceeds the displayed range are filled into the last interval ($\equiv$ bin) of the respective distribution.

In the quantitative evaluation it has to be taken into account, that beam gate events are not recorded proportional to luminosity but proportional to data acquisition time. Therefore, events are weighted with the luminosity of the corresponding run. The efficiency of the veto cuts is then given by

$$\epsilon_{\text{veto}} = \frac{\sum_i \mathcal{L}_i \frac{n_i}{N_i}}{\mathcal{L}} \qquad (4.3)$$

with $\mathcal{L}$ being the total luminosity, $\mathcal{L}_i$ the luminosity of the ith run, N_i the number of beam gate events in the ith run, and n_i the number of beam gate events in the

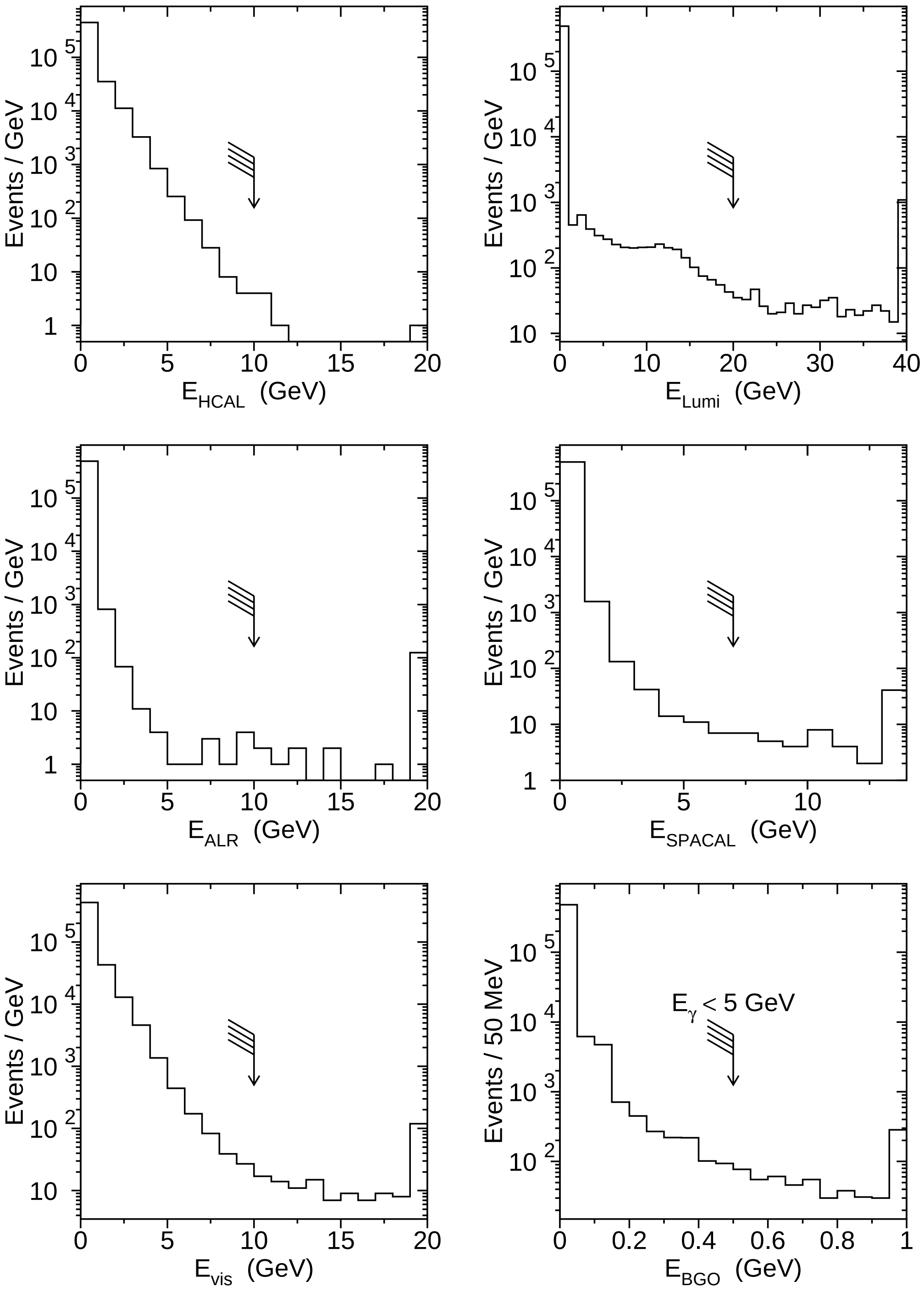

Figure 4.8: *Distributions of veto variables in beam gate events for the 1998 data set.*

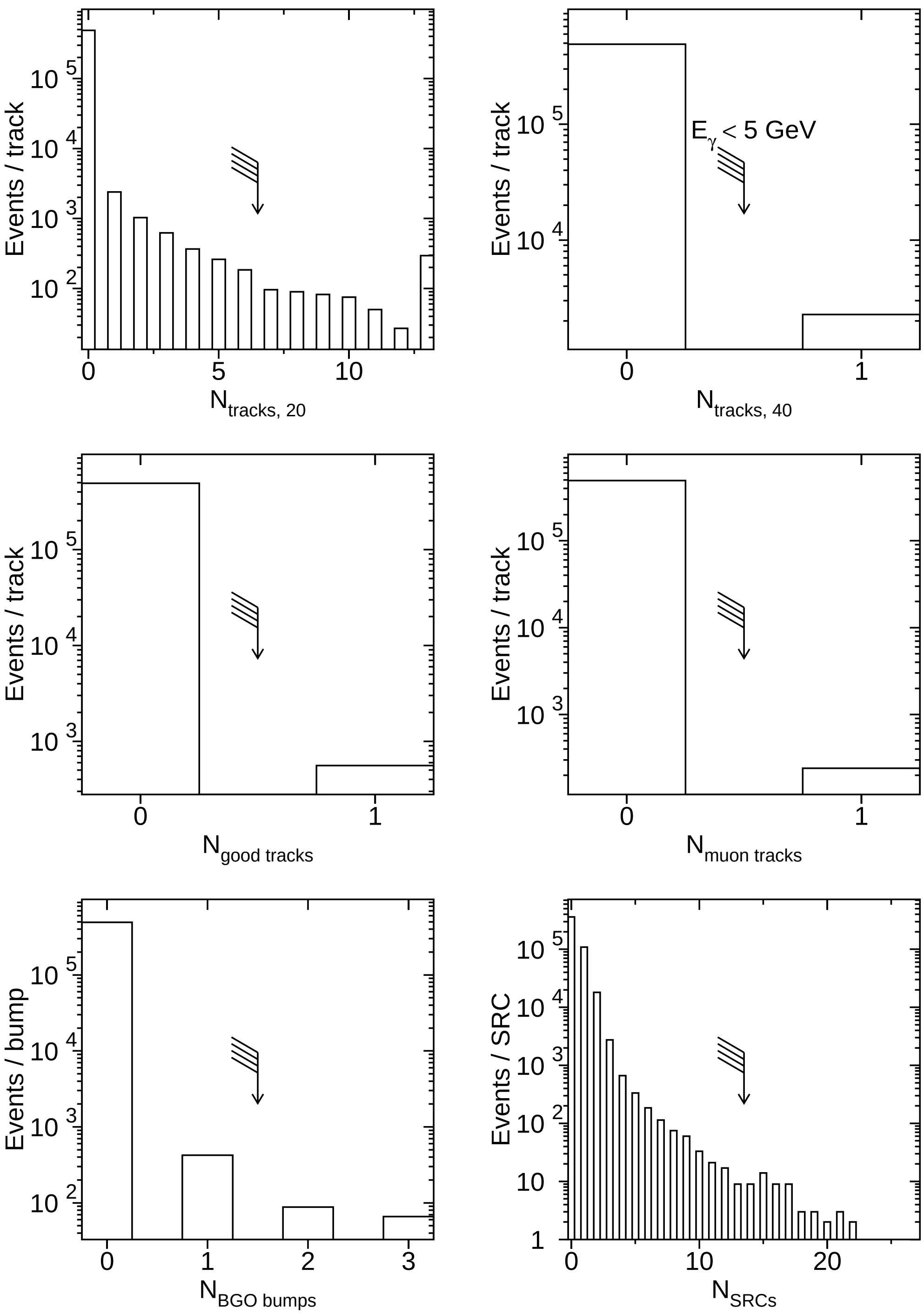

Figure 4.9: *Distributions of veto variables in beam gate events for the 1998 data set.*

	Data	Simulation	Correction
$E_\gamma > 5$ GeV	$(99.33 \pm 0.07)\%$	100%	$(0.67 \pm 0.07)\%$
$E_\gamma > 5$ GeV $p_\mathrm{t} < 20$ GeV	$(96.86 \pm 0.07)\%$	100%	$(3.14 \pm 0.07)\%$
$p_\mathrm{t} > 1.3$ GeV $p_\mathrm{t} < 10$ GeV	$(96.62 \pm 0.07)\%$	100%	$(3.38 \pm 0.07)\%$
$p_\mathrm{t} > 1.3$ GeV $E_\gamma < 5$ GeV	$(96.53 \pm 0.07)\%$	$(99.989 \pm 0.003)\%$	$(3.46 \pm 0.07)\%$

Table 4.6: *Veto cut efficiencies in 1998 for the four kinematic regions used in this analysis. Efficiency for data is estimated using beam gate events and for the simulation a $\nu\bar{\nu}$ (without γ) Monte Carlo sample is exploited.*

ith run passing all cuts from table 4.5. Efficiencies in the four kinematic regions defined above can be read from table 4.6.

On top of that, the efficiency of veto cuts is checked in the Monte Carlo detector simulation. $\nu\bar{\nu}$ events (without initial state radiation) are used for this purpose generated with the `KORALZ` Monte Carlo program. Since neutrinos do not interact with detector material they provide an ideal tool to study detector noise in the simulation. Derived efficiencies are provided in table 4.6. Hereafter, the Monte Carlo simulation is corrected to match data with corrections being listed up in table 4.6. The correction factor for the last three kinematic regions is much larger than for the first region, because of stringent cuts on energies measured in ALR and luminosity monitors. The remaining systematic error originating from limited statistics of beam gate events is an order of magnitude smaller than the systematic error on the photon identification derived in section 4.1 and negligible compared to the total statistical error of the results presented in chapter 5.

4.4 Cosmics in Single Photon Events

In this section the appearance of events with cosmic origin in the single photon sample is studied and means to suppress this event type are presented.

High energetic cosmic rays mainly consisting of protons and heavier nuclei are able to produce, among others, charged pions and kaons in the upper atmosphere which subsequently decay into muons. Due to their fairly long life time of about 2.2 μs, high energetic muons can reach the surface of the earth and even the L3 detector located approximately 50 m underground. At first glance, cosmic muons penetrating L3 leave a track in the muon chambers and are thus rejected by the selection as described in section 4.3. However, for two reasons these cosmic rays could pass the muon chambers undetected: The muon chambers are not hermetically sealed and even at large angles with respect to the beam axis some (small) regions are only covered by one layer and some are even not covered at all. Secondly, the readout time of the various subdetectors is different from one another. The BGO needs by far the longest integration time for energy measurement, whereas all other subdetectors including the muon chambers have a much shorter gate. Since the timing of cosmic rays is not related to the beam crossing, cosmic muons potentially arrive significantly before or after beam crossing, fly through the muon chambers undetected or badly measured, but leave a signal in the BGO. Even then, escaping detection in the muon chambers and punching through the BGO, nevertheless, a muon, with its minimal ionising signature of about 200 MeV energy deposition in the BGO, still, should not look like a photon. However, interacting with the detector material, the cosmic muon could radiate a bremsstrahlung photon, which may be detected in the electromagnetic calorimeter.

Anti-Cosmics Cuts

Several means to suppress this background are listed in the previous sections and shall be discussed here again in the light of its suppression power for cosmics. Clearly, this is obvious for the veto cut on the number of muon tracks, but also the requirements on photon identification are helpful in this context. Since the interaction where a bremsstrahlung photon is created by a cosmic muon does not take place in the nominal interaction point, it is likely that the photon does not enter the BGO perpendicular to the crystal surface, thus not leaving a bump being symmetric under arbitrary rotations. This is measured by the variable "skewness" presented in section 4.1 which is sensitive to the bump shape and provides some discrimination power to suppress cosmic muons. Within the veto cuts (section 4.3), the cut on $E_{\text{bumps}} - E_\gamma$ is helpful in this respect because the muon is possibly identified as a bump with more than 200 MeV energy; with the cut on $N_{\mathrm{tracks},\,40}$, events are suppressed if the muon leaves a TEC track.

Further cuts include an upper limit on the ratio of the number of bumps to the number of crystals in the BGO ($N_{\mathrm{bumps}}/N_{\mathrm{crystals}}$). Cosmics easily produce two bumps, one by the muon and another by the bremsstrahlung photon, but then the muon bump only consists of few crystals which leads to a large ratio. The scintillator is used to ensure the photon recorded to be in time with beam crossing, but only for hard photons the leakage through the BGO is large enough to produce a hit in the scintillator behind the BGO. Therefore, only for events having a photon with energy greater than 15 GeV, at least one scintillator hit within 5 ns around the beam crossing time is required (N_{scint}) to suppress out-of-time cosmics.

In case no in-time scintillator hit is found in a 30° cone behind a photon ($N_{\mathrm{scint,\,bump}} = 0$), a line fit between Z hits detected in the muon chambers and BGO bump is performed. Only Z and no P chamber hits are used, because of the longer integration time for the Z readout, and thus a higher efficiency for out-of-time muons is achieved. If more than four hits are used in the fit ($N_{\mu\mathrm{fit}}$), the distance of fit line to BGO bump ($d_{\mu\mathrm{fit}}$) is smaller than 30 cm, $\chi^2_{\mu\mathrm{fit}}$ of the fit is less than 300, and the distance between the two extreme hits used in the fit ($\mathrm{span}_{\mu\mathrm{fit}}$) is larger than 2 m, then the event is discarded.

The TEC is exploited further to suppress cosmic ray events. If $N_{\mathrm{tracks},\,40}$ is more than one, the acoplanarity between any pair of these tracks ($\phi_{\mathrm{acop\ tracks}}$) must be greater than 20°, and if there is at least one such track, the DCA must be less than 40 mm or the angular difference in ϕ between the track(s) and BGO bumps identified as photons ($\phi_{\mathrm{track-bump}}$) must be larger than 10°. For the last requirement concerning the suppression of cosmics, a straight line is constructed between any pair of BGO bumps and the number of hits measured in the TEC, which are located in a distance not larger than 1 cm to this line ($N_{\mathrm{cosmic\ hits}}$), is counted. An event passes if there are less than 20 hits collected. All special cosmic suppression cuts are enumerated again in table 4.7.

Cosmic Sample Selection

In order to estimate the amount of cosmic ray events passing all selection cuts, a pure sample of out-of-time cosmics is selected to check the discrimination power of the anti-cosmic cuts. Two main characteristics are exploited to ensure the out-

$N_{\text{bumps}}/N_{\text{crystals}}$	$<$	0.12		
$N_{\text{bumps}}/N_{\text{crystals}}$	$<$	0.07	if	$E_\gamma > 5$ GeV
N_{scint}	$\geq$	1	if	$E_\gamma > 15$ GeV
$N_{\mu\text{fit}}$	$\leq$	4	if	$d_{\mu\text{fit}} < 30$ cm, $\chi^2_{\mu\text{fit}} < 300$, $\text{span}_{\mu\text{fit}} > 2$ m, $N_{\text{scint, bump}} = 0$
$\phi_{\text{acop tracks}}$	$>$	20°	if	$N_{\text{tracks, 40}} \geq 2$
$\phi_{\text{track-bump}}$	$>$	10°	if	$N_{\text{tracks, 40}} \geq 1$, DCA > 40 mm
$N_{\text{cosmic hits}}$	$\leq$	20		

Table 4.7: *Anti-cosmics cuts.*

of-time quality. Firstly, no scintillator hit within 5 ns around the beam crossing should be recorded, and secondly the ratio between the BGO energy seen by the level-1 trigger (see section 3.2.7) and the digitised BGO energy should be less than 0.5. The latter cut exploits the out-of-time feature, since the integration time used for the level-1 trigger decision is much shorter than the total readout time for the energy measurement. Furthermore, there must be at least one bump in the BGO with an energy exceeding 1 GeV, no more than 20 GeV measured in the HCAL, less than 1 GeV in the luminosity monitor and 0.1 GeV in the ALR. The cut on zero tracks measured in the muon chambers is also applied. In this manner, a sample of 5016 events is selected in the 1998 data. Energy and angular distributions of the highest energetic bump of an event are shown in figure 4.10. It should be noticed that also bumps with extremely high energy up to about 600 GeV are present. One of these events is shown in figure 4.11 and has a spectacular bump in the barrel region with an energy measured to be 630 GeV. The azimuthal angle in figure 4.10(b) shows two peaks at angles perpendicular to the surface. This seems quite natural since it is the direction of flight for the majority of cosmic muons.

This sample of cosmics is used to estimate the rejection efficiency of the selection cuts. To determine the contamination of cosmics in the final sample all selection cuts need to be introduced before. Hence, the precise method for the number-of-cosmics estimation is explained in section 4.7.

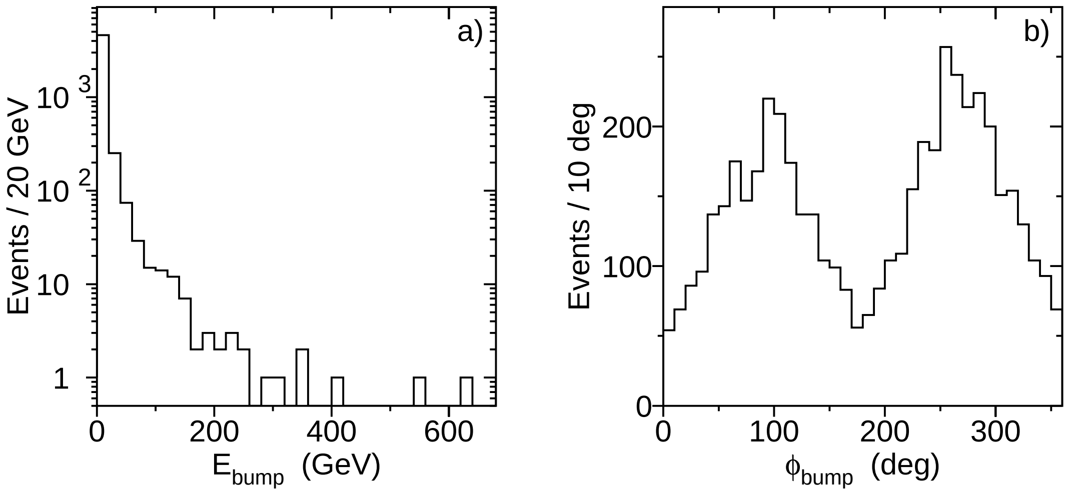

Figure 4.10: *Bump energy (a) and azimuthal angle (b) of the highest energetic bump per event in the cosmic sample selected in 1998.*

4.5 Trigger Efficiency

The only trigger relevant to record events with exclusively photons in the final state is the energy trigger. A detailed description of its various subtriggers is presented in section 3.2.7. There are two methods to determine the trigger efficiency. Firstly, events are selected that are triggered by a different, independent trigger, but should, from a topological point of view, also let the trigger under investigation fire. Then, the trigger efficiency is estimated by simply counting the number of events where the trigger of interest was active. Secondly, a detailed simulation of the trigger conditions is used and applied to the Monte Carlo events.

In general, the second method is applied to match Monte Carlo events with data. In the trigger threshold region, which is the most critical one since here the trigger efficiency changes rapidly, an event class with an independent trigger – so-called “single electron” events – is at hand to check the performance of the simulation. “Single electron” events are radiative Bhabha scattering events where one low energetic electron is scattered into the BGO, a radiated photon escapes undetected along the beam pipe and the other electron (or positron) is detected in the luminosity monitor. These events are triggered by the “single electron” trigger which requires an energy deposition in the luminosity monitor

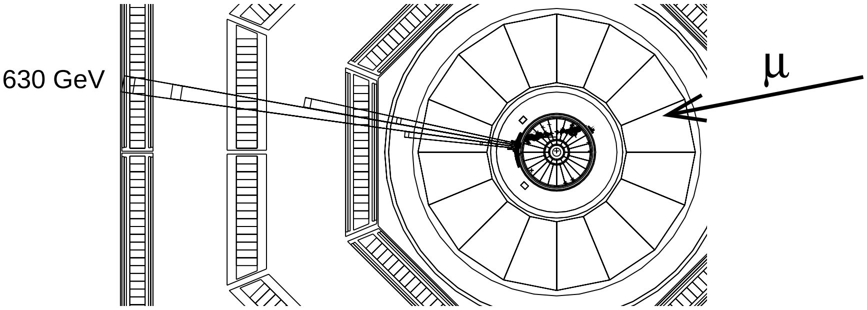

Figure 4.11: *Schematic view of a cosmic muon event candidate recorded in 1998 radiating a bremsstrahlung photon with* 630 GeV *energy. Another, less energetic, bump is visible in the BGO, and the two bumps are connected by a TEC track.*

and a track in the TEC. The electron in the BGO is then used to investigate the single photon and the BGO cluster trigger.

Single Electron Selection

The trigger simulation is performed not only for Monte Carlo events but it is employed during the reconstruction phase of data as well. Due to this benefit, the study is carried out using data only, and thus, on the same event sample simulation is compared with reality. The event selection used for the trigger performance check requires at least one identified electron or photon with a minimum energy of 1 GeV in barrel or 5 GeV in endcaps. Moreover, all veto cuts described in section 4.3 (except for cuts on energies in luminosity monitor and ALR), and all cuts to reject cosmic muon events discussed in section 4.4 are applied. In addition, either the single electron or the TEC trigger (see section 3.2.7) bit must be set. Energy spectra of the identified electromagnetic object for barrel and endcaps are shown in figure 4.12. As expected, low energies are more frequent.

Trigger Performance at Threshold

The trigger efficiency calculated from this event sample is shown for the barrel in figure 4.13(a) and for the endcaps in 4.13(b), both for simulation and actual trigger efficiency. In the barrel, the trigger efficiency increases from zero at about

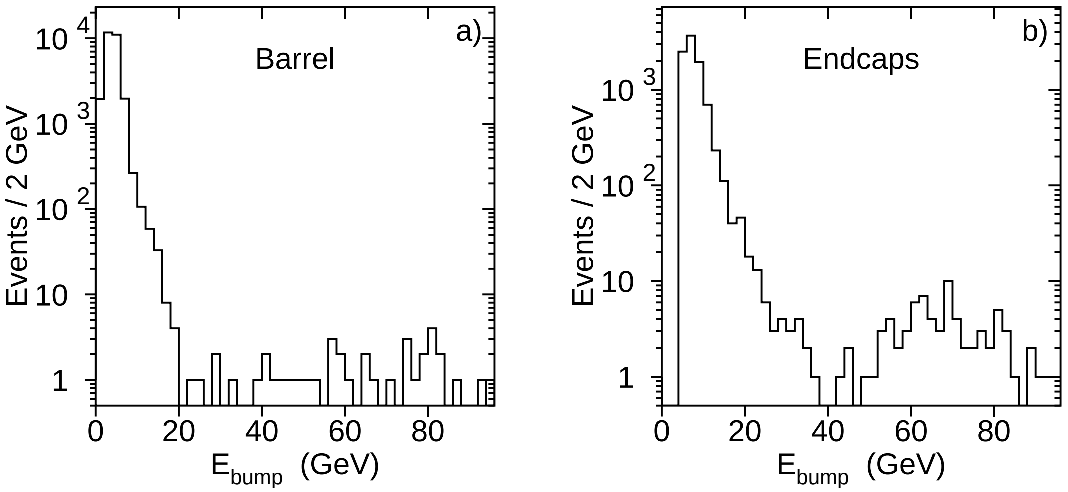

Figure 4.12: *Energy spectra of the identified electromagnetic object in the "single electron" selection in barrel (a) and endcaps (b) for the* 189 GeV *data.*

0.9 GeV – threshold of the single photon trigger – to almost 100% above 8 GeV. In the endcaps, where only the BGO cluster trigger with a threshold at 6 GeV is used and no single photon trigger is installed, the trigger efficiency reaches about 90% at 8 GeV. It can be seen that simulation and actual trigger efficiency do not agree very well with each other in the threshold region, but show a reasonable agreement above threshold. Hence, the simulation is corrected to match the real efficiency around threshold. The difference between simulated and actual efficiency is shown in the lower half of figure 4.13. A discrepancy up to 20% is observed in the threshold region within the endcaps. Here, it seems that the threshold value is somewhat lower for the real trigger than for the simulation. The uncertainty coming from the statistics of "single electron" events is about 5% in the threshold regions, both, in barrel and endcaps. This value, however, is small compared to the statistical error in these regions (about 14% in barrel for $E_\gamma < 1.6$ GeV and about 38% in endcaps for $E_\gamma < 8$ GeV, see section 4.9), and negligible for the measurement of the total $\nu\bar{\nu}\gamma$ cross section (see section 5.1).

Wide Angle Bhabhas

Another physics process to test the trigger efficiency is available in the high energy region. Again, Bhabha events, this time fully contained in the BGO

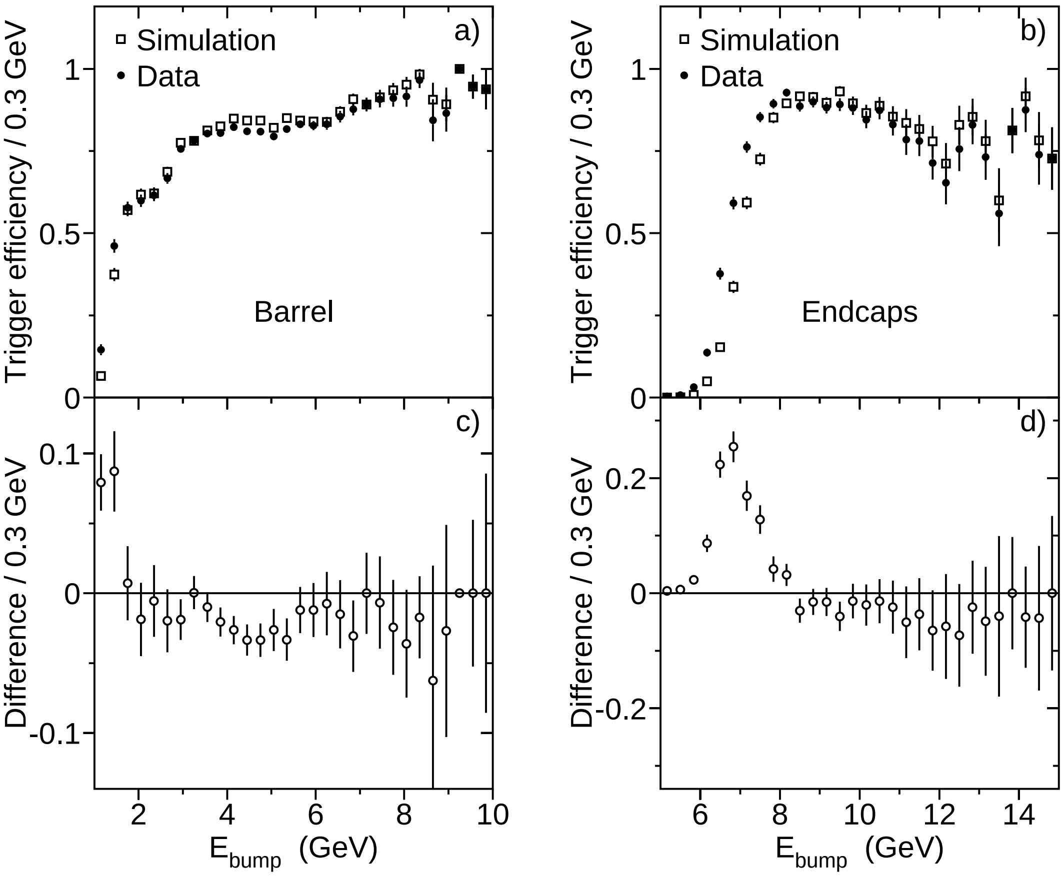

Figure 4.13: *Trigger efficiency in barrel (a) and endcaps (b) and difference between actual and simulated efficiency in barrel (c) and endcaps (d) for the* 189 GeV *data.*

calorimeter, are triggered by the energy trigger and an independent one, namely the TEC trigger. Here, usually at least two high energetic BGO bumps are detected, and thus this test concerns more the multi-photon selection rather than the single photon sample. Nevertheless, this check is done using 3 pb^{-1} of data collected in 1998 at a centre-of-mass energy of 91.312 GeV. The event selection requires one or two electrons or photons with at least one having an energy exceeding 40 GeV, and two (good) tracks with an acoplanarity of at most 1.2°. After this selection, in $(99.41 \pm 0.14)\%$ of the events where the TEC trigger has fired, also the trigger bits of the energy trigger, where no TEC track is explicitly required, were set. For the simulation, the number is $(99.69 \pm 0.10)\%$

showing good agreement with the measurement.

4.6 Standard Model Processes and Final Selection Cuts

Applying photon identification, cosmic rejection and cuts introduced in sections 4.1, 4.3 and 4.4 to data should eventually lead to a sample solely consisting of photons and no other particles in the events. The two Standard Model physics processes with only photons detected in the final state are $\mathrm{e}^+\mathrm{e}^- \to \nu\bar{\nu}\gamma(\gamma)$ and $\mathrm{e}^+\mathrm{e}^- \to \gamma\gamma(\gamma)$. Processes with other final states are strongly suppressed allowing only negligible amounts to pass the cuts. However, there is one exception. As stated in the previous sections, electrons and photons leave the same signature in the BGO and are only distinguished by a track associated to a bump for electrons. On the other hand, the acceptance of the inner tracking system is limited to polar angles larger than $15^\circ - 20^\circ$, and processes with electrons in the final state need to be considered for this reason. There are basically three processes with electrons to be taken into account, which are radiative Bhabha scattering $\mathrm{e}^+\mathrm{e}^- \to \mathrm{e}^+\mathrm{e}^-(\gamma)$, and the two four-fermion processes $\mathrm{e}^+\mathrm{e}^- \to \mathrm{e}^+\mathrm{e}^-\mathrm{e}^+\mathrm{e}^-$ and $\mathrm{e}^+\mathrm{e}^- \to \mathrm{e}^+\mathrm{e}^-\nu\bar{\nu}$.

Monte Carlo Programs

The contribution of the different sources to the final sample is determined with Monte Carlo simulations for the various processes. The Monte Carlo programs used to generate events together with specific kinematic regions, calculated cross sections within these regions and number of events generated are listed in table 4.8. The $\nu\bar{\nu}\gamma(\gamma)$ simulation is performed with `KORALZ` for three light neutrino species. The overlap between the two Bhabha samples is eliminated by accepting only non-radiative events from `BHWIDE` if one electron has an angle smaller than 11° with respect to the beam axis. The `TEEGG` program delivers reasonable results only if the transverse momentum of the generated large angle photon or electron is not too small. For this reason, a minimum transverse momentum (p_t) of 1.3 GeV for the identified photon(s) is required. The cut on the transverse momentum is set to 5 GeV if the energy of the highest energetic photon of the event is larger than 5 GeV and if an eventually detected second photon has energy less than this value.

$e^+e^- \rightarrow$	Generator		Cross section (pb)	Kinematic region	Events generated
$\nu\bar{\nu}(\gamma)$	`KORALZ`	[38]	58.84		610000
$\gamma\gamma(\gamma)$	`GGG`	[183]	21.88	$\lvert\cos\theta_{\gamma 1,2}\rvert < 0.996$	97246
$e^+e^-(\gamma)$	`BHWIDE`	[179]	4016.19	$\lvert\cos\theta_{e1,2}\rvert < 0.996$	2555700
$e^+e^-\gamma(\gamma)$	`TEEGG`	[184]	3597.24	$\lvert\cos\theta_{e1}\rvert > 0.982$	1293995
$e^+e^-e^+e^-$	`DIAG36`	[185]	639.71	$\lvert\cos\theta_{e3,4}\rvert < 0.985$ $m_{e_3e_4} > 3.1$ GeV	399000
$e^+e^-\nu\bar{\nu}(\gamma)$	`EXCALIBUR`	[186]	0.89	$\lvert\cos\theta_{e1}\rvert < 0.996$	19955

Table 4.8: *Standard Model processes, Monte Carlo programs, cross sections at* $\sqrt{s} = 189$ GeV *within the indicated kinematic regions, and the generated number of events.*

Single Photon Cuts

The background sources listed in table 4.8 – starting with $e^+e^- \rightarrow \gamma\gamma(\gamma)$ – all comprise more than one photon or electron in the final state. Nevertheless, the second electromagnetic particle could possibly escape detection in the beam pipe, the BGO by traversing through the crystal's support structure or small gaps between BGO and SPACAL, depositing only a fraction of its energy in active detector material. Therefore, a number of safety cuts applied under special conditions are employed. If the energy measured in the SPACAL is greater than zero and the missing momentum calculated from the identified photons points into the SPACAL bump within 4° in θ ($\Delta\theta_{\mathrm{SPACAL}}$) and 30° in ϕ ($\Delta\phi_{\mathrm{SPACAL}}$), the event is removed from the sample. If the energy of a cluster measured in the hadron calorimeter endcap ($E_{\mathrm{HCAL,\,EC}}$) is greater than 3 GeV, and the identified photon with highest energy is in the opposite (BGO) endcap, the event is discarded. If an energy cluster measured in the HCAL ($E_{\mathrm{HCAL,\,cluster}}$) is greater than 3 GeV, and the acoplanarity between cluster and photon with highest energy of the event ($\phi_{\gamma-\mathrm{HCAL}}$) is less than 15°, the event is cut out. Furthermore, if two calorimetric clusters are present in opposite hemispheres, their opening angle ($\Delta\alpha_{\mathrm{cl}}$) must be smaller than 3.05 rad, and smaller than 3.1 rad in the plane transverse to the beam axis ($\Delta\phi_{\mathrm{cl}}$) if the energy of the most energetic photon exceeds 5 GeV and a potential second photon has an energy less than that value. At last, events are removed where a photon is identified in the ϕ region opposite

p_t	$>$	1.3 GeV		
p_t	$>$	5 GeV	if	$E_{\gamma_1} > 5$ GeV, $E_{\gamma_2} < 5$ GeV
$\Delta\phi_\mathrm{SPACAL}$	$>$	30°	if	$E_\mathrm{SPACAL} > 0$, $\Delta\theta_\mathrm{SPACAL} < 4°$
$E_\mathrm{HCAL,\,EC}$	$<$	3 GeV	if	γ in opposite (BGO) endcap
$E_\mathrm{HCAL,\,cluster}$	$<$	3 GeV	if	$\phi_{\gamma-\mathrm{HCAL}} < 15°$
$\Delta\alpha_\mathrm{cl}$	$<$	3.05 rad	if	$E_{\gamma_1} > 5$ GeV, $E_{\gamma_2} < 5$ GeV
$\Delta\phi_\mathrm{cl}$	$<$	3.1 rad	if	$E_{\gamma_1} > 5$ GeV, $E_{\gamma_2} < 5$ GeV
$N_\mathrm{iTEC\,9,10}$	$=$	0	if	$77° < \phi_\gamma < 101°$

Table 4.9: *Selection cuts.*

to an RFQ hole and a track is measured either in inner TEC sector 9 or sector 10 ($N_\mathrm{iTEC\,9,10}$). These sectors include the ϕ region where the RFQ holes are present. All requirements are enumerated in table 4.9.

Multi-Photon Cuts

If a second high-energetic photon – with energy larger than 5 GeV – is present in the selected sample, further cuts on the missing energy signature must be accommodated to suppress the large background from $\mathrm{e}^+\mathrm{e}^- \to \gamma\gamma(\gamma)$ and Bhabha scattering at lower angles. In general, a minimum total transverse momentum calculated from the measured photon momenta of 3 GeV and a recoil mass greater than 20 GeV are required. If the angle between the two highest energetic photons projected onto the rϕ plane ($\Delta\phi_{\gamma\gamma}$) is larger than 3.1 rad, the recoil mass must be greater than 50 GeV. In case the transverse momentum calculated from the photon momenta is smaller than 30 GeV additional cuts are imposed. Here, the angle in space between the two highest energetic photons of each event ($\Delta\alpha_{\gamma\gamma}$) should be smaller than 3 rad, and the angle projected to the rϕ plane ought to be less than 3.05 rad. If the transverse momentum is smaller than 20 GeV, the polar angle of the missing momentum vector, θ_miss, has to be larger than 7° with respect to the beam axis (equivalent to $\sin\theta_\mathrm{miss}$ greater than 0.122). These cuts are listed in table 4.10.

Distributions of variables cut upon are shown in figure 4.14, where all cuts are applied except for the cut on the displayed quantity. The total number of events in the figures differ from each other, since some cuts are exclusively

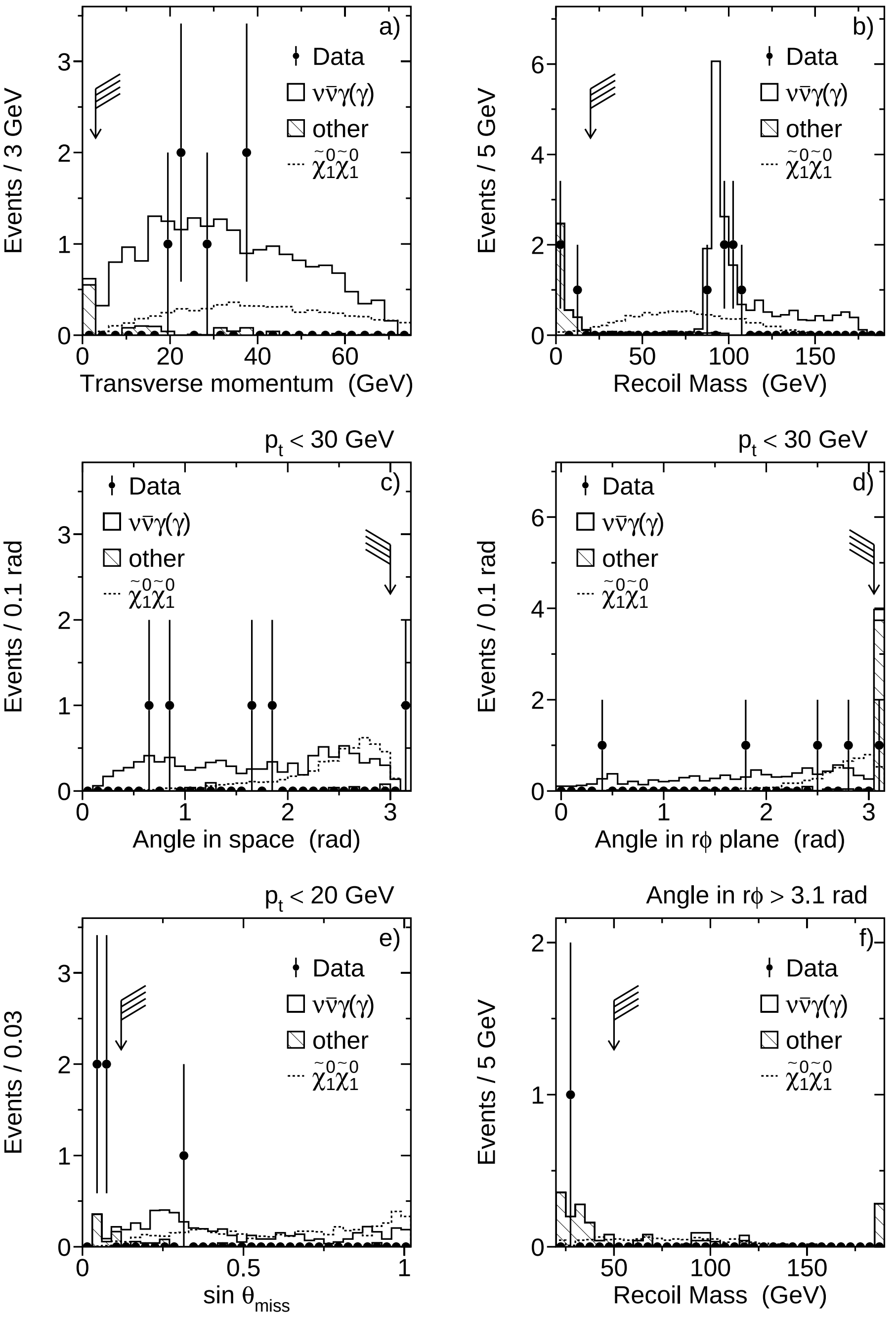

Figure 4.14: *Distributions of variables used if* $E_{\gamma_2} > 5$ GeV *for* $\sqrt{s} =$ 189 GeV*. Other kinematic requirements are specified on top of the individual figures. The* $\tilde{\chi}_1^0\tilde{\chi}_1^0$ *Monte Carlo is normalised to data. Arrows indicate cut positions.*

p_{t}	$>$	3 GeV		
Recoil mass	$>$	20 GeV		
Recoil mass	$>$	50 GeV	if	$\Delta\phi_\gamma > 3.1$ rad
$\Delta\alpha_{\gamma\gamma}$	$<$	3 rad	if	$p_{\mathrm{t}} < 30$ GeV
$\Delta\phi_{\gamma\gamma}$	$<$	3.05 rad	if	$p_{\mathrm{t}} < 30$ GeV
$\sin\theta_{\mathrm{miss}}$	$>$	0.122	if	$p_{\mathrm{t}} < 20$ GeV

Table 4.10: *Multi-photon selection cuts imposed if* $E_{\gamma_2} > 5$ GeV.

applied within certain kinematic requirements, as discussed above. Since the selection also aims to be sensitive to the production of supersymmetric particles with photonic final states, and the kinematic distributions in the multi-photon case can be quite different from $\mathrm{e^+e^-} \rightarrow \nu\bar{\nu}\gamma\gamma(\gamma)$, the Monte Carlo prediction for the process $\mathrm{e^+e^-} \rightarrow \tilde{\chi}_1^0\tilde{\chi}_1^0 \rightarrow \tilde{\mathrm{G}}\tilde{\mathrm{G}}\gamma\gamma$ is also shown. The process is introduced from a phenomenological view point in section 2.2.3. Interpretations of measured data concerning the $\tilde{\chi}_1^0$ pair-production are addressed in section 5.4. The Standard Model background, denoted by "other" in figure 4.14, is mainly composed of $\mathrm{e^+e^-} \rightarrow \gamma\gamma(\gamma)$ events. The distributions show a fair agreement between data and prediction of the Standard Model in all variables.

4.7 Cosmics Contamination

After all cut quantities are presented, their discrimination power against cosmics is evaluated. This is performed using the selected sample of out-of-time cosmics – as described in section 4.4 – by probing the sample with all cuts enumerated in tables 4.1, 4.3, 4.5, 4.9, 4.10, and especially the specific cosmic rejection cuts in table 4.7, except for the cut on the number of in-time scintillator hits. The numbers determined are listed in the upper half of table 4.11, split into two distinct regions separated by the requirement on the energy of the highest energetic photon of an event of 5 GeV.

To compute the number of cosmics expected in the final data sample, the photon selection is run on the full data set but without the cuts identified to have cosmic rejection power in section 4.4 (table 4.7). Only the cut on the number of in-time scintillator hits is imposed. The number of events selected

	$E_\gamma > 5$ GeV	$E_\gamma > 1.3$ GeV $E_\gamma < 5$ GeV
Total number of out-of-time cosmics	1738	3278
Selected number of out-of-time cosmics	4	3
Efficiency	$(0.23 \pm 0.11)\%$	$(0.092 \pm 0.053)\%$
Events after photon selection without anti-cosmic cuts	1353	3961
Number of cosmics expected	3.1 ± 1.5	3.6 ± 2.1

Table 4.11: *Cosmic selection efficiency and number of expected events with cosmic origin in the final sample for* $\sqrt{s} = 189$ GeV.

in this way – after having subtracted the number of events expected from e^+e^- collisions in the final selected photon sample (see section 4.9, table 4.13) where all cuts (including the anti-cosmic cuts) are applied – can be considered as a conservative estimate for the number of events with cosmic origin. They are listed in the lower half of table 4.11. The estimate is conservative since, clearly, also a fraction of events from e^+e^- collisions remains in this sample, which are then cut by the anti-cosmic requirements. Especially, the requirement of at least one scintillator hit within 5 ns of the beam crossing, and the μfit complex (see section 4.4) removes a fraction of e^+e^- events from the sample (the amount is estimated below for the μfit cut). Multiplying the cosmic selection efficiency (see upper half of table 4.11) by the number of events selected in the above described manner determines the number of cosmic ray events expected in the final event sample. The calculated numbers are listed in table 4.11.

μfit Correction

An additional correction on the simulation introduced by the cosmic rejection cut on the number of muon chamber Z hits used in the μfit procedure – described in section 4.4 – has to be considered. Since muon chamber noise concerning Z hits is not simulated it is not yet taken into account. The number of muon chamber Z hits is therefore always zero in the detector simulation if there are no particles penetrating the muon chambers – as it is the case for photonic final states. The amount of noise and thus a correction factor is quantified from data using “single

	Barrel	Endcap $\theta < 36°$	Endcap $\theta > 144°$
Total number of single $e^{\pm}$ events	29570	8188	7959
Events with $N_{\mu\text{fit}} > 4$	736	223	223
(In)efficiency	$(2.49 \pm 0.09)\%$	$(2.72 \pm 0.18)\%$	$(2.80 \pm 0.18)\%$

Table 4.12: *Number of "single electron" events not passing the μfit cut and derived μfit inefficiency for $\sqrt{s} = 189$ GeV.*

electron" events (see also section 4.5). These events are selected using the same cuts as for the single photon selection except requiring exactly one identified electron and no further leptons or photons, one good track (with the criteria of footnote 2 of this chapter on page 72) and no more than one track ($N_{\text{tracks},\,20}$, see section 4.3). Instead of vetoing on the energy measured in the luminosity monitor and in the ALR, a minimum of 50 GeV is required for the sum of the two. Of course, the μfit complex is not cut upon, since it is subject to investigation, but due to the low noise level and the small acceptance for cosmics of the low angle detectors ALR and luminosity monitor, the selected sample is considered as cosmic-free even without this cut applied. Therefore, a value for the number $N_{\mu\text{fit}}$ above zero is noise related. Because the muon chambers consist of barrel and two endcap regions as the BGO, the selected "single electron" sample is split into three parts for the three distinct regions. The distributions for $N_{\mu\text{fit}}$ are displayed in figure 4.15 and the numbers of selected events with and without the μfit cut and the derived additional inefficiency due to muon chamber noise are quoted in table 4.12. The Monte Carlo simulations are thus corrected for the μfit inefficiency.

4.8 Photon Conversion

The possibility of photon conversion and means to select this kind of events is discussed in section 4.1. Here, the event rate in selected data and Monte Carlo simulation samples shall be stated and an estimate of the systematic uncertainty on the selection efficiency due to the amount of disagreement between measure-

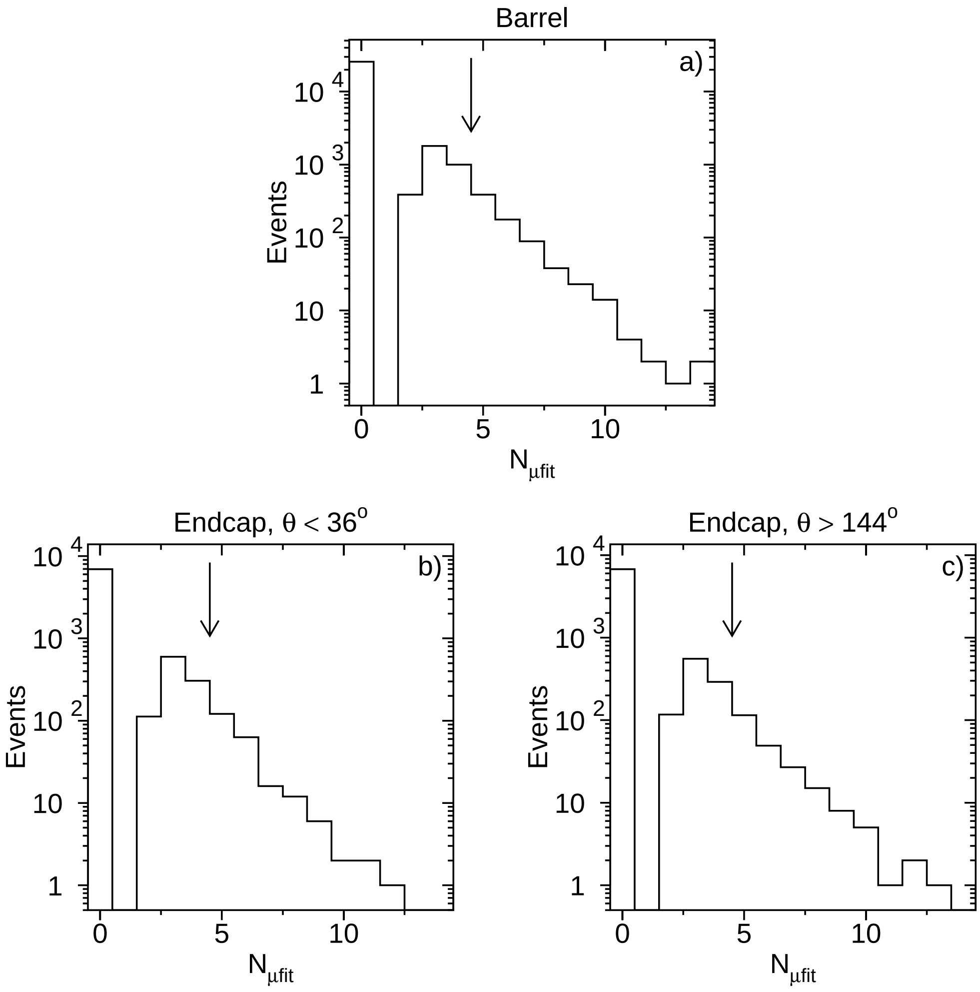

Figure 4.15: *Distributions of $N_{\mu\mathrm{fit}}$ in the "single electron" sample in 1998.*

ment and prediction of the detector simulation is computed.

Conversion Rate

The fact that the amount of material in the inner part of the L3 detector is unchanged since the LEP 2 phase began, leads to the assumption that the photon conversion probability remains the same for the years 1995 to 1998. To decrease the statistical uncertainty while deriving the conversion rate, the results of the respective data taking periods are combined. The number of converted photons found in the sample of selected single and multi-photon events is 36 out of a total of 977 events in the data yielding a conversion rate of $(3.7 \pm 0.6)\%$, whereas

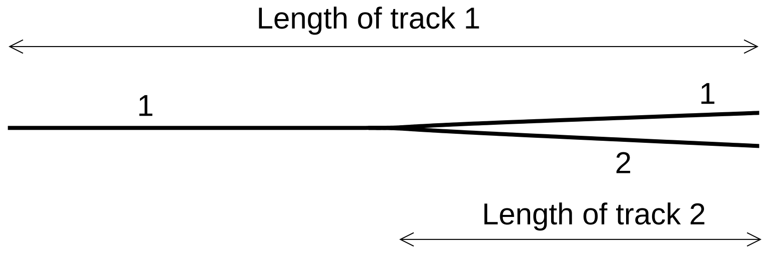

Figure 4.16: *Track splitting of an electron-positron pair originating from a photon conversion.*

the numbers for the prediction of the Monte Carlo simulation are 17.4 out of 998 corresponding to a rate of $(1.74 \pm 0.05)\%$. A clear disagreement between data and prediction of the detector simulation must be stated which accounts for the fact that the amount of material present in the inner regions of the L3 detector is partly not correctly incorporated in the detector simulation. This is, in itself, not critical, since both event types – “direct” photons and converted photons – are selected and in the end they are put together to one photon sample. However, this is only true if all converted photons are caught and no losses occur. Unfortunately, if the two tracks of the electron-positron pair to which a photon converted, are too close together to be resolved by the inner tracking system, thus showing only a single track, the event is not selected because the converted photon can no longer be distinguished from an ordinary electron. In Monte Carlo simulation, this happens in about 48% of all photon conversions.

Photon Conversion Correction

The same disagreement observed between measurement and prediction of the simulation for the rate of selected photon conversions can be assumed to be evolving out of the sample of photon conversions which is not selected, if the ability to resolve two spatially close tracks from each other is reproduced by the Monte Carlo simulation of the detector response. This is tested in a crude way with the selected photon conversion sample by investigating the point on the conversion tracks at which they split, *i.e.* where the track finding algorithm is able to separate one track from the other (see figure 4.16). Since the track reconstruction attaches a hit only to one track, this point in space is equivalent to the difference of the track lengths determined by the track fit. If the difference

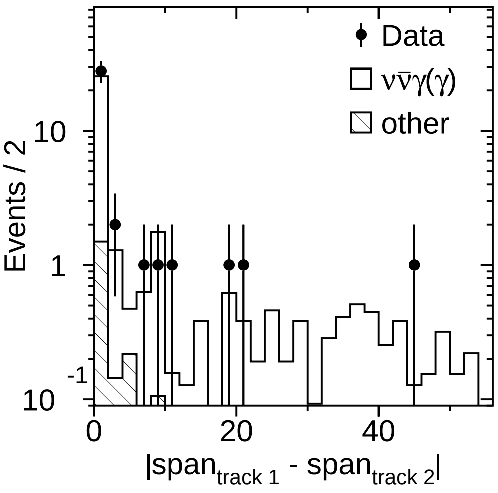

Figure 4.17: *Difference of the span of the two tracks belonging to a converted photon. Simulation is normalised to data.*

in length of the two tracks belonging to a converted photon is, statistically, the same in data and simulation the separation power for spatially close tracks should then be the same. This difference is shown in terms of the difference of the span of the two tracks in figure 4.17. Here, the shape of the distributions and not the absolute normalisation is important, and therefore the simulation is for this purpose normalised to data. Due to the limited statistics, a firm conclusion cannot be drawn, although a tendency towards larger differences and thus a worse resolution in the simulation compared to data is likely but not statistically evident (*e.g.*, for Δspan $>$ 15, 3 events are measured in data with 6 events expected from the simulation, where the *total* expectation is normalised to data, see figure 4.17). In most cases the track lengths of electron-positron pairs are identical which manifests in the peak at zero in figure 4.17. Therefore, the difference in photon conversion rate between data and simulation of (2.0 ± 0.6)% is supposedly the same for the photon conversion rate with unresolved tracks within the quoted error. Monte Carlo simulation is consequently corrected to bring the additional efficiency loss for simulation into agreement with data. A systematic error as large as the error on the correction factor of 0.6% is assigned to the selection efficiency. Since for the low energy part of the selection photon conversion is not taken into account, the simulation is corrected accordingly to cure the discrepancy.

	$E_\gamma > 5$ GeV			$E_\gamma < 5$ GeV
	Total	Barrel	Endcap	
Data	572	297	275	395
$\nu\bar{\nu}\gamma(\gamma)$	567.3	288.9	278.4	48.7
$e^+e^-(\gamma)$	3.5	0.8	2.7	354.8
$\gamma\gamma(\gamma)$	1.7	1.0	0.7	0
$e^+e^-e^+e^-$	0	0	0	3.7
$e^+e^-\nu\bar{\nu}(\gamma)$	1.3	0.4	0.9	0
Cosmic background	3.1	1.1	2.0	3.6
Total expectation	576.9	292.2	284.7	410.8

Table 4.13: *Number of events selected in data, Monte Carlo predictions for the Standard Model processes and expectation of cosmic ray background contributing to the* 189 GeV *data set.*

4.9 Results of the Selection

After all cuts are described and corrections on the Monte Carlo simulation are computed, the selection results in terms of the number of events selected in data and predicted by the simulation are quoted. Due to different dominant contributions from Standard Model processes, the sample is subdivided into two parts. In the hard photon regime with $E_\gamma > 5$ GeV, $\nu\bar{\nu}\gamma(\gamma)$ production is the dominant process, whereas for lower photon energies very low angle radiative Bhabha scattering yields the main contribution. Energy and angular distributions of the measured photon events are shown in figure 4.18. The figures show the inclusive measurement with *at least one* photon selected and not exactly one, *i.e.* events with more than one photon (also see below) are included. The low energy region (figures 4.18(e) and 4.18(f)) stretches only over the barrel because of the trigger threshold of $\sim$6 GeV in the endcaps (see section 4.5). The corresponding event rates are listed in table 4.13 for data and Monte Carlo predictions of the various processes contributing within the different kinematic regions. In general, an excellent agreement between measurement and prediction of the Standard Model within the statistics must be stated, and no hint for new physics processes contributing to the data is observable. Only a slight disagreement in the energy

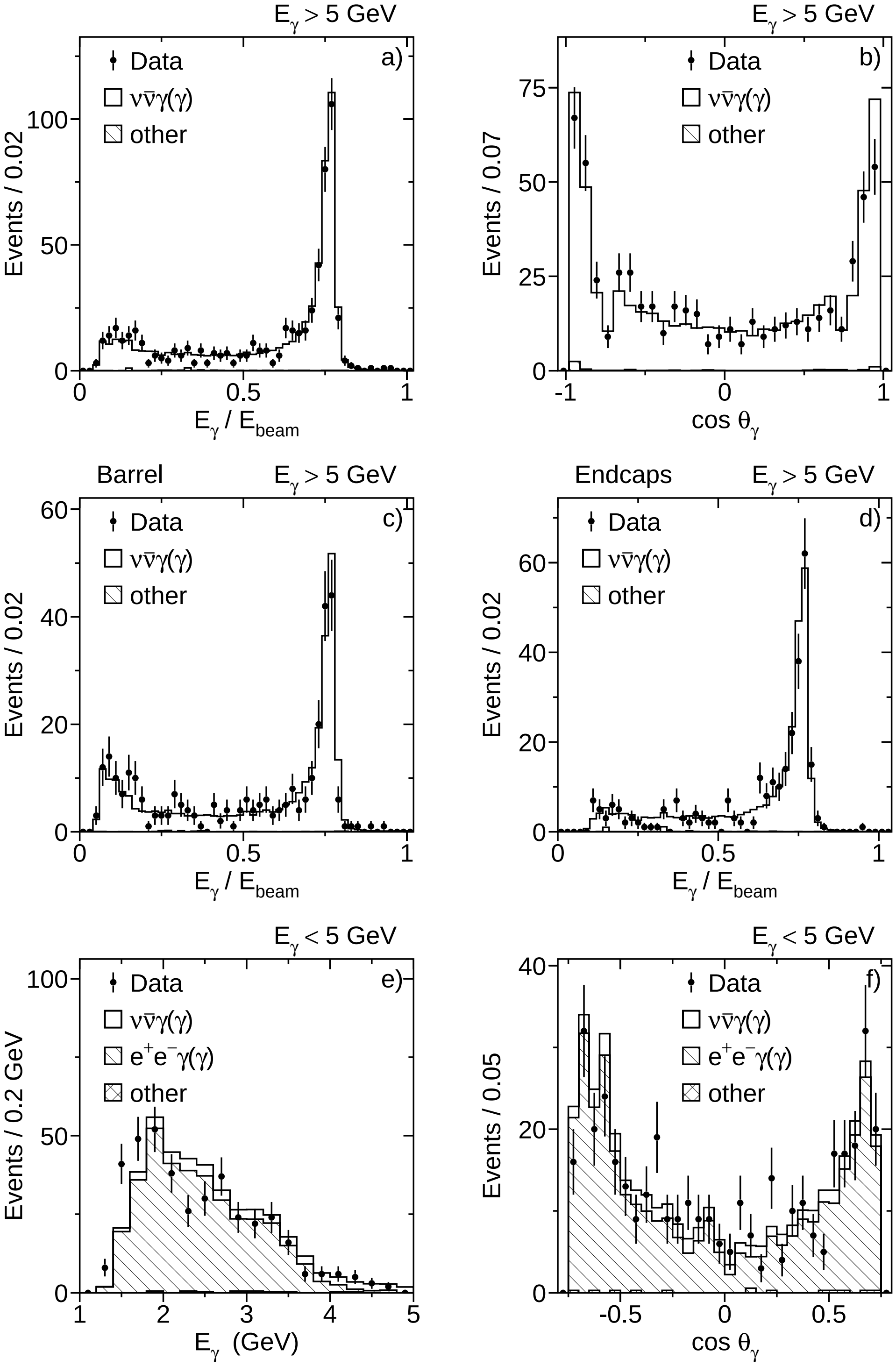

Figure 4.18: *Distributions of hard photon selection (a–d) and soft photons (e,f) for* $\sqrt{s} = 189$ GeV.

$E_{\gamma_1} > 5$ GeV, $E_{\gamma_2} > 1$ GeV					
	Total	γ_1 in Barrel γ_2 in Barrel	Barrel Endcap	Endcap Barrel	Endcap Endcap
Data	21	4	3	4	10
$\nu\bar{\nu}\gamma\gamma(\gamma)$	35.5	7.9	9.7	8.6	9.2
$e^+e^-(\gamma)$	0.1	0	0	0.1	0
$\gamma\gamma(\gamma)$	0.5	0	0.2	0.2	0.1
$e^+e^-e^+e^-$	0	0	0	0	0
$e^+e^-\nu\bar{\nu}(\gamma)$	0.1	0.1	0	0	0
Cosmic background	0	0	0	0	0
Total expectation	36.2	8.0	9.9	8.9	9.3

Table 4.14: *Number of events found in the multi-photon selection in data, Monte Carlo predictions for Standard Model processes and cosmic ray background, that contribute to the* 189 GeV *data set.*

distribution for low energy photons at energies around 1.5 GeV is apparent. The purity of 98% in the high energy region for $\nu\bar{\nu}\gamma(\gamma)$ events is extraordinarily high.

Two typical event pictures are shown in figure 4.19. In figure 4.19(a), a high energetic photon is detected in the endcap. Some HCAL energy behind the photon bump is measured originating from leakage through the BGO, and, furthermore, a small amount of detector noise (see section 4.3) in the other HCAL endcap and in the SPACAL is visible. Figure 4.19(b) shows besides a 46 GeV photon another, very small, energy deposition in the BGO.

Multi-Photon Subsample

For the multi-photon subset, in addition to one photon with more than 5 GeV energy, a second photon with energy greater than 1 GeV is required. The selected sample is dominated by the contribution of the $\nu\bar{\nu}\gamma\gamma(\gamma)$ reaction. The distributions of recoil mass, invariant mass and transverse momentum of the multi-photon system, energy spectra of both photons, and $\cos\theta_{\text{miss}}$ distribution are all shown in figure 4.20. Corresponding event rates are listed in table 4.14 for selected data and Standard Model prediction. An event picture of a two-photon event is shown in figure 4.1. A discrepancy of about 2.5σ between measured

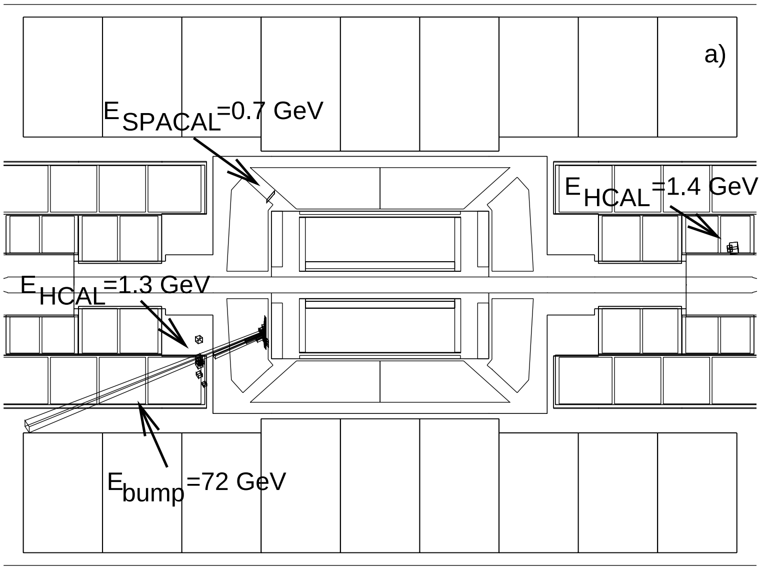

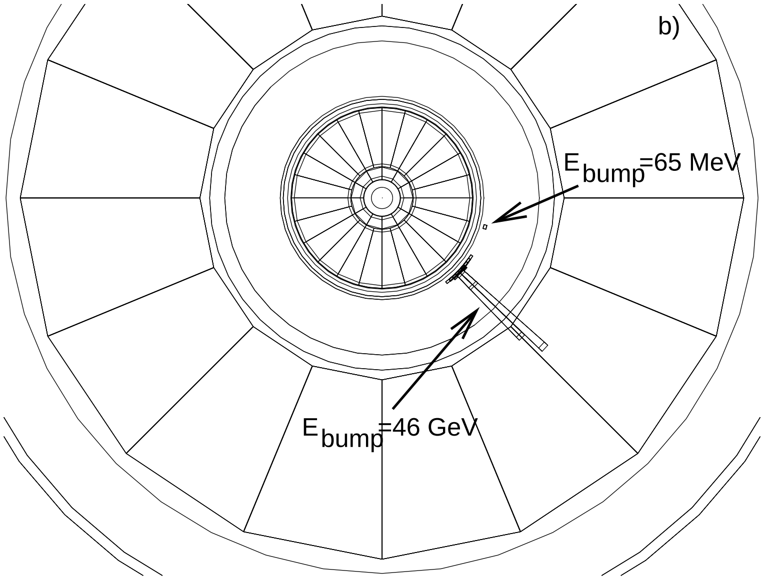

Figure 4.19: *Picture of a single photon event showing a high energetic photon in the endcap with energy leakage into the HCAL behind the bump and two energy clusters from detector noise (a). Picture of another single photon event measured in the barrel with a second energy deposition in the BGO (b).*

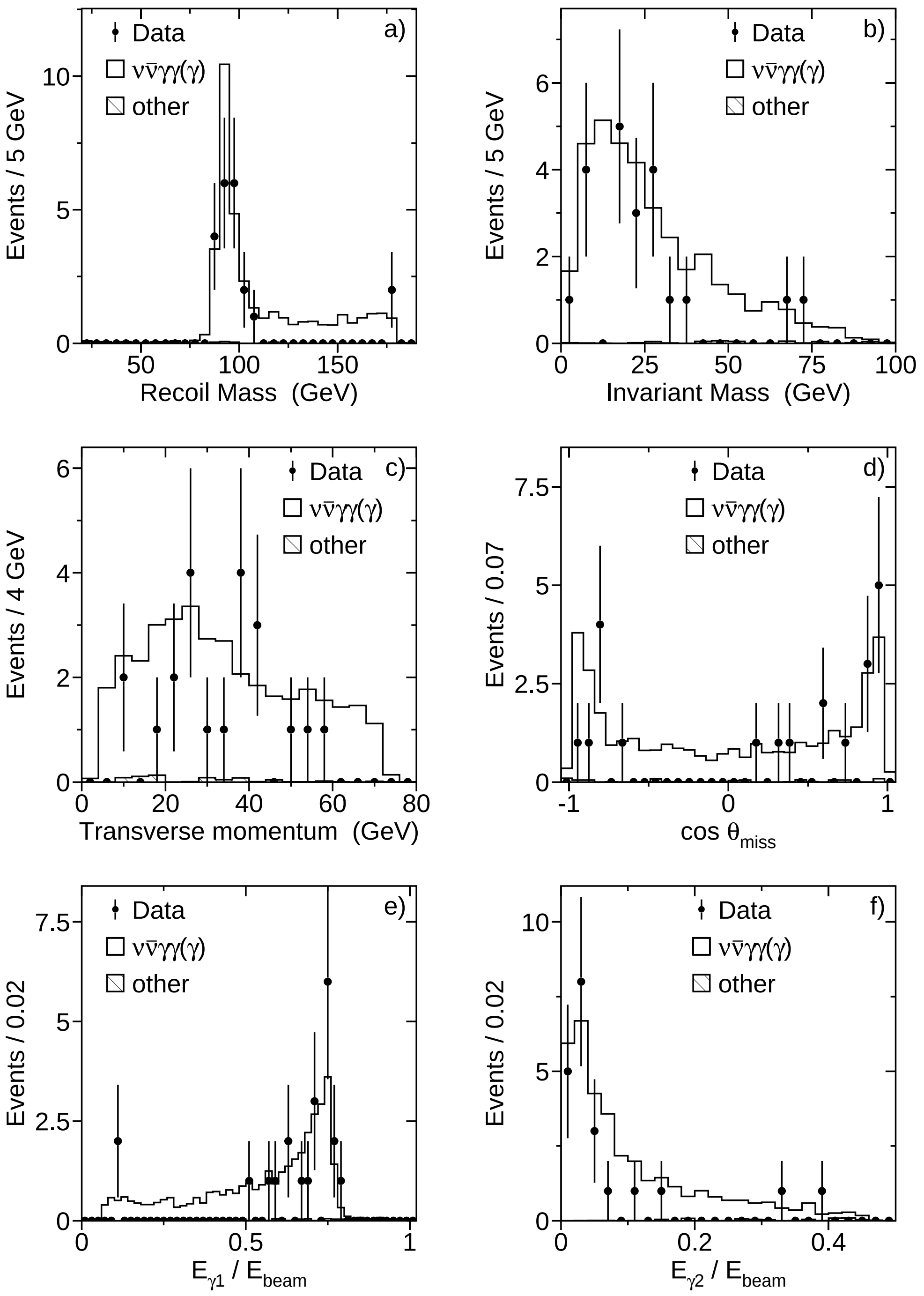

Figure 4.20: *Distributions of recoil (a) and invariant mass (b), transverse momentum of the multi-photon system (c),* $\cos\theta_{\text{miss}}$ *(d), and energies of both photons where* $E_{\gamma_1} > E_{\gamma_2}$ *(e,f) for* $\sqrt{s} = 189$ GeV.

data and prediction of the Standard Model is apparent. It is not located in a certain region of any of the kinematic variables displayed in figure 4.20, except for the recoil mass where the peak region shows a fair agreement, and data events are missing in the tail of large recoil masses. None of the studies performed in the previous sections has shown any anomaly that could create such an effect solely for the multi-photon signature and hidden for the single photon events. Moreover, the theoretical uncertainty on the $\nu\bar{\nu}\gamma\gamma(\gamma)$ production cross section estimated to be 5% (appendix B) cannot accommodate such a big effect. The discrepancy is therefore regarded as a statistical fluctuation as far as new physics interpretations (see chapter 5) are concerned.

Chapter 5

Physics with Photons

In this chapter the results obtained by the single and multi-photon selections presented in the previous chapter are examined to derive physical observables within the framework of the Standard Model in a first step (section 5.1). In the second part limits on processes and particle masses within the various supersymmetric scenarios (sections 5.2 to 5.5), fermiophobic Higgs bosons (section 5.6) and low scale gravity models (section 5.7) introduced in chapter 2 are calculated.

5.1 Neutrino Production

Measurement and interpretation of neutrino pair-production in electron-positron interactions accompanied by initial state radiation is the focus of this section's analysis. The first part is concerned with the measurement of the production cross section for the $\nu\bar{\nu}\gamma(\gamma)$ final state. Here, at least one photon is required to be measured in the acceptance to tag the event. After that, the measured $\nu\bar{\nu}\gamma(\gamma)$ cross section is extrapolated to the total neutrino-pair cross section without the photon requirement. In the second part of this section, the measured energy spectra are used to derive the number of light neutrino families by comparing the result with predictions under the hypothesis of different numbers of neutrino species. Within this section, only events with a photon energy exceeding 5 GeV are used, since below 5 GeV the purity of the $\nu\bar{\nu}\gamma(\gamma)$ sample becomes substantially worse due to the dominant background from radiative low angle Bhabha scattering.

5.1.1 Neutrino Pair-Production Cross Section

The cross section of a reaction is determined by the number of events belonging to the process under investigation, the selection efficiency ϵ, and the luminosity $\mathcal{L}$ as formulated in equation 3.3. However, since the selected data sample is not free of background, the number of measured events, N_{data}, needs to be corrected for by the expected number of background events, N_{bg}, determined by Monte Carlo simulation. Hence, the formula to compute the cross section $\sigma_{\nu\bar{\nu}\gamma(\gamma)}$ reads

$$\sigma_{\nu\bar{\nu}\gamma(\gamma)} \;=\; \frac{N_{\mathrm{data}} - N_{\mathrm{bg}}}{\mathcal{L}\,\epsilon}. \tag{5.1}$$

The ingredients to calculate $\sigma_{\nu\bar{\nu}\gamma(\gamma)}$ at the individual centre-of-mass energies have been derived before – and are listed in tables 3.1 (luminosity), 4.13 and C.8 (data and background numbers), respectively – except for the selection efficiency. All input variables in equation 5.1 evoke an uncertainty which propagates to the cross section determination. At first, a distinction between statistical and systematic error on $\sigma_{\nu\bar{\nu}\gamma(\gamma)}$ is made, where the error on N_{data} is purely statistical following Poisson statistics, and the errors on N_{bg}, $\mathcal{L}$, and ϵ are systematic.

Efficiency

Since first the cross section for neutrino pair-production accompanied by a photon shall be computed, the efficiency is estimated within an acceptance defined as

$$\begin{array}{rcl} E_\gamma & > & 5\ \mathrm{GeV} \\ |\cos\theta_\gamma| & < & 0.97\,. \end{array} \tag{5.2}$$

It is determined by Monte Carlo simulation of the $\nu\bar{\nu}\gamma(\gamma)$ process for $N_\nu = 3$, simulation of the detector response and by applying additional corrections as discussed in detail in chapter 4. The systematic uncertainty on the efficiency calculation is composed of the error caused by the limited amount of Monte Carlo statistics, the photon identification (see section 4.1), and, furthermore, the corrections that had to be installed in regard to imperfect simulation of detector noise (section 4.3 and 4.7), and photon conversion (section 4.8). The corresponding numbers are listed in table 5.1 for all six centre-of-mass energies investigated.

	$\sqrt{s}$ (GeV)					
	189	183	172	161	136	130
$\nu\bar{\nu}\gamma(\gamma)$ Efficiency	0.6077	0.6208	0.6054	0.6035	0.5616	0.6067
MC statistics	0.0021	0.0036	0.0047	0.0065	0.0204	0.0190
Photon identification	0.0034					
Noise correction	0.0007	0.0011	0.0025	0.0022	0.0026	0.0023
μfit correction	0.0018	0.0032	0.0071	0.0077	0.0105	0.0127
γ conversion cor.	0.0060					
Total error	0.0075	0.0085	0.0112	0.0124	0.0241	0.0240

Table 5.1: *Selection efficiencies for $\nu\bar{\nu}\gamma(\gamma)$ production with $N_\nu = 3$ at the different centre-of-mass energies and systematic errors.*

$\nu\bar{\nu}\gamma$ Cross Section

After that, the cross section for $e^+e^- \to \nu\bar{\nu}\gamma(\gamma)$ is calculated, and results for the different centre-of-mass energies are listed in table 5.2 together with the prediction of the Standard Model $\sigma^{\mathrm{theory}}_{\nu\bar{\nu}\gamma(\gamma)}$ for $N_\nu = 3$, the statistical error $\delta\sigma_{\mathrm{stat}}$, the systematic errors $\delta\sigma_{\mathrm{bg}}$, $\delta\sigma_{\mathcal{L}}$, $\delta\sigma_\epsilon$ – yielding $\delta\sigma_{\mathrm{sys}}$ – and the total error $\delta\sigma_{\nu\bar{\nu}\gamma(\gamma)}$ on the cross section. The measured cross sections are displayed graphically in figure 5.1 versus centre-of-mass energy together with the prediction of the Standard Model. Predictions on the cross section for only two or even four generations of light neutrinos are also shown to indicate the sensitivity on that quantity. This will be exploited quantitatively in the next section.

$\nu\bar{\nu}$ Cross Section

Finally, the cross section within the acceptance given by expressions 5.2 is extrapolated to the total cross section of $e^+e^- \to \nu\bar{\nu}(\gamma)$ via

$$\sigma_{\nu\bar{\nu}\gamma(\gamma)} \; = \; \epsilon_{\mathrm{t}} \; \sigma_{\nu\bar{\nu}(\gamma)} \tag{5.3}$$

with the conversion factor

$$\epsilon_{\mathrm{t}} \; = \; \frac{\sigma^{\mathrm{theory}}_{\nu\bar{\nu}\gamma(\gamma)}}{\sigma^{\mathrm{theory}}_{\nu\bar{\nu}(\gamma)}} \, , \tag{5.4}$$

(pb)	$\sqrt{s}$ (GeV)					
	189	183	172	161	136	130
$\sigma_{\nu\bar{\nu}\gamma(\gamma)}$	5.25	5.74	8.58	8.41	12.05	11.93
$\sigma^{\text{theory}}_{\nu\bar{\nu}\gamma(\gamma)}$	5.28	5.54	6.35	7.46	12.54	14.82
$\delta\sigma_{\text{stat}}$	0.22	0.41	1.19	1.18	2.00	1.85
$\delta\sigma_{\text{bg}}$	0.02	0.04	0.12	0.23	0.48	0.29
$\delta\sigma_{\mathcal{L}}$	0.01	0.02	0.06	0.06	0.05	0.05
$\delta\sigma_{\epsilon}$	0.06	0.08	0.16	0.18	0.54	0.48
$\delta\sigma_{\text{sys}}$	0.07	0.09	0.21	0.30	0.72	0.56
$\delta\sigma_{\nu\bar{\nu}\gamma(\gamma)}$	0.23	0.42	1.21	1.22	2.12	1.93

Table 5.2: *Cross sections of* $e^+e^- \to \nu\bar{\nu}\gamma(\gamma)$ *measured at the indicated centre-of-mass energies and cross section errors.*

	$\sqrt{s}$ (GeV)					
	189	183	172	161	136	130
ϵ_{t}	0.0901	0.0928	0.0982	0.1046	0.1210	0.1246
$\sigma^{\text{theory}}_{\nu\bar{\nu}(\gamma)}$ (pb)	58.6	59.8	64.6	71.4	103.6	118.9
$\sigma_{\nu\bar{\nu}(\gamma)}$ (pb)	58.3	61.8	87.3	80.4	99.5	95.8
$\delta\sigma_{\nu\bar{\nu}(\gamma)}$ (pb)	2.7	4.6	12.3	11.7	17.6	15.5

Table 5.3: *Cross sections of* $e^+e^- \to \nu\bar{\nu}(\gamma)$ *measured at the indicated centre-of-mass energies and conversion factor* ϵ_{t} *defined in equation 5.4.*

where the theoretical prediction is computed for $N_\nu = 3$. The conversion factor is determined by the theory and incorporates the fraction of events with initial state radiation inside the acceptance of expression 5.2 to the total $\nu\bar{\nu}(\gamma)$ sample. A theoretical uncertainty on the $\nu\bar{\nu}\gamma(\gamma)$ cross section calculation of 1% (appendix B and [41]) to be assigned to the conversion factor ϵ_{t} is taken into consideration. The calculated numbers are listed in table 5.3 and are presented in figure 5.1 together with a number of measurements carried out by L3 at LEP 1 energies [187–189].

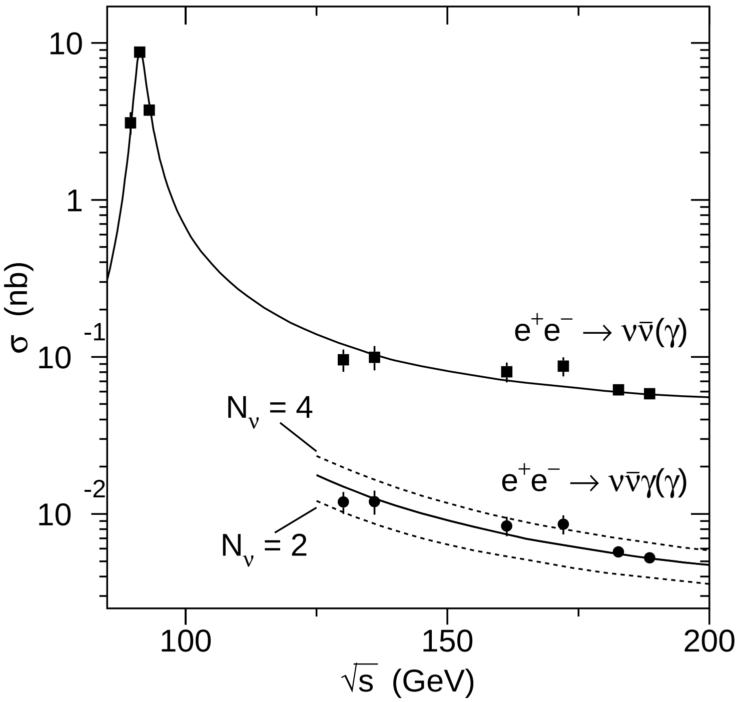

Figure 5.1: *Production cross section of* $\mathrm{e^+e^-} \to \nu\bar{\nu}(\gamma)$ *and* $\mathrm{e^+e^-} \to \nu\bar{\nu}\gamma(\gamma)$ *as function of centre-of-mass energy. Dots with error bars represent* $\nu\bar{\nu}\gamma(\gamma)$ *measurements and squares with error bars are the extrapolation to* $\nu\bar{\nu}(\gamma)$*. Full lines are theoretical predictions for* $N_\nu = 3$ *and dashed lines are predictions for* $N_\nu = 2, 4$ *as indicated.*

5.1.2 Determination of the Number of Neutrino Families

The determination of the number of light neutrino species is straightforward because of the linear dependence of the cross section on the number of families as can be seen in equation 2.12 of chapter 2. The measured photon energy spectrum is compared to the theoretical predictions for $N_\nu = 1 \ldots 5$ (figure 5.2(a) only showing $N_\nu = 2, 3, 4$). Due to the different contributions to the energy spectrum from $\nu_\mathrm{e}\bar{\nu}_\mathrm{e}$ t–channel production via W exchange and $\nu\bar{\nu}$ s–channel production via Z exchange, this method is more powerful than using the total cross section measurement. It is also more correct, because the efficiency entering the cross section measurement is determined only for $N_\nu = 3$. The efficiency is a function of photon energy and the photon energy distribution depends on N_ν (see figure

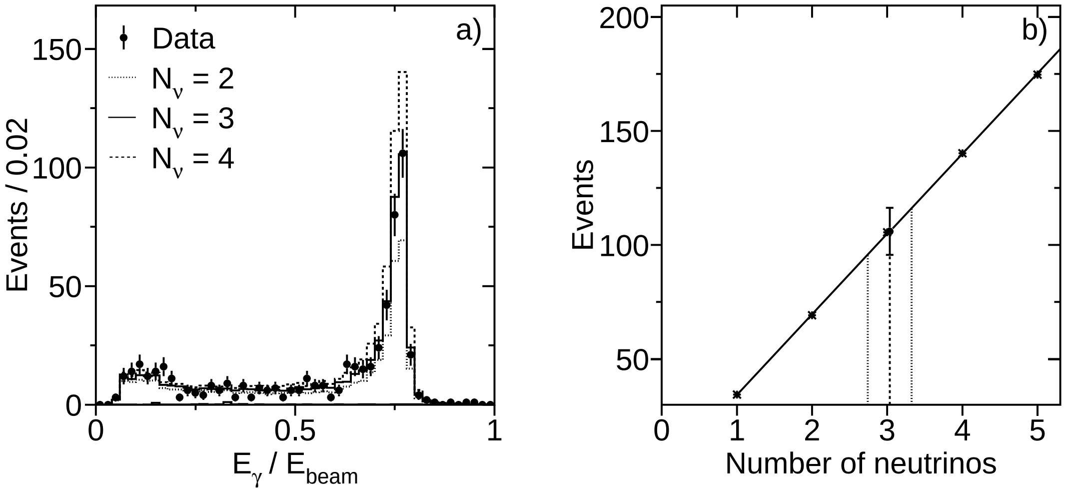

Figure 5.2: *Photon energy spectrum with theoretical predictions for* $N_\nu = 2, 3, 4$ *(a) and number of photon events versus number of neutrinos (b) for the peak point of (a).*

5.2(a)), and thus the cross section measurement is already biased towards $N_\nu = 3$.

Technically, a straight line fit through the five theoretically predicted points for N_ν from one to five is performed for each energy interval; as example the result for the most sensitive interval in the peak is displayed in figure 5.2(b). In addition, the measured number of events with statistical error is displayed on the line, and in this way the (fractional) number of neutrino generations N_ν^i is computed for each energy interval i. In the same manner the statistical error on the number of events measured translates into a statistical error on N_ν^i. Finally, N_ν is computed by the weighted average over all intervals, taking into account the expected error for the average number.

Systematics

To estimate the systematic error on the measurement of the number of light neutrino generations, the total systematic error listed in table 5.2 is added to the theoretical expectation for the number of photon events. Moreover, the theoretical uncertainty on the photon energy spectrum estimated in appendix B and displayed graphically in figure B.1(a), is taken into account by adding the computed theoretical error for each energy interval separately to the expectations

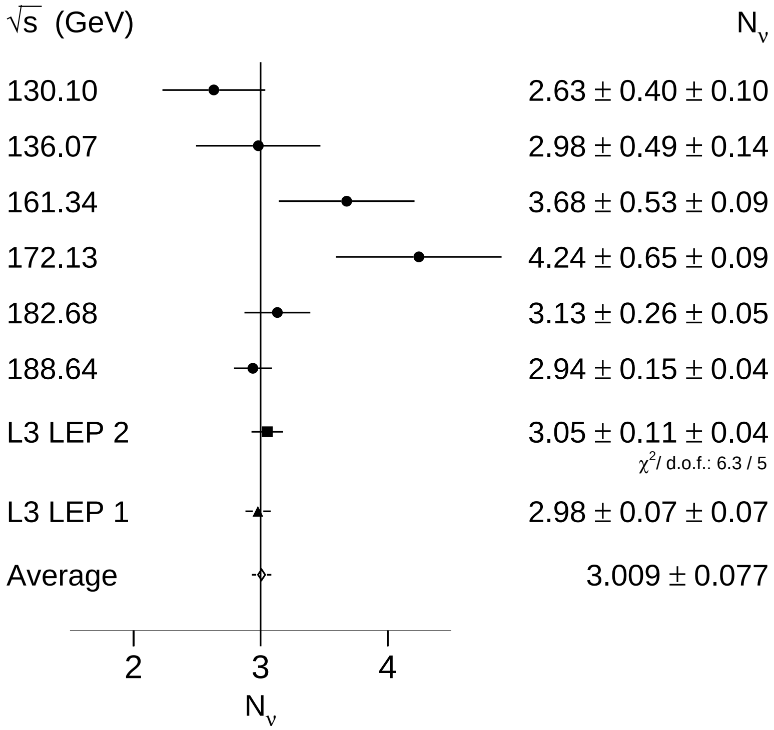

Figure 5.3: *Number of neutrino families and L3 averages with statistical (first) and systematic (second) errors measured from single photon events at LEP 2 and LEP 1.*

for the number of events. The difference of the number of neutrino species calculated in this way to the value without systematic errors determines the total systematic error on the number of light neutrino flavours. The impact of the theoretical uncertainty on the photon energy distribution on the number of neutrinos derived in this way is estimated to be 0.6%.

Results

A compilation of the results for each centre-of-mass energy appears in figure 5.3, where the combined number of light neutrino species for the various centre-of-mass energies of the LEP 2 phase is represented, too. To determine the systematic error on the average LEP 2 value, the systematic error sources are split into two categories: Systematics independent for each centre-of-mass energy and systematics which are fully correlated for the different data taking periods. The independent systematics consisting of all sources listed in tables 5.1 and 5.2, except for errors on photon identification and photon conversion correction, can safely be combined. They are studied for each centre-of-mass energy independently (see also appendix C). Clearly, the systematics 100% correlated over the centre-of-mass energies, which include in addition to photon identification error and photon conversion correction error also the theoretical uncertainty on the energy spectrum, cannot be combined. They remain as systematic error, however, on the average value for the number of light neutrino generations. The number of light neutrino species derived by this measurement is

$$N_\nu \;=\; 3.05 \pm 0.11(\mathrm{stat}) \pm 0.04(\mathrm{sys})\,. \tag{5.5}$$

This measurement is valid only for light neutrinos ($m_\nu < m_\mathrm{Z}/2$), because the greatest contribution stems from the radiative return peak, where an on-shell Z decays into two neutrinos. A feasibility study concerning heavy neutrinos is performed in appendix A.

The precision of the LEP 2 measurement is comparable with the L3 single photon measurement from the LEP 1 phase [189], and thus the two values are combined as indicated in figure 5.3. Systematic errors of the LEP 1 measurement stated in [189] are independent of the systematics entering this measurement. For comparison, the indirect L3 measurement from the invisible width of the Z boson [190] equals $N_\nu = 2.977 \pm 0.014$.

5.2 Calculation of Limits on New Physics

No statistically significant excess of selected data is observed over the amount expected from Standard Model processes, neither in the single photon nor in the multi-photon spectra. Here and in the following, it is assumed that the Standard Model possesses three light neutrino species and three fermion generations. The lack of new physics is quantified in terms of upper limits on event rates of new particle processes. The method used to determine upper limits does not impose further requirements on physics quantities, but rather than that a likelihood is constructed using a distribution discriminating the expected new physics signal from Standard Model background. The way to proceed if more than one variable is at hand to discriminate signal from background processes is explained in section 5.4.1. In this way the full information on the signal is used and even regions with lower signal over background ratio, which otherwise are possibly cut away, can contribute – much less though – to the exclusion. Based on Poisson statistics for the number of observed data events this likelihood function is defined as [191]

$$\mathcal{L}(s) \;=\; \prod_{i=1}^{n} \frac{\mathrm{e}^{-(s_i+b_i)}(s_i+b_i)^{N_i}}{N_i!}\,. \tag{5.6}$$

The product runs over n intervals of the discriminating distribution; N_i, s_i, and b_i are the number of events in data and expected from signal and background processes, respectively, in the ith interval. The total number of signal events s is determined by

$$s \;=\; \sum_{i=1}^{n} s_i\,. \tag{5.7}$$

If no excess in signal regions is observed in data, the likelihood has its maximum at $s = 0$. To derive a confidence level CL for the exclusion of a signal process, first an estimator X_{obs} based on Bayesian probability is formed through [191]

$$X_{\text{obs}}(s) \;=\; \frac{\int_s^\infty \mathcal{L}(x)dx}{\int_0^\infty \mathcal{L}(x)dx}\,. \tag{5.8}$$

The test-statistic X_{obs} measured in data is compared to distributions of the same test-statistic obtained on the basis of a large number, n_{MC}, of reference Monte Carlo experiments in which the presence of a signal is assumed in addition to the background $(s+b)$. Here, the number of outcomes in which $X_{s+b} \leq X_{\text{obs}}$ is counted. After that, the probability to obtain $X_{s+b} \leq X_{\text{obs}}$ is calculated by [192]

$$\mathcal{P}(X_{s+b} \leq X_{\text{obs}}) \;=\; \frac{n_{X_{s+b}\leq X_{\text{obs}}}}{n_{\text{MC}}}\,. \tag{5.9}$$

To determine the probability to exclude a signal in the framework of classical statistics, the probability defined in equation 5.9 needs to be normalised by the probability under the hypothesis of background only being present in the data $\mathcal{P}(X_b \leq X_{\text{obs}})$. The confidence level corresponding to the probability to exclude a signal is given by [192]

$$\text{CL}(s) \;=\; 1 - \frac{\mathcal{P}(X_{s+b} \leq X_{\text{obs}})}{\mathcal{P}(X_b \leq X_{\text{obs}})}\,. \tag{5.10}$$

The distribution of the estimator for the reference Monte Carlo experiments under the background-only hypothesis is used to evaluate the probability of an observed exclusion as well as the average upper limit on the number of signal events expected in the absence of a signal. Exclusions on the number of signal events are determined at the 95% confidence level and are in general transformed into exclusions on the signal cross section using equation 3.3.

Systematics

Systematic errors on the signal and background expectations are taken into account during the generation of Monte Carlo experiments [191]. In each trial experiment, candidate events are generated according to the signal and background distributions smeared to account for the systematic error on the efficiency and the normalisation. A Gaussian distribution with the number of signal and background events, respectively, as mean, and their systematic error as standard deviation is assumed for the smearing. For the calculation of the observed estimator in equation 5.6, however, the nominal expected signal and background numbers are used.

Data Sample

To derive limits on new physics processes within the various frameworks defined in chapter 2, the 189 GeV data sample is analysed. It provides by far the largest sensitivity on processes where new particles are potentially produced since both, statistics and centre-of-mass energy, reached the highest values for this data set compared to previous ones (see table 3.1). However, searches for new physics in single and multi-photon events in data samples with $\sqrt{s} \leq 183$ GeV are published [193–195], but results are superseded by limits presented in the following sections. Moreover, further studies not published for $\sqrt{s} \leq 183$ GeV are carried out.

5.3 Interpretations in Models with Superlight Gravitinos

Theoretical scenarios which can lead to superlight gravitinos are outlined in section 2.2.5. Both processes discussed in this section – $\tilde{\mathrm{G}}\tilde{\mathrm{G}}\gamma$ and $\tilde{\chi}^0_1\tilde{\mathrm{G}}$ production – leave a single or multi-photon signature in the detector. To derive upper limits on the number of events, the low and high energy parts of the photon spectra are merged (figures 4.18(a) and (e)), and the energy spectra obtained in this way for data, Standard Model background and SUSY signal are compared using the method described above.

5.3.1 Gravitino Pair-Production

The process $\mathrm{e}^+\mathrm{e}^- \rightarrow \tilde{\mathrm{G}}\tilde{\mathrm{G}}\gamma$ is simulated with the Monte Carlo generator `SLG` [196], which is based on formulae in [106] taking into account the emission of only one photon. Altogether, 10000 Monte Carlo events are generated with a minimum photon energy of 1 GeV and a minimum angle with respect to the beam axis of 10°. Within these acceptance cuts an efficiency of 27.5% is obtained using the same selection criteria as described in chapter 4.

An upper limit on the number of events from this process at $\sqrt{s} = 189$ GeV of 52.3 events is derived leading to an upper limit on the production cross section of 1.08 pb. The probability to achieve a higher limit than the observed one is 88%, and consequently the average upper limit on the number of events computed in Monte Carlo experiments with background only of 37.2 events is better than the observed one. This difference can be understood when examining the most sensitive region in the energy spectrum for this process, which is the part between photon energies of 5 GeV and 15 GeV (see figure 4.18(a)), where some excess of data compared to the prediction from Standard Model background sources – mainly $\nu\bar{\nu}\gamma$ – is evident. Below 5 GeV the background increases rapidly, and above about 15 GeV the signal decreases (see figure 2.21), yielding a smaller sensitivity.

Within the framework described in [106], the production cross section depends solely on the scale of supersymmetry breaking $\sqrt{F}$. Therefore, the cross section limit is translated into a lower limit on $\sqrt{F}$ of 192.3 GeV. Via equation 2.25 a lower limit on the gravitino mass of

$$m_{\tilde{\mathrm{G}}} \ > \ 8.9 \cdot 10^{-6} \text{ eV} \tag{5.11}$$

is derived at the 95% confidence level. The average lower limit for the gravitino mass corresponding to the average upper limit on the number of events (see above) yields $9.7 \cdot 10^{-6}$ eV.

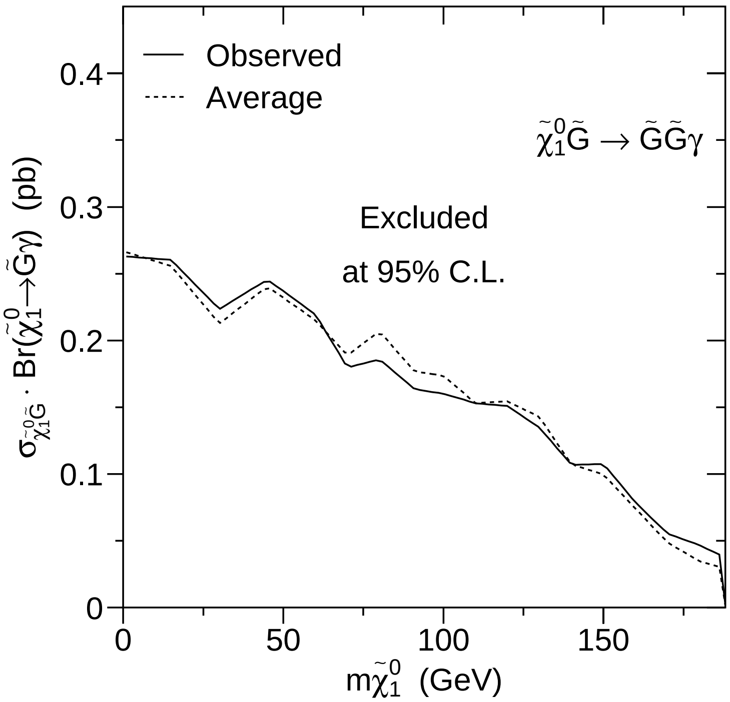

Figure 5.4: *Upper limit on the production cross section for the process* $e^+e^- \to \tilde{\chi}^0_1\tilde{G} \to \tilde{G}\tilde{G}\gamma$ *(solid line) and average limit (dashed line) obtained using Monte Carlo experiments with background only at* $\sqrt{s} = 189$ GeV.

5.3.2 Gravitino-Neutralino Production

If the lightest neutralino has a mass smaller than the centre-of-mass energy and the gravitino is superlight, the associated production of gravitino and neutralino – explained in section 2.2.5 – has a sizable cross section. If the neutralino has a non-vanishing photino component, the radiative decay to gravitino and photon is enhanced as discussed in detail in section 2.2.3. The `SUSYGEN` Monte Carlo program is used to simulate this process for several different neutralino masses, as listed in table 5.4 together with the number of events simulated for each mass point and the selection efficiency. As in the previous subsection, upper limits on the number of events are derived using the full information of the photon energy spectra applying the method described in section 5.2. Observed and expected limits on event rates and cross sections are enumerated in table 5.4 for the individual mass points and graphically shown in figure 5.4 for the cross

$m_{\tilde{\chi}_1^0}$ (GeV)	N_{MC}	ϵ (%)	N_{limit}	$\sigma_{\mathrm{limit}}^{\mathrm{obs}}$ (pb)	$\sigma_{\mathrm{limit}}^{\mathrm{average}}$ (pb)
188	798	79.2	5.3	0.038	0.029
180	818	76.7	6.3	0.047	0.035
170	857	75.8	7.4	0.055	0.049
160	874	76.2	10.6	0.079	0.074
150	905	75.6	14.3	0.108	0.100
140	903	76.5	14.4	0.107	0.107
130	934	74.7	17.8	0.135	0.143
120	965	75.6	20.1	0.151	0.154
110	985	75.5	20.4	0.153	0.153
100	983	73.6	20.8	0.160	0.174
91	1000	72.1	20.8	0.164	0.177
80	994	71.3	23.4	0.186	0.207
70	1000	70.9	22.5	0.180	0.189
60	996	70.1	27.1	0.220	0.215
45	994	64.6	28.0	0.246	0.240
30	996	67.6	26.6	0.223	0.213
15	996	64.9	29.8	0.260	0.256
0.5	994	63.8	29.6	0.263	0.267

Table 5.4: *Number of generated Monte Carlo events* N_{MC}*, selection efficiency* ϵ*, upper limits on number of events* N_{limit}*, cross section limit* $\sigma_{\mathrm{limit}}^{\mathrm{obs}}$*, and average limit on cross section expected in the absence of* $\mathrm{e^+e^-} \rightarrow \tilde{\chi}_1^0\tilde{\mathrm{G}} \rightarrow \tilde{\mathrm{G}}\tilde{\mathrm{G}}\gamma$ *at* $\sqrt{s}$ = 189 GeV *for indicated neutralino masses.*

section limit. Good agreement between observation and expectation is reflected by the general agreement between data and Standard Model prediction over the largest part of the energy spectrum.

LNZ Interpretation

Within the framework of the LNZ model (see section 2.2.5), the production cross section of $\mathrm{e^+e^-} \rightarrow \tilde{\chi}_1^0\tilde{\mathrm{G}}$ depends only on two free parameters chosen to be neutralino and gravitino mass. Hence, the attained cross section limits are transformed into an exclusion region in the $m_{\tilde{\mathrm{G}}}$ versus $m_{\tilde{\chi}_1^0}$ plane as shown in figure 5.5, where gravitino masses below 10^{-5} eV are excluded for neutralino

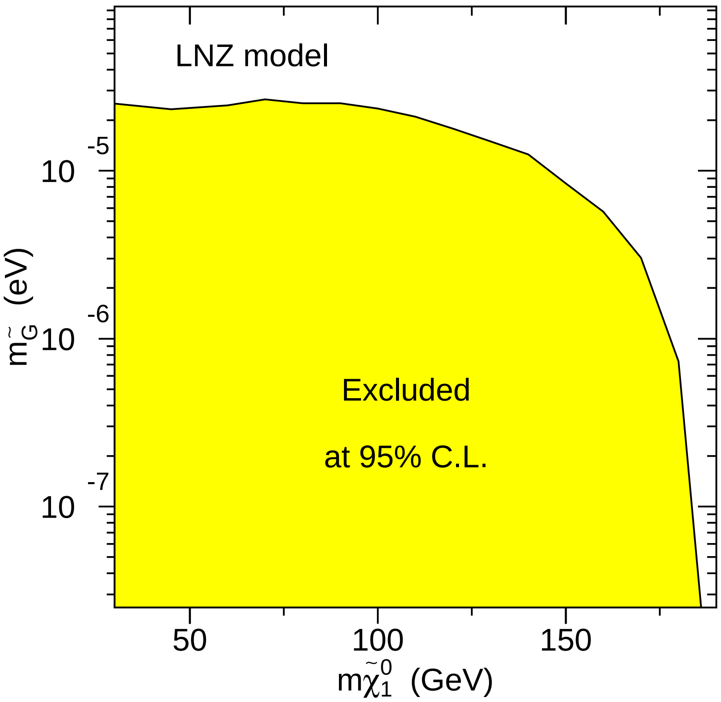

Figure 5.5: *Region excluded at the 95% confidence level within the LNZ model in the plane* $m_{\tilde{G}}$ *versus* $m_{\tilde{\chi}_1^0}$.

masses below 145 GeV. For this exclusion, prompt decay of the neutralino does not need to be assumed, since it is guaranteed throughout the excluded area (see figure 2.10).

5.4 Light Gravitinos and GMSB

In models with gauge-mediated supersymmetry breaking (GMSB) pair-production of neutralinos and their decay to gravitino and photon leads to a signature with two photons and missing energy in the final state as introduced in section 2.2.3. Besides GMSB models, more general SUSY scenarios can yield light gravitinos, thus making the same process possible to occur as shown in section 2.2.5. The first part of this section deals with the derivation of cross section limits and interpretations in general models with light gravitinos, whereas the second part is restricted to GMSB including model dependent mass limits on SUSY particles.

$m_{\tilde{\chi}_1^0}$ (GeV)	N_{MC}	ϵ (%)	N_{limit}	$\sigma_{\mathrm{limit}}^{\mathrm{obs}}$ (pb)	$\sigma_{\mathrm{limit}}^{\mathrm{average}}$ (pb)
94	996	61.9	3.00	0.027	0.029
90	992	60.8	3.15	0.029	0.032
85	998	62.0	3.70	0.034	0.035
80	988	61.4	3.28	0.030	0.037
75	990	61.5	3.45	0.032	0.037
70	988	60.9	3.00	0.028	0.038
60	994	61.6	3.31	0.031	0.039
45	992	59.1	3.60	0.035	0.045
30	984	53.3	4.82	0.051	0.053
15	994	44.0	3.40	0.044	0.063
0.5	988	17.4	3.02	0.098	0.125

Table 5.5: *Number of generated Monte Carlo events* N_{MC}*, selection efficiency* ϵ*, upper limits on number of events* N_{limit}*, cross section limit* $\sigma_{\mathrm{limit}}^{\mathrm{obs}}$*, and average limit on cross section expected in absence of* $\mathrm{e^+e^-} \to \tilde{\chi}_1^0\tilde{\chi}_1^0 \to \tilde{\mathrm{G}}\tilde{\mathrm{G}}\gamma\gamma$ *at* $\sqrt{s} = 189$ GeV *for indicated neutralino masses.*

5.4.1 Neutralino Pair-Production

The process $\mathrm{e^+e^-} \to \tilde{\chi}_1^0\tilde{\chi}_1^0 \to \tilde{\mathrm{G}}\tilde{\mathrm{G}}\gamma\gamma$ is modelled using the `SUSYGEN` Monte Carlo generator for several neutralino mass hypotheses as listed in table 5.5 together with the number of events produced for each mass point and the selection efficiency.

Final Discriminant

For multi-photon events a final discriminant variable is constructed [197, 198], where the energies of the two most energetic photons, their angles, recoil mass, and the angle of the missing momentum vector are combined. Distributions of input variables for data, Standard Model background, and two different neutralino masses – exemplarily chosen to be $m_{\tilde{\chi}_1^0} = 60$ GeV and $m_{\tilde{\chi}_1^0} = 90$ GeV – are shown in figure 5.6. To calculate the final discriminant, at first a probability density function f_j^i is computed for background and signal Monte Carlo processes – denoted by j – and each input quantity i by normalising the various spectra to

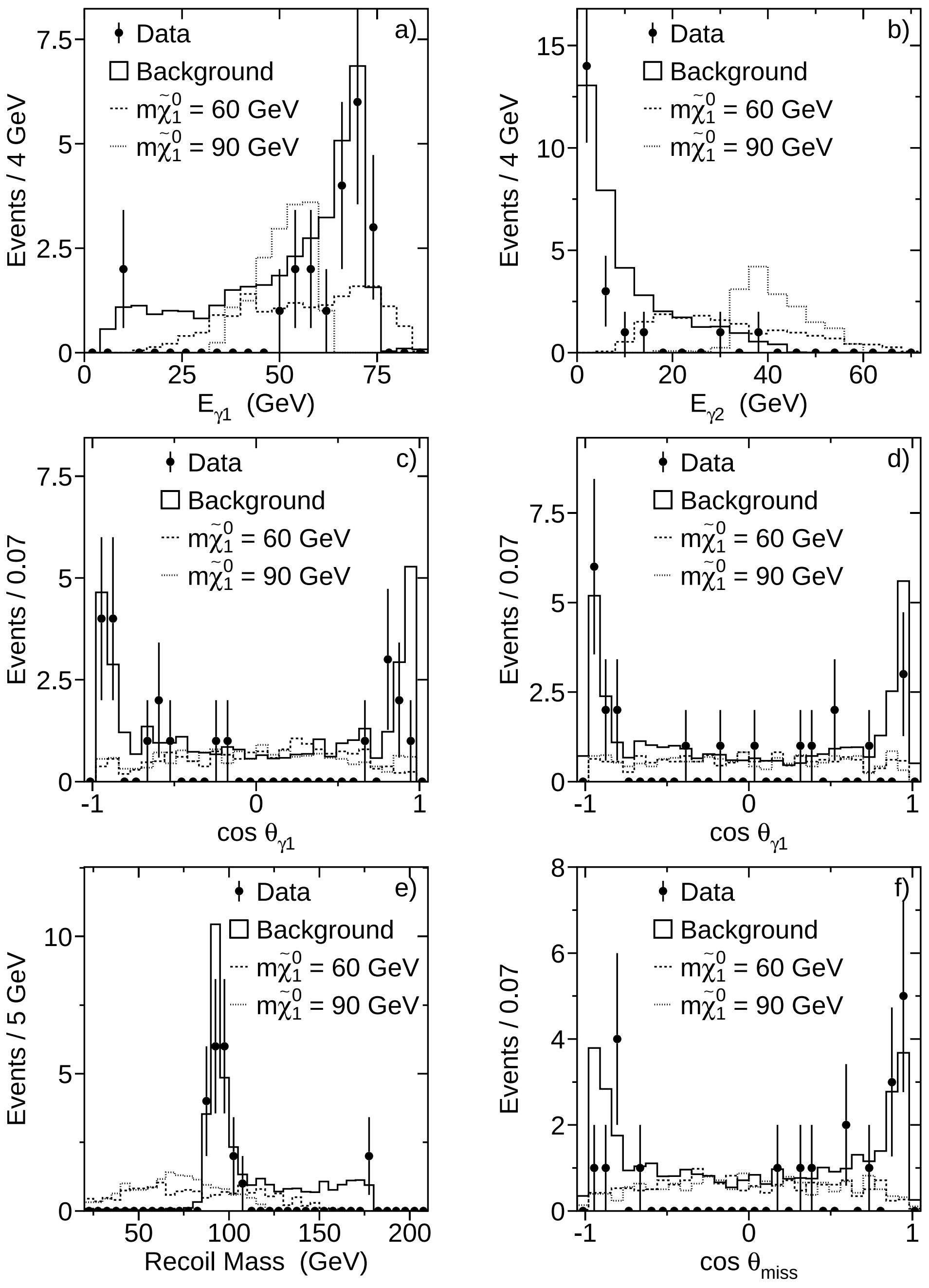

Figure 5.6: *Distributions used to construct the final discriminant for* $\tilde{\chi}^0_1\tilde{\chi}^0_1$ *production. Energy of the most energetic photon (a), energy of the second most energetic photon (b), their angles (c and d), recoil mass (e), and angle of missing momentum vector (f) at* $\sqrt{s}$ = 189 GeV*. Signal Monte Carlo events are normalised to correspond to a cross section of* 0.15 pb.

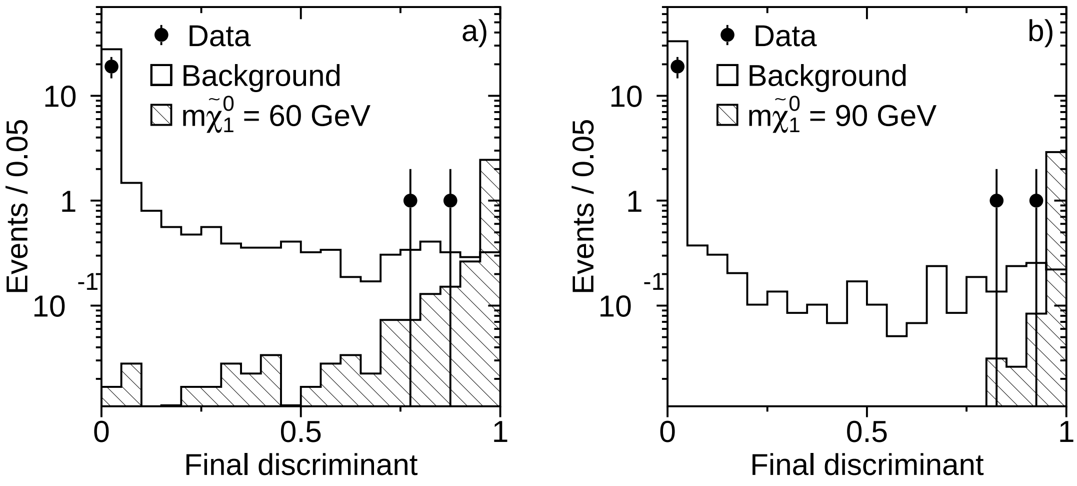

Figure 5.7: *Distributions of the final discriminant variable for* $\tilde{\chi}_1^0\tilde{\chi}_1^0 \rightarrow \tilde{G}\tilde{G}\gamma\gamma$ *with* $m_{\tilde{\chi}_1^0} = 60$ GeV *(a) and* $m_{\tilde{\chi}_1^0} = 90$ GeV *(b). The signal corresponds to the upper limits of* 3.31 *and* 3.15 *events, respectively, derived for these mass points.*

unity. Hereafter, the probability of an event to belong to process j based solely on the value of variable i is calculated by

$$p_j^i(x_i) = \frac{f_j^i(x_i)}{\sum_k f_k^i(x_i)}, \tag{5.12}$$

where x_i are measured values of input variables of an event. The discriminant variable is determined by combining the probabilities for the individual quantities calculating the likelihood that an event belongs to the signal category:

$$F(\vec{x}) = \frac{\prod_i p_{\text{signal}}^i(x_i)}{\sum_j \prod_i p_j^i(x_i)}. \tag{5.13}$$

As examples, the distributions of the final discriminant for $m_{\tilde{\chi}_1^0} = 60$ GeV and $m_{\tilde{\chi}_1^0} = 90$ GeV are displayed in figure 5.7. Here, it can be noticed that the discrepancy between measurement and Standard Model prediction is located in the background and not in the signal region. This holds also for the other mass points and for the heavy gravitino scenario (see section 5.5).

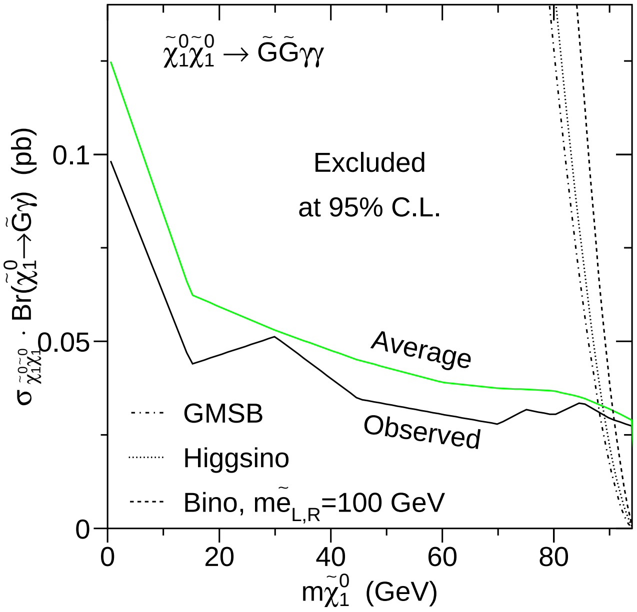

Figure 5.8: *Upper limit on the cross section for the process* $e^+e^- \to \tilde{\chi}_1^0\tilde{\chi}_1^0 \to \tilde{G}\tilde{G}\gamma\gamma$ *(solid line) and average limit (grey line) reached by using Monte Carlo experiments with background only at* $\sqrt{s} = 189$ GeV*. In addition, theoretical predictions for two extreme cases of* $\tilde{\chi}_1^0$ *composition and for the most conservative GMSB prediction are presented.*

Cross Section Limits

Hereafter, the likelihood approach stated in section 5.2 is adopted and the spectra of the discriminant variable for data, background and signal simulations are compared in order to get the 95% confidence level upper limits on the number of events for the individual mass points as listed in table 5.5 together with the respective cross section limits and the average cross section limits obtained in Monte Carlo experiments with background only. The cross section limits are graphically displayed in figure 5.8 versus neutralino mass.

Mass Limits

Theoretical predictions for two extreme cases of neutralino composition[1] – determining its coupling to photon and Z – are sketched in the same figure. In

---

[1] For the higgsino case a 2% photino component is required to ensure the decay into $\gamma\tilde{G}$.

$\tilde{\chi}_1^0$ content	$m_{\tilde{\mathrm{e}}_{\mathrm{L,R}}}$ (GeV)	$m_{\tilde{\chi}_1^0}^{\mathrm{lim}}$ (GeV)
Bino	150	87.9
Bino	100	90.8
Photino	150	88.3
Photino	100	91.1
Higgsino	—	89.0

Table 5.6: *Neutralino mass limits for certain neutralino compositions and selectron masses.*

this way, lower limits on the neutralino mass are derived under the specific assumptions made on neutralino content and selectron mass as listed in table 5.6. Here, besides the results for pure bino and higgsino states, a pure photino is considered.

MSSM Exclusions

The limit on the cross section for $\tilde{\chi}_1^0\tilde{\chi}_1^0$ production times the branching fraction for the radiative decay of $\tilde{\chi}_1^0$ is interpreted in terms of MSSM model parameters, which are introduced in section 2.2.1, as proposed in [95] for the light gravitino case. For example, the excluded region in the M_2 versus μ plane obtained for $\tan\beta = \sqrt{2}$ and $m_0 = 80$ GeV is shown in figure 5.9. The kinematic limit for $\tilde{\chi}_1^0\tilde{\chi}_1^0$ is approached for $\mu < 100$ GeV, whereas elsewhere the cross section for neutralino pair-production is substantially lower than the limit.

CDF Exclusion

Under the assumption that the neutralino is a pure bino [100] an exclusion in the $\tilde{\chi}_1^0$ versus $\tilde{\mathrm{e}}_{\mathrm{L,R}}$ mass plane is derived at the 95% confidence level as shown in figure 5.10. This exclusion is confronted to the light gravitino interpretation of the ee$\gamma\gamma$ event with large transverse missing energy observed by the CDF collaboration [108], which is discussed in section 2.2.6 as one of the main experiment-related motivations for low energy supersymmetry. The kinematics of the event is consistent only with a limited set of $\tilde{\chi}_1^0$ versus $\tilde{\mathrm{e}}_{\mathrm{L,R}}$ mass combinations [100]. The 95% confidence level exclusion obtained in this analysis almost rules out the SUSY interpretation of the CDF event in models with light gravitinos.

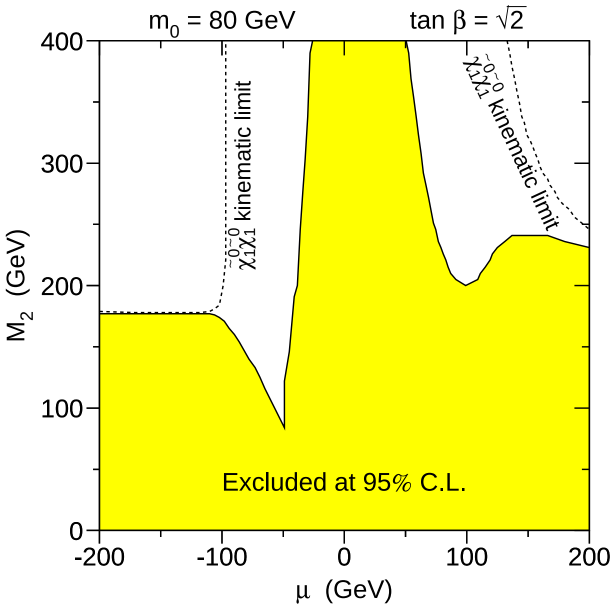

Figure 5.9: *Excluded region in the* M_2 *versus* μ *plane for* $\tan\beta = \sqrt{2}$ *and* $m_0 = 80$ GeV *in the MSSM with light gravitino derived at* $\sqrt{s} = 189$ GeV.

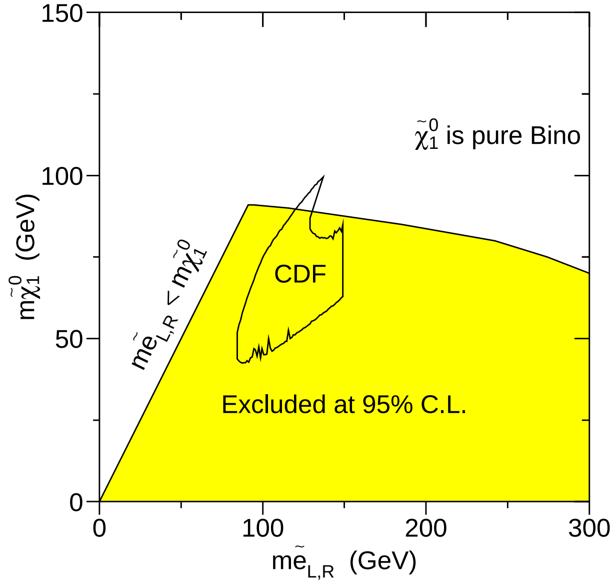

Figure 5.10: *Excluded region for a pure bino neutralino model in the* $\tilde{\chi}_1^0$ *versus* $\tilde{\mathrm{e}}_{\mathrm{L,R}}$ *mass plane compared to the region consistent with the SUSY interpretation of the CDF event in the so-called scalar electron scenario.*

Parameter	Scan range	Step size
Λ (TeV)	10 – 100	1
Λ/M_m	0.01 – 0.1 0.1 – 0.9	0.01 0.1
N_m	1 – 4	1
$\tan\beta$	5 – 40	5
	1, 1.04, 1.1, 1.2, $\sqrt{2}$ 1.7, 2, 3, 50, 60	
sign μ	+, –	

Table 5.7: *Scan ranges and step sizes of GMSB parameters.*

5.4.2 GMSB Interpretations

In minimal models with gauge-mediated SUSY breaking five parameters determine the sparticle sector of the theory as described in section 2.2.3. The parameter space is scanned within the boundaries specified by expression 2.31 and step sizes for the individual parameters as listed in table 5.7.

Assuming a neutralino NLSP scenario, the most conservative cross section obtained within GMSB (see also figure 2.12) is shown in figure 5.8, and a lower limit of

$$m_{\tilde{\chi}^0_1} \; > \; 88.2 \text{ GeV} \tag{5.14}$$

is determined from this measurement at the 95% confidence level.

Using the upper limit on the neutralino production cross section, indirect limits on sparticle masses within the GMSB framework under the above stated assumptions are derived:

$$\begin{array}{lll} m_{\tilde{\chi}^\pm_1} > 154 \text{ GeV} & m_{\tilde{\chi}^0_2} > 158 \text{ GeV} & m_{\tilde{\nu}} > 164 \text{ GeV} \\ m_{\tilde{\mathrm{e}}_\mathrm{L}} > 179 \text{ GeV} & m_{\tilde{\mu}_\mathrm{L}} > 179 \text{ GeV} & m_{\tilde{\tau}_2} > 179 \text{ GeV} \\ & m_{\tilde{\mathrm{t}}_1} > 207 \text{ GeV}\,. & \end{array} \tag{5.15}$$

The limits on $\tilde{\mathrm{e}}_\mathrm{R}$, $\tilde{\mu}_\mathrm{R}$, and $\tilde{\tau}_1$ masses are not listed, since within the assumptions made they are required to be heavier than the $\tilde{\chi}^0_1$, although they can, in principle, be NLSP themselves.

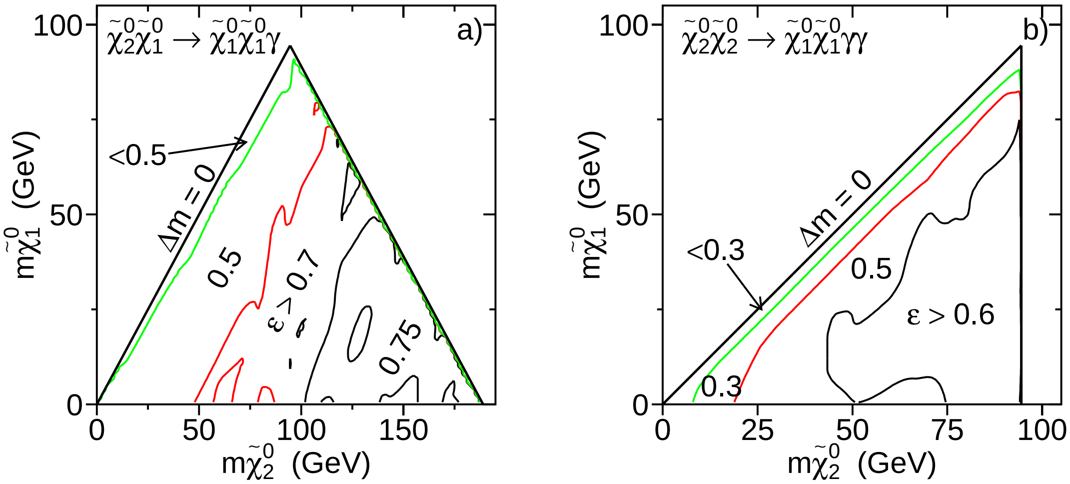

Figure 5.11: *Selection efficiencies for $\tilde\chi_2^0\tilde\chi_1^0$ (a) and $\tilde\chi_2^0\tilde\chi_2^0$ (b) production in the $m_{\tilde\chi_1^0}$ versus $m_{\tilde\chi_2^0}$ plane for $\sqrt{s} = 189$ GeV. Outer triangles mark the kinematically allowed region.*

5.5 Neutralino LSP Scenario

The two processes which can lead to final states with photons and missing energy in neutralino LSP models are outlined in section 2.2.4. Both, the single photon signature arising from $e^+e^- \to \tilde\chi_2^0\tilde\chi_1^0 \to \tilde\chi_1^0\tilde\chi_1^0\gamma$ and the two-photon signature from $e^+e^- \to \tilde\chi_2^0\tilde\chi_2^0 \to \tilde\chi_1^0\tilde\chi_1^0\gamma\gamma$, are simulated with the `SUSYGEN` Monte Carlo program. Events are simulated for a grid of mass points in the $m_{\tilde\chi_1^0}$ versus $m_{\tilde\chi_2^0}$ plane ranging from $m_{\tilde\chi_2^0} = 0.5$ GeV to the kinematic limit in steps of 15 GeV for $m_{\tilde\chi_2^0} < 60$ GeV and 10 GeV for $m_{\tilde\chi_2^0} > 60$ GeV in $m_{\tilde\chi_2^0}$ direction, and ranging from $\Delta m = m_{\tilde\chi_2^0} - m_{\tilde\chi_1^0} = 1$ GeV, 5 GeV, 10 GeV to $m_{\tilde\chi_2^0}$. About 1000 events are simulated for each of the 121 mass points of $\tilde\chi_2^0\tilde\chi_1^0$ production and for each of the 87 mass points of $\tilde\chi_2^0\tilde\chi_2^0$ production, respectively. Selection efficiencies for both processes are displayed in figure 5.11 in the $m_{\tilde\chi_1^0}$ versus $m_{\tilde\chi_2^0}$ plane.

Cross Section Limits

Upper limits on the number of events for both processes are derived as described in the previous sections: For a single photon final state, the energy spectra for data, background and signal Monte Carlo simulation are compared using the

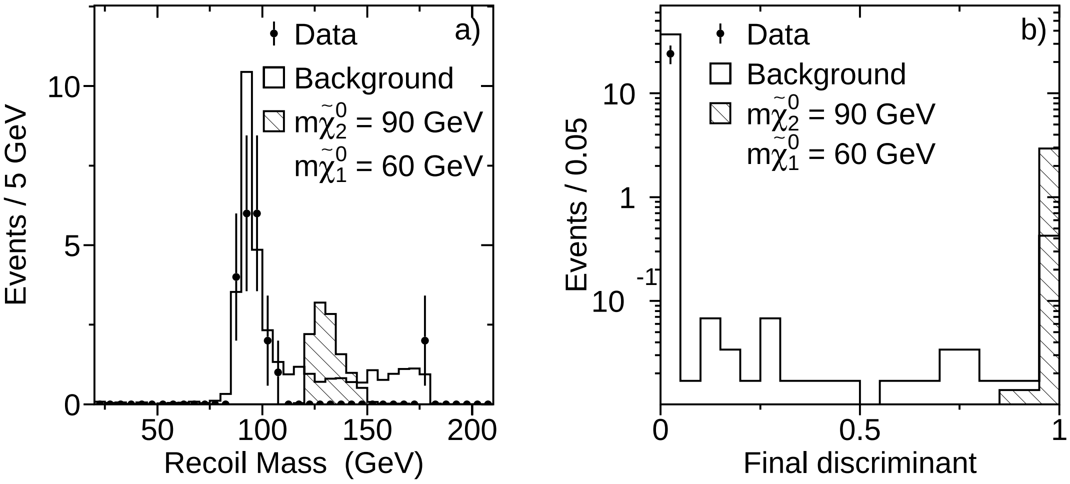

Figure 5.12: *Recoil mass distribution (a) for data, background and signal simulation for* $\tilde{\chi}_2^0\tilde{\chi}_2^0$ *production with a cross section of* 0.1 pb *at* $\sqrt{s} =$ 189 GeV, *and final discriminant for the same mass point corresponding to the upper limit of* 3 *events derived for this mass point.*

method introduced in section 5.2, and for the multi-photon final state a final discriminant variable with the same ingredients as the ones identified in section 5.4 is constructed, which is used to extract the limits from. The recoil mass spectrum for $\tilde{\chi}_2^0\tilde{\chi}_2^0$ production with $m_{\tilde{\chi}_2^0} = 90$ GeV and $m_{\tilde{\chi}_1^0} = 60$ GeV is displayed in figure 5.12 together with the distribution of the final discriminant variable for these mass hypotheses. Photon energy and angle distributions are due to their strong similarity to the ones from $\tilde{\chi}_1^0\tilde{\chi}_1^0$ production not shown. Cross section limits derived in this way are displayed in figure 5.13(a) for $\tilde{\chi}_2^0\tilde{\chi}_1^0$ production and in figure 5.13(b) for $\tilde{\chi}_2^0\tilde{\chi}_2^0$ production.

MSSM Exclusions

The results shown in figure 5.13(a) and (b) are combined and an exclusion in terms of limits on the MSSM parameters – with GUT assumptions – is obtained within the $\tilde{\chi}_1^0$ LSP scenario. The limits on $\tilde{\chi}_1^0\tilde{\chi}_2^0$ and $\tilde{\chi}_2^0\tilde{\chi}_2^0$ production lead to an excluded region in the M_2 versus μ plane as shown in figure 5.14. This exclusion, together with dedicated searches for charginos, neutralinos and scalar leptons, is useful to improve the indirect limit on the mass of the lightest neutralino in the

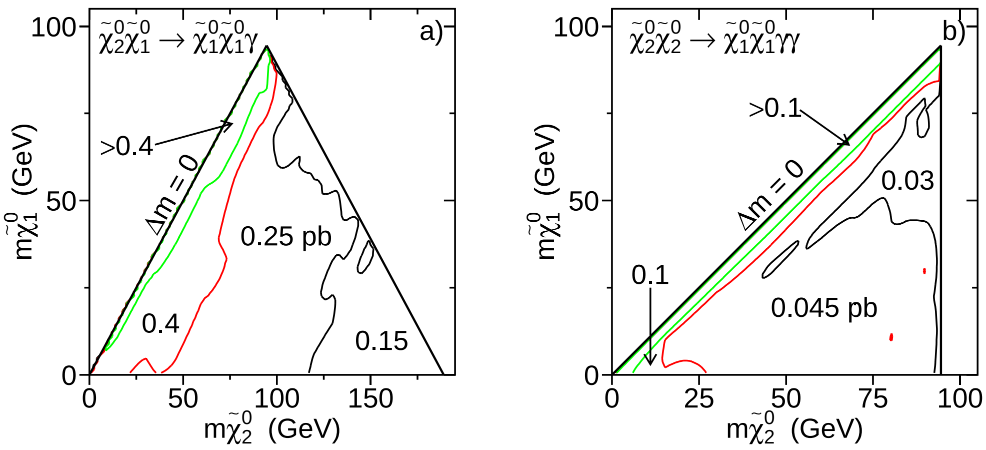

Figure 5.13: *Upper limits at the 95% confidence level on the production cross section in picobarn for* $\tilde\chi^0_2\tilde\chi^0_1$ *production (a) and* $\tilde\chi^0_2\tilde\chi^0_2$ *production (b) assuming 100% branching fraction for* $\tilde\chi^0_2 \to \tilde\chi^0_1\gamma$ *at* $\sqrt{s} = 189$ GeV*. Limits in the low* Δm *region labelled by ">"*σ_{limit} *are worse than the indicated value.*

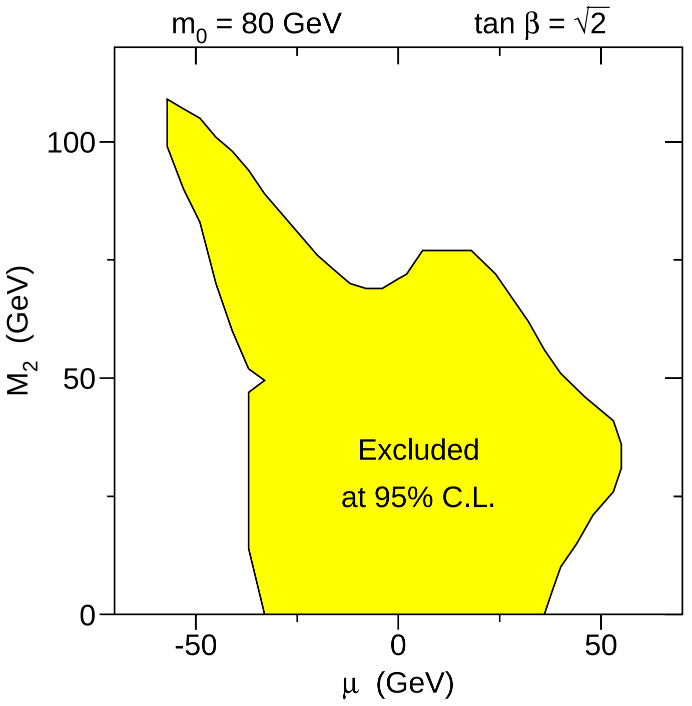

Figure 5.14: *Excluded region in the* M_2 *versus* μ *plane for* $\tan\beta = \sqrt{2}$ *and* $m_0 = 80$ GeV *in the neutralino LSP scenario obtained at* $\sqrt{s} = 189$ GeV.

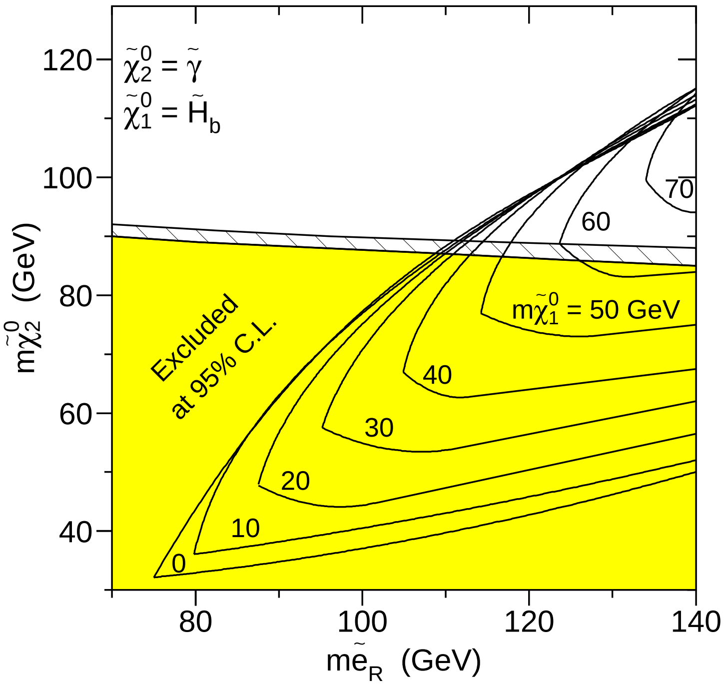

Figure 5.15: *Excluded region in the neutralino selectron mass plane at the 95% confidence level for* $\sqrt{s} = 189$ GeV. *The shaded region corresponds to* $m_{\tilde{e}_L} \gg m_{\tilde{e}_R}$, *while the hatched region is additionally excluded when* $m_{\tilde{e}_L} = m_{\tilde{e}_R}$. *Regions kinematically allowed for the CDF event as a function of* $m_{\tilde{\chi}_1^0}$ *are indicated, where* $\tilde{\chi}_1^0 = \tilde{\mathrm{H}}_b = \tilde{\mathrm{H}}_1^0 \sin\beta + \tilde{\mathrm{H}}_2^0 \cos\beta$.

constrained MSSM with neutralino LSP (see, *e.g.*, discussion in [199]).

CDF Exclusion

Among SUSY interpretations of the ee$\gamma\gamma$ event with large transverse missing energy observed by CDF [108] is a $\tilde{\chi}_1^0$ LSP interpretation, which suggests a high branching fraction for the radiative decay of the $\tilde{\chi}_2^0$ as pointed out in section 2.2.6. The kinematics of this event is consistent only with a limited set of $\tilde{\chi}_2^0$ – $\tilde{\chi}_1^0$ – ẽ mass combinations [119]. Radiative decay is likely when the $\tilde{\chi}_2^0$ is pure photino and the $\tilde{\chi}_1^0$ is pure higgsino as explained in section 2.2.4. With these assumptions, the lower mass limit of $\tilde{\chi}_2^0$ as a function of the scalar electron mass is calculated for mass differences $\Delta m = m_{\tilde{\chi}_2^0} - m_{\tilde{\chi}_1^0}$ greater than 10 GeV as shown in figure 5.15. For each $\tilde{\chi}_2^0$ mass, the exclusion is obtained using the most conservative

m_{h} (GeV)	N_{MC}	ϵ (%)	N_{limit}	$\sigma_{\mathrm{limit}}^{\mathrm{obs}}$ (pb)	$\sigma_{\mathrm{limit}}^{\mathrm{average}}$ (pb)
100	3952	49.6	3.00	0.034	0.036
95	3977	49.8	3.02	0.034	0.036
90	3958	56.5	3.08	0.031	0.034
85	3966	60.2	3.49	0.033	0.033
80	3957	61.4	3.68	0.034	0.034
75	3942	64.4	5.32	0.047	0.034
70	3966	63.1	4.73	0.043	0.036
60	3970	64.8	3.36	0.029	0.035
50	3978	64.2	3.41	0.030	0.038
40	3982	65.5	4.03	0.035	0.037

Table 5.8: *Number of generated Monte Carlo events N_{MC}, selection efficiency ϵ, upper limits on number of events N_{limit}, cross section $\sigma_{\mathrm{limit}}^{\mathrm{obs}}$, and average limit on cross section expected in absence of* $\mathrm{e^+e^-} \rightarrow \mathrm{hZ} \rightarrow \gamma\gamma\nu\bar{\nu}$ *at* $\sqrt{s} = 189$ GeV *for the indicated Higgs masses.*

cross section upper limit for any $\Delta m > 10$ GeV. Regions kinematically allowed for the CDF event are overlayed in the figure. The exclusion reached for equal masses of $\tilde{\mathrm{e}}_{\mathrm{L,R}}$ and for $m_{\tilde{\mathrm{e}}_{\mathrm{L}}} \gg m_{\tilde{\mathrm{e}}_{\mathrm{R}}}$ are pointed out in the interesting mass range for $m_{\tilde{\mathrm{e}}_{\mathrm{R}}}$. A large fraction of the allowed region for the ee$\gamma\gamma$ event is excluded by this analysis.

5.6 Fermiophobic Higgs

In this section the multi-photon selection is used to investigate the process

$$\mathrm{e^+e^-} \rightarrow \mathrm{hZ} \rightarrow \gamma\gamma\nu\bar{\nu}\,. \tag{5.16}$$

About 4000 events are simulated using the `PYTHIA` Monte Carlo program [200] for 10 different mass hypotheses for the Higgs boson as listed in table 5.8 together with the selection efficiency obtained for the criteria described in section 4.

Final Discriminant

Similar to the multi-photon signature in processes involving supersymmetric particles, a final discriminant variable is constructed to combine the information of several physics quantities as introduced in section 5.4.1. However, a slight change with respect to SUSY processes incorporates a different choice of input variables. The recoil mass of the photon system no longer discriminates signal from background processes since the Higgs recoils against the Z boson producing a similar peak structure as observed in $e^+e^- \to \nu\bar{\nu}\gamma\gamma$ events. Instead, the invariant mass of the photons reconstructs the Higgs mass producing a distinct shape of the invariant mass spectrum as shown in figure 5.16(b). Furthermore, the energy of the second most energetic photon, the angles of the two photons, and the angle of the missing momentum vector are used for combination of variables. Their distributions are displayed in figure 5.16(a–e) for a Higgs mass hypothesis of 95 GeV besides the simulation of Standard Model background and measured data. The final discriminant variable is shown in figure 5.16(f) for the same Higgs mass.

Cross Section Limits

Hereafter, the likelihood approach discussed in section 5.2 is adopted, where the spectra of the discriminant variables for data, background and signal simulations are compared in order to get the 95% confidence level upper limits on the number of events for individual mass points. These are all listed in table 5.8 together with the respective cross section limits and the average cross section limits obtained in Monte Carlo experiments with background only. Cross section limits are graphically displayed in figure 5.17(a) versus Higgs mass. Of course, the cross section limits have to be understood as limits on the process of equation 5.16 including the decay into photons, *i.e.* they have to be considered as limits on $\sigma(e^+e^- \to hZ) \cdot Br(h \to \gamma\gamma) \cdot Br(Z \to \nu\bar{\nu})$.

Limit on Branching Fraction and on Higgs Mass

Assuming a cross section for hZ production and a branching fraction for the Z into neutrinos as predicted by the Standard Model, the cross section limits for process 5.16 are transformed into an exclusion for the branching fraction of the Higgs boson into photon pairs as shown in figure 5.17(b). Furthermore, in figure 5.17(b) the $h \to \gamma\gamma$ branching fraction in the Standard Model, computed

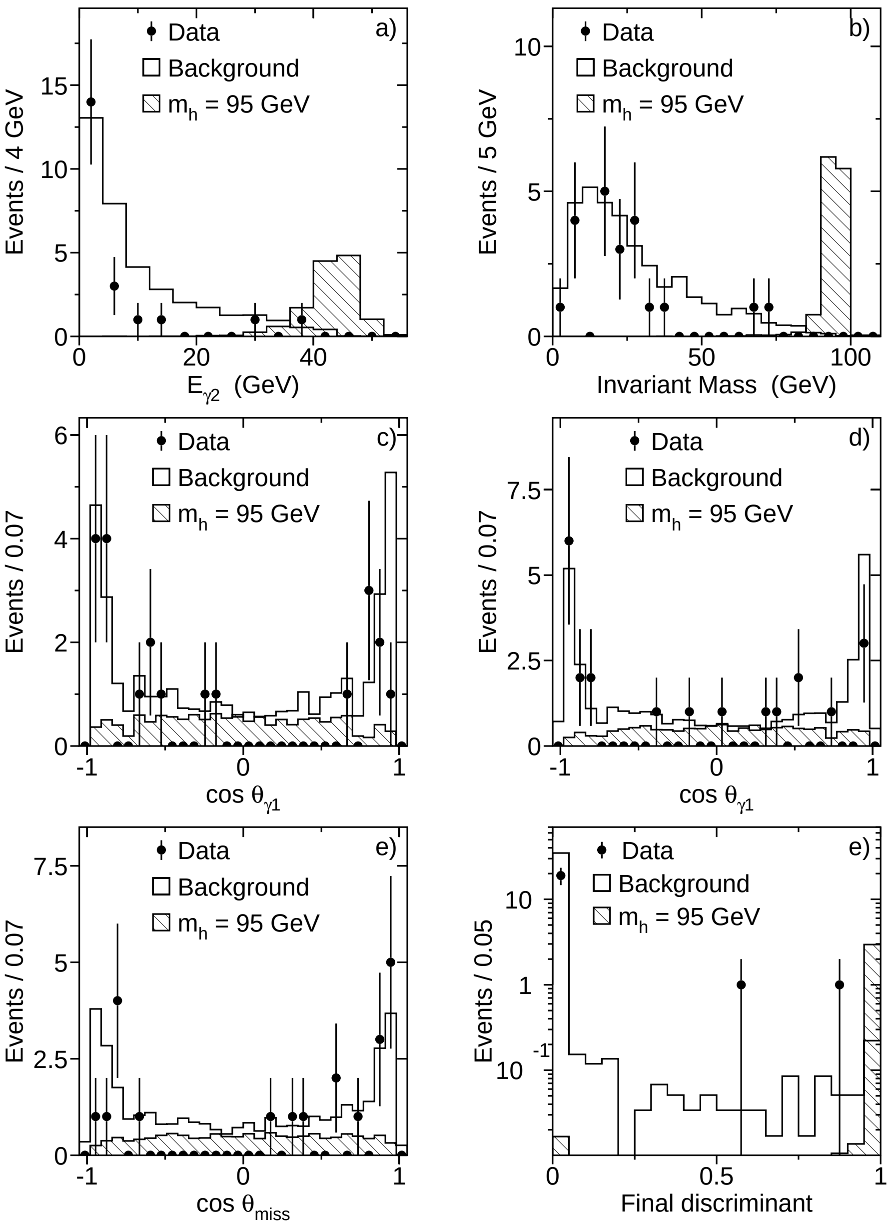

Figure 5.16: *Distributions used to construct the final discriminant for* hZ $\to \gamma\gamma\nu\bar{\nu}$ *production. Energy of the second most energetic photon (a), invariant mass (b), photon angles (c and d), and angle of the missing momentum vector (f) at* $\sqrt{s}$ = 189 GeV*. Signal Monte Carlo events are normalised to correspond to a cross section of* 0.15 pb*. Distribution of the final discriminant (e), where the signal corresponds to the upper limit of 3.02 events derived for this Higgs mass.*

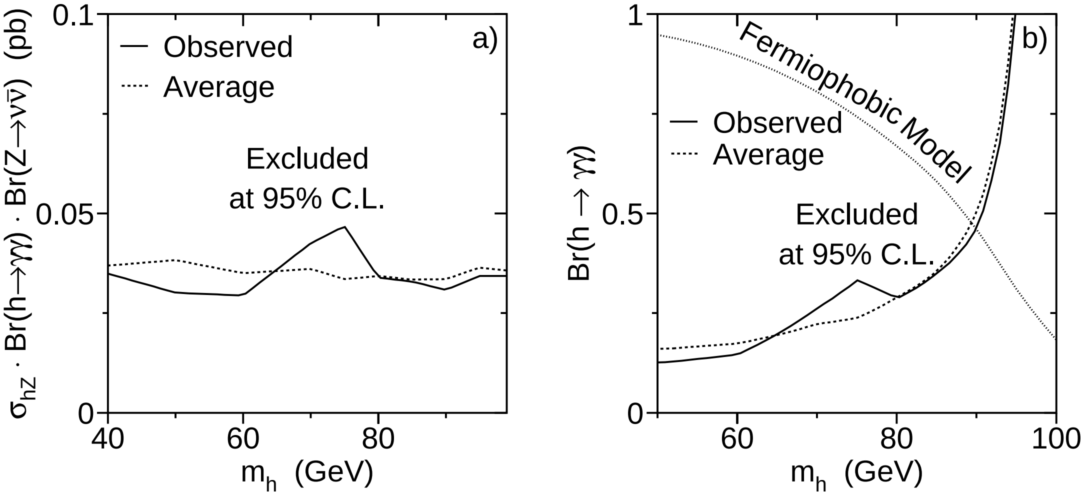

Figure 5.17: *Upper limit on the production cross section for the process* $e^+e^- \to hZ \to \gamma\gamma\nu\bar{\nu}$ *(solid line) and average limit (dashed line) obtained using Monte Carlo experiments with background only at* $\sqrt{s} = 189$ GeV *(a). Limit on the branching fraction* $\mathrm{Br}(h \to \gamma\gamma)$ *assuming Standard Model production cross section and prediction for* $\mathrm{Br}(h \to \gamma\gamma)$ *(dotted line) within the Standard Model, but without fermionic Higgs couplings (b).*

with the help of the program `HDECAY` [201] with fermionic couplings of the Higgs switched off, is shown. A lower mass limit for such a fermiophobic Higgs boson is set to

$$m_h > 89.9 \text{ GeV} \tag{5.17}$$

at the 95% confidence level.

Outlook

Clearly, the sensitivity to fermiophobic Higgs production can be enlarged including Z decays into quarks and charged leptons. An analysis for hadronic final states has already been performed within L3 [202], and a selection of leptonic final states as well as a combination of the results is under way.

δ	ϵ (%)	$\sigma_{\gamma\mathrm{G}}^{\mathrm{lim}}$ (pb)	M_D (GeV)	R (mm)
2	42.8	0.638	1018	$4.6 \cdot 10^{-1}$
3	40.7	0.646	812	$5.1 \cdot 10^{-6}$
4	38.9	0.651	674	$1.8 \cdot 10^{-8}$
5	37.6	0.658	577	$6.1 \cdot 10^{-10}$
6	36.5	0.664	506	$6.6 \cdot 10^{-11}$
7	35.5	0.670	453	$1.4 \cdot 10^{-11}$
8	34.7	0.674	411	$4.2 \cdot 10^{-12}$
9	34.0	0.678	377	$1.7 \cdot 10^{-12}$
10	33.4	0.680	349	$8.3 \cdot 10^{-13}$

Table 5.9: *Selection efficiency ϵ for $\mathrm{e^+e^-} \to \gamma\mathrm{G}$, upper cross section limit, lower limit at the 95% confidence level on the energy scale M_D, and on the radius R as function of the number of extra dimensions δ at $\sqrt{s} = 189$ GeV.*

5.7 Quantum Gravity and Extra Dimensions

Low scale gravity predicts sizeable cross sections for the process $\mathrm{e^+e^-} \to \gamma\mathrm{G}$ as noticed in section 2.3. The study of this reaction leads to exclusions on the energy scale and size of extra dimensions as described in the following.

Analysis Procedure

To convert the theoretical cross section (equation 2.41) into an estimate on the number of events expected from real graviton production, the differential cross section of $\gamma\mathrm{G}$ production in energy and angle is multiplied by efficiency and luminosity. The efficiency is derived from $\nu\bar{\nu}\gamma(\gamma)$ Monte Carlo simulation in a grid in the $x_\gamma - \cos\theta_\gamma$ plane for $E_\gamma > 4$ GeV. The efficiency for $\mathrm{e^+e^-} \to \gamma\mathrm{G}$ within $E_\gamma > 4$ GeV and $\cos\theta_\gamma < 0.97$ is listed in table 5.9 for $2 \leq \delta \leq 10$. The decrease of efficiency with increasing number of extra dimensions is determined by the factor $(1-x)^{\frac{\delta}{2}-1}$ in equation 2.42. The photon spectrum from real graviton production is shown in figure 5.18 together with data and the prediction of the Standard Model background processes.

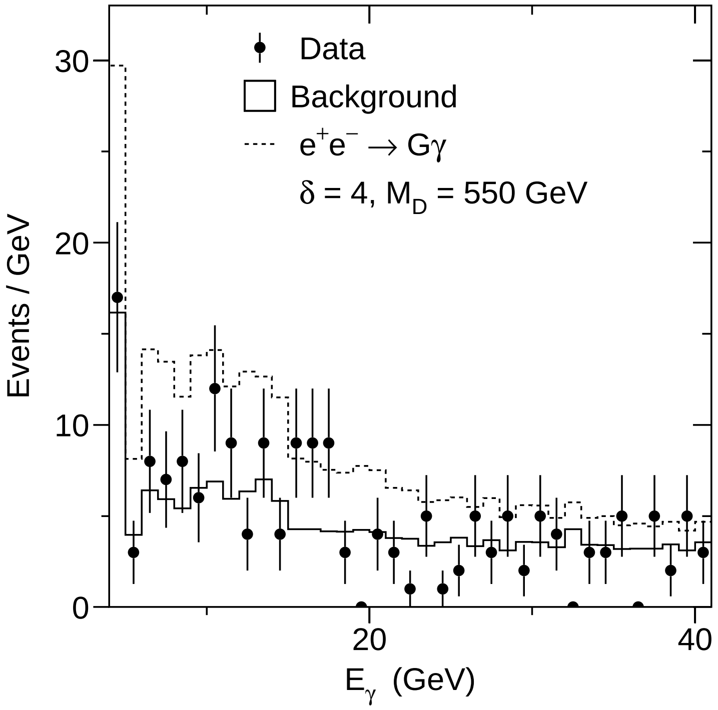

Figure 5.18: *Photon energy spectrum in real graviton production together with data and prediction of the Standard Model at* $\sqrt{s} = 189$ GeV.

Limits

Since good agreement in the single photon spectrum between data and Standard Model prediction is observed, lower limits at the 95% confidence level on the cross section for various values of δ are derived using the likelihood approach described in section 5.2 to compare the photon energy spectra of the signal, expected background and data (listed in table 5.9). Corresponding limits on M_D exceed 1 TeV achieved for $\delta = 2$ as listed in table 5.9 together with the values obtained for any $\delta \leq 10$. The limit on M_D is graphically shown in figure 5.19 versus δ. Exploring formula 2.39, the lower limit on M_D is transformed into an upper limit on the radius of the extra dimensions R, below which gravitational effects deviate from Newtonian physics. Derived values for R are listed in table 5.9.

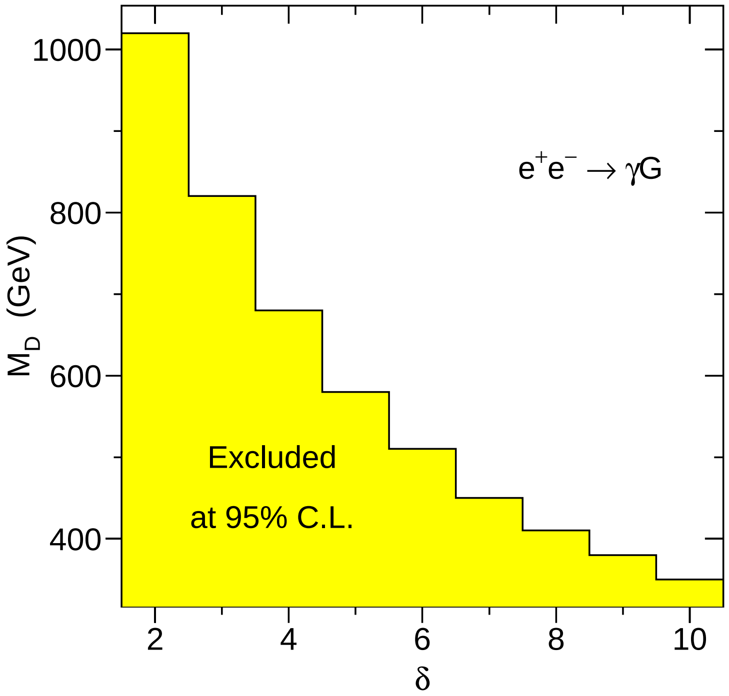

Figure 5.19: *Limits at the 95% confidence level on M_D as function of the number of extra dimensions δ from γG production at $\sqrt{s} = 189$ GeV.*

Chapter 6

Summary, Conclusions and Outlook

In this chapter, the results obtained in this study shall be summarised. In order to draw conclusions, comparisons and combinations with other experiments' findings and with previous L3 results are performed. The thesis then ends with an outlook concerning SUSY discovery prospects in future experiments and offers a preview of preliminary results of the ongoing LEP 2 phase.

6.1 Results of the Analysis

The results of this thesis are twofold. On one side, the production of neutrinos in electron-positron interactions accompanied by initial state radiation is studied at centre-of-mass energies between 130 GeV and 189 GeV. On the other side, the second topic of the thesis is the search for new particles with photons and missing energy in the final state.

Neutrino Physics

In the Standard Model single or multi-photon events with missing energy are produced via the reaction $\mathrm{e}^+\mathrm{e}^- \to \nu\bar{\nu}\gamma(\gamma)$. The cross sections of this process for $E_\gamma > 5$ GeV and $|\cos\theta_\gamma| < 0.97$ at the individual centre-of-mass energies are measured to be

$$\sigma_{\nu\bar{\nu}\gamma(\gamma)} = \begin{array}{r} (11.93 \pm 1.85 \pm 0.56)\ \mathrm{pb} \\ (12.05 \pm 2.00 \pm 0.72)\ \mathrm{pb} \\ (8.41 \pm 1.18 \pm 0.30)\ \mathrm{pb} \\ (8.58 \pm 1.19 \pm 0.21)\ \mathrm{pb} \\ (5.74 \pm 0.41 \pm 0.09)\ \mathrm{pb} \\ (5.25 \pm 0.22 \pm 0.07)\ \mathrm{pb} \end{array} \quad \text{at } \sqrt{s} = \begin{array}{l} 130.10\ \mathrm{GeV} \\ 136.07\ \mathrm{GeV} \\ 161.34\ \mathrm{GeV} \\ 172.13\ \mathrm{GeV} \\ 182.68\ \mathrm{GeV} \\ 188.64\ \mathrm{GeV}\,. \end{array}$$

These measurements are transformed into total cross sections for neutrino pair-production:

$$\sigma_{\nu\bar{\nu}(\gamma)} = \begin{array}{r} (95.8 \pm 15.5)\ \mathrm{pb} \\ (99.5 \pm 17.6)\ \mathrm{pb} \\ (80.4 \pm 11.7)\ \mathrm{pb} \\ (87.3 \pm 12.3)\ \mathrm{pb} \\ (61.8 \pm 4.6)\ \mathrm{pb} \\ (58.3 \pm 2.7)\ \mathrm{pb} \end{array} \quad \text{at } \sqrt{s} = \begin{array}{l} 130.10\ \mathrm{GeV} \\ 136.07\ \mathrm{GeV} \\ 161.34\ \mathrm{GeV} \\ 172.13\ \mathrm{GeV} \\ 182.68\ \mathrm{GeV} \\ 188.64\ \mathrm{GeV}\,. \end{array}$$

The measured photon energy spectra are used to derive the number of light neutrino generations. The combined value determined from all data analysed in this thesis is

$$N_\nu = 3.05 \pm 0.11 \pm 0.04\,,$$

which is in good agreement with the hypothesis of three light neutrino types and supports the Standard Model with its three generations of particles.

Search for New Particles

Since no excess of events with one or more photons and missing energy in the final state is discovered assuming $N_\nu = 3$, upper limits on cross sections of new physics processes are set and lower limits on masses of supersymmetric particles are derived. If the gravitino is the lightest supersymmetric particle and all other SUSY particles are too heavy to be created at LEP energies, gravitino pair-production could be the only process involving SUSY particles accessible at LEP. Such a superlight gravitino may appear in no-scale supergravity models. From an analysis of the process $\mathrm{e^+e^-} \to \tilde{\mathrm{G}}\tilde{\mathrm{G}}\gamma$ a lower limit of

$$m_{\tilde{\mathrm{G}}} > 8.9 \cdot 10^{-6}\ \mathrm{eV}$$

is determined at the 95% confidence level.

Associated production of gravitino and neutralino and successive radiative decay of the neutralino to gravitino and photon gives rise to a single photon and missing energy signature. In order to achieve a sizable cross section for this process, the gravitino needs to be superlight as it is possible in no-scale SUGRA models. Cross section limits depending on the neutralino mass are set and an exclusion region in the $m_{\tilde{\chi}_1^0}$ versus $m_{\tilde{\mathrm{G}}}$ mass plane within the framework of the LNZ model, a special no-scale SUGRA model, is derived.

Pair-production of neutralinos leads to a two-photon and missing energy signature in models with light gravitinos. Here, upper limits on production cross sections are computed for various neutralino mass hypotheses. An exclusion region in the neutralino-selectron mass plane is determined for a pure bino neutralino almost ruling out the SUSY $\tilde{\mathrm{G}}$ LSP interpretation of the single $\mathrm{ee}\gamma\gamma$ event with large transverse missing energy observed by the CDF collaboration. Furthermore, the results are interpreted in terms of MSSM parameters for a model with a light gravitino. Within the framework of gauge-mediated supersymmetry breaking models a lower limit on the neutralino mass of

$$m_{\tilde{\chi}_1^0} \; > \; 88.2 \text{ GeV}$$

is obtained, whereas on the lightest chargino, the second lightest neutralino, the sneutrino, and the right sleptons indirect mass limits better than 150 GeV are calculated under the assumption that the lightest neutralino is the second lightest supersymmetric particle.

If the gravitino is heavy as in supergravity models, then the lightest neutralino becomes the lightest supersymmetric particle. Single or multi-photon signatures with missing energy arise from loop decays of heavier neutralinos into photon and lightest neutralino but occur only in peculiar regions of parameter space. Cross section limits on $\tilde{\chi}_1^0\tilde{\chi}_2^0$ and $\tilde{\chi}_2^0\tilde{\chi}_2^0$ production are evaluated assuming 100% branching fraction for the radiative decay of $\tilde{\chi}_2^0$. An interpretation of the limits is carried out in terms of MSSM parameters for the $\tilde{\chi}_1^0$ LSP scenario. A pure photino content for the $\tilde{\chi}_2^0$ and a pure higgsino composition of the $\tilde{\chi}_1^0$ is motivated by the neutralino LSP interpretation of the CDF event. An exclusion region in the $m_{\tilde{\chi}_2^0}$ versus $m_{\tilde{\mathrm{e}}_\mathrm{R}}$ plane is derived from cross section limits under the assumptions quoted above, ruling out a large fraction of the region kinematically allowed for the CDF event.

Fermiophobic Higgs bosons are searched for investigating the process $\mathrm{e}^+\mathrm{e}^- \rightarrow \mathrm{hZ} \rightarrow \gamma\gamma\nu\bar{\nu}$. Here, cross section limits on this process are determined depending on the Higgs mass and limits on the branching ratio of the Higgs decaying into photons are derived. Moreover, a lower mass limit for such a fermiophobic Higgs boson is set to

$$m_{\mathrm{h}} \; > \; 89.9 \text{ GeV}$$

at the 95% confidence level.

A search for the production of massive gravitons in quantum gravity models with extra spatial dimensions is performed investigating the process $\mathrm{e}^+\mathrm{e}^- \rightarrow \gamma\mathrm{G}$. Lower limits on the energy scale ranging from 1018 GeV to 349 GeV are derived at the 95% confidence level for two to ten extra dimensions. Their size is limited to at most 0.46 mm and at most $8.3 \cdot 10^{-13}$ mm for two and ten extra dimensions, respectively.

6.2 Combinations and Comparisons

In the first part of this section recent neutrino counting measurements are recapitulated, and a new world average value on the number of light neutrino species – including the value found in this study – is computed. The second part deals with investigations within the SUSY framework attained in this thesis in comparison with results from other experiments, and with combinations performed by the SUSY LEP 2 working group.

Neutrino Counting

The most precise measurements of the number of light neutrino types, N_ν, stem from studies of Z boson production in $\mathrm{e}^+\mathrm{e}^-$ collisions. The invisible partial width of the Z, Γ_{inv}, is calculated by subtracting the measured visible partial widths, corresponding to Z decays into quarks and charged leptons, from the total Z width. The invisible width is assumed to be due to N_ν light neutrino flavours, each contributing to the neutrino partial width as determined by the Standard Model. The combined LEP result for this indirect method is $N_\nu = 2.994 \pm 0.011$ [203].

Before the advent of LEP, only limits on the number of neutrino generations could be placed by experiments at lower energy $\mathrm{e}^+\mathrm{e}^-$ colliders measuring the cross section of the process $e^+e^- \to \nu\bar{\nu}\gamma$. The combined limit from these experiments is $N_\nu < 4.8$ at the 95% confidence level [204–208]. This process has a much larger cross section at centre-of-mass energies just above the Z mass and is measured at LEP by the ALEPH, DELPHI, L3, and OPAL experiments [189,209–211] giving an overall result of $N_\nu = 2.996 \pm 0.082$.

The method to determine the number of light neutrino flavours from the measurement of $e^+e^- \to \nu\bar{\nu}\gamma$ has the advantage that the process under investigation is measured. Model assumptions that enter to the calculation are the theoretical description of initial state radiation, which is a pure QED process, and the coupling of Z and W to neutrinos. On the other hand, the indirect method described in the previous paragraph also assumes the Standard Model coupling of the Z to neutrinos and QED to describe initial state radiation for the measurement of the total width of the Z boson from the line-shape of the cross section. Furthermore, for the measurement of the visible partial widths, the Standard Model couplings of the Z to quarks and charged leptons are put into the calculation. Thus, the indirect approach relies on more model assumptions than the direct $\nu\bar{\nu}\gamma$ measurement does.

At LEP 2 energies far above the Z mass, only the DELPHI experiment – besides this experiment – has published preliminary results on the number of light neutrino species [212]: $N_\nu = 2.88 \pm 0.19$. This result is obtained from the cross section measurement of $\nu\bar{\nu}\gamma$ production. The ALEPH and OPAL collaborations published results on the cross section measurement within different kinematic requirements [213–216]:

$$\text{ALEPH:} \quad \sigma_{\nu\bar{\nu}\gamma} = \begin{array}{l} (4.32 \pm 0.34)\ \text{pb at } \sqrt{s} = 183\ \text{GeV} \\ (3.78 \pm 0.20)\ \text{pb at } \sqrt{s} = 189\ \text{GeV} \end{array}$$

for $p_\mathrm{t} > 0.0375\sqrt{s}$ and $|\cos\theta_\gamma| < 0.95$

$$\text{OPAL:} \quad \sigma_{\nu\bar{\nu}\gamma} = \begin{array}{l} (4.71 \pm 0.38)\ \text{pb at } \sqrt{s} = 183\ \text{GeV} \\ (4.23 \pm 0.25)\ \text{pb at } \sqrt{s} = 189\ \text{GeV} \end{array}$$

for $p_\mathrm{t} > 0.025\sqrt{s}$ and $|\cos\theta_\gamma| < 0.966$. These are – similar to the DELPHI approach – converted into a measurement of the number of neutrino families as graphically shown in figure 6.1. A combination of the LEP 2 results of all four LEP experiments – displayed in figure 6.2 – yields $N_\nu = 2.951 \pm 0.077$, where the value coming from this measurement has the greatest sensitivity, *i.e.* the smallest

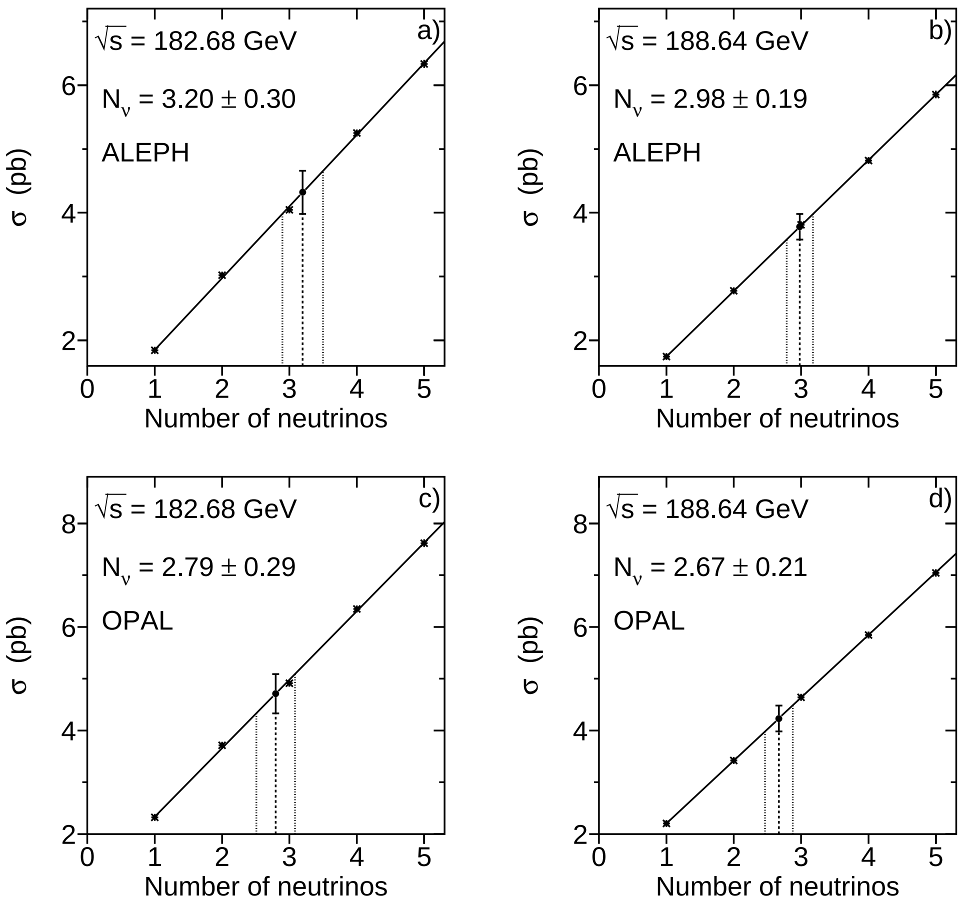

Figure 6.1: *Cross section of* $e^+e^- \to \nu\bar{\nu}\gamma$ *versus number of neutrinos measured by the ALEPH experiment at* $\sqrt{s} = 183$ GeV *(a), at* 189 GeV *(b), and by the OPAL experiment at* 183 GeV *(c) and at* 189 GeV *(d).*

error. A combination with the above stated LEP 1 measurement yields the new world average for the number of light neutrino species of

$$N_\nu \;=\; 2.972 \pm 0.056$$

from the direct method of the $\nu\bar{\nu}\gamma$ measurement. This result is in perfect agreement with the hypothesis of three light neutrino types and supports the Standard Model with its three generations of particle species.

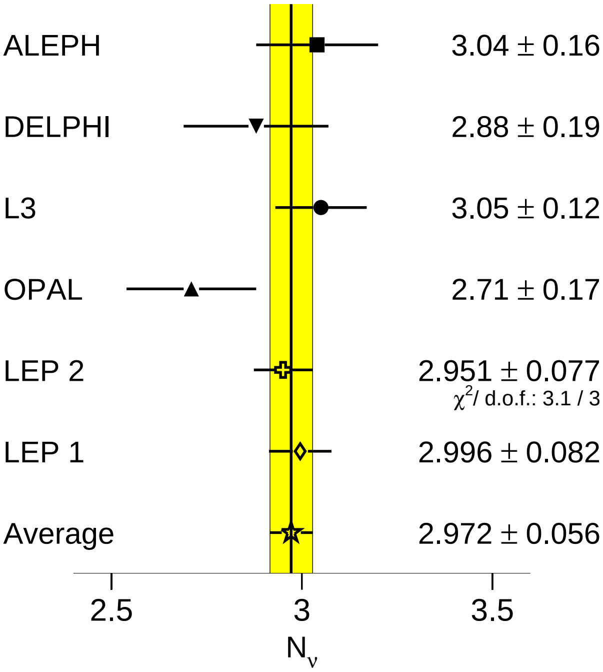

Figure 6.2: *Number of neutrino families measured from single photon events by the four LEP collaborations at LEP 2, LEP 1, and the world average.*

New Physics Searches

Gravitino pair-production is searched for by two other LEP experiments with negative outcome. The preliminary result of DELPHI of $m_{\tilde{G}} > 8.9 \cdot 10^{-6}$ eV [212] is exactly the same as achieved in this analysis, whereas the preliminary ALEPH limit of $m_{\tilde{G}} > 10 \cdot 10^{-6}$ eV [214] is comparable to the average limit of this study of $9.7 \cdot 10^{-6}$ eV expected for the absence of a signal. Unfortunately, neither DELPHI nor ALEPH published their expected limits preventing a comparison of the sensitivity between the experiments. For a combination of the results, signal efficiencies within the acceptance, background expectations and candidate numbers need to be known, yet are not published by the other experiments.

Besides this analysis, the OPAL and DELPHI collaborations search for associated neutralino-gravitino production. OPAL's cross section limits vary from

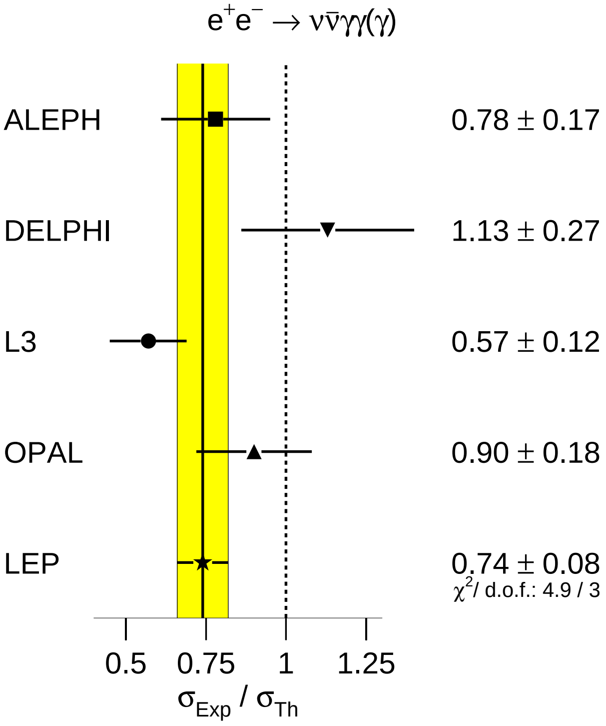

Figure 6.3: *Measurements of $\nu\bar{\nu}\gamma\gamma(\gamma)$ divided by the Standard Model prediction of the four LEP collaborations at $\sqrt{s} = 189$ GeV with the average value.*

35 fb to 175 fb for $m_{\tilde{\chi}^0_1} > 90$ GeV [216], similar to the results of this analysis (see table 5.4 and figure 5.4), whereas the DELPHI limits, between 300 fb and 420 fb for $m_{\tilde{\chi}^0_1} > 50$ GeV [212], are considerably worse. Mass exclusions as presented in figure 5.5 are not published by any other experiment. Only DELPHI sets a lower limit on the neutralino mass of 110 GeV for $m_{\tilde{G}} = 10^{-5}$ eV [212]. For this gravitino mass, the neutralino mass limit achieved by this analysis is 145 GeV.

The discrepancy between measurement and Standard Model prediction observed in the multi-photon channel with missing energy at $\sqrt{s} = 189$ GeV is not seen with the same magnitude by other LEP experiments. In figure 6.3 the measurements of all four LEP experiments at $\sqrt{s} = 189$ GeV divided by the theoretical predictions are shown and an average value is calculated. Besides this analysis, ALEPH and OPAL results show a slight deficit of data compared to the Standard Model prediction, whereas the average value – strongly dominated by

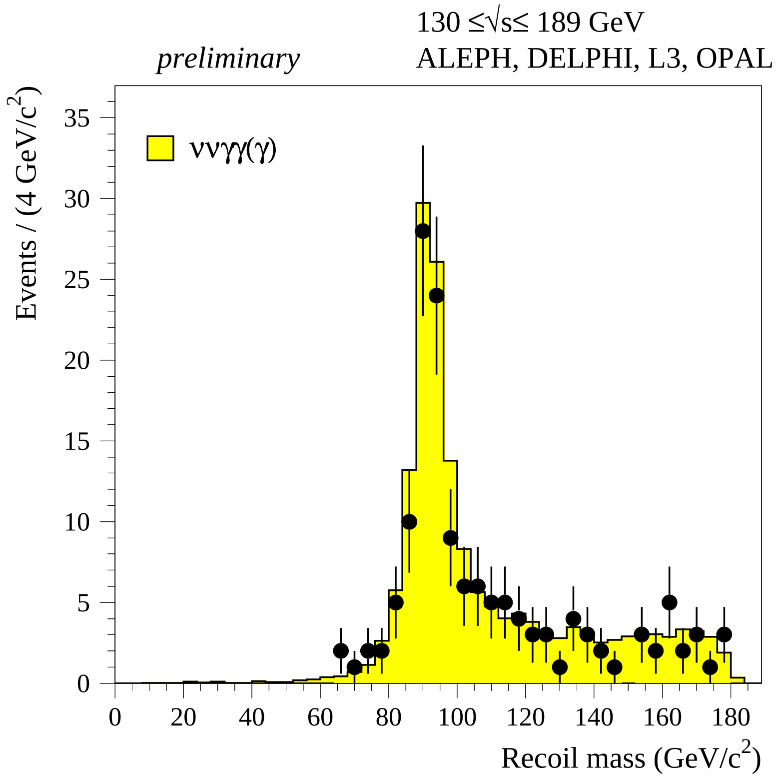

Figure 6.4: *Combined recoil mass distribution of the four LEP collaborations at LEP 2 [217].*

the L3 measurement – ends up below the Standard Model prediction. Combining the results from all LEP 2 centre-of-mass energies up to 189 GeV and all four LEP experiments, a total of 145 events are observed in data with 166.5 events expected within the Standard Model, showing a 1.7σ discrepancy. The combined recoil mass distribution is shown in figure 6.4 [217].

All four LEP collaborations searched for neutralino pair-production in models with light gravitinos, *i.e.* a two-photon plus missing energy signature. The cross section limits vary from 43 fb to 28 fb for $m_{\tilde{\chi}_1^0}$ from 45 GeV to 94 GeV for ALEPH [218], from 56 fb to 39 fb for DELPHI [212], and from 103 fb to 53 fb for OPAL [216], all in the same $m_{\tilde{\chi}_1^0}$ range. The limits obtained by this analysis – 35 fb to 27 fb – as listed in table 5.5 and displayed in figure 5.8, are the best cross section limits from all four collaborations. The LEP 2 SUSY working group combined the results of the four collaborations and derived an exclusion region

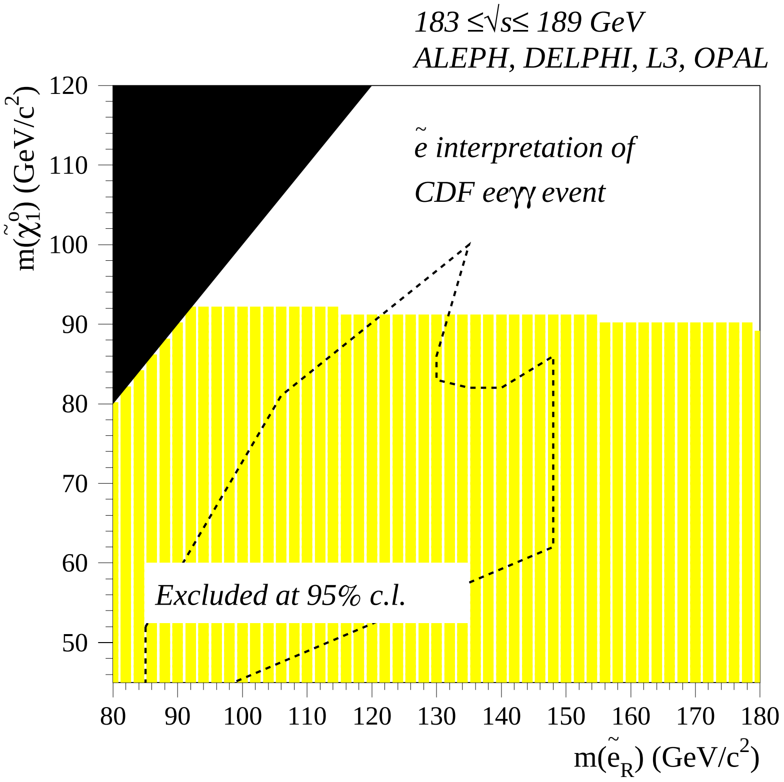

Figure 6.5: *Combined exclusion region of the four LEP collaborations at LEP 2 in the* $\tilde{\chi}_1^0$ *versus* $\tilde{\mathrm{e}}_{\mathrm{L,R}}$ *mass plane compared to the region consistent with the supersymmetric interpretation of the CDF event in the so-called scalar electron scenario [217].*

in the neutralino-selectron mass plane shown in figure 6.5 [217], similar to the analysis result within this work presented in figure 5.10.

Only the ALEPH collaboration has performed a parameter scan within GMSB models [218], similar to the one presented in section 5.4.2. There, besides the neutralino NLSP hypothesis, slepton NLSP scenarios are investigated (see also section 2.2.3 and [87]). Within the neutralino NLSP hypothesis, a lower limit on the neutralino mass of 86 GeV is derived to be compared to 88.2 GeV determined by this analysis. The CDF collaboration searched for neutralino and chargino production in proton-antiproton collisions at the TEVATRON collider at the Fermi National Accelerator Laboratory, Batavia, USA [108]. Within GMSB with neutralino NLSP, they derived limits of 65 GeV on the neutralino mass and

120 GeV on the chargino mass. The indirect limit on the chargino mass determined by this analysis – listed in equation 5.15 – is 154 GeV. Results obtained by the D∅ collaboration on neutralino and chargino searches in models with light gravitinos [219] are not interpreted within GMSB models, but within a less restricted MSSM-like model. Limits of 77 GeV on the neutralino mass and of 150 GeV on the chargino mass are reported.

Preliminary results on single and multi-photon final states up to $\sqrt{s} = 189$ GeV in neutralino LSP models are reported by all LEP collaborations. $\tilde{\chi}^0_1\tilde{\chi}^0_2$ production with $\tilde{\chi}^0_2 \rightarrow \tilde{\chi}^0_1\ \gamma$ decay is searched for by the ALEPH [214] and by the OPAL experiments [216] yielding similar results as the ones presented in section 5.5. Upper limits on the production cross section for $\tilde{\chi}^0_2\tilde{\chi}^0_2$ production derived by ALEPH [214], OPAL [216] and DELPHI [212] are considerably worse than the ones determined in section 5.5 and shown in figure 5.13(b).

Conclusion

In conclusion, the precise measurement of neutrino pair-production accompanied by initial state radiation in electron-positron collisions performed within this thesis improved the knowledge of one of the most fundamental quantities in high energy physics – the number of elementary particle generations – substantially.

Furthermore, the negative result of the search for new physics processes yielded a drastic confinement of the mass region, where new particles are likely to be found. In general, the fact that supersymmetry has so far escaped detection at LEP 2 due to an “unlucky numerical accident” in nature’s choice of parameters while still solving the naturalness problem is investigated in [220]. There, it is concluded that this is very unlikely. Concerning GMSB models investigated here, this is even more unlikely due to the more stringent bounds on the neutralino mass and the relative lightness predicted for sleptons [220].

6.3 Experimental Prospects of Supersymmetry

Finding new particles heavier than today’s boundaries requires a higher energy and/or a higher interaction rate than available at present to produce and detect them. Besides the ongoing LEP 2 phase, two projects at hadron colliders will open up new discovery potentials in the near future. The upgraded TEVATRON

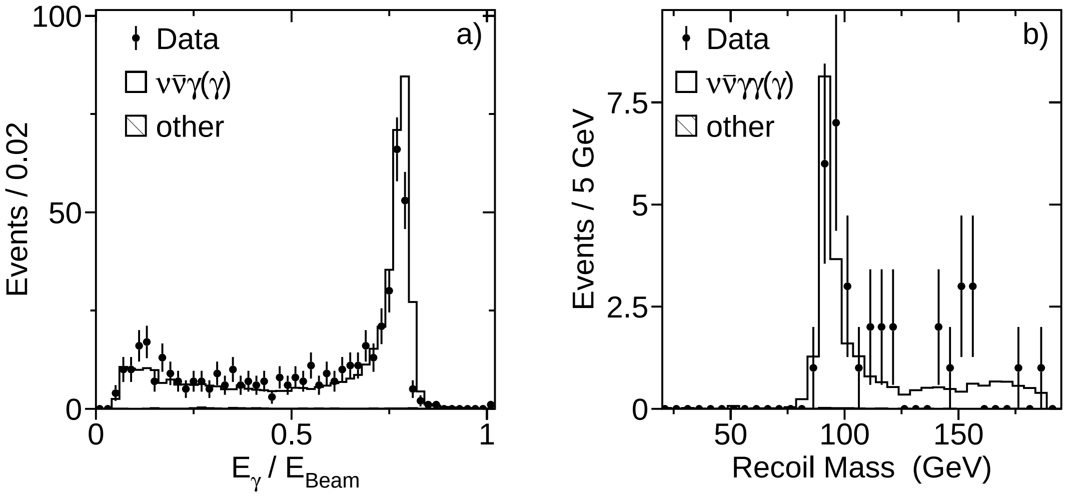

Figure 6.6: *Photon energy normalised to beam energy for single and multi-photon events at* $\sqrt{s} = 192$ GeV, 196 GeV *and 200 GeV (a) and recoil mass distribution of the multi-photon subsample (b).*

with its newly built main injector will start producing physics events in the year 2000 with slightly increased centre-of-mass energy around 2 TeV with respect to previous runs and much higher integrated luminosity (about 20 times as much as taken until now). In the year 2005 the Large Hadron Collider (LHC), situated at CERN, will start operation with proton-proton collisions at a centre-of-mass energy of 14 TeV. Currently, an enormous amount of activity is going on to study the prospects of discovering supersymmetry at those accelerators [221–224]. For precision studies of a then discovered supersymmetric theory, a linear e^+e^- collider (LC) is an optimal tool. Several designs for a LC operating at centre-of-mass energies between 500 GeV and 2 TeV are presently in discussion [225] and studies concerning measurements of SUSY parameters are being carried out [225, 226].

In 1999 LEP increased its centre-of-mass energy from 192 GeV in the beginning of the data taking phase to 196 GeV, and, finally, 200 GeV of centre-of-mass energy were reached. A total luminosity of 29.2 pb^{-1} and 81.4 pb^{-1} is recorded at 192 GeV and 196 GeV, respectively, whereas the luminosity at 200 GeV until September 1999 is 48 pb^{-1}. Preliminary results of the single and multi-photon selection showing the current status are presented here. Altogether 474 single and multi-photon events are selected in data with $E_\gamma > 5$ GeV and $|\cos\theta_\gamma| < 0.97$ with 477.4 events expected from Standard Model processes (474 from $\nu\bar{\nu}\gamma(\gamma)$). The photon energy distribution is shown in figure 6.6(a). No statistically significant excess of data compared to the prediction is observed, although the shape of the distributions do not agree with each other as well as for previous centre-of-mass energies, reflecting the preliminary status of the analysis. Requiring a second photon with at least 1 GeV energy yields 35 events selected in data compared to an expectation of 25 events. Looking at the recoil mass distribution – figure 6.6(b) – of the photon system the excess of data is not localised in a specific region, although some clustering is visible at large recoil masses, where eleven events are found for $m_{\mathrm{rec}} > 140$ GeV with 5.4 expected. Obviously, this result is too preliminary and its statistics too low to draw conclusions concerning the discovery of new physics, but possibly the gate to the supersymmetric world opens up right now.

Appendix A

Massive Neutrinos

This analysis is carried out in collaboration with Peter Molnár and is published within the L3 Collaboration as L3 Internal Note 2321 [227].

Introduction

The Standard Model uses three generations of leptons and quarks for the description of nature. Most cited evidence for the existence of three generations are LEP 1 measurements of the number of light neutrino flavours from the invisible width of the Z boson, which results in $N_\nu = 2.994 \pm 0.011$ [203]. The term "light" in this sense means that the mass of neutrino species must be less than half the Z mass in order to allow the Z to decay into these particles. A similar result $N_\nu = 3.00 \pm 0.08$ [2, 189] is achieved selecting initial state radiation events on the Z peak. These results are also interpreted as a limit on the mass of a fourth generation stable neutrino of about 45 GeV [228]. In the energy regime of LEP 2, the centre-of-mass energy is increased above the Z peak and reaches 200 GeV, allowing the production of heavy neutrinos from off-shell Z bosons, as heavy as about 100 GeV.

Since stable neutrinos are undetectable for LEP experiments, one has to exploit the fact that the beam electrons tend to emit photons before they annihilate to Z bosons. These photons are mainly emitted along the beam pipe and are thus also undetectable, but a fraction of them ends up in the detector and are thus the finger print of neutrino production.

Data Sample and Simulation

Basis of this feasibility study are results from the single photon analysis described in chapters 4 and 5.1 of about 250 pb^{-1} taken at centre-of-mass energies between $\sqrt{s} = 161$ GeV and $\sqrt{s} = 189$ GeV, as well as the expectation of 200 pb^{-1} at $\sqrt{s} = 200$ GeV. Moreover, production of heavy neutrinos is studied for a centre-of-mass energy of 500 GeV, which is proposed for a future linear collider.

The stable heavy neutrino signal is modelled with the Monte Carlo event generator `NUNUGPV` [40,41] for centre-of-mass energies of 183, 189, 200, and 500 GeV. This generator is capable of generating neutrino pairs with up to three initial state radiation photons. The Standard Model branch of this generator was already tested in [229]. In addition to three light neutrinos, a fourth generation stable heavy neutrino can be produced. This analysis is performed for five stable heavy neutrino masses of 45, 47, 60, 75, and 90 GeV based on a sample of 10000 Monte Carlo events for each neutrino mass and each centre-of-mass energy.

Distributions and Cross Sections

The energy distribution of the highest energetic photon is displayed in figure A.1. While for 45 GeV neutrinos pair-production still occurs through radiative return to the on-shell Z and the corresponding decay into two neutrinos, this is not possible for heavier neutrinos. This fact is expressed due to an accumulation of events in the Standard Model and the 45 GeV branch at E_γ/E_{beam} around 0.75, while no such accumulation is observable for heavier neutrinos. No other distinctive feature of the heavy neutrino distributions are observed. For a centre-of-mass energy of 500 GeV the importance of the radiative return in neutrino pair-production vanishes, although still visible in figure A.1(d) close to $E_\gamma \approx E_{\text{beam}}$. To account for detector response the photon energy must be larger than 5 GeV. This cut is also used in the analysis discussed in section 5.1.

Angular distributions of heavy neutrinos and Standard Model neutrinos are also very similar, as can be seen in figure A.2. The fiducial detector volume is accounted for with cuts at 14° and 166° in the polar angle θ (chapter 4). After applying these two cuts heavy neutrinos make up fractions of 0.1% to 4.6% (90 GeV to 45 GeV) of all single photon events at $\sqrt{s} = 183$ GeV and a fraction of 0.6% (all masses) at $\sqrt{s} = 500$ GeV. These numbers are displayed in more detail in figure A.1. Corresponding cross sections in the fiducial volume ranging from

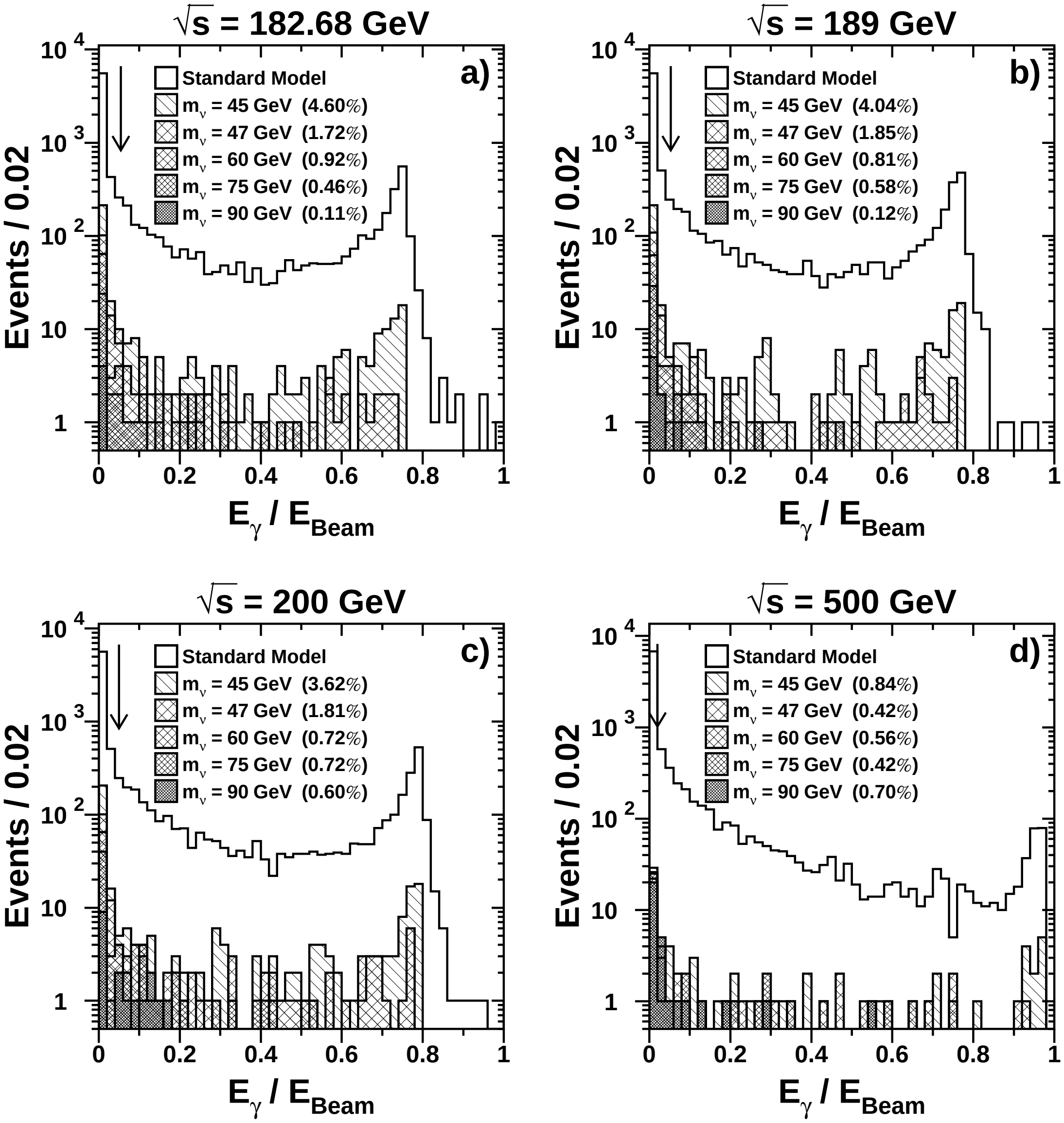

Figure A.1: *Distribution of scaled photon energy of three Standard Model neutrino flavours and stable heavy neutrinos with masses of* 45, 47, 60, 75, *and* 90 GeV *for centre-of-mass energies of* 183 GeV *(a),* 189 GeV *(b),* 200 GeV *(c), and* 500 GeV *(d). The arrow indicates the position of the phase space cut of* 5 GeV*. Numbers in brackets account for the fraction of heavy neutrino events as compared to Standard Model events for all phase space cuts (see text) applied.*

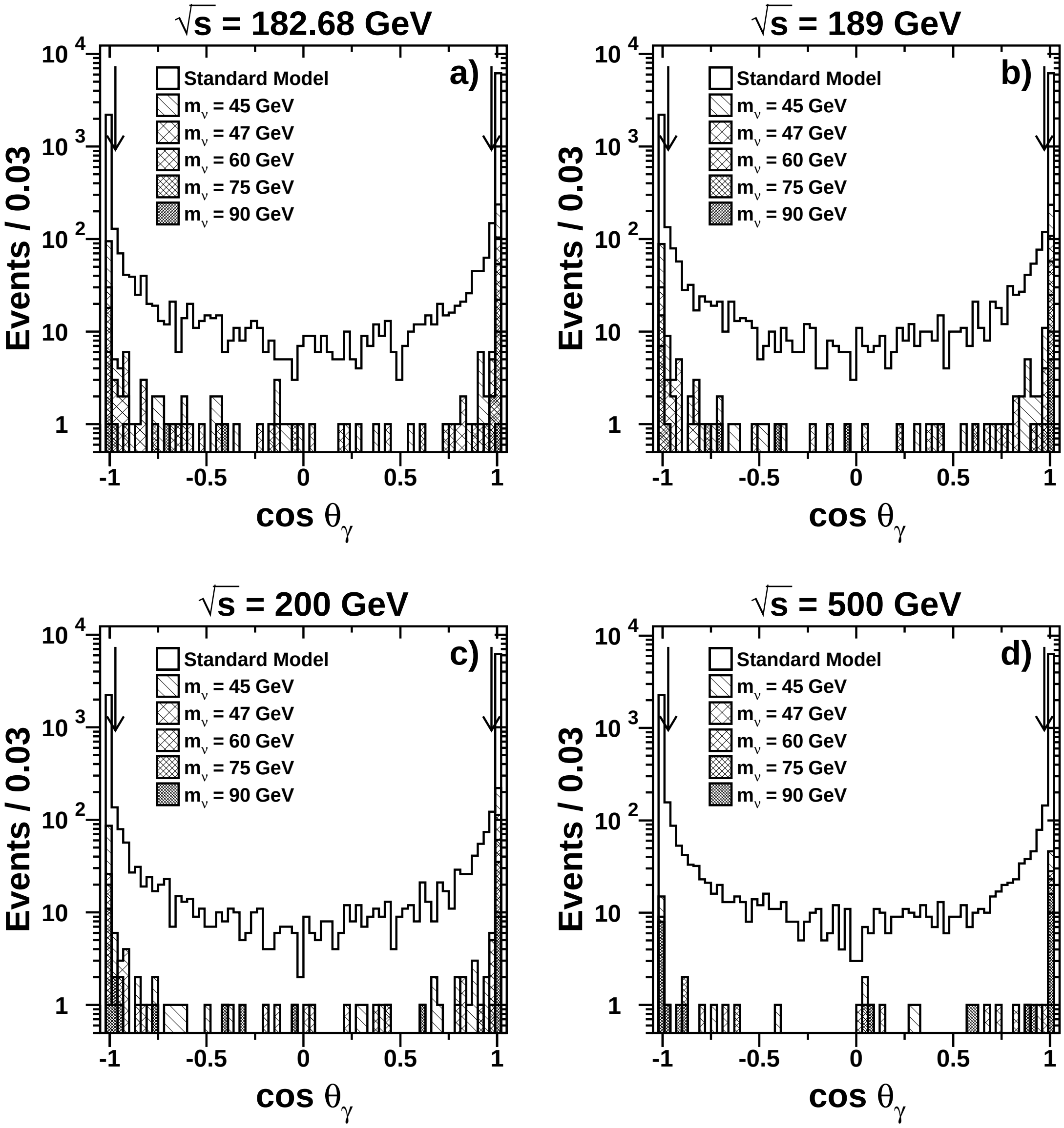

Figure A.2: *Distribution of photon polar angle of three Standard Model neutrino flavours and stable heavy neutrinos with masses of* 45, 47, 60, 75, *and* 90 GeV *for the centre-of-mass energies of* 183 GeV *(a),* 189 GeV *(b),* 200 GeV *(c), and* 500 GeV *(d). The arrow indicates the position of the phase space cuts at* 14° *and* 166°*.*

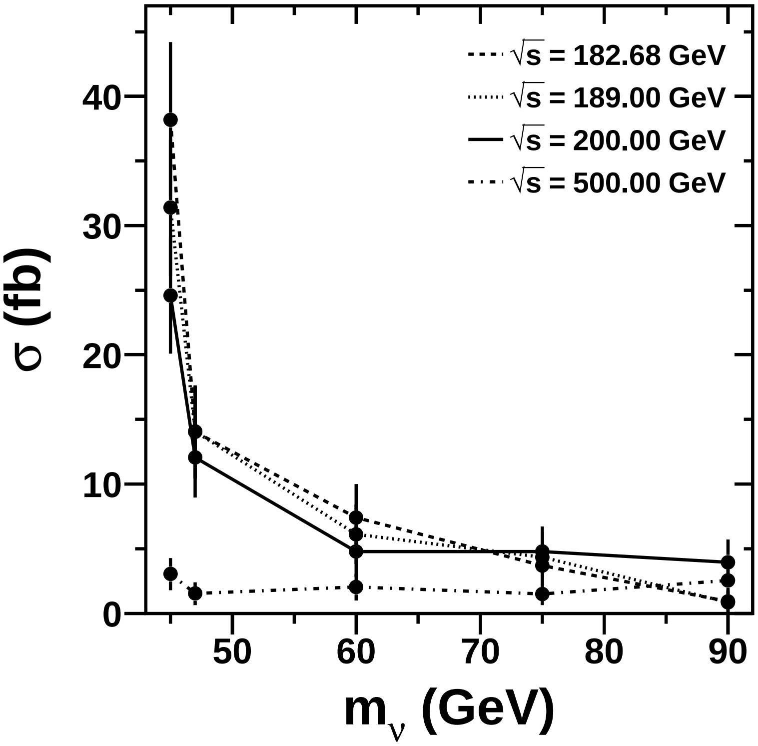

Figure A.3: *Production cross section of stable heavy neutrino pairs with accompanied photon after applying the phase space cuts of* $E_\gamma > 5$ GeV *and* $14^\circ < \theta_\gamma < 166^\circ$ *as function of the stable heavy neutrino mass* m_ν*. Lines indicate the centre-of-mass energies of* 183, 189, 200, *and* 500 GeV.

$\approx$1 fb up to $\approx$40 fb are shown in figure A.3. While for a centre-of-mass energy of $\sqrt{s} = 500$ GeV the cross section hardly changes with the mass of the heavy neutrino, this is not the case for lower centre-of-mass energies, where neutrino pair-production through radiative return still plays a dominant role.

Discovery Potential

Arguing that for discovering a new particle one needs at least an effect of five statistical standard deviations, these cross sections are converted directly into integrated luminosities needed for a discovery at LEP 2 and at future Linear Colliders. The selection efficiency of the single photon signal is assumed to be

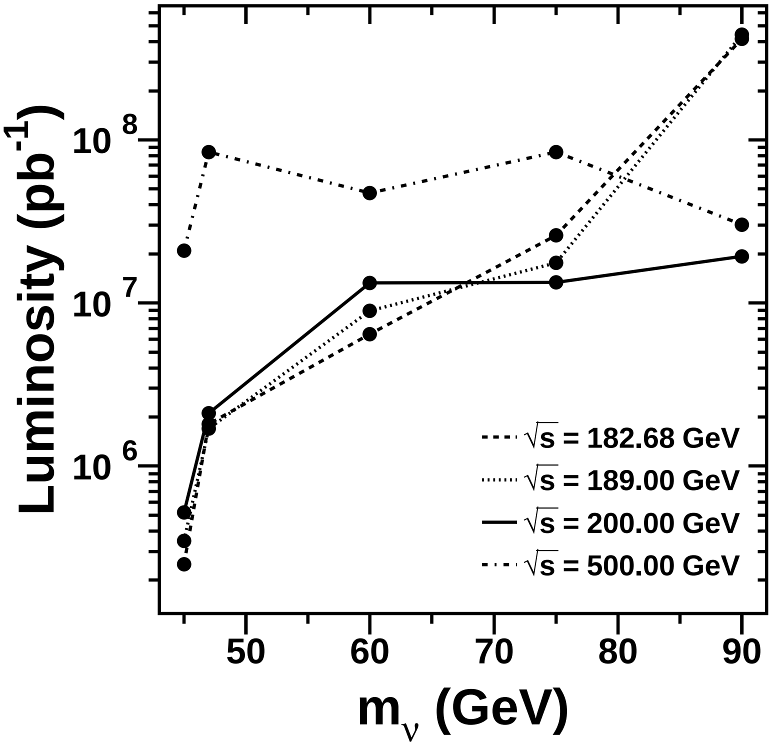

Figure A.4: *Luminosity necessary for discovering (effect of five statistical standard deviations) stable heavy neutrinos as function of the stable heavy neutrino mass. Lines indicate the centre-of-mass energies of* 183, 189, 200, *and* 500 GeV.

61% (see chapter 5.1) at all $\sqrt{s}$ values. The corresponding luminosity numbers can be read off figure A.4. A 60 GeV stable heavy neutrino can therefore only be discovered at LEP 2 if about 5000 fb^{-1} (10^6 pb^{-1}) of luminosity is collected, which is way out of reach of LEP 2 (LEP 2 luminosity = 4×250 pb^{-1} within 3 years). A discovery at the linear collider requires even more integrated luminosity.

Appendix B

Event Generators for Neutrino Pair-Production

The two Monte Carlo generators `KORALZ` [38] and `NUNUGPV` [40,41] are compared in order to estimate the systematic uncertainty on the single and multi-photon measurement introduced by the theory. The two programs are described in section 2.1.1. Differential cross sections in photon energy and angle in the single photon case (figure B.1), as well as recoil and invariant mass distributions for at least two photons in the final state (figures B.2 – B.4) produced by both programs are investigated for $\sqrt{s} = 189$ GeV.

Definition of Variables and Acceptance

The recoil mass of photon(s) is defined by equation 2.14 and the invariant mass is given by

$$m_{\mathrm{inv}} = \sqrt{E_\gamma^2 - |\vec{p}_\gamma|^2}\,, \tag{B.1}$$

where $E_\gamma = \sum_i E_{\gamma i}$ and $\vec{p}_\gamma = \sum_i \vec{p}_{\gamma i}$ are total energy and momentum of the photons. The acceptance for the single photon case is obtained by requiring the highest energetic photon of an event to have an energy greater than 5 GeV and a polar angle with respect to the beam direction larger than 10 degrees. The energy of the photon with the second highest energy has to exceed 1 GeV and its polar angle must be larger than 10 degrees to classify an event as a two-photon event. These acceptance definitions are similar to what is defined in the selection described in chapter 4.

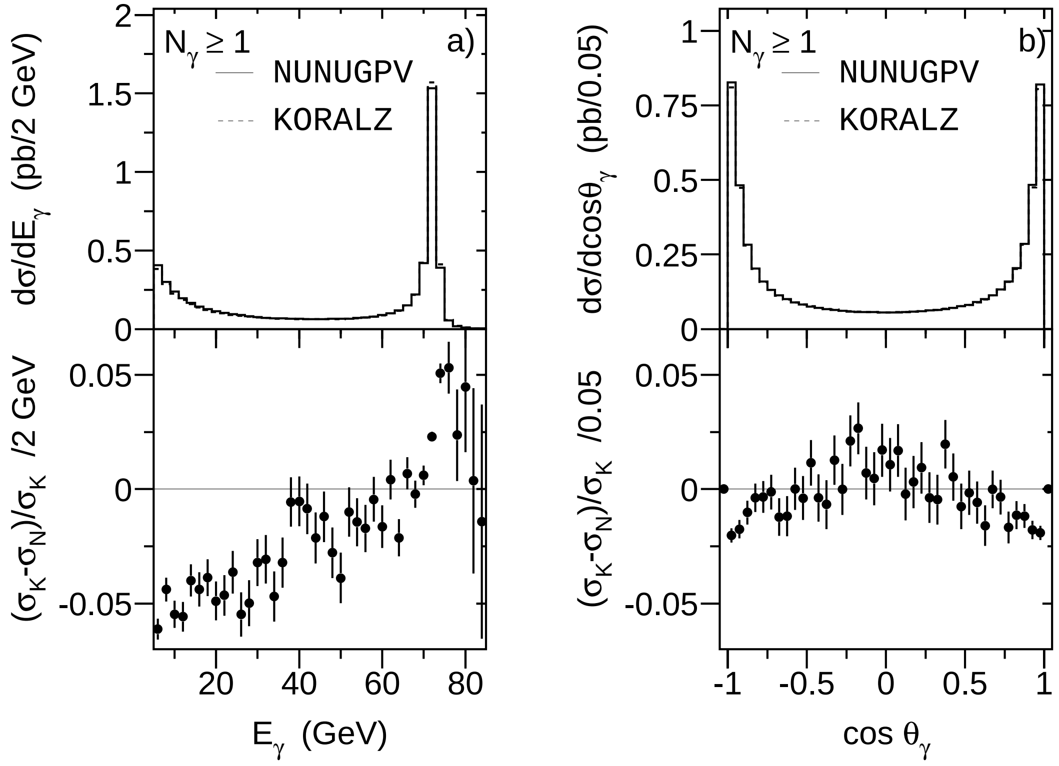

Figure B.1: *Differential cross sections in photon energy (a) and* $\cos\theta_\gamma$ *(b) for predictions of* `NUNUGPV` *(full line) and* `KORALZ` *(dashed line). There has to be at least one photon in the acceptance as defined in the text. In the lower half, the relative differences between the two programs are shown.*

Results on Total Cross Section

Total accepted cross sections as well as the number of Monte Carlo events generated for both programs are listed in table B.1. Agreement of the programs, as far as the total cross section for the single photon signature is concerned, is fairly good. Compared to an expected statistical error on the production cross section of $\sim 3\%$[1], the systematic theoretical uncertainty of 1% is rather small. A similar statement is made concerning the multi-photon sample, where the systematic theoretical error calculated from the difference between the two programs is 5%

---

[1] The statistical error is estimated on the basis of an integrated luminosity of 250 pb^{-1}, which is about the amount taken from 1996 to 1998 and a selection efficiency of $\sim 60\%$ (see section 5.1).

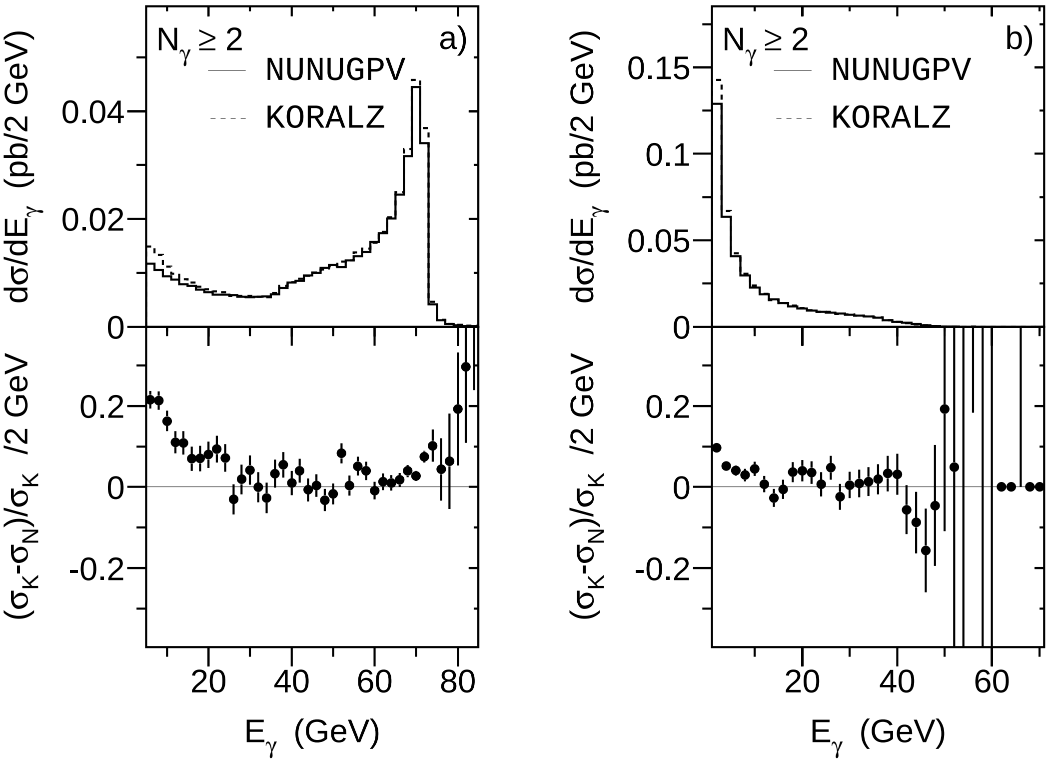

Figure B.2: *Differential cross sections in photon energy for the most energetic (a) and the second most energetic photon (b) in the event for predictions of* `NUNUGPV` *(full line) and* `KORALZ` *(dashed line). There have to be at least two photons in the acceptance as defined in the text. In the lower half, the relative differences between the two programs are shown.*

and the expected statistical error is around 12%.

Results on Differential Cross Sections

For the counting of the number of neutrino species (section 5.1.2) and new particle searches (sections 5.3 to 5.7) the uncertainty in the distributions of the relevant kinematic variables is important, too. Crucial variables in the single photon signature are the energy of the photon and its polar angle. The relative difference of the Monte Carlo predictions can be read off the lower part of figures B.1(a) for the energy and B.1(b) for the angle. Error bars in these figures account for finite statistics entering the calculations. For smaller photon energies

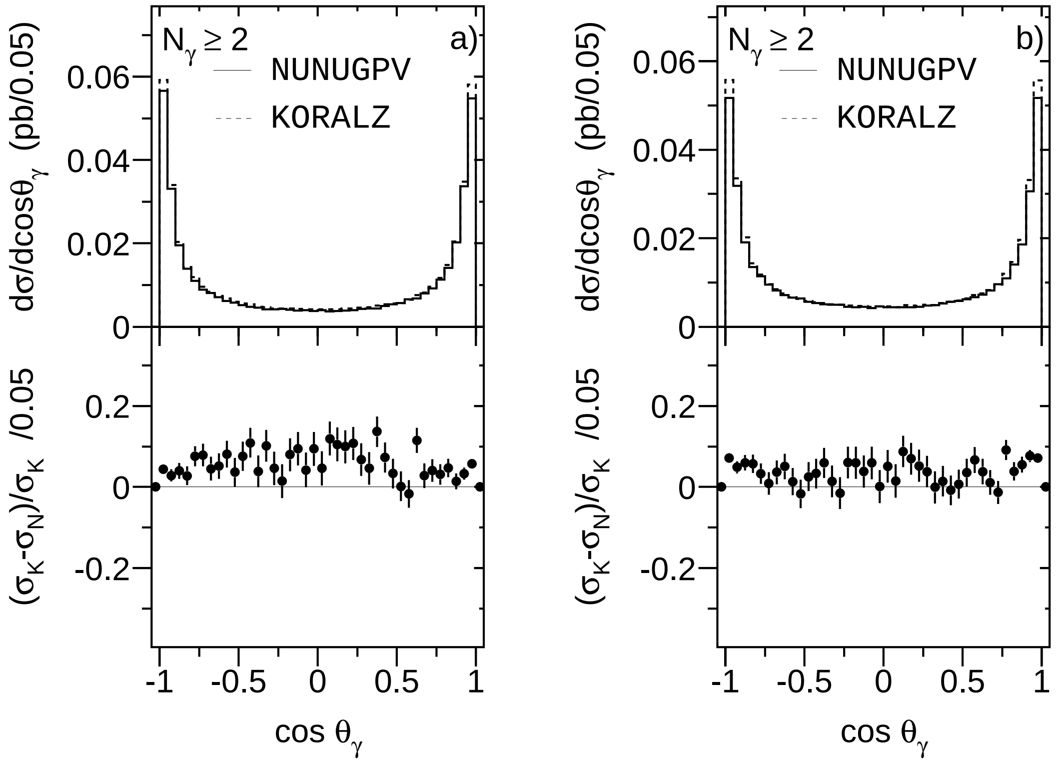

Figure B.3: *Differential cross sections in* $\cos\theta_\gamma$ *for most energetic (a) and second most energetic photon (b) in the event for predictions of* `NUNUGPV` *(full line) and* `KORALZ` *(dashed line). There have to be at least two photons in the acceptance as defined in the text. In the lower half the relative differences between the two programs are shown.*

(up to 30 GeV) the difference is about 5% and in the peak a 2.5% difference is visible. The angular distribution shows deviations up to 2%.

In the multi-photon sample differences up to 20% are visible in the energy spectra B.2. Here, especially for low energetic photons, the difference is large. Angular distributions B.3 do not show deviations in specific regions exceeding the relative difference in the total cross section of 5% and statistical fluctuations. For the recoil mass B.4(a), there is a difference of 15% to 20% in the peak region and up to 25% for large recoil masses; the invariant mass spectrum B.4(b) shows a deviation ranging from 35% for the lowest values to about 15% on average for medium invariant masses.

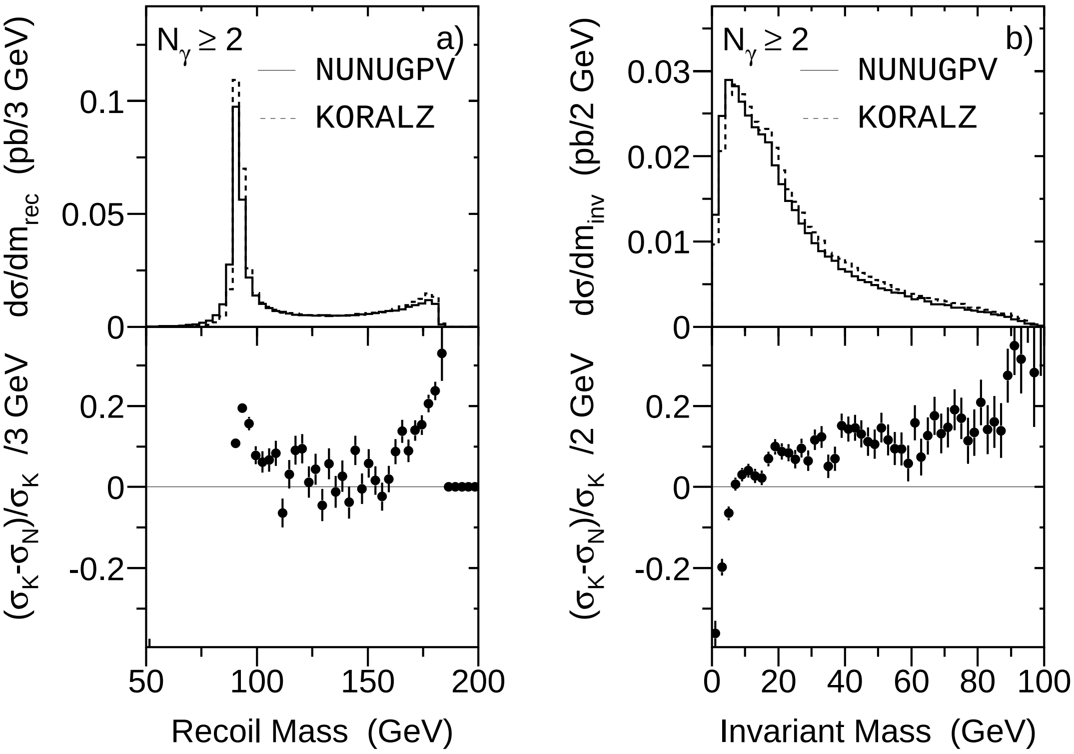

Figure B.4: *Differential cross sections in recoil mass (a) and invariant mass (b) of the multi-photon signature for predictions of* `NUNUGPV` *(full line) and* `KORALZ` *(dashed line). There have to be at least two photons in the acceptance as defined in the text. In the lower half, the relative differences between the two programs are shown.*

Conclusion

Theoretical uncertainties on total cross sections for one or two photons in the acceptance are not critical as far as comparisons with measurements are concerned (see, *e.g.*, section 5.1.1 or figure 6.3) since the experimental error is much larger. As shown in section 5.1.2, the uncertainty in the energy distribution for the single photon events does not contribute much to the total error on the number of light neutrino flavours. Concerning the multi-photon measurement, the observed discrepancy (figure 4.20(a)) is not located in the same region in the recoil mass distribution, namely for large recoil masses between about 110 GeV and 170 GeV, as the difference found in the theoretical distributions (figure B.4(a)). Therefore,

	$\nu\bar{\nu}\gamma(\gamma)$		$\nu\bar{\nu}\gamma\gamma(\gamma)$	
	Cross section	Events	Cross section	Events
`KORALZ`	6.133 pb	1572370	0.448 pb	114901
`NUNUGPV`	6.192 pb	1669605	0.426 pb	114868
Difference	0.058 pb		0.022 pb	
Rel. Difference	1%		5%	

Table B.1: *Accepted cross sections for* $e^+e^- \to \nu\bar{\nu}\gamma(\gamma)$ *and* $e^+e^- \to \nu\bar{\nu}\gamma\gamma(\gamma)$ *estimated by* ***`KORALZ`*** *and* ***`NUNUGPV`*** *and number of events generated within the acceptance as defined in the text.*

the theoretical uncertainty does not provide an explanation for the discrepancy between measurement and prediction.

Appendix C

Photon Distributions at Energies below 184 GeV

In this appendix distributions, correction factors and results for centre-of-mass energies listed in table 3.1 – except for the 189 GeV data – are presented. Details of the selection are introduced in chapter 4 and are not repeated here. Corresponding numbers for the 189 GeV data are enumerated in the above mentioned chapter.

Measurement of Energy and Angle

Figure C.1 shows energy distributions of back-to-back Bhabha scattering events as explained in section 4.2 for $\sqrt{s} = 183$ GeV. Spectra for centre-of-mass energies not displayed show a very similar behaviour. The important fit parameters P_2 and P_3, which are interpreted as shift of the peak position and BGO resolution following equation 4.2 are listed in table C.1. The resolution improves for higher centre-of-mass energies corresponding to more recent years reflecting the better understanding of the BGO calorimeter as well as the improved calibration method. For $\sqrt{s} \leq 172$ GeV the Xenon calibration method is used [144,145,230,231], whereas in more recent years (and higher centre-of-mass energies) the refined RFQ calibration reaches better results [143,232,233]. The Monte Carlo prediction is smeared during the reconstruction phase with a double Gaussian (see section 4.2) to match the data resolution.

Angular resolutions for the various centre-of-mass energies calculated in the way described in section 4.2 are listed in table C.2. Corresponding spectra are

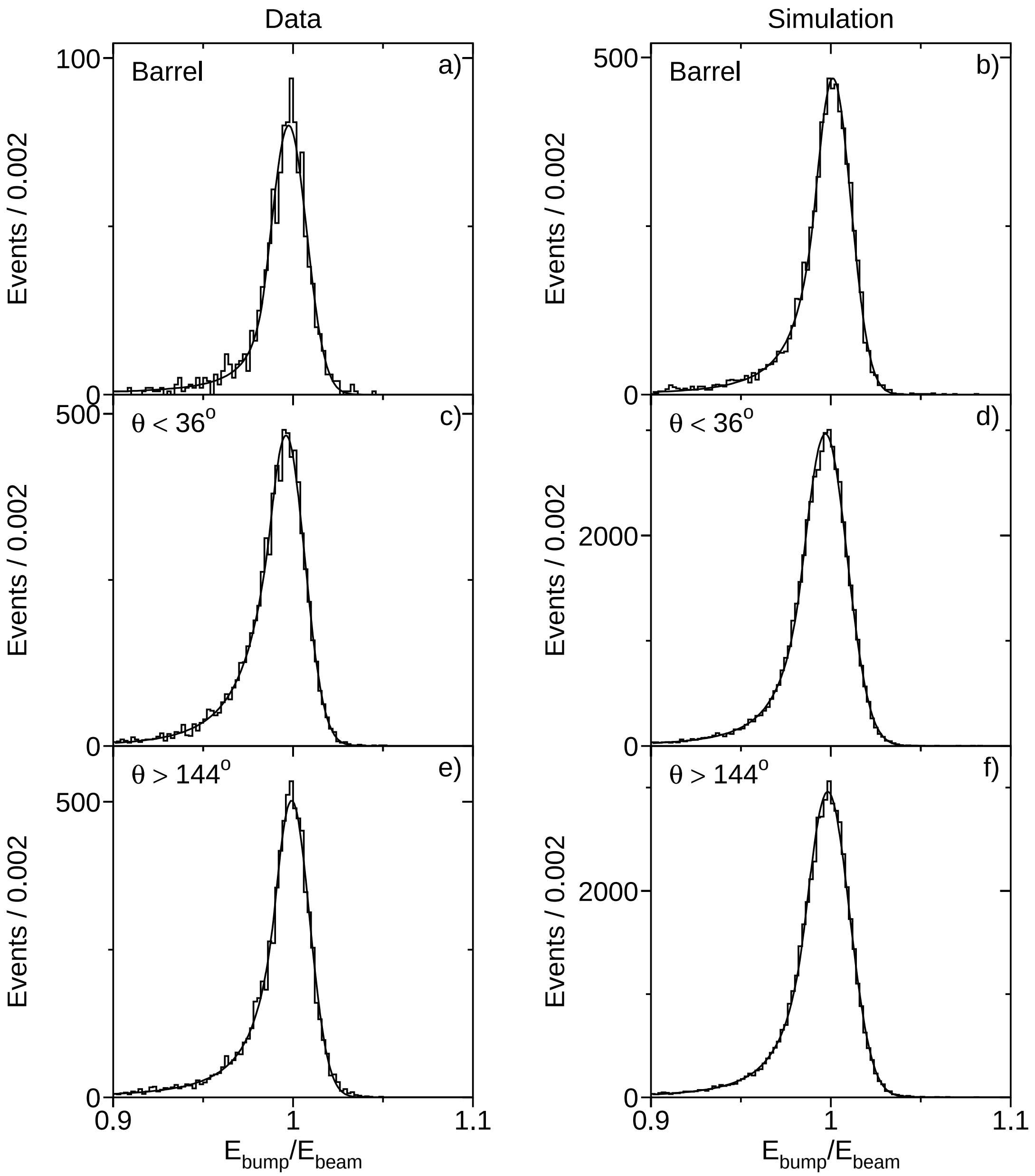

Figure C.1: *Energy distributions for data (left hand side) and Monte Carlo simulation (right hand side) normalised to beam energy for* $\sqrt{s} = 183$ GeV. *Barrel region (a and b) as well as endcap regions (c to f) are shown.*

		Barrel	Endcap $\theta < 36^\circ$	Endcap $\theta > 144^\circ$
$\sqrt{s}$ = 183 GeV				
P_2	Data	$(-2.41\pm0.45)\cdot10^{-3}$	$(-3.94\pm0.27)\cdot10^{-3}$	$(-0.81\pm0.20\cdot10^{-3}$
	MC	$(1.68\pm0.22)\cdot10^{-3}$	$(-3.032\pm0.094)\cdot10^{-3}$	$(-1.701\pm0.097)\cdot10^{-3}$
P_3	Data	$(10.01\pm0.42)\cdot10^{-3}$	$(10.43\pm0.19)\cdot10^{-3}$	$(9.95\pm0.17)\cdot10^{-3}$
	MC	$(10.02\pm0.22)\cdot10^{-3}$	$(12.12\pm0.071)\cdot10^{-3}$	$(12.05\pm0.075)\cdot10^{-3}$
$\sqrt{s}$ = 172 GeV				
P_2	Data	$(0.38\pm1.31)\cdot10^{-3}$	$(-11.36\pm0.36)\cdot10^{-3}$	$(-10.49\pm0.38)\cdot10^{-3}$
	MC	$(-0.17\pm0.67)\cdot10^{-3}$	$(-2.72\pm0.20)\cdot10^{-3}$	$(-1.65\pm0.22)\cdot10^{-3}$
P_3	Data	$(17.3\pm1.3)\cdot10^{-3}$	$(11.36\pm0.43)\cdot10^{-3}$	$(11.76\pm0.44)\cdot10^{-3}$
	MC	$(14.8\pm0.54)\cdot10^{-3}$	$(12.89\pm0.18)\cdot10^{-3}$	$(14.77\pm0.19)\cdot10^{-3}$
$\sqrt{s}$ = 161 GeV				
P_2	Data	$(-0.3\pm1.5)\cdot10^{-3}$	$(-9.66\pm0.32)\cdot10^{-3}$	$(-9.90\pm0.31)\cdot10^{-3}$
	MC	$(0.24\pm0.43)\cdot10^{-3}$	$(-2.39\pm0.15)\cdot10^{-3}$	$(-1.6\pm0.14)\cdot10^{-3}$
P_3	Data	$(17.0\pm1.8)\cdot10^{-3}$	$(11.53\pm0.40)\cdot10^{-3}$	$(11.49\pm0.38)\cdot10^{-3}$
	MC	$(15.02\pm0.38)\cdot10^{-3}$	$(12.46\pm0.14)\cdot10^{-3}$	$(14.58\pm0.16)\cdot10^{-3}$
$\sqrt{s}$ = 136 GeV				
P_2	Data	$(-1.7\pm1.4)\cdot10^{-3}$	$(-3.13\pm0.74)\cdot10^{-3}$	$(0.44\pm0.77)\cdot10^{-3}$
	MC	$(1.86\pm0.91)\cdot10^{-3}$	$(-1.93\pm0.45)\cdot10^{-3}$	$(-0.32\pm0.50)\cdot10^{-3}$
P_3	Data	$(15.0\pm1.6)\cdot10^{-3}$	$(11.40\pm0.57)\cdot10^{-3}$	$(10.32\pm0.79)\cdot10^{-3}$
	MC	$(14.75\pm0.78)\cdot10^{-3}$	$(13.03\pm0.57)\cdot10^{-3}$	$(12.22\pm0.50)\cdot10^{-3}$
$\sqrt{s}$ = 130 GeV				
P_2	Data	$(-0.7\pm1.1)\cdot10^{-3}$	$(-5.89\pm0.57)\cdot10^{-3}$	$(-1.57\pm0.52)\cdot10^{-3}$
	MC	$(2.9\pm1.5)\cdot10^{-3}$	$(-1.68\pm0.48)\cdot10^{-3}$	$(-0.63\pm0.47)\cdot10^{-3}$
P_3	Data	$(13.7\pm1.1)\cdot10^{-3}$	$(12.17\pm0.50)\cdot10^{-3}$	$(12.81\pm0.51)\cdot10^{-3}$
	MC	$(13.6\pm1.5)\cdot10^{-3}$	$(11.46\pm0.53)\cdot10^{-3}$	$(12.45\pm0.54)\cdot10^{-3}$

Table C.1: *Parameters P_2 (energy shift) and P_3 (resolution) of the fit to energy spectra (e.g. in figure C.1 at $\sqrt{s}$ = 183 GeV) for data and Monte Carlo simulation (MC) at the indicated centre-of-mass energies.*

$\sqrt{s}$ (GeV)	Data	Simulation
183	0.0788 ± 0.0020	0.0598 ± 0.0008
172	0.0875 ± 0.0072	0.0572 ± 0.0011
161	0.0960 ± 0.0063	0.0729 ± 0.0010
136	0.1180 ± 0.0123	0.0785 ± 0.0045
130	0.1111 ± 0.0098	0.0816 ± 0.0056

Table C.2: *Azimuthal angle resolution of the BGO (e.g. corresponding to figure C.2 for* $\sqrt{s} = 183$ GeV*) for data and Monte Carlo simulation at various centre-of-mass energies.*

shown in figure C.2 for $\sqrt{s} = 183$ GeV.

Veto Cuts and Detector Noise

The effect of veto cuts described in section 4.3 on detector noise for the data taking periods from 1995 to 1997 are presented in this paragraph. The analysis is performed using randomly triggered beam gate events. Figures for the various centre-of-mass energies corresponding to figures 4.8 and 4.9 are not shown due to their strong similarity to the graphs presented in section 4.3 for $\sqrt{s} = 189$ GeV. Efficiencies in the four kinematic regions defined in section 4.3 can be read from table C.3.

Trigger Efficiency

The study of the trigger efficiency described in section 4.5 is performed for all centre-of-mass energies under investigation. Graphs corresponding to figures 4.12 and 4.13 are displayed in C.3 and C.4 for $\sqrt{s} = 183$ GeV. Other centre-of-mass energies are also investigated quantitatively, but are not shown here for no qualitatively new information is provided.

Standard Model Processes and Final Selection Cuts

The processes of the Standard Model that contribute to the single and multi-photon analysis are the same for all analysed centre-of-mass energies but, of course, the cross sections vary. Therefore, the equivalents of table 4.8 in section

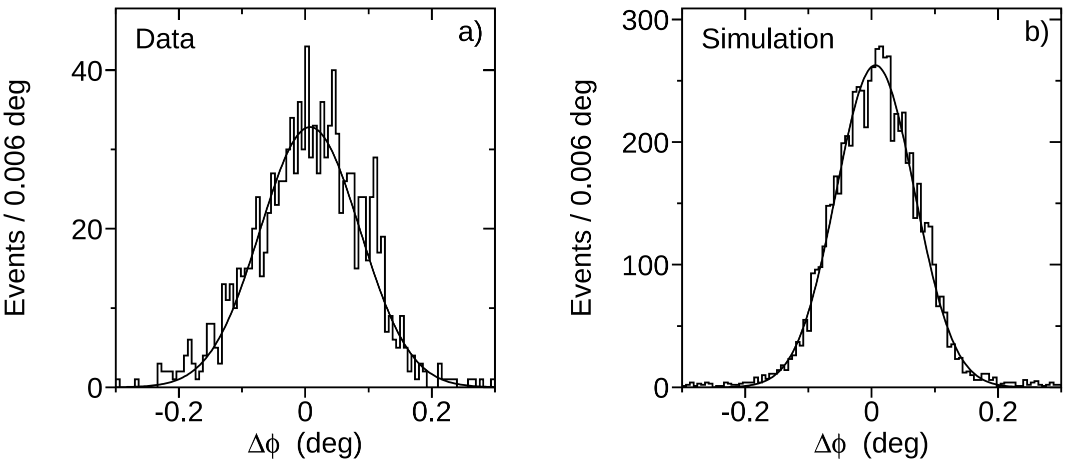

Figure C.2: *Difference in azimuthal angle between track prediction and bump measurement for data (a) and Monte Carlo simulation (b) at* $\sqrt{s} =$ 183 GeV.

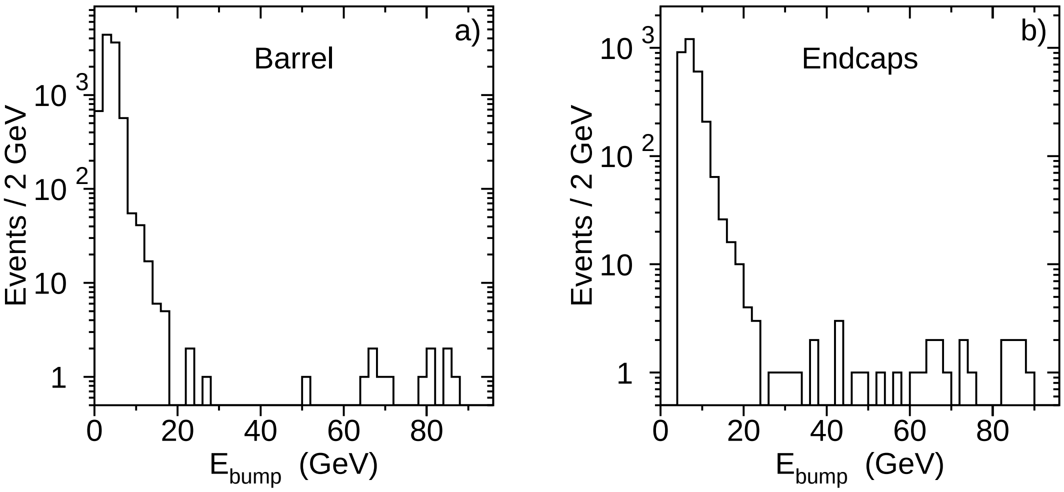

Figure C.3: *Energy spectra of the identified electromagnetic object in the "single electron" selection in barrel (a) and endcaps (b) for the* 183 GeV *data.*

$\sqrt{s} = 183$ GeV	Data	Simulation	Correction
$E_\gamma > 5$ GeV	$(99.17 \pm 0.11)\%$	100%	$(0.83 \pm 0.11)\%$
$E_\gamma > 5$ GeV $p_\mathrm{t} < 20$ GeV	$(96.67 \pm 0.11)\%$	100%	$(3.33 \pm 0.11)\%$
$p_\mathrm{t} < 10$ GeV	$(96.67 \pm 0.11)\%$	100%	$(3.33 \pm 0.11)\%$
$E_\gamma < 5$ GeV	$(96.50 \pm 0.11)\%$	$(99.993 \pm 0.005)\%$	$(3.50 \pm 0.11)\%$

$\sqrt{s} = 172$ GeV	Data	Simulation	Correction
$E_\gamma > 5$ GeV	$(98.28 \pm 0.25)\%$	$(99.948 \pm 0.020)\%$	$(1.67 \pm 0.25)\%$
$E_\gamma > 5$ GeV $p_\mathrm{t} < 20$ GeV	$(95.96 \pm 0.25)\%$	$(99.948 \pm 0.020)\%$	$(3.99 \pm 0.25)\%$
$p_\mathrm{t} < 10$ GeV	$(95.85 \pm 0.25)\%$	$(99.948 \pm 0.020)\%$	$(4.10 \pm 0.25)\%$
$E_\gamma < 5$ GeV	$(95.79 \pm 0.25)\%$	$(98.32 \pm 0.11)\%$	$(2.57 \pm 0.27)\%$

$\sqrt{s} = 161$ GeV	Data	Simulation	Correction
$E_\gamma > 5$ GeV	$(99.07 \pm 0.22)\%$	100%	$(0.93 \pm 0.22)\%$
$E_\gamma > 5$ GeV $p_\mathrm{t} < 20$ GeV	$(97.55 \pm 0.22)\%$	100%	$(2.45 \pm 0.22)\%$
$p_\mathrm{t} < 10$ GeV	$(97.45 \pm 0.22)\%$	100%	$(2.55 \pm 0.22)\%$
$E_\gamma < 5$ GeV	$(97.32 \pm 0.22)\%$	$(98.51 \pm 0.15)\%$	$(1.21 \pm 0.27)\%$

$\sqrt{s} = 136$ GeV	Data	Simulation	Correction
$E_\gamma > 5$ GeV	$(99.45 \pm 0.25)\%$	100%	$(0.55 \pm 0.25)\%$
$E_\gamma > 5$ GeV $p_\mathrm{t} < 20$ GeV	$(92.07 \pm 0.26)\%$	100%	$(7.93 \pm 0.26)\%$
$p_\mathrm{t} < 10$ GeV	$(92.05 \pm 0.26)\%$	100%	$(7.95 \pm 0.26)\%$
$E_\gamma < 5$ GeV	$(91.93 \pm 0.26)\%$	$(97.86 \pm 0.64)\%$	$(6.06 \pm 0.67)\%$

$\sqrt{s} = 130$ GeV	Data	Simulation	Correction
$E_\gamma > 5$ GeV	$(99.57 \pm 0.23)\%$	100%	$(0.43 \pm 0.23)\%$
$E_\gamma > 5$ GeV $p_\mathrm{t} < 20$ GeV	$(95.47 \pm 0.23)\%$	100%	$(4.53 \pm 0.23)\%$
$p_\mathrm{t} < 10$ GeV	$(95.43 \pm 0.23)\%$	100%	$(4.57 \pm 0.23)\%$
$E_\gamma < 5$ GeV	$(95.09 \pm 0.23)\%$	$(97.86 \pm 0.64)\%$	$(2.83 \pm 0.68)\%$

Table C.3: *Veto cut efficiencies in 1995 to 1997 for the four kinematic regions used in this analysis. Efficiency for data is estimated using beam gate events, whereas for simulation a $\nu\bar{\nu}$ Monte Carlo program is used.*

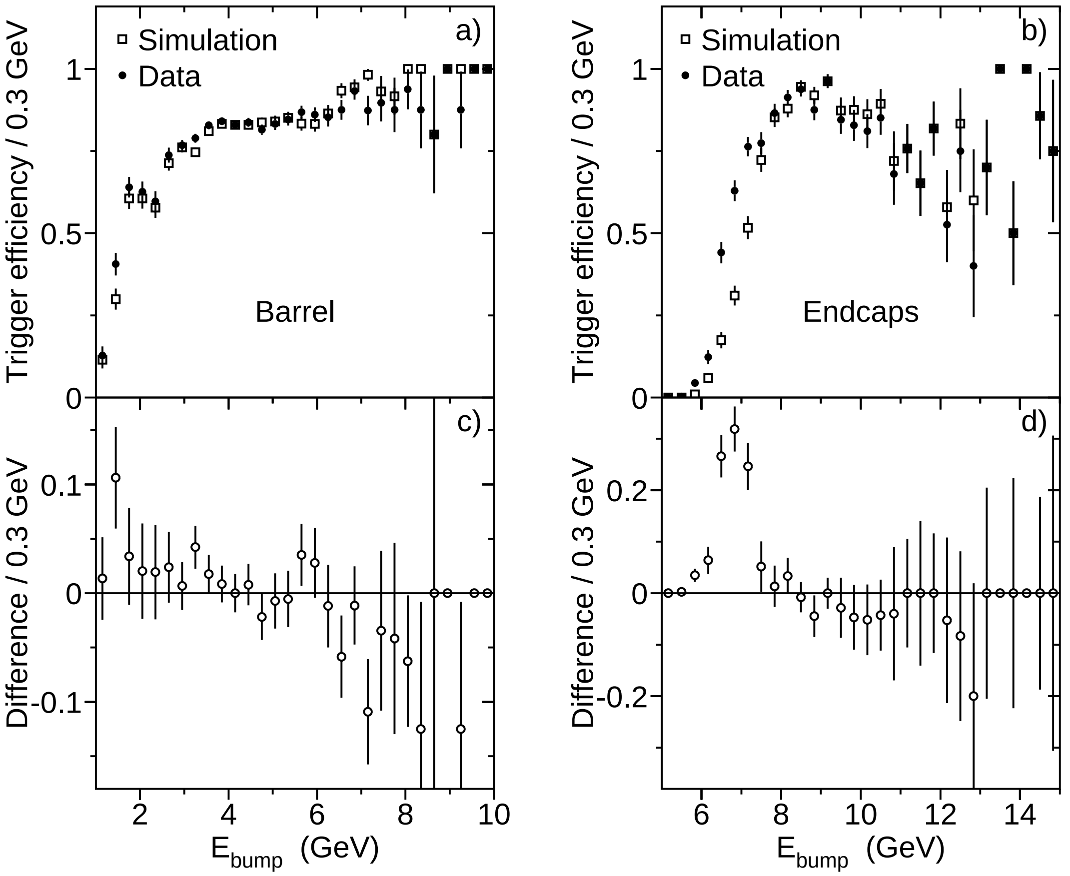

Figure C.4: *Trigger efficiency in barrel (a) and endcaps (b) and correction for bad simulation in barrel (c) and endcaps (d) for* 183 GeV *data.*

4.6 are shown in tables C.4 and C.5. For centre-of-mass energies higher than 180 GeV, the wide angle Bhabha generator `BHWIDE` has a smaller theoretical error [234] than the program `BHAGENE` [235]. Hence, `BHWIDE` is used from $\sqrt{s}$ = 183 GeV upwards. Low angle Bhabha scattering events, simulated with `TEEGG`, include the fourth order contribution, *i.e.* up to two hard photons, only for centre-of-mass energies above 180 GeV. Below this energy, weighted events with only one hard photon are generated explaining the difference in cross sections.

Distributions of variables used in the multi-photon analysis when $E_{\gamma_2} >$ 5 GeV are shown in figure C.5 for $\sqrt{s}$ = 183 GeV. Remaining centre-of-mass energies are not displayed since the statistics is very low and the cuts do not have a large impact.

$\sqrt{s} = 183$ GeV				
$e^+e^- \rightarrow$	Generator	Cross section (pb)	Kinematic region	Events generated
$\nu\bar{\nu}(\gamma)$	`KORALZ` [38]	60.37		199897
$\gamma\gamma(\gamma)$	`GGG` [183]	23.36	$\lvert\cos\theta_{\gamma_{1,2}}\rvert < 0.996$	48095
$e^+e^-(\gamma)$	`BHWIDE` [179]	4292.00	$\lvert\cos\theta_{e_{1,2}}\rvert < 0.996$	1361236
$e^+e^-\gamma(\gamma)$	`TEEGG` [184]	3707.07	$\lvert\cos\theta_{e_1}\rvert > 0.982$	499425
$e^+e^-e^+e^-$	`DIAG36` [185]	680.94	$\lvert\cos\theta_{e_{3,4}}\rvert < 0.985$ $m_{e_3e_4} > 3$ GeV	209872
$e^+e^-\nu\bar{\nu}(\gamma)$	`EXCALIBUR` [186]	0.84	$\lvert\cos\theta_{e_1}\rvert < 0.996$	23965

$\sqrt{s} = 172$ GeV				
$e^+e^- \rightarrow$	Generator	Cross section (pb)	Kinematic region	Events generated
$\nu\bar{\nu}(\gamma)$	`KORALZ` [38]	66.61		99978
$\gamma\gamma(\gamma)$	`GGG` [183]	26.29	$\lvert\cos\theta_{\gamma_{1,2}}\rvert < 0.996$	30000
$e^+e^-(\gamma)$	`BHAGENE` [235]	1930.60	$\lvert\cos\theta_{e_{1,2}}\rvert < 0.99$	520052
$e^+e^-\gamma(\gamma)$	`TEEGG` [184]	9974.60	$\lvert\cos\theta_{e_1}\rvert > 0.994$	422008
$e^+e^-e^+e^-$	`DIAG36` [185]	2889.80	$\lvert\cos\theta_{e_{3,4}}\rvert < 0.985$ $m_{e_3e_4} > 1.5$ GeV	101818

$\sqrt{s} = 161$ GeV				
$e^+e^- \rightarrow$	Generator	Cross section (pb)	Kinematic region	Events generated
$\nu\bar{\nu}(\gamma)$	`KORALZ` [38]	72.06		50000
$\gamma\gamma(\gamma)$	`GGG` [183]	30.10	$\lvert\cos\theta_{\gamma_{1,2}}\rvert < 0.996$	30000
$e^+e^-(\gamma)$	`BHAGENE` [235]	2195.31	$\lvert\cos\theta_{e_{1,2}}\rvert < 0.99$	427913
$e^+e^-\gamma(\gamma)$	`TEEGG` [184]	10744.45	$\lvert\cos\theta_{e_1}\rvert > 0.98$	468226
$e^+e^-e^+e^-$	`DIAG36` [185]	2813.50	$\lvert\cos\theta_{e_{3,4}}\rvert < 0.985$ $m_{e_3e_4} > 1.5$ GeV	120000

Table C.4: *Monte Carlo programs used, cross sections at* $\sqrt{s} = 183$ GeV, 172 GeV *and* 161 GeV *within the indicated kinematic regions, and number of events generated.*

$\sqrt{s}$ = 136 GeV				
$e^+e^- \rightarrow$	Generator	Cross section (pb)	Kinematic region	Events generated
$\nu\bar{\nu}(\gamma)$	`KORALZ` [38]	105.40		5000
$\gamma\gamma(\gamma)$	`GGG` [183]	42.30	$\lvert\cos\theta_{\gamma 1,2}\rvert < 0.996$	4986
$e^+e^-(\gamma)$	`BHAGENE` [235]	3062.50	$\lvert\cos\theta_{e_{1,2}}\rvert < 0.99$	48889
$e^+e^-\gamma(\gamma)$	`TEEGG` [184]	199.30	$\lvert\cos\theta_{e_1}\rvert > 0.99$ $\lvert\cos\theta_{e_2}\rvert < 0.99$ $\lvert\cos\theta_{\gamma}\rvert > 0.99$	998
$e^+e^-e^+e^-$	`DIAG36` [185]	1189.00	$\lvert\cos\theta_{e_{3,4}}\rvert < 0.829$ $m_{e_3e_4} > 1$ GeV	99916

$\sqrt{s}$ = 130 GeV				
$e^+e^- \rightarrow$	Generator	Cross section (pb)	Kinematic region	Events generated
$\nu\bar{\nu}(\gamma)$	`KORALZ` [38]	119.80		5000
$\gamma\gamma(\gamma)$	`GGG` [183]	45.57	$\lvert\cos\theta_{\gamma 1,2}\rvert < 0.996$	5000
$e^+e^-(\gamma)$	`BHAGENE` [235]	3351.00	$\lvert\cos\theta_{e_{1,2}}\rvert < 0.99$	45420
$e^+e^-\gamma(\gamma)$	`TEEGG` [184]	219.60	$\lvert\cos\theta_{e_1}\rvert > 0.99$ $\lvert\cos\theta_{e_2}\rvert < 0.99$ $\lvert\cos\theta_{\gamma}\rvert > 0.99$	998
$e^+e^-e^+e^-$	`DIAG36` [185]	1293.80	$\lvert\cos\theta_{e_{3,4}}\rvert < 0.829$ $m_{e_3e_4} > 1$ GeV	99976

Table C.5: *Monte Carlo programs used, cross sections at* $\sqrt{s}$ = 136 GeV *and* 130 GeV *within the indicated kinematic regions, and number of events generated.*

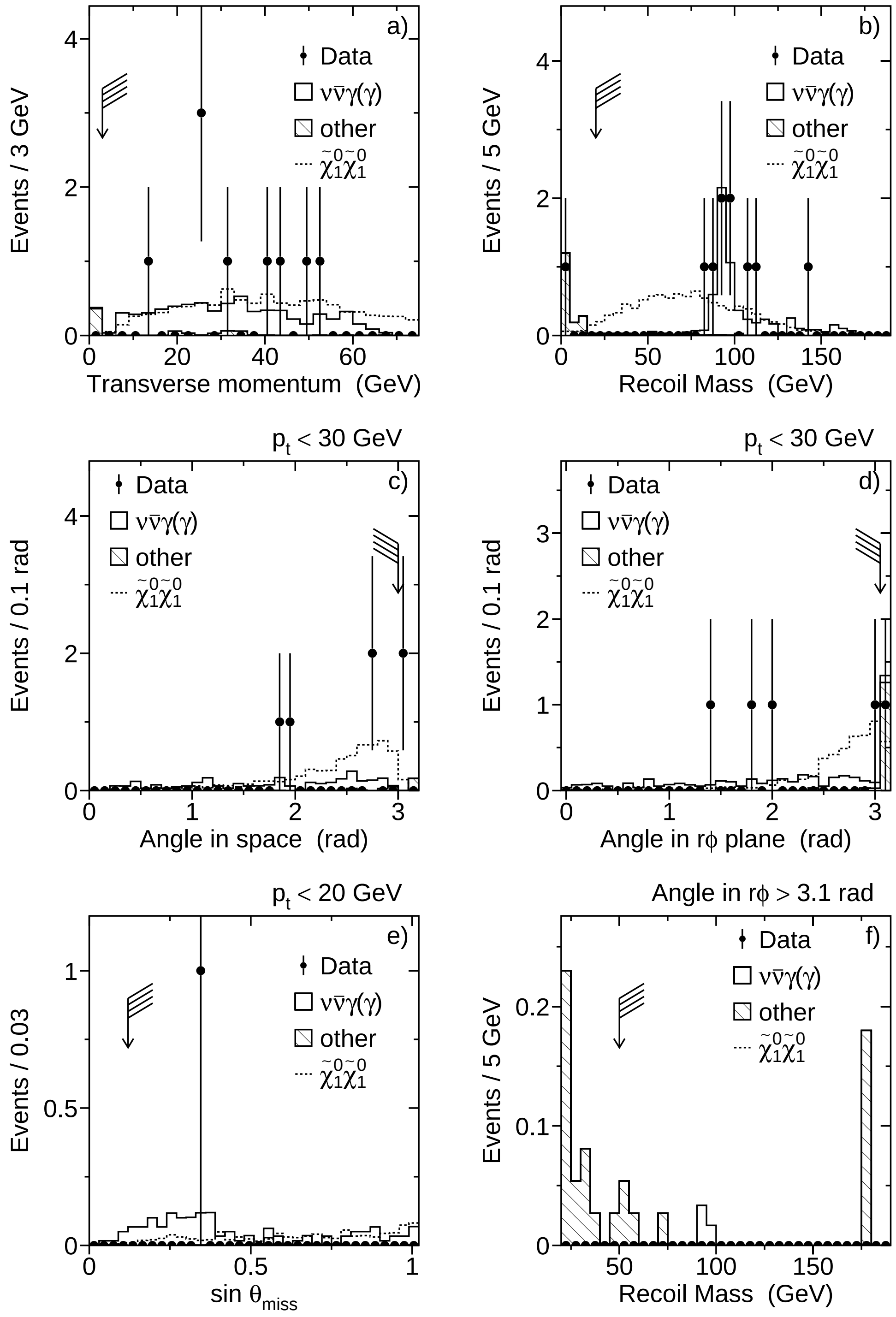

Figure C.5: *Distributions of variables used if* $E_{\gamma_2} > 5$ GeV *for* $\sqrt{s} =$ 183 GeV. *Arrows indicate cut positions.*

	$E_\gamma > 5$ GeV	$E_\gamma < 5$ GeV
$\sqrt{s} = 183$ GeV		
Efficiency	$(0.41 \pm 0.20)\%$	$(0.174 \pm 0.087)\%$
Number of cosmics expected	2.9 ± 1.4	1.70 ± 0.85
$\sqrt{s} = 172$ GeV		
Efficiency	$(0.36 \pm 0.36)\%$	$(0.16 \pm 0.16)\%$
Number of cosmics expected	0.72 ± 0.72	0.85 ± 0.85
$\sqrt{s} = 161$ GeV		
Efficiency	$(0.70 \pm 0.41)\%$	0% ($\leq 0.37\%$ at 95% C.L.)
Number of cosmics expected	2.3 ± 1.3	≤ 2.9 at 95% C.L.
$\sqrt{s} = 136$ GeV		
Efficiency	$(1.03 \pm 0.72)\%$	$(1.06 \pm 0.53)\%$
Number of cosmics expected	1.47 ± 1.03	3.2 ± 1.6
$\sqrt{s} = 130$ GeV		
Efficiency	$(0.63 \pm 0.62)\%$	$(0.27 \pm 0.27)\%$
Number of cosmics expected	0.93 ± 0.92	0.8 ± 0.8

Table C.6: *Cosmic selection efficiency and number of expected events with cosmic origin in the final sample for* $\sqrt{s} = 183$ GeV *to* 130 GeV.

Cosmics Contamination

The cosmics contamination found in data sets from 130 GeV to 183 GeV centre-of-mass energies is calculated regarding the method described in sections 4.4 and 4.7. The number of cosmic events expected and the selection efficiency corresponding to table 4.11 are listed in tables C.6 for the lower centre-of-mass energies.

The additional correction introduced by the μfit cut due to muon chamber noise is computed for each data set separately. Because distributions for the respective energy points look very similar, they are not shown here. Only values for correction factors are listed in table C.7.

$\sqrt{s}$	Barrel	Endcap $\theta < 36°$	Endcap $\theta > 144°$
183 GeV	$(2.20 \pm 0.15)\%$	$(2.35 \pm 0.30)\%$	$(2.63 \pm 0.32)\%$
172 GeV	$(1.51 \pm 0.27)\%$	$(2.59 \pm 0.71)\%$	$(2.22 \pm 0.66)\%$
161 GeV	$(1.53 \pm 0.25)\%$	$(2.80 \pm 0.77)\%$	$(2.39 \pm 0.68)\%$
136 GeV	$(1.17 \pm 0.24)\%$	$(2.12 \pm 1.05)\%$	$(0.48 \pm 0.48)\%$
130 GeV	$(0.89 \pm 0.20)\%$	$(3.65 \pm 1.27)\%$	$(2.18 \pm 0.97)\%$

Table C.7: *Correction factors due to the μfit cut derived form "single electron" events for* $\sqrt{s} = 130$ GeV *to* 183 GeV.

Results of the Selection

Measured single photon spectra for the individual data sets are displayed in figures C.6 to C.10. For $\sqrt{s} = 130$ GeV and 136 GeV the low energy part ($E_\gamma < 5$ GeV) is missing, for here, the dominant background of low angle radiative Bhabha scattering is not simulated. The corresponding event rates are enumerated in table C.8. For the multi-photon subset ($E_{\gamma_1} > 5$ GeV and $E_{\gamma_2} > 1$ GeV), the respective graphs are found in figures C.11 for recoil and invariant mass, while table C.8 shows measured and expected event rates.

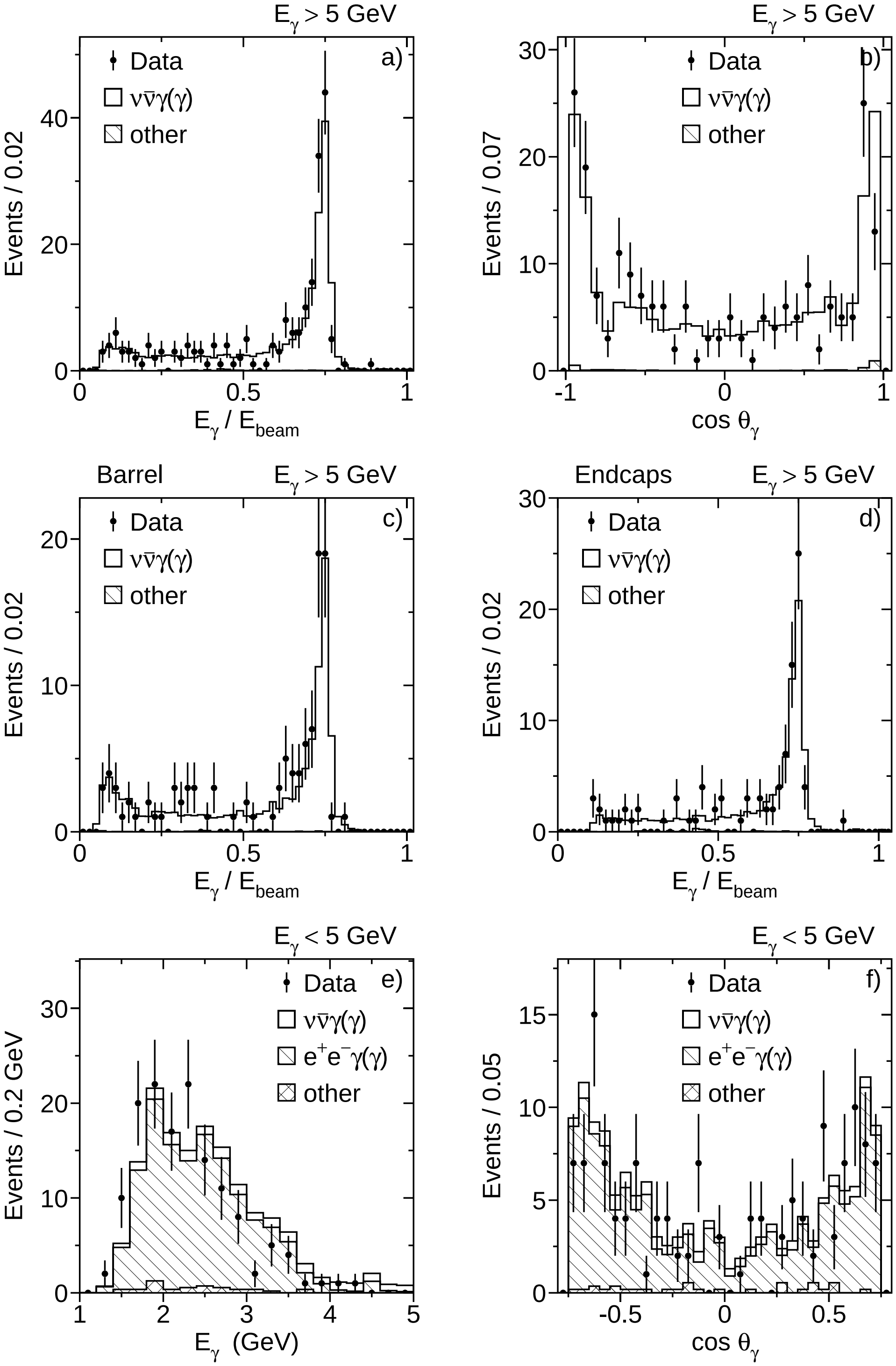

Figure C.6: *Distributions of hard photon selection (a–d) and soft photons (e,f) for* $\sqrt{s} = 183$ GeV.

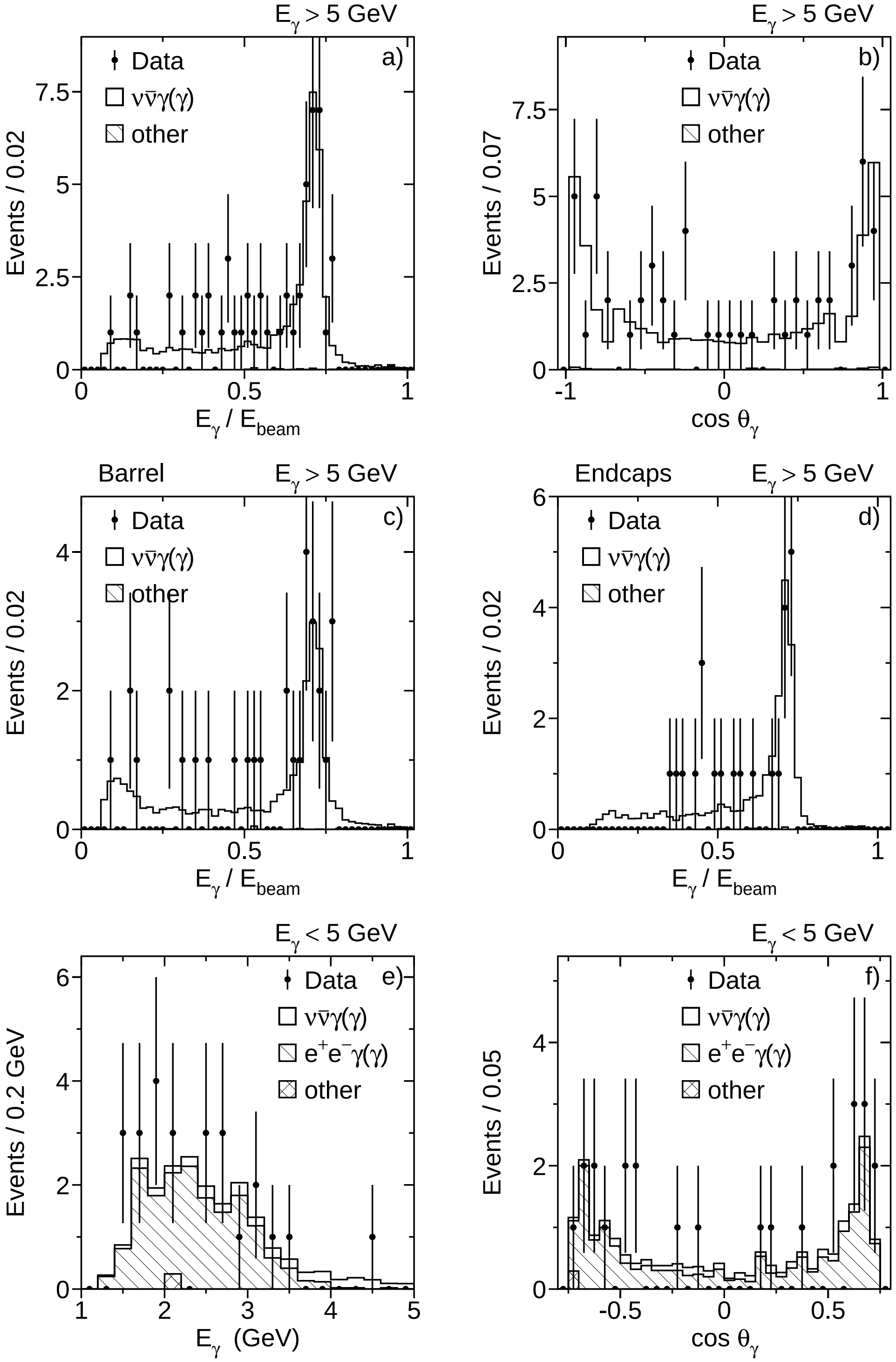

Figure C.7: *Distributions of hard photon selection (a–d) and soft photons (e,f) for* $\sqrt{s} = 172$ GeV.

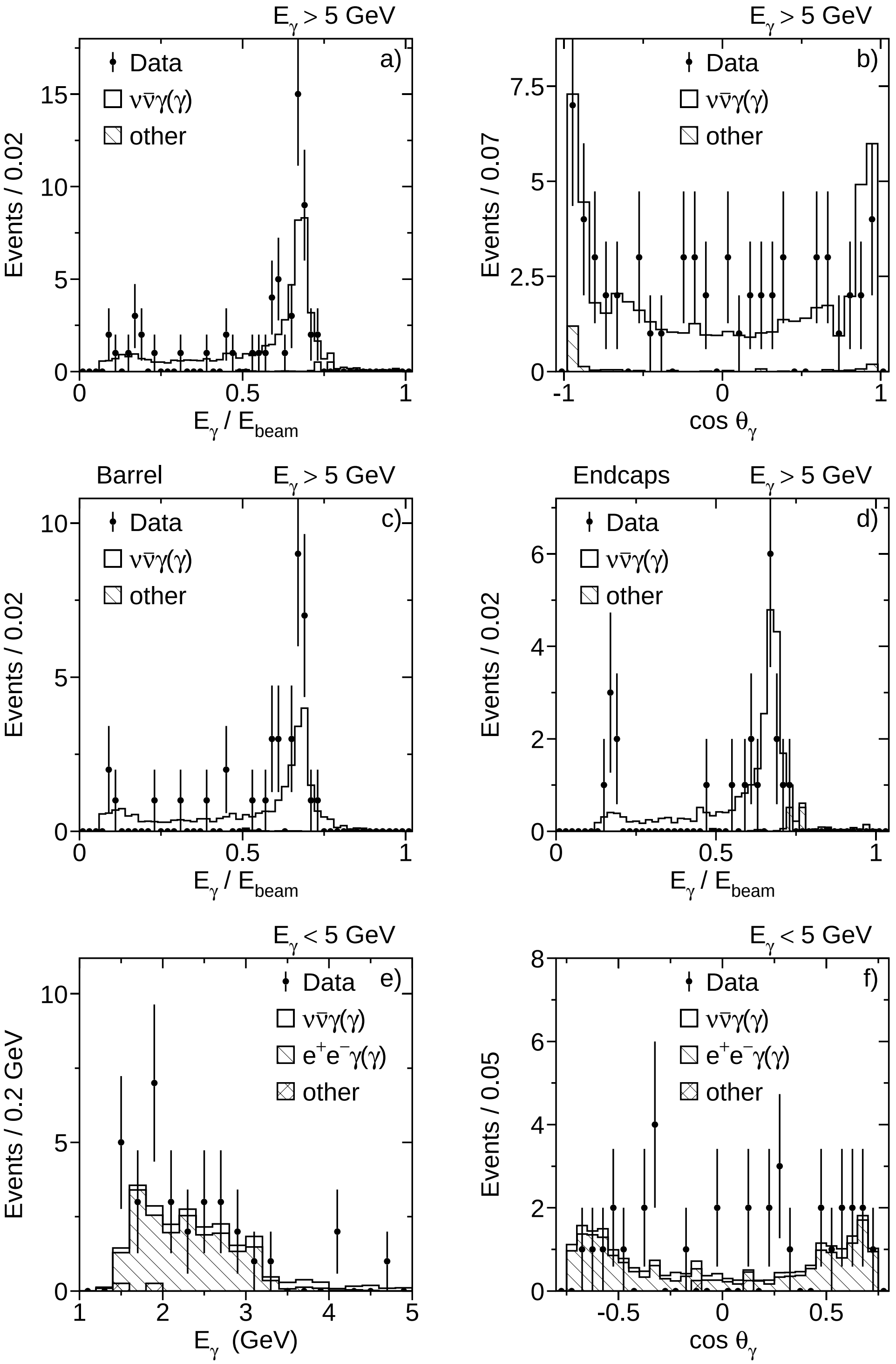

Figure C.8: *Distributions of hard photon selection (a–d) and soft photons (e,f) for* $\sqrt{s} = 161$ GeV.

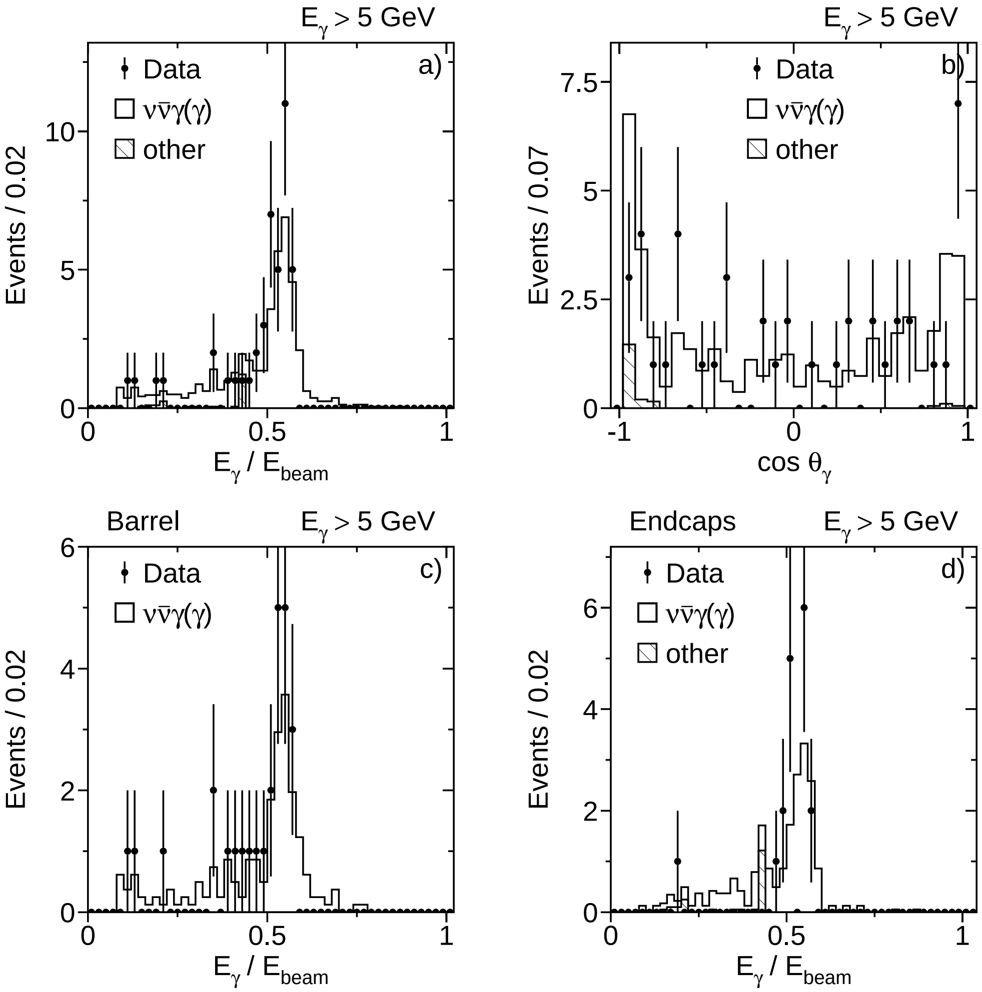

Figure C.9: *Distributions of hard photon selection (a–d) for* $\sqrt{s} = 136$ GeV.

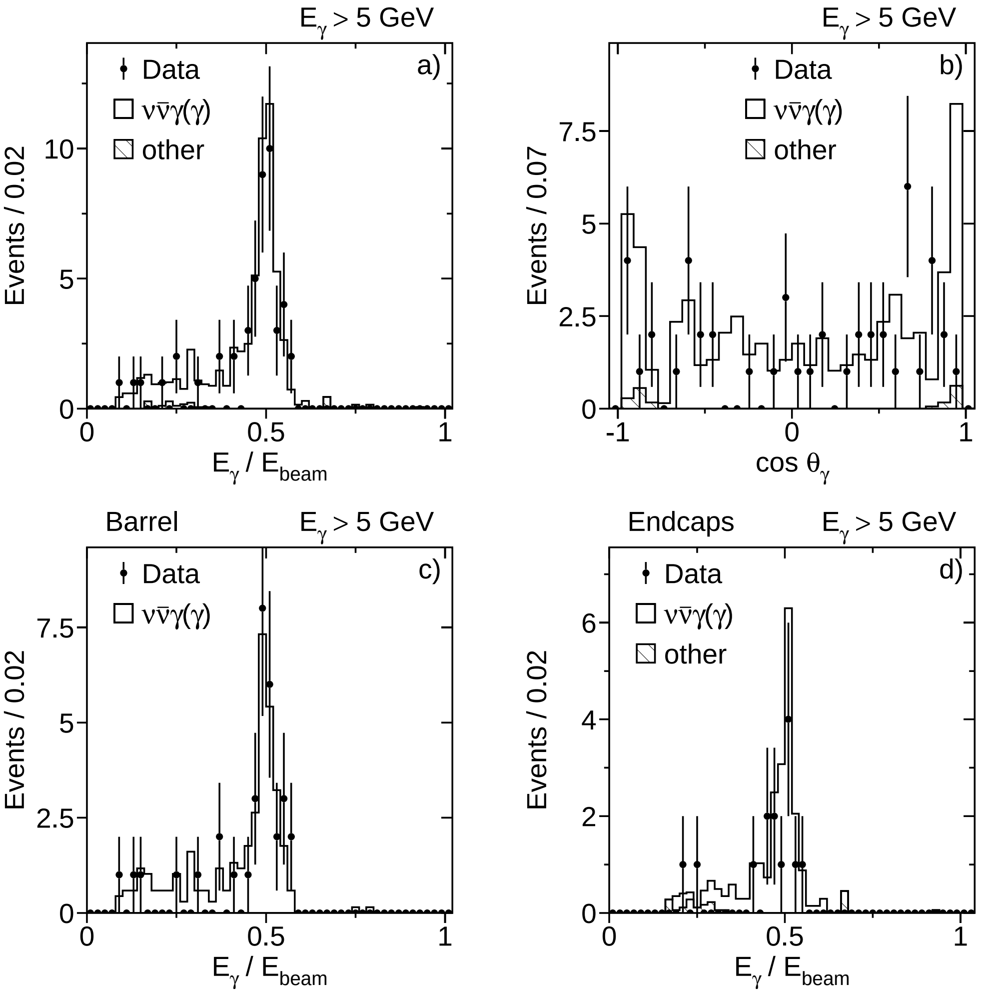

Figure C.10: *Distributions of hard photon selection (a–d) for* $\sqrt{s} = 130$ GeV.

$\sqrt{s}$	Region		Data	$\nu\bar{\nu}\gamma(\gamma)$	$e^+e^-(\gamma)$	$\gamma\gamma(\gamma)$	$e^+e^-e^+e^-$	$e^+e^-\nu\bar{\nu}(\gamma)$	Cosmics	Total
183 GeV	$E_\gamma > 5$ GeV	Total	202	192.0	1.4	0.6	0	0.4	2.9	197.3
		Barrel	107	99.5	0.1	0.3	0	0.2	1.0	101.1
		Endcap	95	92.5	1.3	0.3	0	0.2	1.9	96.2
	$E_\gamma < 5$ GeV		141	16.2	129.2	0	5.4	0	1.7	152.5
	$E_{\gamma1} > 5$ GeV, $E_{\gamma2} > 1$ GeV		14	12.0	0.1	0.2	0	0.1	0	12.4
172 GeV	$E_\gamma > 5$ GeV	Total	54	44.3	0.1	0.3	0	–	0.7	45.4
		Barrel	30	22.3	0	0.1	0	–	0.2	22.6
		Endcap	24	22.0	0.1	0.2	0	–	0.5	22.8
	$E_\gamma < 5$ GeV		25	3.0	17.0	0	0.3	–	0.9	21.2
	$E_{\gamma1} > 5$ GeV, $E_{\gamma2} > 1$ GeV		4	3.2	0.1	0	0	–	0	3.3
161 GeV	$E_\gamma > 5$ GeV	Total	59	52.5	1.4	0.6	0	–	2.3	56.8
		Barrel	37	27.7	0.1	0.3	0	–	0.8	28.9
		Endcap	22	24.8	1.3	0.3	0	–	1.5	27.9
	$E_\gamma < 5$ GeV		33	3.6	18.7	0	0.5	–	0	22.8
	$E_{\gamma1} > 5$ GeV, $E_{\gamma2} > 1$ GeV		2	3.9	0.3	0.1	0	–	0	4.3
136 GeV	$E_\gamma > 5$ GeV	Total	43	41.0	1.2	0.8	0	–	1.5	44.5
		Barrel	26	22.2	0	0	0	–	0.5	22.7
		Endcap	17	18.8	1.2	0.8	0	–	1.0	21.8
	$E_{\gamma1} > 5$ GeV, $E_{\gamma2} > 1$ GeV		3	2.5	0	0	0	–	0	2.5
130 GeV	$E_\gamma > 5$ GeV	Total	47	58.7	0.5	1.4	0	–	0.9	61.5
		Barrel	33	37.2	0	0	0	–	0.3	37.5
		Endcap	14	21.5	0.5	1.4	0	–	0.6	24.0
	$E_{\gamma1} > 5$ GeV, $E_{\gamma2} > 1$ GeV		1	5.3	0.5	0	0	–	0	5.8

Table C.8: *Number of events selected in data and Monte Carlo predictions for Standard Model processes that contribute at the indicated centre-of-mass energies.*

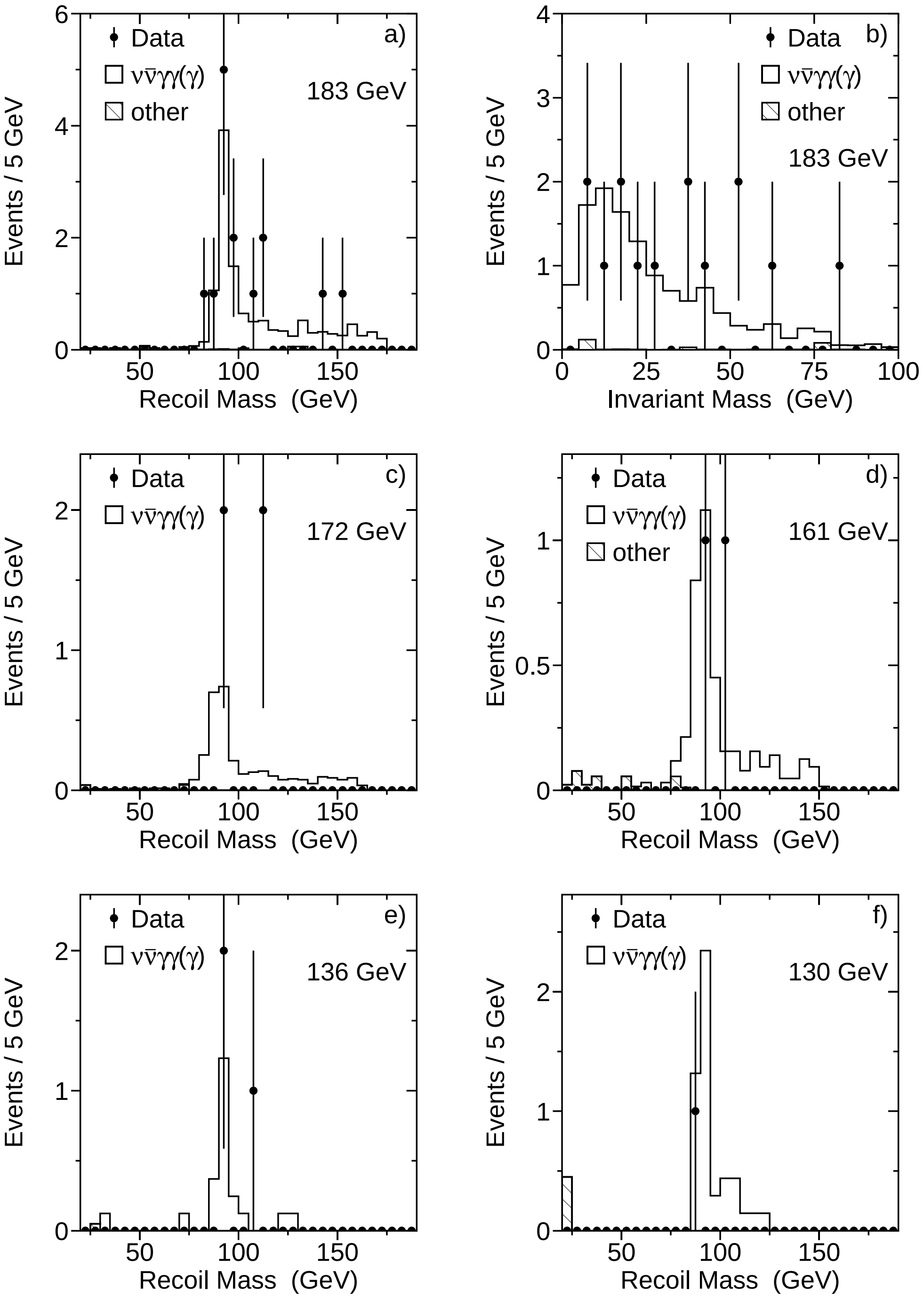

Figure C.11: *Distributions of recoil (a,c,d,e,f) and invariant mass (b) for* $\sqrt{s}$ = 183 GeV *(a,b),* 172 GeV *(c),* 161 GeV *(d),* 136 GeV *(e), and* 130 GeV *(f) for the multi-photon subsample.*

Bibliography

[1] S.L. Glashow, Nucl. Phys. **22** (1961) 579;
S. Weinberg, Phys. Rev. Lett. **19** (1967) 1264;
A. Salam, *Elementary Particle Theory*, ed. N. Svartholm, Stockholm, (Almquist and Wiksell, 1968), p. 367.

[2] C. Caso *et al.*, *Review of Particle Physics*, Eur. Phys. J. **C 3** (1998) 1.

[3] P.W. Higgs, Phys. Lett. **12** (1964) 132;
F. Englert and R. Brout, Phys. Rev. Lett. **13** (1964) 321;
G.S. Guralnik *et al.*, Phys. Rev. Lett. **13** (1964) 585.

[4] L. Maiani, Proc. Summer School on Particl Physics, Gif-sur-Yvette, 1979 (IN2P3, Paris, 1980) p. 3;
G. 't Hooft, in: G. 't Hooft *et al.*, eds., *Recent Developments in Field Theories* (Plenum Press, New York, 1980);
E. Witten, Nucl. Phys. **B 188** (1981) 513;
R.K. Kaul, Phys. Lett. **B 109** (1982) 19.

[5] Y.A. Gol'fand and E.P. Likhtman, Sov. Phys. JETP **13** (1971) 323.

[6] D.V. Volkhov and V.P. Akulov, Phys. Lett. **B 46** (1973) 109;
J. Wess and B. Zumino, Nucl. Phys. **B 70** (1974) 39;
P. Fayet and S. Ferrara, Phys. Rep. **C 32** (1977) 249;
A. Salam and J. Strathdee, Fortschr. Phys. **26** (1978) 57.

[7] H.P. Nilles, Phys. Rep. **110** (1984) 1;
H.E. Haber and G.L. Kane, Phys. Rep. **117** (1985) 75;
R. Barbieri, Nuovo Cimento **11** no.4 (1988) 1.

[8] M. Dine and A.E. Nelson, Phys. Rev. **D 48**, (1993) 1277;
M. Dine, A.E. Nelson and Y. Shirman, Phys. Rev. **D 51**, (1995) 1362;
M. Dine, A.E. Nelson, Y. Nir and Y. Shirman, Phys. Rev. **D 53**, (1996) 2658.

[9] E. Cremmer, S. Ferrara, C. Kounnas and D.V. Nanopoulos, Phys. Lett. **B 133** (1983) 61.

[10] J. Ellis, A. Lahanas, D.V. Nanopoulos and K. Tamvakis, Phys. Lett. **B 134** (1984) 429.

[11] J. Ellis, C. Kounnas and D.V. Nanopoulos, Nucl. Phys. **B 241** (1984) 406.

[12] J. Ellis, C. Kounnas and D.V. Nanopoulos, Nucl. Phys. **B 247** (1984) 373.

[13] L.J. Hall, J. Lykken and S. Weinberg, Phys. Rev. **D 27** (1983) 2359.

[14] S.K. Soni and H.A. Weldon, Phys. Lett. **B 126** (1983) 215;
Y. Kawamura, H. Murayama and M. Yamaguchi, Phys. Rev. **D 51** (1995) 1337.

[15] S. Ambrosanio and B. Mele, Phys. Rev. **D 53** (1996) 2541.

[16] N. Arkani-Hamed, S. Dimopoulos and G. Dvali, Phys. Lett. **B 429** (1998) 263.

[17] K. Hagiwara and M.L. Stong, Z. Phys. **C 62** (1994) 99.

[18] A.G. Akeroyd, Phys. Lett. **B 368** (1996) 89.

[19] A. Stange, W. Marciano and S. Willenbrock, Phys. Rev. **D 49** (1994) 1354.

[20] H. Haber, G. Kane and T. Sterling, Nucl. Phys. **B 161** (1979) 493.

[21] J.F. Gunion, R. Vega and J. Wudka, Phys. Rev. **D 42** (1990) 1673.

[22] A. Barroso, L. Brücher and R. Santos, Phys. Rev. **D 60** (1999) 035005.

[23] L. Brücher and R. Santos, *Experimental Signatures of Fermiophobic Higgs Bosons*, hep-ph/9901293, 1999.

[24] J. Ellis, M.K. Gaillard and D.V. Nanopoulos, Nucl. Phys. **B 106** (1976) 292.

[25] A.D. Dolgov, L.B. Okun and V.I. Zakharov, Nucl. Phys. **B 41** (1972) 197.

[26] E. Ma and J. Okada, Phys. Rev. Lett. **41** (1978) 287.

[27] K.J.F. Gaemers, R. Gastmans and F.M. Renard, Phys. Rev. **D 19** (1979) 1605.

[28] F. Halzen and A.D. Martin, *Quarks & Leptons: An Introductory Course in Modern Particle Physics*, (Wiley, 1984).

[29] F. Zwirner, in 1997 European School of High-Energy Physics, 25 May–7 June 1997, Menstrup, Denmark, ed. N. Ellis and M. Neubert, (CERN, Geneva, Switzerland (CERN 98-03), 1998), p. 293.

[30] M. Gell-Mann, Acta Phys. Austriaca Suppl. **IX** (1972) 733;
H. Fritsch and M. Gell-Mann, 16th International Conference on High Energy Physics, 1972, Batavia, ed. J.D. Jackson and A. Roberts, (National Accelerator Laboratory, 1972);
H. Fritzsch, M. Gell-Mann and H. Leytwyler, Phys. Lett. **B 47** (1973) 365;
D.J. Gross and F. Wilczek, Phys. Rev. Lett. **30** (1973) 1343;
D.J. Gross and F. Wilczek, Phys. Rev. **D 8** (1973) 3633;
H.D. Politzer, Phys. Rev. Lett. **30** (1973) 1346;
G. 't Hooft, Nucl. Phys. **B 33** (1971) 173.

[31] N. Cabibbo, Phys. Rev. Lett. **10** (1963) 531,
M. Kobayashi and K. Maskawa, Prog. Theo. Phys. **49** (1973) 652.

[32] P. McNamara, *Report from the LEP Higgs Working Group*, Talk given at the LEP C, CERN, Geneva, September 1999.

[33] Z. Szillási, *Direct and Indirect SM Higgs Search at LEP*, Talk given at EPS99 in Tampere, Finnland, July 1999,
`http://l3www.cern.ch/conferences/ps/Szillasi_EPS99.ps.gz`.

[34] H. Yukawa, Proc. Phys. Math. Soc. Jap. **17** (1935) 48.

[35] Super-Kamiokande Collab., Y. Fukuda *et al.*, Phys. Rev. Lett. **81** (1998) 1562.

[36] R.D. Field and R.P. Feynman, Nucl. Phys. **B 136** (1978) 1.

[37] V.D. Barger and R.J.N. Phillips, *Collider Physics*, volume 71 of *Frontiers in Physics*, (Addison-Wesley, Redwood City, California, 1987).

[38] S. Jadach, B.F.L. Ward and Z. Wąs, Comp. Phys. Comm. **79** (1994) 503.

[39] D.R. Yennie, S.C. Frautschi and H. Suura, Ann. Phys. **13** (1961) 379.

[40] G. Montagna, O. Nicrosini and F. Piccinini, Comp. Phys. Comm. **98** (1996) 206.

[41] G. Montagna, M. Moretti, O. Nicrosini and F. Piccinini, Nucl. Phys. **B 541** (1999) 31.

[42] F.A. Berends *et al.*, Nucl. Phys. **B 301** (1988) 583.

[43] P.A.M. Dirac, Proc. R. Soc. London **A 117** (1928) 610.

[44] C.D. Anderson, Phys. Rev. **43** (1933) 491.

[45] P. Fayet and S. Ferrara, Phys. Rep. **32** (1977) 251.

[46] M.E. Peskin, in 1996 European School of High-Energy Physics, 1–14 Sep 1996, Carry-le-Rouet, France, ed. N. Ellis and M. Neubert, (CERN, Geneva, Switzerland (CERN-97-03), 1997), p. 304.

[47] U. Amaldi, W. de Boer and H. Fürstenau, Phys. Lett. **B 260** (1991) 47.

[48] P. Langacker and M. Luo, Phys. Rev. **D 44** (1991) 817.

[49] J. Ellis, S. Kelley and D.V. Nanopoulos, Nucl. Phys. **B 373** (1992) 55.

[50] P. Fayet, Phys. Lett. **B 69** (1977) 489;
G. Farrar and P. Fayet, Phys. Lett. **B 76** (1978) 575.

[51] P. Fayet, Nucl. Phys. **B 90** (1975) 104;
A. Salam and J. Strathdee, Nucl. Phys. **B 87** (1975) 85.

[52] J. Ellis, J.S. Hagelin, D.V. Nanopoulos, K. Olive and M. Srednicki, Nucl. Phys. **B 238** (1984) 453.

[53] S. Wolfram, Phys. Lett. **B 82** (1979) 65.

[54] P.F. Smith and J.R.J. Bennett, Nucl. Phys. **B 149** (1979) 525.

[55] G.R. Farrar, Nucl. Phys. Proc. Suppl. **62** (1998) 485.

[56] K. Inoue, A. Kakuto, H. Komatsu and S. Takeshita, Prog. Theor. Phys. **67** (1982) 1889.

[57] K. Inoue, A. Kakuto, H. Komatsu and S. Takeshita, Prog. Theor. Phys. **68** (1982) 927.

[58] L. Ibanez and G.G. Ross, Phys. Lett. **B 110** (1982) 215.

[59] L. Alvarez-Gaume, M. Claudson and M.B. Wise, Nucl. Phys. **B 207** (1982) 96.

[60] J. Ellis, L. Ibanez and G.G. Ross, Phys. Lett. **B 113** (1982) 283.

[61] L. Alvarez-Gaume, J. Polchinski and M.B. Wise, Nucl. Phys. **B 221** (1983) 495.

[62] L.E. Ibanez and C. Lopez, Phys. Lett. **B 126** (1983) 54.

[63] J. Ellis, J.S. Hagelin, D.V. Nanopoulos and K. Tamvakis, Phys. Lett. **B 125** (1983) 275.

[64] J.F. Gunion, H.E. Haber, G. Kane and S. Dawson, *The Higgs Hunter's Guide*, volume 80 of *Frontiers in Physics*, (Addison-Wesley, Redwood City, California, 1990).

[65] S.L. Glashow and S. Weinberg, Phys. Rev. **D 15** (1977) 1958.

[66] S. Dimopoulos and H. Georgi, Nucl. Phys. **B 193** (1981) 150.

[67] L. Girardello and M. Grisaru, Nucl. Phys. **B 194** (1982) 65.

[68] J. Goldstone, Nuovo Cimento **19** (1961) 154.

[69] J. Goldstone, A. Salam and S. Weinberg, Phys. Rev. **127** (1962) 965.

[70] J. Ellis, in 1998 European School of High-Energy Physics, 23 Aug–5 Sep 1998, St. Andrews, Scotland, ed. N. Ellis and J. March-Russell, (CERN, Geneva, Switzerland (CERN 99-04), 1999), p. 64.

[71] P. Fayet, Phys. Lett. **B 84** (1979) 421.

[72] P. Fayet, Phys. Lett. **B 86** (1979) 272.

[73] S. Dreser and B. Zumino, Phys. Rev. Lett. **38** (1977) 1433;
D.V. Volkov and V.A. Soroka, JETP Lett. **18** (1973) 312.

[74] For a review on gauge-mediated supersymmetry breaking see
G.F. Giudice and R. Rattazzi, *Theories with Gauge-Mediated Supersymmetry Breaking*, Submitted to Phys. Rep., CERN-TH/97-380, hep-ph/9801271.

[75] J.A. Bagger, K. Matchev, D.M. Pierce and R.J. Zhang, Phys. Rev. Lett. **78** (1997) 1002; erratum *ibid. 78* (1997) 2497.

[76] S. Dimopoulos, S. Thomas and J.D. Wells, Nucl. Phys. **B 488** (1997) 39.

[77] H. Baer, F. Paige, S.D. Protopopescu and X. Tata, in Proceedings of the Workshop on Physics at Current Accelerators and Supercolliders, Argonne, Ill., Jun 2–5, 1993, ed. J.L. Hewitt, A.R. White and D. Zeppenfeld, (Argonne National Laboratory, 1993), p. 703.

[78] S. Ambrosanio, *Introduction to Gauge-Mediated Supersymmetry Breaking Models*, Invited Talk at the Humboldt University Berlin, November 1998, `http://www.desy.de/~ambros/MyPhysics.html`.

[79] J. Ellis, K. Enqvist and D.V. Nanopoulos, Phys. Lett. **B 147** (1984) 99.

[80] J. Ellis, K. Enqvist and D.V. Nanopoulos, Phys. Lett. **B 151** (1985) 357.

[81] S. Ambrosanio, G. Kane, G. Kribs, S. Martin and S. Mrenna, Phys. Rev. **D 54** (1996) 5395.

[82] J.A. Bagger, K. Matchev, D.M. Pierce and R. Zhang, Phys. Rev. **D 55** (1997) 3188.

[83] A. Bartl, H. Fraas and W. Majerotto, Nucl. Phys. **B 278** (1986) 1.

[84] S. Ambrosanio and B. Mele, Phys. Rev. **D 52** (1995) 3900.

[85] S. Ambrosanio, G.D. Kribs and S.P. Martin, Phys. Rev. **D 56** (1997) 1761.

[86] S. Katsanevas and P. Morawitz, Comp. Phys. Comm. **112** (1998) 227.

[87] A. Pohl, *Search for Scalar Muons with the L3 Detector at* $\sqrt{s} = 183$ GeV, Diplomarbeit, Humboldt-Universität zu Berlin, 1998.

[88] H.P. Nilles, Phys. Rep. **110** (1984) 1.

[89] P. Nath, R. Arnowitt and A.H. Chamseddine, *Applied* $N = 1$ *Supergravity*, (World Scientific, Singapore, 1984).

[90] R. Arnowitt and P. Nath, in Particles and Fields, Proceedings of the 7th Summer School Jorge Andre Swieca, Sao Paulo, Brazil, 10–23 January 1993, ed. O.J.P. Eboli and V.O. Rivelles, (World Scientific, Singapore, 1994).

[91] T. Hebbeker, *Can the Sneutrino be the Lightest Supersymmetric Particle?*, Preprint HUB-EP-99/47, Humboldt-Universität zu Berlin, 1999.

[92] G.L. Kane and G. Mahlon, Phys. Lett. **B 408** (1997) 222.

[93] P. Fayet, Phys. Lett. **B 69** (1977) 489.

[94] P. Fayet, Phys. Lett. **B 70** (1977) 461.

[95] J. Ellis, J.L. Lopez and D.V. Nanopoulos, Phys. Lett. **B 394** (1997) 354.

[96] I. Antoniadis, J. Ellis, J. Hagelin and D.V. Nanopoulos, Phys. Lett. **B 194** (1987) 231.

[97] J. Ellis, J. Hagelin, S. Kelley and D.V. Nanopoulos, Nucl. Phys. **B 311** (1989) 1.

[98] J.L. Lopez, D.V. Nanopoulos and A. Zichichi, Phys. Rev. **D 49** (1994) 343.

[99] J.L. Lopez, D.V. Nanopoulos and A. Zichichi, Int. J. Mod. Phys. **A 10** (1995) 4241.

[100] J.L. Lopez and D.V. Nanopoulos, Phys. Rev. **D 55** (1997) 4450.

[101] J.L. Lopez, D.V. Nanopoulos and A. Zichichi, Phys. Rev. Lett. **77** (1996) 5168.

[102] J.L. Lopez, D.V. Nanopoulos and A. Zichichi, Phys. Rev. **D 55** (1997) 5813.

[103] P. Fayet, Phys. Lett. **B 117** (1982) 460.

[104] O. Nachtmann, A. Reiter and M. Wirbel, Z. Phys. **C 27** (1985) 577.

[105] A. Brignole, F. Feruglio and F. Zwirner, Nucl. Phys. **B 501** (1997) 332.

[106] A. Brignole, F. Feruglio and F. Zwirner, Nucl. Phys. **B 516** (1998) 13.

[107] S. Park, in Proceedings of the 10th Topical Workshop on Proton-Antiproton Collider Physics, Batavia, IL, 9–13 May 1995, ed. R. Raja and J. Yoh, (AIP, New York, 1995), p. 62.

[108] CDF Collab., F. Abe *et al.*, Phys. Rev. Lett. **81** (1998) 1791.

[109] S. Dimopoulos, M. Dine, S. Raby and S. Thomas, Phys. Rev. Lett. **76** (1996) 3494.

[110] S. Ambrosanio, G. Kane, G. Kribs, S. Martin and S. Mrenna, Phys. Rev. Lett. **76** (1996) 3498.

[111] D. Stump, M. Wiest and C.-P. Yuan, Phys. Rev. **D 54** (1996) 1936.

[112] G. Dvali, G. Giudice and A. Pomarol, Nucl. Phys. **B 478** (1996) 31.

[113] S. Dimopoulos, S. Thomas and J. Wells, Phys. Rev. **D 54** (1996) 3283.

[114] K. Baku, C. Kolda and F. Wilczek, Phys. Rev. Lett. **77** (1996) 3070.

[115] A. Faraggi, Phys. Lett. **B 387** (1996) 775.

[116] A. Cohen, D. Kaplan and A. Nelson, Phys. Lett. **B 388** (1996) 588.

[117] M. Dine, Y. Nir and Y. Shirman, Phys. Rev. **D 55** (1997) 1501.

[118] J.L. Lopez and D.V. Nanopoulos, Mod. Phys. Lett. **A 11** (1996) 2473.

[119] S. Ambrosanio, G. Kane, G. Kribs, S. Martin and S. Mrenna, Phys. Rev. **D 55** (1996) 1372.

[120] J.C. Long, H.W. Chan and J.C. Price, Nucl. Phys. **B 539** (1999) 23.

[121] W. Taylor IV, in High Energy Physics and Cosmology. Proceedings, Summer School, Trieste, Italy, June 2–July 4, 1997, ed. E. Gava *et al.*, (World Scientific, Singapore, 1998), p. 192.

[122] P. Horava and E. Witten, Nucl. Phys. **B 460** (1996) 506.

[123] P. Horava and E. Witten, Nucl. Phys. **B 475** (1996) 94.

[124] I. Antoniadis, N. Arkani-Hamed, S. Dimopoulos and G. Dvali, Phys. Lett. **B 436** (1998) 257.

[125] G. Shiu and S.H.H. Tye, Phys. Rev. **D 58** (1998) 106007.

[126] Z. Kakushadze and S.H.H. Tye, Nucl. Phys. **B 548** (1999) 180.

[127] G.F. Giudice, R. Rattazzi and J.D. Wells, Nucl. Phys. **B 544** (1999) 3.

[128] M. Lamont, in Proceedings of the Workshop on LEP-SPS Performance - Chamonix IX -, Chamonix, January 25–29, 1999, ed. J. Poole, (CERN, Geneva, Switzerland, 1999), p. 163.

[129] The LEP Polarization Collaboration, L. Arnaudon *et al.*, Phys. Lett. **B 284** (1992) 431.

[130] L. Arnaudon *et al.*, Z. Phys. **C 66** (1995) 45.

[131] The LEP Energy Working Group Collaboration, *LEP Energy Calibration above the* W *Pair-Production Threshold*, Preprint LEP ECAL/98-02, ICHEP-98/352, CERN, 1998.

[132] M.D. Hildreth, *Evaluation of the LEP Centre-of-Mass Energy above the* W *Pair-Production Threshold*, Preprint hep-ex/9810005, CERN, 1998, to be published in proceedings of the "International Conference on High Energy Physics (ICHEP98)", Vancouver, BC, 23–29 July 1998.

[133] The LEP Energy Working Group Collaboration, A. Blondel *et al.*, *Evaluation of the LEP Centre-of-Mass Energy above the* W*-Pair Production Threshold*, Preprint CERN-EP/98-191, CERN-SL/98-073, CERN, 1998, Submitted to Eur. Phys. J. **C**.

[134] L3 Collab., B. Adeva *et al.*, Nucl. Inst. Meth. **A 289** (1990) 35.

[135] ALEPH Collab., D. Decamp *et al.*, Nucl. Inst. Meth. **A 294** (1990) 127.

[136] DELPHI Collab., P. Aarnio *et al.*, Nucl. Inst. Meth. **A 303** (1991) 233.

[137] OPAL Collab., K. Ahmet *et al.*, Nucl. Inst. Meth. **A 305** (1991) 275.

[138] A. Adam *et al.*, Nucl. Inst. Meth. **A 383** (1996) 342.

[139] T. Van Rhee, F. Filthaut and F. Linde, *VSAT Status and Performance*, L3 Internal Note 2117, 1997.

[140] W.R. Leo, *Techniques for Nuclear and Particle Physics Experiments: A How-to Approach*, (Springer-Verlag, Berlin, Heidelberg, New York, 1994).

[141] H. Ma *et al.*, Nucl. Inst. Meth. **A 274** (1989) 113.

[142] H. Ma, H. Newman, R.Y. Zhu and R. Hamm, Nucl. Inst. Meth. **A 281** (1989) 469.

[143] A. Favara *et al.*, *Calibration of the L3 BGO Calorimeter Using an RFQ Accelerator*, 1999, Submitted to Nucl. Phys. **B**.

[144] G. Morand, *Développement et Utilisation du Système de Moniteur au Xénon du Calorimétre Électromagnétique de l'Expérience L3*, Ph.D. Thesis, University of Geneva, L3 Internal Note 1016, 1991.

[145] C. Cecchi *et al.*, *BGO Calibration at LEP 2*, L3 Internal Note 1892, 1995.

[146] J.A. Bakken *et al.*, L3 BGO Collab., *Calibration of the L3 Electromagnetic Calorimeter in Electron Beam*, L3 Internal Note 1712, 1995.

[147] G. Basti *et al.*, Nucl. Inst. Meth. **A 374** (1996) 293.

[148] M. Acciarri *et al.*, Nucl. Inst. Meth. **A 351** (1994) 300.

[149] K. Deiters *et al.*, Nucl. Inst. Meth. **A 323** (1992) 162.

[150] G. Alkhazov *et al.*, *Forward Tracking Chamber (FTC) in the L3 Detector. Part 1 General Description*, L3 Internal Note 1862, 1995.

[151] D. Prokofiev *et al.*, *Forward Tracking Chamber (FTC) in the L3 Detector. Part 2. The FTC Performance and Alignment in the L3 Setup.*, L3 Internal Note 1895, 1995.

[152] U. Uwer, *The L3 Scintillation Counter System: Description and Status*, L3 Internal Note 2003, 1996.

[153] O. Adriani *et al.*, Nucl. Inst. Meth. **A 302** (1991) 53.

[154] G. Chiefari *et al.*, Nucl. Inst. Meth. **A 277** (1989) 187.

[155] S. Lanzano *et al.*, Nucl. Inst. Meth. **A 289** (1990) 335.

[156] M. Chemarin *et al.*, Nucl. Inst. Meth. **A 349** (1994) 345.

[157] I.C. Brock *et al.*, Nucl. Inst. Meth. **A 381** (1996) 236.

[158] R. Bizzarri *et al.*, Nucl. Inst. Meth. **A 283** (1989) 799.

[159] R. Bizzarri, F. Cesaroni, S. Gentile, G. Lunadei, M. Fukushima and T. Hebbeker, Nucl. Inst. Meth. **A 317** (1992) 463.

[160] R. Bagnaia, R. Bizzarri, F. Cesaroni, S. Gentile and G. Lunadei, Nucl. Inst. Meth. **A 323** (1992) 528.

[161] R. Bagnaia, R. Bizzarri, F. Cesaroni, S. Gentile and T. Hebbeker, Nucl. Inst. Meth. **A 324** (1993) 101.

[162] M. Bourquin *et al.*, Nucl. Inst. Meth. **A 411** (1998) 275.

[163] P. Bene *et al.*, Nucl. Inst. Meth. **A 306** (1991) 150.

[164] T. Dai and M. Fukushima, *L3 Level-1 Muon Trigger*, L3 Internal Note 668, 1989.

[165] Y. Bertsch *et al.*, Nucl. Inst. Meth. **A 340** (1994) 309.

[166] S.P. Beingessner *et al.*, Nucl. Inst. Meth. **A 340** (1994) 322.

[167] C. Dionisi *et al.*, Nucl. Inst. Meth. **A 336** (1993) 78.

[168] R. Brun *et al.*, GEANT 3, CERN DD/EE/84-1 (Revised), September 1987.

[169] H. Fesefeldt, RWTH Aachen, PITHA 85/02, 1985.

[170] S. Jadach *et al.*, Comp. Phys. Comm. **70** (1992) 305;
S. Jadach *et al.*, Phys. Lett. **B 353** (1995) 349;
S. Jadach *et al.*, Phys. Lett. **B 353** (1995) 362.

[171] The LEP Energy Working Group Collaboration, *Energies for LEP 1.5 Run*, Preprint LEP ECAL/97-04, CERN, 1997.

[172] The LEP Energy Working Group Collaboration, *Preliminary LEP Energy Calibration for 1997 Data*, Preprint LEP ECAL/98-01, CERN, 1998.

[173] The LEP Energy Working Group Collaboration, *Evaluation of the LEP Centre-of-Mass Energy for Data Taken in 1998*, Preprint LEP ECAL/99-01, CERN, 1999.

[174] L3 Collab., M. Acciarri *et al.*, Phys. Lett. **B 370** (1996) 195.

[175] L3 Collab., M. Acciarri *et al.*, Phys. Lett. **B 407** (1997) 361.

[176] L3 Collab., M. Acciarri *et al.*, Phys. Lett. **B 436** (1998) 437.

[177] S. Blyth, July 1999, Private Communication.

[178] B.F.L. Ward, S. Jadach, M. Melles and S.A. Yost, Phys. Lett. **B 450** (1999) 262.

[179] S. Jadach, W. Placzek and B.F.L. Ward, Phys. Lett. **B 390** (1997) 298.

[180] I.C. Brock, `Mn_Fit:` *A Fitting and Plotting Package Using* `MINUIT`, L3 Internal Note 918, 1996, The function used is labelled as ”Crystal Ball line shape“.

[181] M. Gataullin, *RFQ-Calibration*, L3 Internal Note 2422, 1999.

[182] D. Duchesneau, Private Communication, 1999.

[183] F.A. Berends and R. Kleiss, Nucl. Phys. **B 186** (1981) 22.

[184] D. Karlen, Nucl. Phys. **B 289** (1987) 23.

[185] F.A. Berends, P.H. Daverfeldt and R. Kleiss, Nucl. Phys. **B 253** (1985) 441.

[186] F.A. Berends, R. Pittau and R. Kleiss, Comp. Phys. Comm. **85** (1995) 437.

[187] L3 Collab., B. Adeva *et al.*, Phys. Lett. **B 275** (1992) 209.

[188] L3 Collab., O. Adriani *et al.*, Phys. Lett. **B 292** (1992) 463.

[189] L3 Collab., M. Acciarri *et al.*, Phys. Lett. **B 431** (1998) 199.

[190] L3 Collab., M. Acciarri *et al.*, *Precise Determination of Z Parameters*, Preprint EPS-HEP99/259, L3, 1999.

[191] A. Favara and M. Pieri, *Confidence level estimation and analysis optimisation*, Preprint DFF-278/4/1997, INFN, 1997.

[192] The LEP Collaborations ALEPH, DELPHI, L3, OPAL, the LEP Working Group for Higgs Boson Searches, *Lower Bound for the Standard Model Higgs Boson Mass from Combining the Results of the Four LEP Experiments*, Preprint CERN-EP/98-046, CERN, 1998.

[193] The L3 Collaboration, M. Acciarri *et al.*, Phys. Lett. **B 415** (1997) 299.

[194] The L3 Collaboration, M. Acciarri *et al.*, Phys. Lett. **B 444** (1998) 503.

[195] L3 Collab., M. Acciarri *et al.*, *Search for Low Scale Gravity Effects in* e^+e^- *Collisions at LEP*, Preprint L3 182, L3, 1999, Accepted by Phys. Lett. **B**.

[196] G. Carlino, C. Dionisi and S. Giagu, *Superlight Gravitino Mass Limit from Single Photon Events in* e^+e^- *Collisions at* $\sqrt{s} = 183$ GeV *at LEP*, L3 Internal Note 2222, 1998.

[197] OPAL Collab., K. Ackerstaff *et al.*, Eur. Phys. J. **C 1** (1998) 425.

[198] L3 Collab., M. Acciarri *et al.*, *Search for the Standard Model Higgs Boson in* e^+e^- *Interactions at* $\sqrt{s} = 189$ GeV, Preprint CERN-EP/99-080, CERN, 1999, Accepted by Phys. Lett. **B**.

[199] L3 Collab., M. Acciarri *et al.*, Eur. Phys. J. **C 4** (1998) 207.

[200] T. Sjöstrand, Comp. Phys. Comm. **82** (1994) 74.

[201] A. Djouadi, J. Kalinowski and M. Spira, Comp. Phys. Comm. **108** (1998) 56.

[202] L3 Collab., M. Acciarri *et al.*, *Search for Higgs Boson Decaying into Two Photons in* $\mathrm{e^+e^-}$ *Interactions at* $\sqrt{s} = 189$ GeV, Preprint EPS-HEP99/238, L3, 1999.

[203] The LEP Collaborations ALEPH, DELPHI, L3, OPAL, the LEP Electroweak Working Group and the SLD Heavy Flavor and Electroweak Groups, *A Combination of Preliminary Electroweak Measurements and Constraints on the Standard Model*, Preprint LEPEWWG/99-01, CERN, 1999.

[204] VENUS Collab., K. Abe *et al.*, Phys. Lett. **B 232** (1989) 431.

[205] ASP Collab., C. Hearty *et al.*, Phys. Rev. **D 39** (1989) 3207.

[206] CELLO Collab., H.J. Behrend *et al.*, Phys. Lett. **B 215** (1988) 186.

[207] MAC Collab., W.T. Ford *et al.*, Phys. Rev. **D 33** (1986) 3472.

[208] H. Wu, MARK J experiment, Ph.D. Thesis, Univ. Hamburg, 1986.

[209] ALEPH Collab., D. Buskulic *et al.*, Phys. Lett. **B 313** (1993) 520.

[210] DELPHI Collab., P. Abreu *et al.*, Z. Phys. **C 74** (1997) 577.

[211] OPAL Collab., R. Akers *et al.*, Z. Phys. **C 65** (1995) 47.

[212] DELPHI Collab., P. Checchia *et al.*, *Photon Events with Missing Energy at LEP 2*, Preprint EPS-HEP99/141, DELPHI, 1999.

[213] ALEPH Collab., R. Barate *et al.*, Phys. Lett. **B 429** (1998) 201.

[214] ALEPH Collab., *Single and Multi-Photon Production in* $\mathrm{e^+e^-}$ *Collisions at a Centre-of-Mass Energy of* 188.6 GeV, Preprint EPS-HEP99/429, ALEPH, 1999.

[215] OPAL Collab., G. Abbiendi *et al.*, Eur. Phys. J. **C 8** (1999) 23.

[216] OPAL Collab., *Search for Anomalous Photonic Events with Missing Energy in* e^+e^- *Collisions at* $\sqrt{s} = 189$ GeV, Preprint EPS-HEP99/62, OPAL, 1999.

[217] The LEP Collaborations ALEPH, DELPHI, L3, OPAL, the LEP 2 SUSY Working Group, *Acoplanar Photon Pairs*, Preprint LEPSUSYWG/99-04.2, CERN, 1999.

[218] ALEPH Collab., *Search for Gauge-Mediated SUSY Breaking Topologies at* $\sqrt{s} \sim 189$ GeV, Preprint EPS-HEP99/420, ALEPH, 1999.

[219] DØ Collab., B. Abbott *et al.*, Phys. Rev. Lett. **80** (1998) 442.

[220] L. Giusti, A. Romanino and A. Strumia, Nucl. Phys. **B 550** (1999) 3.

[221] See for example:
Conference on Higgs and Supersymmetry: Search & Discovery, 8–11 March, 1999, Gainesville, Florida,
`http://www.phys.ufl.edu/~rfield/higgs_susy.html`;
SUSY 99, 7th International Conference on Supersymmetries in Physics, 14–19 June, 1999, Fermi National Accelerator Laboratory, Batavia, Illinois,
`http://fnpx03.fnal.gov/conferences/susy99/`.

[222] J.-M. Qian, *Sensitivity to Gauge-Mediated Supersymmetry Breaking Models of the Fermilab Upgraded Tevatron Collider*, Preprint FERMILAB-FN-680, DØ, 1998.

[223] H. Baer, P.G. Mercadante, F. Paige, X. Tata and Y. Wang, Phys. Lett. **B 435** (1998) 109.

[224] I. Hinchliffe and F.E. Paige, *Measurements in Gauge-Mediated SUSY Breaking Models at LHC*, Preprint LBNL-42401, BNL-HET-98/37, LBNL, BNL, 1998.

[225] See, *e.g.*, the webpage `http://hepwww.physics.yale.edu/lc/`.

[226] S. Ambrosanio and G.A. Blair, *Measuring Gauge-Mediated Supersymmetry Breaking Parameters at a* 500 GeV e^+e^- *Linear Collider*, Preprint CERN-TH/99-109, DESY 98-199, CERN, DESY, 1999, Submitted to Eur. Phys. J. **C**.

[227] P. Molnár and D. Ruschmeier, *Searching for Fourth Generation Stable Heavy Neutrinos with L3 – a Feasibility Study*, L3 Internal Note 2321, 1998.

[228] ALEPH Collab., D. Decamp *et al.*, Phys. Lett. **B 236** (1990) 511;
DELPHI Collab., P. Abreu *et al.*, Phys. Lett. **B 274** (1992) 230;
L3 Collab., B. Adeva *et al.*, Phys. Lett. **B 251** (1990) 321;
OPAL Collab., G. Alexander *et al.*, Z. Phys. **C 52** (1991) 175.

[229] J. Busenitz, *Comparison of Single Photon Event Generators at LEP 2 Energies*, L3 Internal Note 2172, 1997.

[230] C. Cecchi, *Status Report BGO Calibrations*, L3 Internal Note 2080, 1997.

[231] C. Cecchi, *BGO Calibrations*, L3 Internal Note 2089, 1997.

[232] V. Chaturvedi, A. Favara, M. Gataullin and A. Shvorob, *BGO Calibration with RFQ*, L3 Internal Note 2206, 1997.

[233] M. Gataullin, *BGO Calibration*, L3 Internal Note 2319, 1998.

[234] A. Hirstius, *Measurement of Bhabha Scattering at* $\sqrt{s} = 189$ GeV *and the Running of* α_{QED} *with the L3 Detector*, Diplomarbeit, Humboldt-Universität zu Berlin, 1999.

[235] J.H. Field, Phys. Lett. **B 323** (1994) 432;
J.H. Field and T. Riemann, Comp. Phys. Comm. **94** (1996) 53.

Acknowledgements

First and foremost, I thank my advisor Thomas Hebbeker for the support and guidance he lent me throughout the time of this dissertation.

I owe a debt of gratitude to Alvise Favara who answered all of my many questions concerning all steps of the analysis and who contributed in a direct and important way to this work since his 1997 photon selection has been starting point of my research.

My collaboration with Peter Molnár and Andreas Kopp has proven to be extremely fruitful and their friendly competition has improved the quality of my work. Together with Martin W. Grünewald and Ho Jong Lee, they guided me through the jungle of statistical methods.

I would like to thank Professor S.C.C. Ting for his impressive leadership and the high density of citable instructions on presentation and analysis issues he provided the L3 community with.

The running of the LEP ring and the L3 experiment and the analysis of its data requires literally hundreds of people. I wish to express my gratitude to the CERN accelerator division for the excellent performance of the LEP machine. I acknowledge the effort of the physicists, engineers and technicians who have participated in the construction and maintenance of this experiment.

The SUSY group in L3 has also proved to be an invaluable source of learning. I had many helpful conversations with Sylvie Rosier, Michel Chemarin, Jean Fay, and Alfons Weber about SUSY interpretations, single photon studies and BGO topics. Marco Pieri helped me overcome many difficulties I had especially in the beginning of my work in the L3 collaboration.

I enjoyed very much the pleasant working environment provided by the members of the particle physics groups at Humboldt University in Berlin, especially during lunch and coffee breaks. My colleagues from the L3 DESY Zeuthen group always offered a great hospitality when I came to Zeuthen as a guest.

A final thank you goes to Martina Allendorf who as a non-specialist has read through all this strange stuff and has considerably improved my English.

Lebenslauf

Persönliche Daten

Name : Daniel Ruschmeier
Geburtsdatum : 16.12.1968
Geburtsort : Minden
Wohnort : 10961 Berlin
Straße : Solmsstraße 6
Telefon : 030-6948515
E-mail : rusch@physik.hu-berlin.de

Schulbildung	1975-1979	Grundschule Heerstraße in Troisdorf
	1979-1988	Städtisches Gymnasium Troisdorf-Sieglar
	1988	Abitur
Wehrdienst	1988-1989	
Studium	1989-	Albert-Ludwigs-Universität Freiburg
	1991	Vordiplom in Physik
	1991-1992	University of Sussex at Brighton, Großbritannien, ERASMUS Stipendium
	1993	Praktikum im Positronen-Emissions-Tomographie-Labor des Max-Planck-Instituts für neurologische Forschung in Köln
	1994	Forschungsaufenthalt am CERN im Rahmen der Diplomarbeit und Mitwirkung bei der Datenauswertung des Experiments PS202 (JETSET) als Technical Student
	1995	Diplom in Physik
	1996-1999	Wissenschaftlicher Mitarbeiter der Humboldt-Universität zu Berlin und Mitglied des Graduiertenkollegs „Strukturuntersuchungen, Präzisionstests und Erweiterungen des Standardmodells der Elementarteilchenphysik“

Hiermit erkläre ich, daß ich diese Arbeit selbständig verfaßt habe und keine anderen als die angegebenen Quellen und Hilfsmittel benutzt habe.